

VU Research Portal

Cycloaddition Reactions: Design Principles from Quantum Chemical Analyses

Yu, Song

2021

document version

Publisher's PDF, also known as Version of record

[Link to publication in VU Research Portal](#)

citation for published version (APA)

Yu, S. (2021). *Cycloaddition Reactions: Design Principles from Quantum Chemical Analyses*. [PhD-Thesis - Research and graduation internal, Vrije Universiteit Amsterdam].

General rights

Copyright and moral rights for the publications made accessible in the public portal are retained by the authors and/or other copyright owners and it is a condition of accessing publications that users recognise and abide by the legal requirements associated with these rights.

- Users may download and print one copy of any publication from the public portal for the purpose of private study or research.
- You may not further distribute the material or use it for any profit-making activity or commercial gain
- You may freely distribute the URL identifying the publication in the public portal ?

Take down policy

If you believe that this document breaches copyright please contact us providing details, and we will remove access to the work immediately and investigate your claim.

E-mail address:

vuresearchportal.ub@vu.nl

VRIJE UNIVERSITEIT

CYCLOADDITION REACTIONS

DESIGN PRINCIPLES FROM QUANTUM CHEMICAL ANALYSES

ACADEMISCH PROEFSCHRIFT

ter verkrijging van de graad Doctor of Philosophy aan
de Vrije Universiteit Amsterdam,
op gezag van de rector magnificus
prof.dr. C.M. van Praag,
in het openbaar te verdedigen
ten overstaan van de promotiecommissie
van de Faculteit der Bètawetenschappen
op dinsdag 14 december 2021 om 13.45 uur
in een bijeenkomst van de universiteit,
De Boelelaan 1105

door

Song Yu

geboren te Hubei, China

promotor: prof.dr. F.M. Bickelhaupt

copromotor: dr. T.A. Hamlin

promotiecommissie:
prof.dr. T.N. Grossmann
dr. A. De Cozar
dr. R.W.A. Havenith
prof.dr. M.A. Gruden
prof.dr. M. De Freitas

This work has been financially supported by the Netherlands Organization for Scientific Research (NWO), the China Scholarship Council (CSC), and the Dutch Astrochemistry Network (DAN).

Contents

Contents.....	V
Chapter 1 Introduction.....	1
1.1 Cycloaddition Reactions	2
1.1.1 Diels-Alder Reactions.....	2
1.1.2 1,3-Dipolar Cycloadditions.....	4
1.2 Factors Affecting the Cycloaddition Reactivity	5
1.2.1 Heteroatom.....	6
1.2.2 Geometry.....	6
1.2.3 Catalyst	8
1.2.4 External Electric Field	10
1.3 This Thesis	11
1.4 References	13
Chapter 2 Theories and Models.....	19
2.1 Quantum Chemistry.....	20
2.2 Density Functional Theory.....	21
2.3 Activation Strain Model of Reactivity.....	23
2.4 References	25
Chapter 3 A Benchmark Study of the DFT Methods for Cycloaddition Reactions.....	29
3.1 Introduction	30
3.2 Results and Discussion.....	30
3.3 Conclusions	32
3.4 References	33
Chapter 4 How Heteroatoms Affect the Diels-Alder Reactivity of 1,3-Butadienes	35
4.1 Introduction	36

4.2	Computational Details.....	38
4.3	Results and Discussion.....	40
4.3.1	Diels-Alder Reactivity of CCCC, NCCC, NCCN, OCCC, and OCCO	41
4.3.2	Diels-Alder Reactivity of CCCC, CNCC, and CNNC	44
4.3.3	Diels-Alder Reactivity of CNCC, NCNC, and NNCC.....	47
4.4	Conclusions	48
4.5	References	49
4.6	Appendices	54
Chapter 5 How Heteroatoms and Geometries Affect 1,3-Dipolar Cycloadditions of Allenes..		57
5.1	Introduction	58
5.2	Computational Details.....	60
5.3	Results and Discussion.....	62
5.3.1	1,3-Dipolar Cycloadditions of Linear Allenes	62
5.3.2	1,3-Dipolar Cycloadditions of Cyclic Allenes	68
5.4	Conclusions	73
5.5	Reference.....	74
5.6	Appendices	79
Chapter 6 How Oriented External Electric Fields Modulate Diels-Alder Reactions.....		87
6.1	Introduction	88
6.2	Computational Details.....	90
6.3	Results and Discussion.....	91
6.3.1	Definition of the Directions of Oriented External Electric Fields.....	91
6.3.2	Oriented External Electric Field in the <i>z</i> Direction	93
6.3.3	Oriented External Electric Field in the <i>y</i> Direction.....	97
6.3.4	Oriented External Electric Field in the <i>x</i> Direction.....	100
6.3.5	Inverse Electron Demand Diels-Alder Reactions	102
6.4	Conclusions	103
6.5	References	104

6.6 Appendices	109
Chapter 7 How Brønsted Acids Catalyze Aza-Diels-Alder Reactions.....	115
7.1 Introduction	116
7.2 Results and Discussion.....	118
7.2.1 Brønsted Acid-Catalyzed Reactions	118
7.2.2 Brønsted Superacid-Catalyzed Reactions	122
7.3 Conclusions	126
7.4 References	127
7.5 Appendices	131
Summary	141
Samenvatting	145
Acknowledgements.....	147
List of Publications	149

Chapter 1 Introduction

1.1 Cycloaddition Reactions

Cycloadditions are a class of chemical reactions that can be used to construct cyclic compounds from two or more unsaturated molecules. In particular, concerted cycloaddition reactions (pericyclic cycloadditions) are the most common and fundamental cycloadditions to easily furnish cyclic or polycyclic scaffolds in a single step under mild conditions. These reactions all share in common a concerted cyclic transition state where the formation of the new bonds and the breaking of the old bonds occurs simultaneously. Pericyclic cycloadditions include three main subclasses: Diels-Alder reactions, 1,3-dipolar cycloadditions, and cheletropic reactions. The first two types of reactions correspond to the addition of one π system (dienophile or dipolarophile) to the other π system (diene or dipole), whereby two σ -bonds are formed between the end of each π system. Cheletropic reactions are a class of cycloaddition reactions between a non- π system and a π system, in which two new σ bonds are made to the same atom of the non- π system. This thesis is dedicated to a study of Diels-Alder reactions and 1,3-dipolar cycloadditions because they exhibit remarkable reactivity, regioselectivity, and stereoselectivity, and are widely used in organic synthesis, material science, and biological chemistry.

1.1.1 Diels-Alder Reactions

The Diels-Alder reaction, depicted in **Figure 1.1**, introduced by Otto Diels and Kurt Alder for the first time in 1928,^[1] is a class of pericyclic reaction between a conjugated diene and an unsaturated compound (dienophile). The proceeding of the Diels-Alder reaction requires a *s-cis* structure of the diene. Therefore, the rigidity and the initial dihedral angle of the backbone are essential factors determining the Diels-Alder reactivity of the diene.^[2] More importantly, the Diels-Alder reaction relies on an interaction between a 4π -electron system of the diene and a 2π -electron system of the dienophile which leads to the formation of two new σ -bonds and one new π -bond. According to the Woodward-Hoffmann rules,^[3] the suprafacial interaction between these two π systems, i.e., $\pi 4_s + \pi 2_s$, requires no additional orbital symmetry-imposed energetic barrier. As a consequence, Diels-Alder reactions are commonly used in the construction of 6-membered cyclic structures and have occupied an important position in all fields of chemistry.^[4]

While Diels-Alder reactions normally feature 1,3-butadienes and alkenes or alkynes as the reactants, the Diels-Alder reactions between hetero-dienes and hetero-dienophiles, that is, hetero-

Diels-Alder reactions, are also common. Depending on the heteroatom present in the substrate, hetero-Diels-Alder reactions can be classified into two subtypes: aza-Diels-Alder reactions and oxo-Diels-Alder reactions. An aza-Diels-Alder reaction is when nitrogen is present in the diene or dienophile and is a convenient method to synthesize nitrogen-containing heterocycles^[5] that are common motifs in pharmaceuticals and natural products.^[6] Moreover, aza-Diels-Alder reactions of 1,2,4,5-tetrazines (six-membered analog of benzene where 1,2,4,5-positions are replaced with nitrogen) are used in time-critical applications such as the bioorthogonal reactions, due to their exceptionally high cycloaddition reactivity.^[7] In oxo-Diels-Alder reactions, carbonyl-containing compounds are featured as the diene or dienophile, but due to their relatively low reactivity, Lewis acids are usually applied to catalyze the reactions.^[8] Oxo-Diels-Alder reactions are utilized in the asymmetric synthesis of pyran derivatives.^[9]

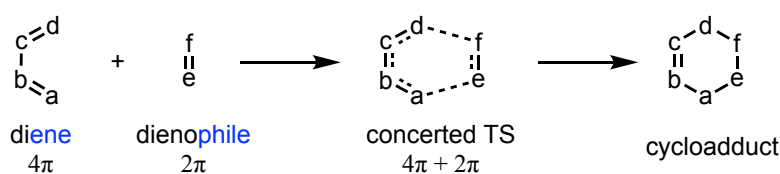


Figure 1.1 Diels-Alder reaction.

Frontier molecular orbital (FMO) theory is commonly employed to rationalize the reactivity and selectivity of pericyclic reactions.^[10] **Figure 1.2** schematically shows the FMOs of the diene and dienophile and two key orbital interactions between these FMOs, that is, the interaction between the HOMO of the diene and the LUMO of the dienophile (normal electron demand (NED) interaction) and the interaction between the LUMO of the diene and the HOMO of the dienophile (inverse electron demand (IED) interaction). The NED interaction plays a crucial role in the Diels-Alder reaction between the electron-rich diene and electro-deficient dienophile, whereas the IED interaction dominates the Diels-Alder reaction between the electron-deficient diene and electron-rich dienophile, because the corresponding NED or IED interaction has a smaller (more favorable) energy gap than the other. One must not forget that the orbital overlap between these FMOs is also important for determining the strength of these orbital interactions.

In addition to the stabilizing (HOMO–LUMO) orbital interactions, several other interactions between the reactants, such as the electrostatic interaction and destabilizing orbital interactions between occupied orbitals (Pauli repulsion), are also responsible for the reactivity of Diels-Alder reactions, and this will be discussed in detail in the following chapters.

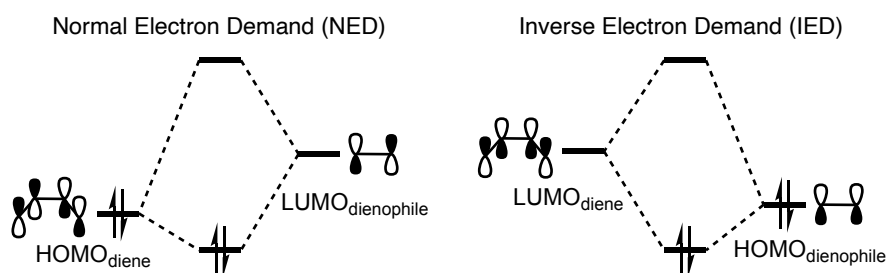


Figure 1.2 Key FMO interactions in the Diels-Alder reaction.

1.1.2 1,3-Dipolar Cycloadditions

The 1,3-dipolar cycloaddition represents another common class of pericyclic reaction. In 1,3-dipolar cycloadditions, 1,3-dipoles, a class of compounds with 4π electrons and charge delocalized over three consecutive atoms, react with dipolarophiles to furnish 5-membered cyclic structures (**Figure 1.3**). The 1,3-dipolar cycloaddition was first conceptualized by Smith in 1938,^[11] and the scope of 1,3-dipolar cycloaddition along with detailed mechanistic understanding was established in the 1960s primarily by Huisgen.^[12] Over the years, 1,3-dipolar cycloadditions have become one of the most important reactions and have found utility in a wide range of fields in chemistry, including organic synthesis,^[13] material science,^[14] medicinal chemistry,^[15] and biological chemistry.^[16]

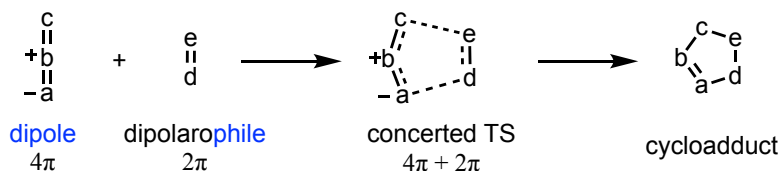


Figure 1.3 1,3-Dipolar cycloaddition.

A number of 1,3-dipolar compounds are suitable for 1,3-dipolar cycloadditions.^[13] These dipoles can be divided into two types: the allyl-type and the propargyl/allenyl-type. The allyl-type 1,3-dipoles are bent in geometry and can be described by the zwitterionic resonance structures, $a=b^+-c^- \leftrightarrow a^--b^+=c$, while the propargyl/allenyl-type 1,3-dipoles have linear structures and can be represented by $a=b^+-c^- \leftrightarrow a^-=b^+=c$. Pseudo-diradical, pseudo-radical, or carbenoid structures have also been proposed for some of the 1,3-dipoles.^[17] The common dipolarophiles are alkynes or alkenes, normally with substituents or in cyclic geometries. Heteroalkenes, that is, imines or carbonyls, are also suitable dipolarophiles in 1,3-dipolar cycloadditions.

Most 1,3-dipolar cycloadditions proceed via a concerted asynchronous pathway, which has been confirmed by experimental observations.^[12, 18] A stepwise mechanistic pathway has also been suggested in some exceptional cases.^[19] Over the course of the concerted 1,3-dipolar cycloaddition, the 4π -electron system of the 1,3-dipole interacts with the 2π -electron system of the dipolarophile in a $\pi 4_s + \pi 2_s$ fashion. According to the Woodward-Hoffmann rules,^[3] two types of symmetry-allowed FMO interactions take place during this process (**Figure 1.4**). Similar to the Diels-Alder reaction, the interaction between the HOMO of the 1,3-dipole and the LUMO of the dipolarophile governs the reaction of the electron-rich 1,3-dipole and the electron-deficient dipolarophile, whereas the interaction between the LUMO of the 1,3-dipole and the HOMO of the dipolarophile controls the reaction between the electron-deficient 1,3-dipole and the electron-rich dipolarophile. In practice, both two types of FMO interactions are essential for the reactivity of 1,3-dipolar cycloadditions.

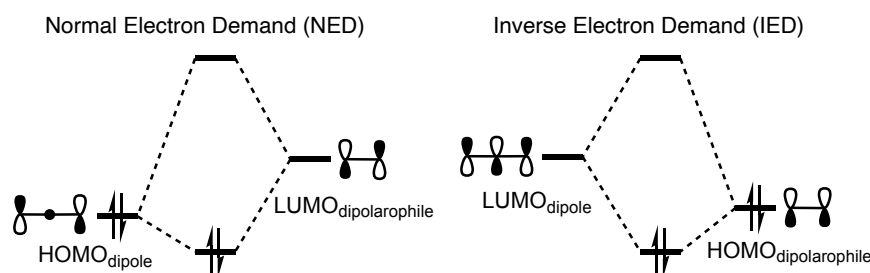


Figure 1.4 Key FMO interactions in the 1,3-dipolar cycloaddition.

1.2 Factors Affecting the Cycloaddition Reactivity

Several factors can influence the reactivity of cycloaddition reactions. Quite possibly the most fundamental factors would be the electronic and steric properties of the reactants. For instance, the composition of the reactant, such as the heteroatom, will have a direct impact on the cycloaddition reactivity. The molecular geometry of the reactant is another critical factor to consider as it can modify not just the steric hindrance of a cycloaddition partner but also the electronic properties and thus the reactivity. Secondly, external factors, such as the catalyst or the external field, have also been shown to be convenient tools to tune the cycloaddition reactivity. For instance, Lewis acids are often utilized to promote cycloaddition reactions. More recently, oriented external electric fields have shown to efficiently activate Diels-Alder reactions. In this section, we introduce in detail these fundamental factors that can affect the cycloaddition reactivity as described above.

1.2.1 Heteroatom

The molecular composition of the reactant in the cycloaddition reaction, such as the presence of a heteroatom and its respective position, has a direct influence on the reactivity. For instance, the aromatic compounds benzene and 1-azine (pyridine) are normally unreactive dienes for Diels-Alder reactions and harsh conditions, such as high temperature and pressure, or the use of a catalyst is necessary to promote the Diels-Alder reactions of benzene and 1-azine.^[20] The 1,2-diazines (pyridazines) substituted with additional electron-withdrawing groups, however, can undergo smooth inverse electron demand Diels-Alder reactions with electron-rich dienophiles.^[21] 1,2,4,5-Tetrazines, on the other hand, are highly reactive dienes in Diels-Alder reactions and are widely used in the field of rapid reactions, such as bioorthogonal chemistry.^[22] Thus, it becomes evident that the nature and number of heteroatom have a profound influence on cycloaddition reactivity.

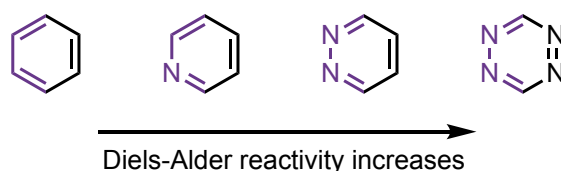


Figure 1.5 Diels-Alder reactivity of aromatic compounds.

1.2.2 Geometry

The molecular geometry of the reactant is another critical internal factor that can tune the cycloaddition reactivity with a notable example being the strain-promoted cycloaddition. The classic 1,3-dipolar cycloaddition between azide and alkyne requires an elevated temperature or increased pressure to proceed at a reasonable reaction rate.^[12] Sharpless and co-workers circumvented this obstacle by developing the copper(I)-catalyzed 1,3-dipolar cycloaddition, which can proceed at ambient temperatures (**Figure 1.6a**).^[23] In 2004, Bertozzi and co-workers developed the strain-promoted azide-alkyne 1,3-dipolar cycloadditions (SPAACs, **Figure 1.6b**), in which azides react with strained cyclooctyne derivatives readily under physiological conditions in the absence of auxiliary reagents.^[24] Due to the high reaction rates, SPAACs have found multiple applications in biological chemistry including as an effective labelling method for target biomolecules in living cells. Traditionally, a release of the ring strain or the reduced activation strain (or distortion energy) has been regarded as the driving force for the enhanced cycloaddition reactivity of strained cyclic compounds.^[25] However, a distortion/interaction-activation strain

model (D/I-ASM) analysis by the groups of Bickelhaupt and Houk elucidated that the lowered activation energies for the 1,3-dipolar cycloadditions of strained alkynes (**Figure 1.6b**) come from the reduced strain energies together with enhanced frontier molecular orbital interactions.^[26a] Key findings based on the Kohn-Sham molecular orbital theory revealed that the pre-distortion of backbone for smaller cycloalkynes can profoundly affect both the energy and shape of the FMOs, which in turn manifest into the enhanced orbital interactions in cycloaddition reactions.^[26a]

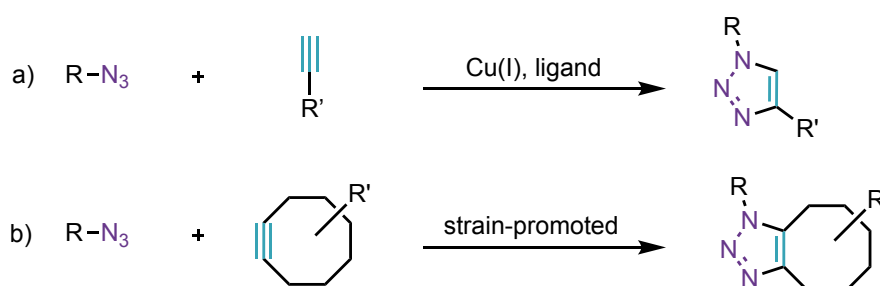


Figure 1.6 a) Cu(I)-catalyzed azide-alkyne 1,3-dipolar cycloaddition; b) Strain-promoted azide-alkyne 1,3-dipolar cycloaddition.

Another example is the Diels-Alder reaction between tetrazine and the strained cycloalkene. Sauer and co-workers performed a systematic study on the Diels-Alder reactivity between tetrazine and a series of strained cycloalkenes as the dienophiles.^[27] For the cycloaddition between 3,6-bis-trifluoromethyl-1,2,4,5-tetrazine and the strained cycloalkene in dioxane at 20 °C, the reactivity continuously decreases as the ring size of the dienophile increases on going from cyclopropane to cyclohexene, with the reaction rate spanning 6 orders of magnitude (**Figure 1.7**).^[27] The exceptionally high reaction rates of the Diels-Alder cycloadditions between tetrazines and strained cycloalkenes also render them as the useful tools for *in vivo* bioorthogonal applications.^[22] Again, Bickelhaupt and Houk revealed, by performing D/I-ASM analyses, that the reactivity difference of cycloalkenes in Diels-Alder reactions (**Figure 1.7**) arises from a difference in frontier molecular orbital interactions.^[26b]

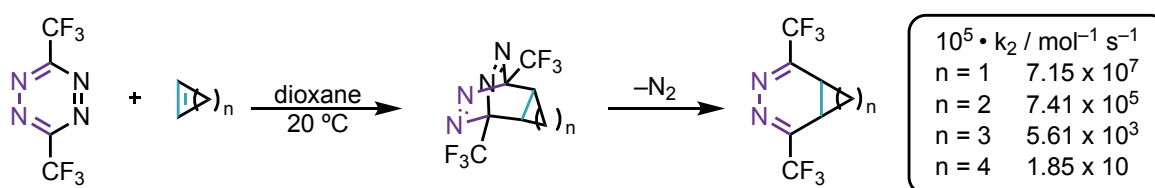


Figure 1.7 Diels-Alder reactions between 3,6-bis-trifluoromethyl-tetrazine and cycloalkenes.

Taken altogether, it becomes clear that the variation in the molecular geometry of a reactant does not just change the steric hindrance encountered for the reactant during the course of the reaction, but also the electronic structure of the reactant and thus the cycloaddition reactivity.

1.2.3 Catalyst

Catalysis is a common and convenient method to tune the Diels-Alder reactivity. Various catalysts are employed to invoke an enhancement of reactivity for different types of Diels-Alder reactions. From the perspective of FMO interactions, the catalysis of Diels-Alder reactions can be classified into four types, as summarized in **Figure 1.8**. For the NED-Diels-Alder reactions, that is, reactions where the primary electron interactions are controlled by $\text{HOMO}_{\text{diene}}\text{-LUMO}_{\text{dienophile}}$, electron-withdrawing auxiliaries such as Lewis acids are used to accelerate the reactions via complexation to the dienophile. The electron-withdrawing groups can stabilize the $\text{LUMO}_{\text{dienophile}}$ and induce diminished NED energy gaps to enhance the donor-acceptor interactions (see mode (a) in **Figure 1.8**).^[28] A classic example of this is the Lewis acid-catalyzed Diels-Alder reaction of isoprene and methyl acrylate (**Figure 1.9a**).^[29]

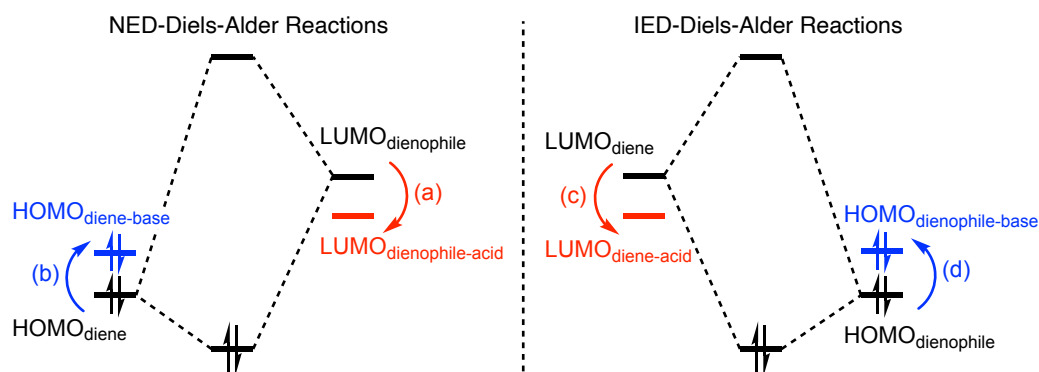


Figure 1.8 Catalysis modes for NED- and IED-Diels-Alder reactions.

The other activation mode for the NED-Diels-Alder reactions is the activation of the diene. Electron-donating auxiliaries, such as Lewis bases, can destabilize the $\text{HOMO}_{\text{diene}}$ and thus lead to diminished NED energy gaps and enhanced donor-acceptor interactions (mode (b) in **Figure 1.8**). This catalysis is much less common compared to Lewis acid-catalyzed NED-Diels-Alder reactions. The Diels-Alder reactions between 3-hydroxy-2-pyrones with electron-deficient dienophiles are efficiently catalyzed by Lewis bases, such as amines (**Figure 1.9b**).^[30] Another example is the base-catalyzed NED-Diels-Alder reaction between anthrones and electron-deficient dienophiles.^[31]

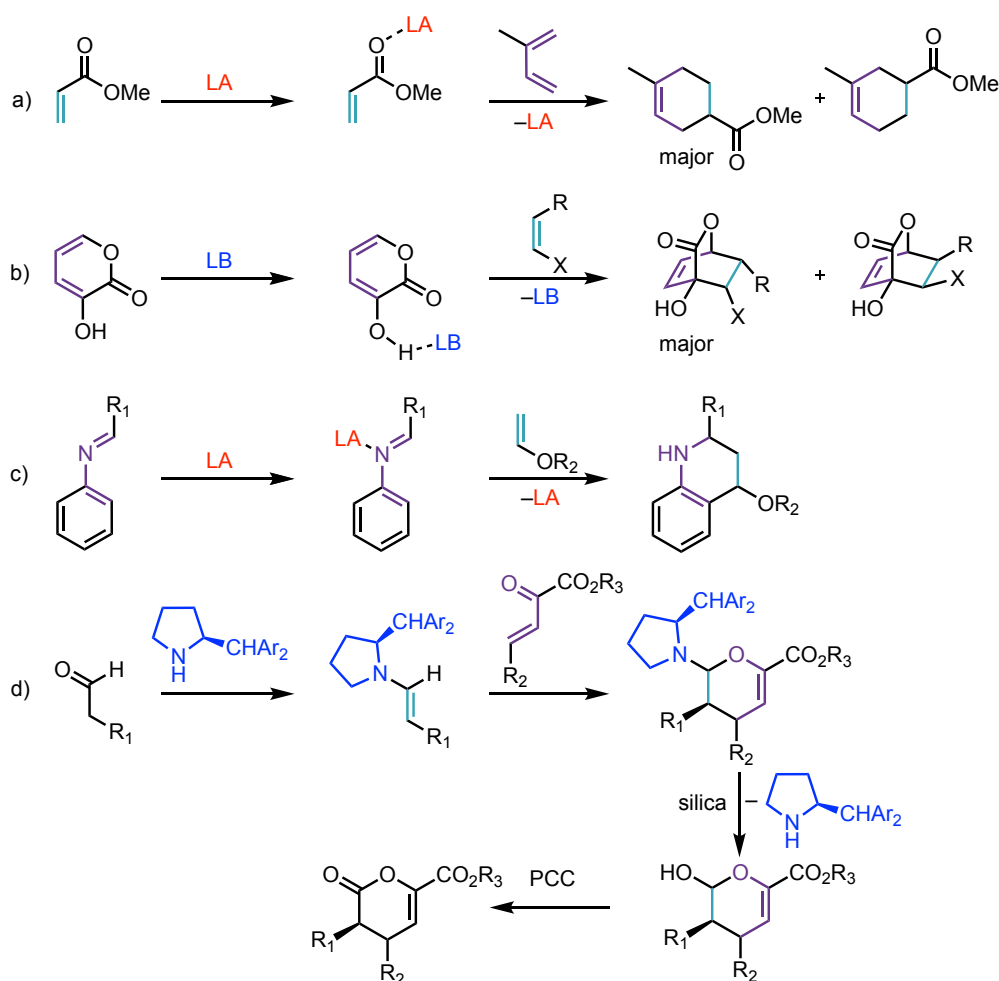


Figure 1.9 Examples of catalyzed NED- and IED-Diels-Alder reactions.

For the IED-Diels-Alder reactions, the opposite strategy must be adopted because, in this case, FMO interactions of $\text{LUMO}_{\text{diene}}\text{-HOMO}_{\text{dienophile}}$ dominate the reactions. In other words, acids catalyze the IED-Diels-Alder reactions by lowering the $\text{LUMO}_{\text{diene}}$ (mode (c) in **Figure 1.8**), while bases accelerate the IED-Diels-Alder reactions by raising the $\text{HOMO}_{\text{dienophile}}$ (mode (d) in **Figure 1.8**).^[32] The Povarov reaction, for instance, is a notable class of acid-catalyzed IED-Diels-Alder reaction where aryl imines react with the electron-rich dienophiles in the presence of Lewis or Brønsted acids to afford quinoline derivatives (**Figure 1.9c**).^[33] Another classic example is the IED-Diels-Alder reaction between 3-carbonmethoxy-2-pyrones and the electron-rich dienophiles catalyzed by lanthanide Lewis acids.^[34] On the other hand, Jørgensen described the base-catalyzed IED-Diels-Alder reactions of activated dienophiles and showed that the aliphatic aldehydes react with β,γ -unsaturated α -ketoesters in the presence of the chiral pyrrolidine to afford pyran-2-one derivatives (**Figure 1.9d**).^[35] The catalysis is induced by the condensation of the chiral amine with carbonyl groups to generate highly reactive dienophile intermediates that feature the destabilized

HOMO_{dienophile} in the IED-Diels-Alder reactions. After the hydrolysis and oxidation by pyridinium chlorochromate (PCC), the final products pyran-2-ones are obtained. This type of amine-catalyzed IED-Diels-Alder reactions have also been reported by several groups and have been extended to a diverse range of systems.^[36]

1.2.4 External Electric Field

Electric field-catalyzed non-redox reactions,^[37] including the cycloaddition reactions,^[38] have long been studied in the aspect of both theoretical and experimental chemistry. In 2010, Shaik and co-workers predicted the effect of different oriented external electric fields on the Diels-Alder reaction between cyclopentadiene and maleic anhydride (**Figure 1.10a**): a) an electric field oriented along the reaction axis, that is, the electric field along the direction of the newly forming bonds, can catalyze (positive field) or inhibit (negative field) the reaction; b) an electric field perpendicular to the reaction axis and the bond-forming plane will lead to an enhanced *endo* (negative field) or *exo* (positive field) selectivity; c) an electric field along the C=C double bond of maleic anhydride has a negligible effect on both the reactivity or selectivity of the reaction.

In 2016, Coote and co-workers experimentally verified the theoretical prediction of Shaik^[38a] by showcasing the Diels-Alder reaction between furan and a norbornylogous bridge that were separately tethered to a gold STM tip and a gold surface, respectively (**Figure 1.10b**).^[39a] In this way, the electric field was aligned along the reaction axis and induced a fivefold increase in the frequency of the formation of the single-molecule junction. Hong and co-workers later confirmed that the reactivity of the studied Diels-Alder reaction remains unaltered under an electric field aligned to the C=C double bond of the dienophile by using an electric field-mediated single-molecule reaction (**Figure 1.10c**).^[39b]

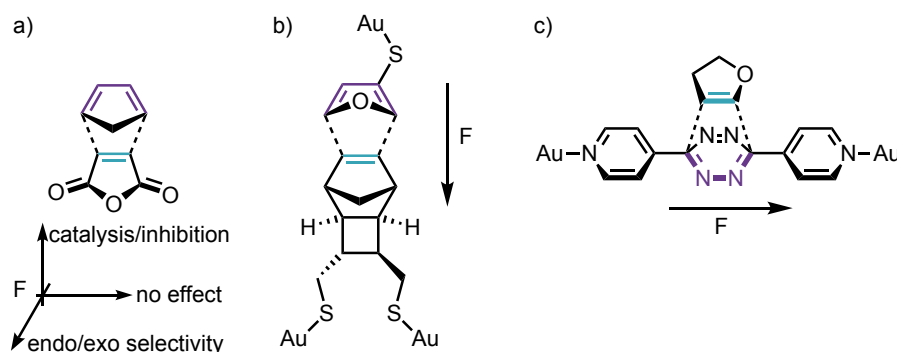


Figure 1.10 Theoretical predictions and experimental verifications of the oriented external electric field-modulated Diels-Alder reactions.

1.3 This Thesis

The objective of this thesis is to reveal the underlying mechanisms of how the internal and external factors as described in the previous section, including the heteroatom, molecular geometry of the reactant, catalyst, and external electric field, influence the cycloaddition reactivity. The insights yielded from this study can serve as the fundamental principles for the understanding and rational design of more cycloaddition reactions. To that end, we selected four representative uncatalyzed or catalyzed cycloadditions and performed systematic investigations on them by using density functional theory (DFT) calculations and state-of-the-art quantum chemical analysis methods, such as the activation strain model (ASM), canonical energy decomposition analysis (EDA), and Kohn-Sham molecular orbital (KS-MO) theory.

Firstly, the thesis includes this chapter as an introduction to the research subject, followed by an overview of theories and models of this thesis in Chapter 2. Chapter 3 presents a benchmark study of the DFT methods for cycloaddition reactions. Therein, 24 1,3-dipolar cycloadditions were benchmarked using the highly accurate G3B3 method as the reference and several exchange and correlation functionals, including PBE, OLYP, BP86, BLYP, with and without explicit dispersion corrections, were screened to assess their accuracies and to determine which of them perform the best for calculating the trends in cycloaddition reactivity. The best DFT method was employed in all subsequent studies.

In Chapter 4, we rationalize the effect of the heteroatom on the cycloaddition reactivity by investigating the Diels-Alder reactivity of a systematic series of hetero-1,3-butadienes using DFT calculations at the BP86/TZ2P level. Firstly, we compared the archetypal 1,3-butadiene (CCCC) and the hetero-1,3-butadienes containing a single heteroatom at the terminal site, i.e., 2-propen-1-imine (NCCC) and acrolein (OCCC). Then, we extended to the hetero-1,3-butadienes with an additional heteroatom at the second terminal site, that is, NCCN and OCCO. Lastly, the Diels-Alder reactivity of the hetero-1,3-butadiene with one nitrogen in the backbone (CNCC) and those with two nitrogen atoms (NNCC, NCNC, CNNC) were analyzed.

In Chapter 5, we investigate the effect of the heteroatom substitution and geometry of the reactant on the cycloaddition reactivity between allenes and archetypal partners. To that end, we quantum chemically studied the reactivity, site-, and regioselectivity of 1,3-dipolar cycloadditions of allenes, including the archetypal allene (i.e., propadiene), heteroallenes, and cyclic allenes. We

established that the formation of the 1,5-adduct is favored over the 1,4-adduct for all 1,3-dipolar cycloadditions of allenes and identified the most reactive regions of all heteroallenes. Then, we evaluated the 1,3-dipolar cycloaddition reactivity of heteroallenes. In addition, we systematically assessed the cycloaddition reactivity of cycloallene by modifying its ring size. A relation between the cycloaddition reactivity of allene and the geometry of allene was established and the underlying mechanism was disclosed using KS-MO theory.

As the oriented external electric field (OEEF) is capable of catalyzing cycloadditions and can even induce *endo/exo* selectivity to these reactions, in Chapter 6, we transition to the study of the OEEF-catalyzed Diels-Alder reaction between cyclopentadiene and maleic anhydride by using the quantitative ASM and EDA method, to pinpoint the origin of the catalytic and stereoselective effect of the OEEF. Our quantitative analyses unveiled the key physical factors leading to the enhanced or inhibited reactivity of the Diels-Alder reaction under the OEEF along the reaction axis, and factors dictating the varied stereoselectivity of the Diels-Alder reaction under the OEEF perpendicular to the plane of the reaction axis. Furthermore, for the first time, we evaluated the effect of the OEEF on the IED-Diels-Alder reaction, which, unexpectedly, exhibits an opposite response to the OEEF.

In Chapter 7, we turn to reveal the influence of the catalyst on the cycloaddition reactivity. For this purpose, we selected to study the Brønsted acid-catalyzed aza-Diels-Alder reactions of 2-aza-dienes, because the protonation can vastly enhance the reactivity of 2-aza-dienes in the Diels-Alder reactions with ethylene. We found that the activation energy systematically decreases as the basic sites of the diene progressively become protonated. Our ASM and KS-MO analyses traced the origin of this enhanced reactivity to i) “Pauli-lowering catalysis” for *mono*-protonated 2-aza-dienes and ii) “LUMO-lowering catalysis” for *multi*-protonated 2-aza-dienes. We illustrated how the novel concept of “Pauli-lowering catalysis” is overruled by the traditional concept of “LUMO-lowering catalysis” when the degree of LUMO stabilization is extreme as in the case of *multi*-protonated 2-aza-dienes. Moreover, we revealed how the degree of asynchronicity in the transition state of the Diels-Alder reaction is the result of two counteracting factors: the minimization of the destabilizing Pauli repulsions (asynchronous mode) and the maximization of the stabilizing orbital and electrostatic interactions (synchronous mode).

Lastly, the thesis is concluded with a summary and acknowledgements.

1.4 References

- [1] O. Diels, K. Alder, *Justus Liebigs Ann. Chem.* **1928**, 460, 98–122.
- [2] J. H. Baraban, M.-A. Martin-Drumel, P. B. Changala, S. Eibenberger, M. Nava, D. Patterson, J. F. Stanton, G. B. Ellison, M. C. McCarthy, *Angew. Chem.* **2018**, 130, 1839–1843; *Angew. Chem. Int. Ed.* **2018**, 57, 1821–1825.
- [3] a) R. B. Woodward, R. Hoffmann, *J. Am. Chem. Soc.* **1965**, 87, 395–397; b) R. B. Woodward, R. Hoffmann, *J. Am. Chem. Soc.* **1965**, 87, 2046–2048; c) R. B. Woodward, R. Hoffmann, *Angew. Chem. Int. Ed. Engl.* **1969**, 8, 781–853.
- [4] a) K. C. Nicolaou, S. A. Snyder, T. Montagnon, G. Vassilikogiannakis, *Angew. Chem. Int. Ed.* **2002**, 41, 1668–1698; b) M. A. Tasdelen, *Polym. Chem.* **2011**, 2, 2133–2145.
- [5] a) L. F. Tietze, G. Ketschau, *Stereoselective Heterocyclic Synthesis I*, Springer, New York, **1997**; b) D. L. Boger, S. N. Weinreb, *Hetero Diels-Alder Methodology in Organic Synthesis*, Academic Press, San Diego, **2012**.
- [6] a) P. M. Weintraub, J. S. Sabol, J. M. Kane, D. R. Borcherdig, *Tetrahedron* **2003**, 59, 2953–2989; b) M. G. P. Buffat, *Tetrahedron* **2004**, 60, 1701–1729; c) V. Eschenbrenner-Lux, K. Kumar, H. Waldmann, *Angew. Chem. Int. Ed.* **2014**, 53, 11146–11157.
- [7] a) T. Reiner, B. M. Zeglis, *J. Labelled Compd. Radiopharm.* **2014**, 57, 285–290; b) C. Denk, D. Svatunek, S. Mairinger, J. Stanek, T. Filip, D. Matscheko, C. Kuntner, T. Wanek, H. Mikula, *Bioconjugate Chem.* **2016**, 27, 1707–1712; c) T. Lappchen, R. Rossin, T. R. van Mourik, G. Gruntz, F. J. M. Hoeben, R. M. Versteegen, H. M. Janssen, J. Lub, M. S. Robillard, *Nucl. Med. Biol.* **2017**, 55, 19–26; d) R. Rossin, S.M. vandenBosch, W. ten Hoeve, M. Carvelli, R. M. Versteegen, J. Lub, M. S. Robillard, *Bioconjugate Chem.* **2013**, 24, 1210–1217; e) M. Wang, D. Svatunek, K. Rohlfing, Y. Liu, H. Wang, B. Giglio, H. Yuan, Z. Wu, Z. Li, J. Fox, *Theranostics* **2016**, 6, 887–895.
- [8] a) A. Pałasz, *Top. Curr. Chem.* **2016**, 374, 24; b) X. Hu, Y. Zhou, Y. Lu, S. Zou, L. Lin, X. Liu, X. Feng, *J. Org. Chem.* **2018**, 83, 8679–8687; c) K. N.Houk, R. W. Strozier, *J. Am. Chem. Soc.* **1973**, 95, 4094–4096.

- [9] a) M. Bednarski, S. Danishefsky, *J. Am. Chem. Soc.* **1983**, *105*, 3716–3717; b) H. Pellissier, *Tetrahedron* **2009**, *65*, 2839–2877; c) A. Taheri kal Koshvandi, M. M. Heravi, *Tetrahedron: Asymmetry* **2017**, *28*, 1506–1556.
- [10] a) K. N. Houk, *Acc. Chem. Res.* **1975**, *8*, 361–369; b) D. H. Ess, K. N. Houk, *J. Am. Chem. Soc.* **2008**, *130*, 10187–10198.
- [11] L. I. Smith, *Chem. Rev.* **1938**, *23*, 193–285.
- [12] a) R. Huisgen, *Angew. Chem. Int. Ed. Engl.* **1963**, *2*, 565–598; b) R. Huisgen, *Angew. Chem. Int. Ed. Engl.* **1963**, *2*, 633–645.
- [13] A. Padwa, W. H. Pearson, Eds., *Synthetic Applications of 1,3-Dipolar Cycloaddition Chemistry toward Heterocycles and Natural Products*. John Wiley & Sons, New York, **2003**.
- [14] a) J.-F. Lutz, *Angew. Chem. Int. Ed.* **2007**, *46*, 1018–1025; b) J. P. Collman, N. K. Devaraj, C. E. D. Chidsey, *Langmuir* **2004**, *20*, 1051–1053.
- [15] a) G. C. Tron, T. Pirali, R. A. Billington, P. L. Canonico, G. Sorba, A. A. Genazzani, *Med. Res. Rev.* **2008**, *28*, 278–308. b) C. D. Hein, X. M. Liu, D. Wang, *Pharm. Res.* **2008**, *25*, 2216–2230; c) P. Thirumurugan, D. Matosiuk, K. Jozwiak, *Chem. Rev.* **2013**, *113*, 4905–4979.
- [16] a) J. C. Jewett, C. R. Bertozzi, *Chem. Soc. Rev.* **2010**, *39*, 1272–1279; b) X. Ning, J. Guo, M. A. Wolfert, G.-J. Boons, *Angew. Chem. Int. Ed.* **2008**, *47*, 2253–2255; *Angew. Chem.* **2008**, *120*, 2285–2287.
- [17] a) L. R. Domingo, M. Ríos-Gutiérrez, *Molecules* **2017**, *22*, 750; b) L. R. Domingo, M. J. Aurell, P. Pérez, *Tetrahedron* **2014**, *70*, 4519–4525; c) L. R. Domingo, M. Ríos-Gutiérrez, P. Pérez, *J. Org. Chem.* **2018**, *83*, 2182–2197.
- [18] a) R. Huisgen, *J. Org. Chem.* **1976**, *41*, 403–419; b) R. Huisgen, *J. Org. Chem.* **2002**, *33*, 2291–2297.
- [19] a) R. A. Firestone, *J. Org. Chem.* **1968**, *33*, 2285–2290; b) K. N. Houk, J. Sims, C. R. Watts, L. J. Luskus, *J. Am. Chem. Soc.* **1973**, *95*, 7301–7315; c) R. Huisgen, G. Mloston, E. Langhals, *J. Am. Chem. Soc.* **1986**, *108*, 6401–6402.
- [20] a) S. Cossu, F. Garris, O. DeLucchi, O. Synlett **1997**, *12*, 1327–1334; b) M. D. Chordia, P. L. Smith, S. H. Meiere, M. Sabat, W. D. Harman, *J. Am. Chem. Soc.* **2001**, *123*, 10756–

- 10757; c) P. M. Graham, D. A. Delafuente, W. Liu, W. H. Myers, M. Sabat, W. D. Harman, *J. Am. Chem. Soc.* **2005**, *127*, 10568–10572.
- [21] a) H. Neunhoeffler, G. Werner, *Tetrahedron Lett.* **1972**, *13*, 1517–1518; b) H. Neunhoeffler, G. Werner, *Liebigs Ann. Chem.* **1973**, 437–442.
- [22] a) M. L. Blackman, M. Royzen, J. M. Fox, *J. Am. Chem. Soc.* **2008**, *130*, 13518–13519; b) N. K. Devaraj, R. Weissleder, S. A. Hilderbrand, *Bioconjugate Chem.* **2008**, *19*, 2297–2299; c) D. M. Patterson, L. A. Nazarova, B. Xie, D. N. Kamber, J. A. Prescher, *J. Am. Chem. Soc.* **2012**, *134*, 18638–18643.
- [23] a) V. V. Rostovtsev, L. G. Green, V. V. Fokin, K. B. Sharpless, *Angew. Chem.* **2002**, *114*, 2708–2711; *Angew. Chem. Int. Ed.* **2002**, *41*, 2596–2599; b) Q. Wang, T. R. Chan, R. Hilgraf, V. V. Fokin, K. B. Sharpless, M. G. Finn, *J. Am. Chem. Soc.* **2003**, *125*, 3192–3193.
- [24] N. J. Agard, J. A. Prescher, C. R. Bertozzi, *J. Am. Chem. Soc.* **2004**, *126*, 15046–15047.
- [25] a) R. S. Paton, S. Kim, A. G. Ross, S. J. Danishefsky, K. N. Houk, *Angew. Chem.* **2011**, *123*, 10550–10552; *Angew. Chem. Int. Ed.* **2011**, *50*, 10366–10368; b) F. Liu, R. S. Paton, S. Kim, Y. Liang, K. N. Houk, *J. Am. Chem. Soc.* **2013**, *135*, 15642–15649.
- [26] a) T. A. Hamlin, B. J. Levandowski, A. K. Narsaria, K. N. Houk, F. M. Bickelhaupt, *Chem. Eur. J.* **2019**, *25*, 6342–6348; b) B. J. Levandowski, T. A. Hamlin, F. M. Bickelhaupt, K. N. Houk, *J. Org. Chem.* **2017**, *82*, 8668–8675.
- [27] a) F. Thalhammer, U. Wallfahrer, J. Sauer, *Tetrahedron Lett.* **1990**, *31*, 6851–6854; b) J. Sauer, *Chem. Heterocycl. Compd.* **1995**, *31*, 1140–1154.
- [28] a) I. Fleming, *Frontier Orbitals and Organic Chemical Reactions*, Wiley, New York, **1976**; I. Fleming, *Molecular Orbitals and Organic Chemical Reactions*, Wiley, Hoboken, **2009**; b) K. N. Houk, *Acc. Chem. Res.* **1975**, *8*, 361–369; c) M. J. R. Dewar, *Molecular Orbital Theory for Organic Chemists*, Prentice-Hall, Englewood Cliffs, **1975**; d) W. T. Borden, *Modern Molecular Orbital Theory for Organic Chemists*, Prentice-Hall, Englewood Cliffs, **1975**.
- [29] a) T. Inukai, M. Kasai, *J. Org. Chem.* **1965**, *30*, 3567–3569; b) T. Inukai, T. Kojima, *J. Org. Chem.* **1966**, *31*, 1121–1123; c) T. Inukai, T. Kojima, *J. Org. Chem.* **1967**, *32*, 872–875.

- [30] a) H. Okamura, T. Iwagawa, M. Nakatani, *Tetrahedron Lett.* **1995**, *36*, 5939–5942; b) H. Okamura, Y. Nakamura, T. Iwagawa, M. Nakatani, *Chem. Lett.* **1996**, 193–194; c) H. Okamura, K. Morishige, T. Iwagawa, M. Nakatani, *Tetrahedron Lett.* **1998**, *39*, 1211–1214; d) H. Okamura, Y. Nakamura, T. Iwagawa, M. Nakatani, *Tetrahedron Lett.* **2000**, *41*, 8317–8321; e) H. Okamura, H. Shimizu, Y. Nakamura, T. Iwagawa, M. Nakatani, *Tetrahedron Lett.* **2000**, *41*, 4147–4150; f) H. Okamura, H. Shimizu, T. Iwagawa, M. Nakatani, *Tetrahedron Lett.* **2001**, *57*, 1903–1908; g) H. Shimizu, H. Okamura, N. Yamashita, T. Iwagawa, M. Nakatani, *Tetrahedron Lett.* **2001**, *57*, 8649–8651.
- [31] a) M. Koerner, B. Rickborn, *J. Org. Chem.* **1989**, *54*, 6–9; b) M. Koerner, B. Rickborn, *J. Org. Chem.* **1990**, *55*, 2662–2672; c) O. Riant, H. B. Kagan, *Tetrahedron Lett.* **1989**, *30*, 7403–7406; d) O. Riant, H. B. Kagan, L. Ricard, *Tetrahedron*, **1994**, *50*, 4543–4554.
- [32] X. Jiang, R. Wang, *Chem. Rev.* **2013**, *113*, 5515–5546.
- [33] a) L. S. Povarov, B. M. Mikhailov, *Izv. Akad. Nauk SSR, Ser. Khim.* **1963**, 953–956; b) L. S. Povarov, *Russ. Chem. Rev.* **1967**, *36*, 656–670; c) V. V. Kouznetsov, *Tetrahedron* **2009**, *65*, 2721–2750; d) G. A. Swan, *J. Chem. Soc. D* **1969**, 20a–20a; e) R. B. Roy, G. A. Swan, *Chem. Commun. (London)* **1968**, 1446–1447; f) K.-D. Hesse, *Justus Liebigs Ann. Chem.* **1970**, *741*, 117–123; g) V. V. Kouznetsov, *Tetrahedron* **2009**, *65*, 2721–2750; h) D. Leca, F. Gaggini, J. Cassayre, O. Loiseleur, S. N. Pieniazek, J. A. R. Luft, K. N. Houk, *J. Org. Chem.* **2007**, *72*, 4284–4287.
- [34] a) I. E. Markó, G. R. Evans, *Tetrahedron Lett.* **1994**, *35*, 2771–2774; b) I. E. Markó, G. R. Evans, J.-P. Declercq, *Tetrahedron* **1994**, *50*, 4557–4574; c) I. E. Markó, G. R. Evans, J.-P. Declercq, J. Feneau-Dupont, B. Tinant, *Bull. Soc. Chim. Belg.* **1994**, *103*, 295–297; d) G. H. Posner, J.-C. Carry, J. K. Lee, D. S. Bull, H. Dai, *Tetrahedron Lett.* **1994**, *35*, 1321–1324; e) G. H. Posner, F. Eydoux, J. K. Lee, D. S. Bull, *Tetrahedron Lett.* **1994**, *35*, 7541–7544; f) I. E. Markó, G. R. Evans, P. Seres, I. Chellé, Z. Janousek, *Pure Appl. Chem.* **1996**, *68*, 113–122; g) G. H. Posner, H. Dai, D. S. Bull, J. K. Lee, F. Eydoux, Y. Ishihara, W. Welsh, N. Pryor, S. Petr, *J. Org. Chem.* **1996**, *61*, 671–676; h) I. E. Markó, I. Chellé-Regnaut, B. Leroy, S. L. Warriner, *Tetrahedron Lett.* **1997**, *38*, 4269–4272; i) X.-W. Liang, Y. Zhao, X.-G. Si, M.-M. Xu, J.-H. Tan, Z. M. Zhang, C.-G. Zheng, C. Zheng, Q. Cai,

- Angew. Chem. Int. Ed.* **2019**, *58*, 14562–14567; j) X.-G. Si, Z.-M. Zhang, C.-G. Zheng, Z.-T. Li, Q. Cai, *Angew. Chem. Int. Ed.* **2020**, *59*, 18412–18417.
- [35] K. Juhl, K. A. Jørgensen, *Angew. Chem.* **2003**, *115*, 1536–1539; *Angew. Chem. Int. Ed.* **2003**, *42*, 1498–1501.
- [36] a) S. Samanta, J. Krause, T. Mandal, C.-G. Zhao, *Org. Lett.* **2007**, *9*, 2745–2748; b) F. A. Hernandez-Juan, D. M. Cockfield, D. J. Dixon, *Tetrahedron Lett.* **2007**, *48*, 1605–1608; c) Y. Zhao, X.-J. Wang, J.-T. Liu, *Synlett* **2008**, *7*, 1017–1020; d) J.-L. Li, T.-Y. Liu, Y.-C. Chen, *Acc. Chem. Res.* **2012**, *45*, 1491–1500.
- [37] a) S. Shaik, D. Mandal, R. Ramanan, *Nat. Chem.* **2016**, *8*, 1091–1098; b) S. Shaik, R. Ramanan, D. Danovich, D. Mandal, *Chem. Soc. Rev.* **2018**, *47*, 5125–5145; c) S. Ciampi, N. Darwish, H. M. Aitken, I. Díez-Pérez, M. L. Coote, *Chem. Soc. Rev.* **2018**, *47*, 5146–5164; d) S. Shaik, D. Danovich, J. Joy, Z. Wang, T. Stuyver, *J. Am. Chem. Soc.* **2020**, *142*, 12551–12562.
- [38] a) R. Meir, H. Chen, W. Lai, S. Shaik, *ChemPhysChem* **2010**, *11*, 301–310; Corrigendum: *ChemPhysChem* **2020**, *21*, 1737–1737; b) Z. Wang, d. Danovich, R. Ramanan, S. Shaik, *J. Am. Chem. Soc.* **2018**, *140*, 13350–13359; c) H. M. Aitken, M. L. Coote, *Phys. Chem. Chem. Phys.* **2018**, *20*, 10671–10676; d) C. Q. He, C. C. Lam, P. Yu, Z. Song, M. Chen, Y.-H. Lam, S. Chen, K. N. Houk, *J. Org. Chem.* **2020**, *85*, 2618–2625.
- [39] a) A. C. Aragonès, N. L. Haworth, N. Darwish, S. Ciampi, N. J. Bloomfield, G. G. Wallace, I. Diez-Perez, M. L. Coote, *Nature* **2016**, *531*, 88–91; b) X. Huang, C. Tang, J. Li, L.-C. Chen, J. Zheng, P. Zhang, J. Le, R. Li, X. Li, J. Liu, Y. Yang, J. Shi, Z. Chen, M. Bai, H.-L. Zhang, H. Xia, J. Cheng, Z.-Q. Tian, W. Hong, *Sci. Adv.* **2019**, *5*, eaaw3072.

Chapter 2 Theories and Models

2.1 Quantum Chemistry

Quantum chemistry is one of the branches of chemistry that applies quantum mechanical principles to the study of chemical systems. The first step is to solve the Schrödinger equation (or Dirac equation when the relativistic effect is included).^[1] In the framework of quantum mechanics, the state of a system can be completely expressed by a wavefunction (Ψ) and there exists a linear Hermitian operator corresponding to every observable in classical mechanics. Therefore, solving a time-independent Schrödinger equation of the energy operator H leads to the wavefunctions of the stationary states of the system and the total energies E corresponding to the states (Eq. 2.1).

$$H\Psi = E\Psi \quad (2.1)$$

To apply this equation, we need to write down the total energy operator of the system, that is, Hamiltonian H , which accounts for the kinetic and potential energies of all particles constituting this system. For a chemical system, such as an atom or a molecule, the Hamiltonian includes the kinetic energy of all nuclei (T_N) and electrons (T_e), and the potential energy emerging from the nucleus-electron (V_{Ne}), nucleus-nucleus (V_{NN}), and electron-electron (V_{ee}) interactions. The Born-Oppenheimer approximation^[2] assumes that the electrons move in a fixed frame of the nuclei. This assumption is based on the huge mass difference between the electrons and nuclei: the mass of a proton is 1800 times that of an electron. Therefore, the electrons move much faster than the nuclei so that the electrons can be assumed to move around the fixed nuclei. Accordingly, we can compute the wavefunction (Ψ_e) of the electrons moving around the stationary nuclei, and the kinetic energy term of nuclei (T_N) and potential energy term of the nucleus-nucleus interactions (V_{NN}) do not appear in the Hamiltonian H_e for the electronic Schrödinger equation (Eq. 2.2).

$$H_e\Psi_e = (T_e + V_{Ne} + V_{ee})\Psi_e = E_e\Psi_e \quad (2.2)$$

The V_{Ne} is the potential energy term to describe the electrostatic attraction between the nuclei and electrons. This external potential is created and solely determined by the positions of all nuclei. Therefore, the solution of the electronic Schrödinger equation (Eq. 2.2), E_e , of a molecule is a function of the nuclear frame, i.e., the molecular geometry. In practice, we compute the E_e for the molecule in various geometries to obtain the potential energy surface. In this way,

we locate the energy minimum of the geometry of a molecule and obtain more information, such as the molecular vibrations.

To obtain a potential energy surface, one must solve the electronic Schrödinger equation (Eq. 2.2) for each potential energy term V_{Ne} . However, an analytical solution for the Schrödinger equation (Eq. 2.2) is only possible for one-electron systems, such as the hydrogen atom and the dihydrogen cation.^[3] For many-body systems, the normal cases in chemical problems, we need to take approximations giving us acceptable results for practical problems. Fortunately, a number of approximation methods have been developed and successfully applied in multiple systems. For instance, the Hartree-Fock (HF) method^[4] assumes that the electronic wavefunction Ψ_e of an N -electron system can be approximated by a single Slater determinant of N one-electron wavefunctions (i.e., orbitals). The one-electron wavefunctions are computed by making a mean-field approximation, that is, every single electron is subjected to a mean-field created by the nuclei and all of the other electrons, and then solving a simple one-electron Schrödinger equation. A Slater determinant, rather than the simple product, of these one-electron wavefunctions, is used to satisfy the anti-symmetric rule of wavefunctions. The major flaw of the HF method comes from the mean-field approximation that neglects the electron-electron correlations, which should be completely accounted for in the V_{ee} term. The improvement of the HF method, by adding the electron-electron correlation, leads to the more accurate, but also computationally expensive, post-HF methods, such as the Møller–Plesset (MP) perturbation theory,^[5] configuration interaction (CI),^[6] and coupled-cluster (CC)^[7] methods.

2.2 Density Functional Theory

Density functional theory (DFT) provides an alternative framework for solving many-body problems. This method finds its roots in the Thomas-Fermi model^[8] from the 1920s and was provided with a firm theoretical background later on by the Hohenberg-Kohn (HK) theorems^[9]. The HK theorems state that the ground state energy E of a many-electron system is uniquely determined by the electron density $n(\mathbf{r})$. In other words, the total energy E of the many-electron system can be expressed by a functional of the electron density $n(\mathbf{r})$ (Eq. 2.3). This framework reduces the problem of N electrons with $3N$ spatial variables in the wavefunction method to a problem of three spatial variables in the DFT method. Furthermore, the HK theorems demonstrate

that the ground-state electron density of a system can be obtained by minimizing this energy functional.

$$E = E[n(\mathbf{r})] \quad (2.3)$$

However, the explicit expression of the functional $E[n(\mathbf{r})]$ is unknown, because two of the components, the kinetic energy functional $T[n(\mathbf{r})]$ and the electron-electron potential functional $V_{ee}[n(\mathbf{r})]$, are unknown. This theory was then further developed by Walter Kohn and Lu Jeu Sham, leading to the Kohn-Sham (KS) DFT.^[10] In this model, they assume that there exists an auxiliary system of non-interacting electrons subjected to an effective potential V^{eff} , which has the electron density of the auxiliary system $n_s(\mathbf{r})$ identical to that of the real system $n(\mathbf{r})$. In other words, solving a one-electron Schrödinger equation of the V^{eff} (Eq.2.4) results in KS orbitals $\phi_i(\mathbf{r})$, which, in turn, construct the exact electron density of the real system by adding the contribution of all occupied KS orbitals (Eq. 2.5).

$$(T_s + V^{\text{eff}})\phi_i(\mathbf{r}) = \varepsilon_i\phi_i(\mathbf{r}) \quad (2.4)$$

$$n(\mathbf{r}) = n_s(\mathbf{r}) = \sum |\phi_i(\mathbf{r})|^2 \quad (2.5)$$

The functional of the total energy $E[n(\mathbf{r})]$, therefore, can be decomposed into the kinetic energy term of non-interacting electrons $T_s[n(\mathbf{r})]$ and the potential energy term of non-interacting electrons $V^{\text{eff}}[n(\mathbf{r})]$. The $V^{\text{eff}}[n(\mathbf{r})]$ consists of the following contributions: $V_{\text{ext}}[n(\mathbf{r})]$, $E_H[n(\mathbf{r})]$, and $E_{\text{XC}}[n(\mathbf{r})]$ (Eq. 2.6). The first functional $V_{\text{ext}}[n(\mathbf{r})]$ accounts for the external potential energy created by nuclei; the second functional, i.e., the Hartree energy $E_H[n(\mathbf{r})]$, originates from the Coulomb interactions between non-interacting electrons; the last term, exchange-correlation (XC) functional $E_{\text{XC}}[n(\mathbf{r})]$ corrects the difference between the $T_s[n(\mathbf{r})]$ and $E_H[n(\mathbf{r})]$ of the auxiliary system with the $T[n(\mathbf{r})]$ and $E_{ee}[n(\mathbf{r})]$ of the real system.

$$E[n(\mathbf{r})] = T_s[n(\mathbf{r})] + V^{\text{eff}}[n(\mathbf{r})] = T_s[n(\mathbf{r})] + V_{\text{ext}}[n(\mathbf{r})] + E_H[n(\mathbf{r})] + E_{\text{XC}}[n(\mathbf{r})] \quad (2.6)$$

The expressions for the functionals T_s , V_{ext} and E_H are explicit. An analytic expression for E_{XC} , however, is unknown yet. A lot of effort has been made to make approximations for the XC functional, such as the local density approximation (LDA) and generalized gradient approximation (GGA). Fortunately, a large number of approximated XC functionals have been formulated now

and already embedded in computational chemistry software, where we can choose readily for the study of almost any chemical system.

2.3 Activation Strain Model of Reactivity

The activation strain model (ASM) ^[11] is a tool used throughout this thesis to aid in the understanding of chemical reactivity. A brief introduction to this methodology is presented below and the interested reader can find a detailed description and step-by-step protocol on how to use this model in practical chemical problems in ref. 11b and ref. 11a, respectively.

Multiple theoretical models of reactivity, such as the valence bond (VB)^[12] theory and frontier molecular orbital (FMO)^[13] theory, have been developed and used in various chemical reactions. In the context of the VB theory, the energy profile along the course of the thermal reaction can be constructed by mixing several crossing curves, which respectively represent the energy profiles of different resonance states of the reacting system. This model studies the reactivity from an overall system and can answer questions such as, why there is a low or a high activation barrier and in which situation substantial resonance stabilization of the transition state can be expected.^[14] On the other hand, the FMO theory provides a framework for the qualitative analysis of reactivity by inspecting symmetry-allowed interactions between the reactants.^[13] Our activation strain model constitutes a significant extension of the FMO theory, by considering all types of interactions between the reactants. Moreover, the ASM approach also takes into account the deformation of the reactants that occurs upon reaction.

In the ASM analysis, the bonding energy along the coordinate (ξ) of the reaction, $\Delta E(\xi)$, is decomposed into two contributions (Eq. 2.7): the strain energy term $\Delta E_{\text{strain}}(\xi)$, and the interaction energy term $\Delta E_{\text{int}}(\xi)$. The destabilizing $\Delta E_{\text{strain}}(\xi)$ term is the energy required for the distortion of individual reactants from the reference geometries, for instance, the equilibrium geometries. The rigidity of the reactant structure together with the degree of the distortion determine the magnitude of the $\Delta E_{\text{strain}}(\xi)$. Moreover, the $\Delta E_{\text{strain}}(\xi)$ term consists of contributions from each reactant (Eq. 2.8). The stabilizing $\Delta E_{\text{int}}(\xi)$ term accounts for the energy along with all types of interactions between the distorted reactants. An ASM analysis along the entire progress of the reaction reveals how the energy profile of the reaction evolves with the interplay between the $\Delta E_{\text{strain}}(\xi)$ and $\Delta E_{\text{int}}(\xi)$, and, therefore, answers the question of why the activation energy is high or low. The $\Delta E_{\text{int}}(\xi)$ term

can be further decomposed, by means of the energy decomposition analysis (EDA),^[15] into three physically meaningful terms: $\Delta E_{\text{Pauli}}(\xi)$, $\Delta V_{\text{elstat}}(\xi)$, and $\Delta E_{\text{oi}}(\xi)$ (Eq. 2.9).

$$\Delta E(\xi) = \Delta E_{\text{strain}}(\xi) + \Delta E_{\text{int}}(\xi) \quad (2.7)$$

$$\Delta E_{\text{strain}}(\xi) = \Delta E_{\text{strain}_A}(\xi) + \Delta E_{\text{strain}_B}(\xi) \quad (2.8)$$

$$\Delta E_{\text{int}}(\xi) = \Delta E_{\text{Pauli}}(\xi) + \Delta V_{\text{elstat}}(\xi) + \Delta E_{\text{oi}}(\xi) \quad (2.9)$$

Assuming that the distorted reactants A and B are the fragments of the complex AB and are infinitely far away from each other. The two fragments have the electron densities ρ_A and ρ_B , with the corresponding wavefunctions ψ_A and ψ_B and electronic energies E_A and E_B , respectively. The ΔV_{elstat} term is the classical electrostatic interaction between these two fragments as they are brought from infinity to their positions in the complex AB, giving rise to the density sum $\rho_{A+B} = \rho_A + \rho_B$, and the corresponding product wavefunction $\psi_A\psi_B$. It consists of the Coulombic repulsion between the nuclei of the fragments and between the unperturbed electron densities ρ_A and ρ_B , with the attractive interactions between the nuclei of one fragment and the electron density of the other fragment (**Figure 2.1a**). The total electrostatic interaction between the fragments in the chemically relevant distances is usually attractive. In other words, the ΔV_{elstat} is a stabilizing (negative) term.

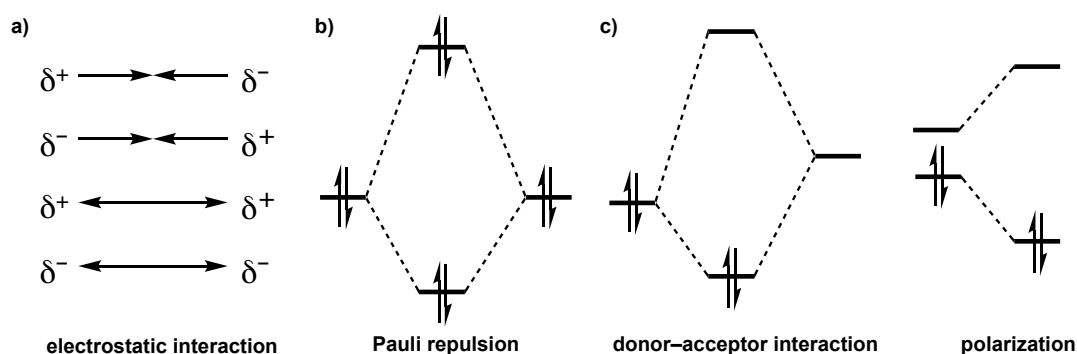


Figure 2.1 Schematic representations of the a) electrostatic interaction, b) Pauli repulsion, and c) orbital interaction in the molecular orbital model.

The ΔE_{Pauli} term is the energy change along with an antisymmetrization by the operator A and normalization by the constant N of the wavefunction $\psi_A\psi_B$, in order to obey the Pauli principle. This leads to the intermediate wavefunction $\psi^0 = N A \psi_A \psi_B$ and the corresponding energy E^0 . Thus, the $\Delta E^0 = E^0 - E_A - E_B = \Delta V_{\text{elstat}} + \Delta E_{\text{Pauli}}$ and $\Delta E_{\text{Pauli}} = \Delta E^0 - \Delta V_{\text{elstat}}$. The Pauli repulsion accounts for the interactions between the electrons with the same spin, being the origin of the steric repulsion. It is responsible for, for example, the 4-electron interactions between the doubly occupied orbitals

from the different fragments (**Figure 2.1b**). In the last step, the system is allowed to relax from ψ^0 to the final state ψ^{AB} with the energy E^{AB} . The energy change along with this step is the orbital interaction energy $\Delta E_{oi} = E^{AB} - E^0$. The ΔE_{oi} is a stabilizing (negative) term, accounting for the charge transfers (interactions between occupied orbitals of one fragment and unoccupied orbitals of the other fragment) and polarizations (unoccupied-occupied orbital mixing on one fragment due to the presence of the other fragment) (**Figure 2.1c**). The ASM analysis can be done by using the PyFrag program,^[16] which is a ‘wrapper’ for the Amsterdam Modeling Suite (ASM)^[17] and allows for the energy decomposition analysis (EDA) implemented in the ASM along the entire potential energy surface. The newest version of the program, PyFrag 2019,^[16a] is also able to import the coordinates of the reaction path and directly proceed with the ASM analysis workflow using either ASM, Gaussian, ORCA, or Turbomole.

2.4 References

- [1] a) E. Schrödinger, *Ann. Phys.* **1926**, *384*, 361–376; b) E. Schrödinger, *Phys. Rev.* **1926**, *28*, 1049–1052; c) P. A. M. Dirac, *Proc. R. Soc. Lond. A* **1928**, *117*, 610–624.
- [2] M. Born, R. Oppenheimer, *Annalen der Physik* **1927**, *389*, 457–484.
- [3] I. N. Levine, *Quantum chemistry, 7th edition*, Prentice Hall: Upper Saddle River, **2013**.
- [4] a) D. R. Hartree, *Math. Proc. Camb. Philos. Soc.* **1928**, *24*, 89–312; b) J. C. Slater, *Phys. Rev.* **1928**, *32*, 339–348; c) J. A. Gaunt, *Math. Proc. Camb. Philos. Soc.* **1928**, *24*, 328–342; d) J. C. Slater, *Phys. Rev.* **1930**, *35*, 210–211; e) V. Fock, *Z. Phys.* **1930**, *61*, 126–148; f) V. Fock, *Z. Phys.* **1930**, *62*, 795–805; g) D. R. Hartree, W. Hartree, *Proc. R. Soc. Lond. A* **1935**, *15*, 9–33.
- [5] C. Møller, M. S. Plesset, *Phys. Rev.* **1934**, *46*, 618–622.
- [6] U. Fano, *Phys. Rev.* **1961**, *124*, 1866–1878.
- [7] a) G. D. Purvis III, R. J. Bartlett, *J. Chem. Phys.* **1982**, *76*, 1910–1918; b) K. Raghavachari, G. W. Trucks, J. A. Pople, M. Head-Gordon, *Chem. Phys. Lett.* **1989**, *157*, 479–483.
- [8] a) L. H. Thomas, *Math. Proc. Camb. Philos. Soc.* **1927**, *23*, 542–548; b) E. Fermi, *Z. Phys.* **1928**, *48*, 73–79.
- [9] P. Hohenberg, W. Kohn, *Phys. Rev.* **1964**, *136*, 864–871.

- [10] W. Kohn, L. J. Sham, *Phys. Rev.* **1965**, *140*, 1133–1138.
- [11] a) P. Vermeeren, T. A. Hamlin, F. M. Bickelhaupt, *Chem. Commun.* **2021**, *57*, 5880–5896; b) P. Vermeeren, S. C. C. van der Lubbe, C. Fonseca Guerra, F. M. Bickelhaupt, T. A. Hamlin, *Nat. Protoc.* **2020**, *15*, 649–667; c) F. M. Bickelhaupt, K. N. Houk, *Angew. Chem. Int. Ed.* **2017**, *56*, 10070–10086; *Angew. Chem.* **2017**, *129*, 10204–10221; d) F. M. Bickelhaupt, K. N. Houk, *Angew. Chem.* **2017**, *129*, 10204–10221; e) D. H. Ess, K. N. Houk, *J. Am. Chem. Soc.* **2008**, *130*, 10187–10198; f) L. P. Wolters, F. M. Bickelhaupt, *Wiley Interdiscip. Rev.: Comput. Mol. Sci.* **2015**, *5*, 324–343; g) I. Fernández, F. M. Bickelhaupt, *Chem. Soc. Rev.* **2014**, *43*, 4953–4967; h) W.-J. van Zeist, F. M. Bickelhaupt, *Org. Biomol. Chem.* **2010**, *8*, 3118–3127.
- [12] a) A. Pross, S. S. Shaik, *Acc. Chem. Res.* **1983**, *16*, 363–370; b) S. S. Shaik, P. C. Hiberty, *A Chemist's Guide to Valence Bond Theory*, Wiley-Interscience, Hoboken, **2008**; c) D. Usharani, W. Lai, C. Li, H. Chen, D. Danovich, S. Shaik, *Chem. Soc. Rev.* **2014**, *43*, 4968–4988.
- [13] a) R. Hoffmann, *Angew. Chem. Int. Ed. Engl.* **1982**, *21*, 711–724; *Angew. Chem.* **1982**, *94*, 725–739; b) K. Fukui, *Angew. Chem. Int. Ed. Engl.* **1982**, *21*, 801–809; *Angew. Chem.* **1982**, *94*, 852–861; c) I. Fleming, *Molecular Orbitals and Organic Chemical Reactions*, Wiley, Chichester, **2009**; d) T. A. Albright, J. K. Burdett, M. H. Whangbo, *Orbital Interactions in Chemistry, 2nd edition*, Wiley, Hoboken, **2013**.
- [14] a) D. J. Mitchell, H. B. Schlegel, S. S. Shaik, S. Wolfe, *Can. J. Chem.* **1985**, *63*, 1642–1648; b) S. Shaik, A. Shurki, *Angew. Chem. Int. Ed.* **1999**, *38*, 586–625; *Angew. Chem.* **1999**, *111*, 616–657; c) W. Lai, C. Li, H. Chen, S. Shaik, *Angew. Chem. Int. Ed.* **2012**, *51*, 5556–5578 ; *Angew. Chem.* **2012**, *124*, 5652–5676; d) B. Braidia, C. Walter, B. Engels, P. Hiberty, *J. Am. Chem. Soc.* **2010**, *132*, 7631–7637; e) D. Usharani, D. Janar-danan, C. Li, S. Shaik, *Acc. Chem. Res.* **2013**, *46*, 471–482; f) D. Usharani, D. C. Lacy, A. S. Borovik, S. Shaik, *J. Am. Chem. Soc.* **2013**, *135*, 17090–17104; g) J. Li, S. Zhou, J. Zhang, M. Schlangen, T. Weiske, D. Usharani, S. Shaik, H. Schwarz, *J. Am. Chem. Soc.* **2016**, *138*, 7973–7981; h) J. Li, S. Zhou, J. Zhang, M. Schlangen, D. Usharani, S. Shaik, H. Schwarz, *J. Am. Chem. Soc.* **2016**, *138*, 11368–11377.

- [15] a) F. M. Bickelhaupt, E. J. Baerends in *Reviews in Computational Chemistry* (Eds: K. B. Lipkowitz, D. B. Boyd), Wiley, Hoboken, **2000**, pp 1–86; b) R. van Meer, O. V. Gritsenko, E. J. Baerends, *J. Chem. Theory Comput.* **2014**, *10*, 4432; c) L. Zhao, M. von Hopffgarten, D. M. Andrada, G. Frenking, *WIREs Comput. Mol. Sci.* **2018**, *8*, e1345; d) T. A. Hamlin, P. Vermeeren, C. Fonseca Guerra, F. M. Bickelhaupt, “Energy decomposition analysis in the context of quantitative molecular orbital theory” in *Complementary Bonding Analysis* (Ed: S. Grabowsky), De Gruyter, Berlin, Boston, **2021**, pp 199–212.
- [16] a) X. Sun, T. M. Soini, J. Poater, T. A. Hamlin, F. M. Bickelhaupt, *J. Comput. Chem.* **2019**, *40*, 2227–2233; b) W. J. van Zeist, C. Fonseca Guerra, F. M. Bickelhaupt, *J. Comp. Chem.* **2008**, *29*, 312–315.
- [17] AMS 2020, SCM, Theoretical Chemistry, Vrije Universiteit, Amsterdam, The Netherlands, <http://www.scm.com>.

Chapter 3 A Benchmark Study of the DFT Methods for Cycloaddition Reactions

This chapter previously appeared in

Eur. J. Org. Chem. **2019**, 378–386.

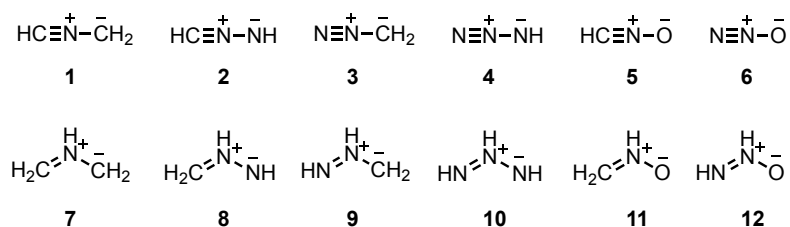
Trevor A. Hamlin, Dennis Svatunek, Song Yu, Lars Ridder, Ivan Infante, Lucas Visscher,
F. Matthias Bickelhaupt

(The author contributed partially to this work)

This chapter presents a benchmark study of the density functional theory (DFT) methods for cycloaddition reactions. 24 1,3-dipolar cycloaddition reactions were benchmarked using the highly accurate G3B3 method as the reference. Several exchange and correlation functionals, including PBE, OLYP, BP86, BLYP, both with and without explicit dispersion corrections, were screened to assess their accuracies and to determine which of these computationally efficient functionals perform the best for calculating the trends in the activation and reaction energetics of cycloaddition reactions. The BP86/TZ2P method was found to produce the smallest errors for the activation and reaction enthalpies of cycloaddition reactions. However, when the non-covalent interactions are suspected to play a role, BLYP-D3/TZ2P would likely yield accurate barriers.

3.1 Introduction

In previous studies, composite ab initio methods, as well as density functional theory (DFT) methods, have been used to study cycloaddition reactions.^[1] The composite ab initio methods are most accurate but computationally demanding and are limited to small systems. DFT methods are most frequently employed for quantum mechanical calculations of 1,3-dipolar cycloadditions because of the balance between accuracy and efficiency. In this study, we performed a benchmark study of DFT methods for cycloaddition reactions, by using the composite ab initio method G3B3 as a reference.^[2] The QMflows^[3] package was used to evaluate the performance of BP86, BP86-D3, PBE, PBE-D3, BLYP, BLYP-D3, and OLYP exchange and correlation functionals in conjunction with the TZ2P basis set in reproducing the G3B3-computed activation and reaction enthalpies^[4] for 24 1,3-dipolar cycloaddition reactions between dipoles **1–12** (Scheme 3.1) and both ethylene and acetylene. The Amsterdam Density Functional suite^[5] was used for all calculations. Grimme's DFT-D3^[6] dispersion corrections were included in our study to determine an optimal method that can be used when dispersion interactions are expected to be present.



Scheme 3.1 Dipoles **1–12** included in the benchmark study.

3.2 Results and Discussion

We utilized QMflows^[3] to benchmark various GGA functionals in ADF, with and without explicit dispersion corrections, to assess their accuracies and to determine an affordable method for larger systems. This highly automated workflow explores the potential energy surface (PES) for the reactions between dipoles **1–12** and dipolarophiles, ethylene and acetylene. This first involves optimizations of the reactants (dipole and dipolarophile) and the cycloadduct. Next, the PES is scanned by the symmetric elongation of the newly forming bonds of the cycloadduct, with a series of constrained geometry optimizations. The highest point on this PES is then used as the input for the transition state calculation. Vibrational frequencies are then calculated for all stationary points

in order to assess whether they are energy minima or first-order saddle points. Upon completion of these steps, the results are then automatically processed and the requested energy values, in our case the activation (ΔH^\ddagger) and reaction (ΔH_{rxn}) enthalpies are printed. The energetic results are compared to the reference energies obtained from the high-level G3B3 data.^[4]

The computed G3B3, reproduced from a study by Houk and coworkers,^[4] and XC/TZ2P (where XC = BP86, BP86-D3, PBE, PBE-D3, BLYP, BLYP-D3, and OLYP) activation enthalpies (ΔH^\ddagger) and reaction enthalpies (ΔH_{rxn}) for cycloadditions of **1–12** (Scheme 3.1) with ethylene and acetylene are presented in Table 3.1 and Table 3.2, respectively. All enthalpies are computed with respect to separate, optimized reactants. The mean deviations (MD), mean absolute deviations (MAD), standard deviations (SD), and maximum errors (negative and positive) relative to the corresponding G3B3-calculated energies are included in Table 3.3.

Table 3.1 Calculated activation enthalpies (ΔH^\ddagger) and reaction enthalpies (ΔH_{rxn}) (in kcal mol⁻¹) for 1,3-dipolar cycloadditions between **1–12** and ethylene. All were based on TZ2P basis set.

dipole	G3B3		BP86		BP86-D3		PBE		PBE-D3		BLYP		BLYP-D3		OLYP	
	ΔH^\ddagger	ΔH_{rxn}	ΔH^\ddagger	ΔH_{rxn}	ΔH^\ddagger	ΔH_{rxn}	ΔH^\ddagger	ΔH_{rxn}	ΔH^\ddagger	ΔH_{rxn}	ΔH^\ddagger	ΔH_{rxn}	ΔH^\ddagger	ΔH_{rxn}	ΔH^\ddagger	ΔH_{rxn}
1	6.0	-69.1	6.0	-58.6	2.3	-61.5	4.4	-62.8	2.5	-3.72	9.6	-48.6	5.6	-50.7	13.1	-54.9
2	7.4	-58.0	6.8	-48.0	3.3	-50.5	5.3	-51.1	3.6	-52.3	9.9	-35.7	6.2	-40.6	13.8	-43.0
3	15.1	-32.6	13.8	-25.0	10.2	-27.6	12.2	-28.1	9.0	-30.7	17.6	-16.2	13.6	-20.2	21.1	-20.4
4	20.9	-20.4	17.3	-14.1	14.4	-16.3	15.9	-16.8	14.4	-17.8	21.0	-4.6	17.9	-7.4	25.7	-8.1
5	12.2	-40.3	10.4	-32.9	7.1	-35.1	9.0	-35.2	7.4	-36.3	13.2	-25.5	9.6	-27.0	17.0	-27.4
6	27.8	-4.8	22.6	-1.6	19.9	-3.5	21.3	-3.5	20.0	-4.4	25.7	4.3	22.8	3.2	31.5	5.5
7	1.3	-63.4	2.1	-52.0	-2.5	-55.6	0.5	-55.5	-1.9	-57.3	6.2	-41.6	1.3	-44.9	9.6	-47.9
8	8.0	-44.9	7.8	-35.4	3.4	-38.1	6.0	-38.0	3.8	-40.0	12.7	-24.8	8.0	-28.3	15.4	-29.1
9	16.7	-29.8	15.7	-20.4	11.8	-23.4	14.0	-23.0	12.1	-24.5	20.9	-11.2	16.6	-14.4	24.4	-13.5
10	13.4	-29.6	12.2	-20.8	8.1	-21.6	10.5	-21.2	8.5	-22.6	16.6	-10.5	12.2	-13.7	20.4	-11.7
11	23.2	-16.3	20.8	-8.5	21.3	-11.8	23.6	-10.5	21.9	-11.8	29.5	-1.2	25.9	-4.2	18.8	-0.3
12	29.6	-4.2	25.4	3.9	22.1	-0.1	24.3	1.1	22.7	-0.1	28.9	8.5	25.3	5.7	35.1	11.3

Table 3.2 Calculated activation enthalpies (ΔH^\ddagger) and reaction enthalpies (ΔH_{rxn}) (in kcal mol⁻¹) for 1,3-dipolar cycloadditions between **1–12** and acetylene. All were based on TZ2P basis set.

dipole	G3B3		BP86		BP86-D3		PBE		PBE-D3		BLYP		BLYP-D3		OLYP	
	ΔH^\ddagger	ΔH_{rxn}	ΔH^\ddagger	ΔH_{rxn}	ΔH^\ddagger	ΔH_{rxn}	ΔH^\ddagger	ΔH_{rxn}	ΔH^\ddagger	ΔH_{rxn}	ΔH^\ddagger	ΔH_{rxn}	ΔH^\ddagger	ΔH_{rxn}	ΔH^\ddagger	ΔH_{rxn}
1	6.0	-69.1	6.0	-58.6	2.3	-61.5	4.4	-62.8	2.5	-3.72	9.6	-48.6	5.6	-50.7	13.1	-54.9
2	7.4	-58.0	6.8	-48.0	3.3	-50.5	5.3	-51.1	3.6	-52.3	9.9	-35.7	6.2	-40.6	13.8	-43.0
3	15.1	-32.6	13.8	-25.0	10.2	-27.6	12.2	-28.1	9.0	-30.7	17.6	-16.2	13.6	-20.2	21.1	-20.4
4	20.9	-20.4	17.3	-14.1	14.4	-16.3	15.9	-16.8	14.4	-17.8	21.0	-4.6	17.9	-7.4	25.7	-8.1
5	12.2	-40.3	10.4	-32.9	7.1	-35.1	9.0	-35.2	7.4	-36.3	13.2	-25.5	9.6	-27.0	17.0	-27.4
6	27.8	-4.8	22.6	-1.6	19.9	-3.5	21.3	-3.5	20.0	-4.4	25.7	4.3	22.8	3.2	31.5	5.5
7	1.3	-63.4	2.1	-52.0	-2.5	-55.6	0.5	-55.5	-1.9	-57.3	6.2	-41.6	1.3	-44.9	9.6	-47.9
8	8.0	-44.9	7.8	-35.4	3.4	-38.1	6.0	-38.0	3.8	-40.0	12.7	-24.8	8.0	-28.3	15.4	-29.1
9	16.7	-29.8	15.7	-20.4	11.8	-23.4	14.0	-23.0	12.1	-24.5	20.9	-11.2	16.6	-14.4	24.4	-13.5
10	13.4	-29.6	12.2	-20.8	8.1	-21.6	10.5	-21.2	8.5	-22.6	16.6	-10.5	12.2	-13.7	20.4	-11.7
11	23.2	-16.3	20.8	-8.5	21.3	-11.8	23.6	-10.5	21.9	-11.8	29.5	-1.2	25.9	-4.2	18.8	-0.3
12	29.6	-4.2	25.4	3.9	22.1	-0.1	24.3	1.1	22.7	-0.1	28.9	8.5	25.3	5.7	35.1	11.3

The BP86/TZ2P method outperforms all other methods for the calculation of activation enthalpies and has an MD and MAD of only -1.9 and 2.3 kcal mol⁻¹, respectively. The BP86 reaction enthalpies are, on average, 6.1 kcal mol⁻¹ higher than G3B3 values. Inclusion of Grimme's

D3 dispersion corrections (BP86-D3/TZ2P), yields consistently lower activation enthalpies, with MAD of 5.0 kcal mol⁻¹. Reaction enthalpies using this method are slightly more accurate, having slightly more favorable MD, MAD, and SD values. PBE/TZ2P and PBE-D3/TZ2P are both less accurate (larger MD and MAD) than BP86/TZ2P in the calculation of activation enthalpies, but are only slightly better for calculating reaction enthalpies. The BLYP/TZ2P and OLYP/TZ2P methods both overestimate barriers and perform very poorly in calculating reaction enthalpies. The BLYP-D3/TZ2P method performs well in calculating activation enthalpies (MAD = 1.9 kcal mol⁻¹), but reaction enthalpies deviate significantly from the G3B3 values.

Table 3.3 Summary of statistical analysis (in kcal mol⁻¹): mean deviations ΔH_{MD} , mean absolute deviations ΔH_{MAD} , standard deviation ΔH_{SD} , maximum negative $\Delta H_{\text{max}(-)}$ and positive $\Delta H_{\text{max}(+)}$ error relative to G3B3-computed enthalpies of activation and reaction energies for 1,3-dipolar cycloaddition reactions between **1–12** with ethylene and acetylene.

	BP86	BP86-D3	PBE	PBE-D3	BLYP	BLYP-D3	OLYP
$\Delta H_{\text{MD}}^{\ddagger}$	-1.9	-5.0	-3.3	-4.9	1.8	-1.4	5.3
$\Delta H_{\text{MAD}}^{\ddagger}$	2.3	5.0	3.4	5.0	2.7	1.9	5.6
$\Delta H_{\text{SD}}^{\ddagger}$	2.2	1.7	2.1	1.9	2.6	2.1	2.7
$\Delta H_{\text{max}(-)}^{\ddagger}$	-6.2	-8.3	-7.4	-8.4	-3.0	-4.8	-4.4
$\Delta H_{\text{max}(+)}^{\ddagger}$	0.8	[a]	0.4	[a]	4.8	2.8	9.2
$\Delta H_{\text{rxn MD}}$	6.1	4.4	4.1	2.1	15.1	12.9	12.5
$\Delta H_{\text{rxn MAD}}$	6.3	4.6	4.5	3.8	15.5	13.4	12.5
$\Delta H_{\text{rxn SD}}$	3.5	3.0	3.4	4.6	5.7	5.2	3.5
$\Delta H_{\text{rxn max}(-)}$	-2.2	-3.1	-4.1	-14	-5.4	-7.9	[a]
$\Delta H_{\text{rxn max}(+)}$	12.4	10.6	9.9	9.2	22.3	19.7	19.6

[a] No computed activation enthalpy higher than the G3B3 value.

3.3 Conclusions

We suggest using the BP86/TZ2P for the calculations of cycloaddition reactions when dispersion energies are expected to be negligible. However, when non-covalent interactions are suspected to play a role, BLYP-D3/TZ2P would likely yield accurate barriers. After weighing the performance and cost of the DFT functionals, we select the BP86/TZ2P method for the following studies in this thesis.

3.4 References

- [1] a) D. H. Ess, K. N. Houk, *J. Am. Chem. Soc.* **2008**, *130*, 10187–10198; b) D. H. Ess, K. N. Houk, *J. Am. Chem. Soc.* **2007**, *129*, 10646–10647; c) G. O. Jones, D. H. Ess, K. N. Houk, *Helv. Chim. Acta* **2005**, *88*, 1702–1710.
- [2] A. G. Baboul, L. A. Curtiss, P. C. Redfern, K. Raghavachari, *J. Chem. Phys.* **1999**, *110*, 7650–7657.
- [3] F. Zapata, L. Ridder, J. Hidding, C. R. Jacob, I. Infante, L. Visscher, *J. Chem. Inf. Model.* **2019**, *59*, 7, 3191–3197.
- [4] Y. Lan, L. Zou, Y. Cao, K. N. Houk, *J. Phys. Chem. A* **2011**, *115*, 13906–13920.
- [5] a) G. te Velde, F. M. Bickelhaupt, E. J. Baerends, C. Fonseca Guerra, S. J. A. van Gisbergen, J. G. Snijders, T. Ziegler, *J. Comput. Chem.* **2001**, *22*, 931–967; b) C. Fonseca Guerra, J. G. Snijders, G. te Velde, E. J. Baerends, *Theor. Chem. Acc.* **1998**, *99*, 391–403; c) ADF, SCM Theoretical Chemistry; Vrije Universiteit: Amsterdam, The Netherlands, **2016**; <http://www.scm.com>.
- [6] S. Grimme, J. Antony, S. Ehrlich, H. Krieg, *J. Chem. Phys.* **2010**, *132*, 154104.

Chapter 4 How Heteroatoms Affect the Diels-Alder Reactivity of 1,3-Butadienes

This chapter previously appeared as

ChemistryOpen **2018**, 7, 995–1004.

Song Yu, Hans M. de Bruijn, Dennis Svatunek, Trevor A. Hamlin, F. Matthias Bickelhaupt

In this chapter, we studied the Diels-Alder reactivity of a systematic series of hetero-1,3-butadienes by using density functional theory at the BP86/TZ2P level. Activation strain analyses provided physical insight into the factors controlling the relative cycloaddition reactivities of aza- and oxa-1,3-butadienes. Dienes with a terminal heteroatom, such as 2-propen-1-imine (**NCCC**) or acrolein (**OCCC**), are less reactive than the archetypal 1,3-butadiene (**CCCC**), primarily owing to weaker orbital interactions between the more electronegative heteroatoms with ethylene. Thus, the addition of the second heteroatom at the other terminal position (**NCCN** and **OCCO**) further reduces the Diels-Alder reactivity. However, the introduction of a nitrogen atom in the backbone (**CNCC**) leads to an enhanced reactivity, owing to a less Pauli repulsion resulting from the polarization of the HOMO in **CNCC** towards the nitrogen atom and away from the terminal carbon atom. The Diels-Alder reactions of ethenyl-diazene (**NNCC**) and 1,3-diaza-butadiene (**NCNC**), which contain heteroatoms at both the terminal and backbone positions, are much more reactive due to less activation strain compared to **CCCC**.

4.1 Introduction

One of the most iconic reactions in the field of organic chemistry are the Diels-Alder cycloadditions. Since Diels-Alder reactions were first described by Otto Diels and Kurt Alder in 1928,^[1] these [4+2] cycloadditions between 1,3-dienes and unsaturated dienophiles have found broad applications in the synthesis of 6-membered unsaturated ring systems. Diels-Alder reactions have played an important role in all fields of chemistry, from total synthesis^[2] to material science.^[3] While the archetypal [4+2] cycloadditions described by Diels and Alder featured alkenes and 1,3-dienes as reactants, reactions between hetero-dienes and hetero-dienophiles are possible.^[4] These hetero-Diels-Alder reactions are important synthetic methods for the formation of heterocycles.

One can differentiate between different subtypes of hetero-Diels-Alder reactions. The most common classification is based on the hetero-element present in the substrates. The introduction of nitrogen into the diene or dienophile leads to aza-Diels-Alder cycloadditions. These reactions are commonly used in total synthesis for the formation of nitrogen-containing heterocyclic scaffolds. Notable examples employing aza-Diels-Alder reactions as a key step include, among many others,^[5] the synthesis of streptonigrone by Boger and co-workers,^[6] ipalbidine by Danishefsky and co-workers,^[7] (+)-reserpine by Jacobsen and co-workers,^[8] and phyllanthine by Weinreb and co-workers^[9] (**Figure 4.1**).

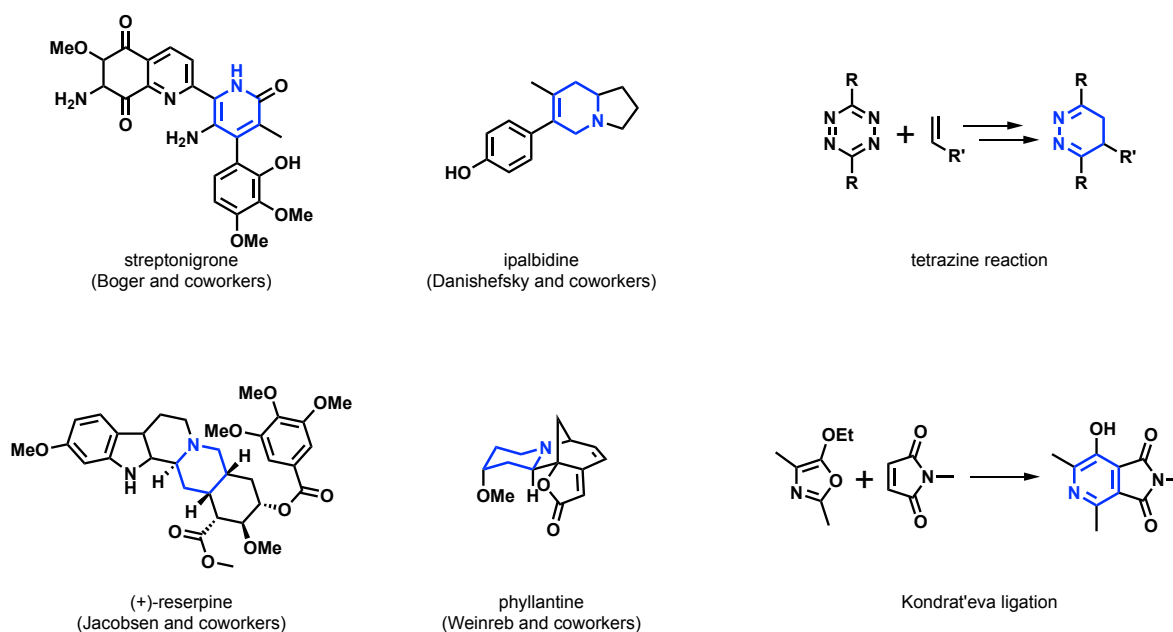


Figure 4.1 Notable natural products synthesized using an aza-Diels-Alder reaction as key step and two bioorthogonal ligations based on aza-Diels-Alder reactions.

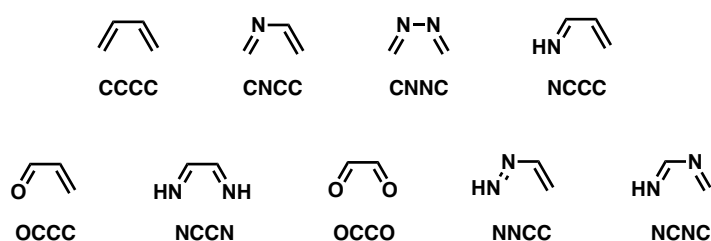
Another important aza-Diels-Alder cycloaddition is the reaction between 1,2,4,5-tetrazines and electron-rich dienophiles. In 1964, Sauer reported on the reaction of tetrazines with dienophiles.^[10] This bioorthogonal cycloaddition proceeds through an inverse electron demand Diels-Alder reaction, followed by a cyclo-reversion under the loss of nitrogen, and was independently introduced by Fox and co-workers^[11] and Weissleder and co-workers^[12] in 2008. This ligation is often used in time-critical applications,^[13] due to the exceptionally high possible second-order rate constants of up to $3,300,000 \text{ M}^{-1} \text{ s}^{-1}$.^[14] Due to the range of possible dienophiles, this bioorthogonal reaction can be applied in various applications. While *trans*-cyclooctenes are used for high reactivity, cyclopropenes^[15] can be used for metabolic incorporation,^[16] due to their smaller size. Introduction of a carbamate in allylic position to the double bond of a *trans*-cyclooctene allows for "click-to-release" reactions,^[17] opening up the possibility for targeted drug delivery.^[18] The use of vinylboronic acids^[19] can lead to high selectivity towards 2-pyridyl^[20] or 2-hydroxyphenyl^[21] substituted 1,2,4,5-tetrazines, as recently shown by Bonger and co-workers. Other bioorthogonal ligations based on aza-Diels-Alder reactions include the 1,2,4-triazine ligation introduced by Prescher and co-workers^[22] and a variant of the Kondrat'eva reaction introduced by Jouanno *et al.* (**Figure 4.1**).^[23]

Another subtype of hetero-Diels-Alder reactions are oxo-Diels-Alder cycloadditions. In these [4+2] cycloadditions, carbonyl compounds are used as dienophiles or 1,3-dienes.^[4, 24] Due to the low reactivity of such reaction partners in predominantly inverse electron demand Diels-Alder reactions Lewis acid catalysis,^[25] cinchona alkaloid-derived amine catalysis,^[26] or N-heterocyclic carbene organo-catalysis^[27] is often used. This also opens the possibility of enantioselective Diels-Alder cycloadditions forming pyran derivatives.^[28]

Reactivities of aza- and oxo-hetero-Diels-Alder cycloadditions are found within a wide range, from unreactive to very highly reactive as observed in tetrazine ligation reactions^[14] or the Diels-Alder reactions of superelectrophiles, which show good yields with the quite unreactive ethylene at reasonably low pressure and room temperature.^[29] However, while the kinetics of several examples of such hetero-Diels-Alder reactions have been the subject of experimental and theoretical studies,^[30] to the best of our knowledge only one study on the influence of single nitrogen or oxygen atoms within the 1,3-diene on the kinetics of Diels-Alder cycloadditions has been conducted. Houk and co-workers have investigated the reactivity of cyclic and acyclic 1- and 2-azadienes in Diels-Alder reactions with ethylene.^[31] They could show that the activation barrier

height correlates very well with distortion energies at the transition state obtained from the distortion/interaction analysis (activation strain model) developed by Bickelhaupt and Houk.^[32] They also noted that the position of the transition state is shifted along the reaction coordinate for different systems. However, comparing interaction and strain energies for different systems at their respective transition state can lead to skewed conclusions, as for cycloadditions both the interaction and strain energy often increases along the reaction coordinate.^[32, 33] This means that for reactions following Hammond's postulate, systems with lower barriers of activation, and therefore earlier transition states, should have lowered strain energies at the transition state associated with them. Hence, these reactions often seem to be strain-controlled, even when the interaction energy is the key causal factor.

Therefore, the activation strain analysis should be performed at either a consistent point of the reaction coordinate or, even better, along the entire reaction coordinate. This approach has been successfully used in the past to provide quantitative insight into cycloadditions such as 1,3-dipolar cycloadditions,^[34] [3+2] cycloadditions^[35] and Diels-Alder reactions.^[33b, 36] We, therefore, aimed for an in-depth systematic investigation on the factors controlling the reactivity of oxo- and aza-hetero-dienes (**Scheme 4.1**) in Diels-Alder cycloadditions using the activation strain model in combination with a quantitative molecular orbital (MO) theory and associated canonical energy decomposition scheme. This allows for quantitative analysis of different factors influencing the reactivity, such as strain energy, Pauli repulsion, orbital interactions, and electrostatic interactions.



Scheme 4.1 1,3-Butadienes included in the study.

4.2 Computational Details

All calculations were carried out in *adf2017*^[37] using the BP86^[38] functional in combination with the TZ2P^[39] basis set. This exchange and correlation functional have been proven to adequately reproduce relative trends in activation energies and reaction energies for various cycloadditions.^[40] Vibrational frequency calculations were performed to verify energy minima and transition

states.^[41] Local minima had zero imaginary frequencies, while transition states had a single imaginary frequency. The intrinsic reaction coordinate (IRC) method was used to follow the imaginary eigenvector towards both the reactant complex and the cycloadduct. All relative energies are with respect to the *s-cis* conformation of the diene. Optimized structures were illustrated using CYLview.^[42]

Quantitative analyses of the activation barriers associated with the studied Diels-Alder reactions are obtained by means of the activation strain model (ASM), which involves decomposing the potential energy surface $\Delta E(\zeta)$ along the reaction coordinate ζ into the strain $\Delta E_{\text{strain}}(\zeta)$ associated with the structural deformation of the reactants from their equilibrium geometry and the interaction $\Delta E_{\text{int}}(\zeta)$ between the deformed reactants.^[32, 43] The $\Delta E_{\text{strain}}(\zeta)$ is determined by the rigidity of the reactants and by the extent to which they must deform in order to achieve the geometry of the transition state. The $\Delta E_{\text{int}}(\zeta)$ is usually stabilizing and is related to the electronic structure of the reactants and how they are mutually oriented over the course of the reaction:

$$\Delta E(\zeta) = \Delta E_{\text{strain}}(\zeta) + \Delta E_{\text{int}}(\zeta)$$

A deeper understanding of the interaction energy can be obtained using an energy decomposition analysis (EDA),^[44] in which the $\Delta E_{\text{int}}(\zeta)$ between the deformed reactants is decomposed, within the conceptual framework provided by the Kohn-Sham molecular orbital (KS-MO) model, into three physically meaningful terms:

$$\Delta E_{\text{int}}(\zeta) = \Delta V_{\text{elstat}}(\zeta) + \Delta E_{\text{Pauli}}(\zeta) + \Delta E_{\text{oi}}(\zeta)$$

The $\Delta V_{\text{elstat}}(\zeta)$ term corresponds to the classical electrostatic interaction between unperturbed charge distributions $\rho_A(r) + \rho_B(r)$ of the deformed fragments A and B and is usually attractive. The Pauli repulsion $\Delta E_{\text{Pauli}}(\zeta)$ comprises the destabilizing interactions between occupied orbitals and is responsible for any steric repulsion. The orbital interaction $\Delta E_{\text{oi}}(\zeta)$ accounts for charge transfer (interaction between occupied orbitals on one fragment with unoccupied orbitals of the other fragment) and polarization (empty-occupied orbital mixing on one fragment due to the presence of another fragment).

In activation strain diagrams and associated EDA plots in this study, the IRC is projected onto the average distance of two newly forming bonds. The resulting reaction coordinate ζ undergoes a well-defined change in the course of the reaction from the reactant complex to the transition state and cycloadducts. The analyses along the reaction coordinate were performed with the aid of the PyFrag program.^[45]

4.3 Results and Discussion

Figure 4.2 shows transition state structures for Diels-Alder reactions between butadiene or hetero-butadienes and ethylene (e). The computed activation energies (blue) and reaction energies (red), in kcal mol⁻¹, are shown below each structure. The archetypal Diels-Alder reaction between 1,3-butadiene (CCCC) and e has a moderate activation energy of 15.2 kcal mol⁻¹. The hetero-butadienes CNNC, NCCC, OCCC, NCCN, and OCCO are less reactive towards e compared to CCCC. Diels-Alder reactions of the hetero-butadienes containing a single heteroatom in the backbone (CNCC, NNCC, NCNC) are more reactive than the reaction of CCCC, the fastest cycloaddition being with ethenyl-diazene (NNCC).

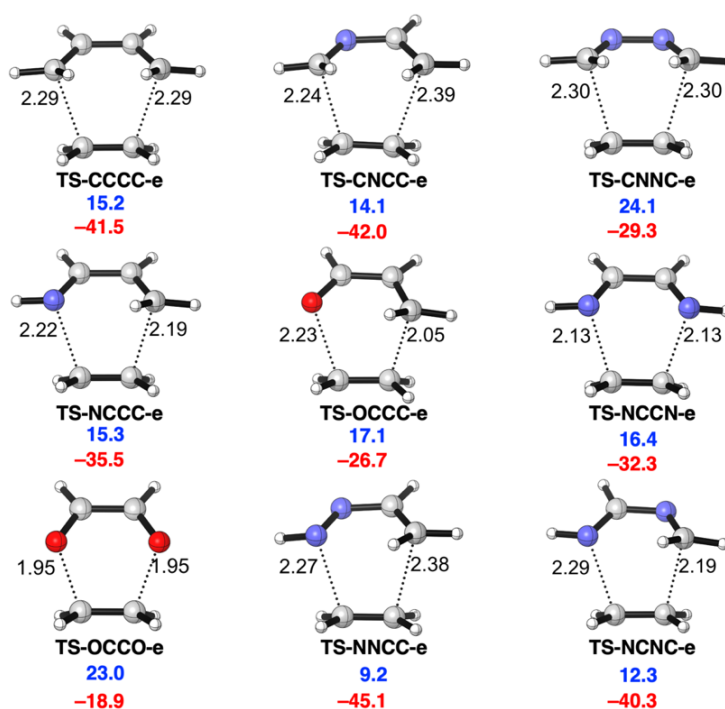


Figure 4.2 Transition state structures with forming bond lengths (Å), activation energies (ΔE^\ddagger , blue, kcal mol⁻¹), and reaction energies (ΔE_{rxn} , red, kcal mol⁻¹) for Diels-Alder reactions between 1,3-butadiene or hetero-1,3-butadienes and ethylene (e), computed at the BP86/TZ2P level.

The distances of forming bonds in the transition states are shown in **Figure 4.2**. Compared to the transition state **TS-CCCC**, with the forming bond distance of 2.29 Å, **TS-NCCC**, **TS-OCCC**, **TS-NCCN**, and **TS-OCCO** have shorter average forming bonds. The shift towards later transition states is consistent with higher barrier energies and less exothermic reaction energies. **TS-CNCC** and **TS-NNCC** have longer average forming bonds than **TS-CCCC**, and the reactions of **CNCC** and **NNCC** have lower barrier energies and are more exothermic than the reaction of **CCCC**. The cases outlined above are in line with the Hammond's postulate. However, **TS-NCNC** has a shorter average bond forming distance and the reaction is less exothermic than **TS-CCCC**, but also has a lower barrier than **TS-CCCC**. **TS-CNNC** has a longer average bond forming distance than **TS-CCCC**, but the barrier is much higher, and the reaction is much less exothermic compared to **TS-CCCC**. To provide a rationale for the differences in activation barriers for these Diels-Alder reactions, we undertook a combined activation strain and energy decomposition analysis study. The results are summarized below in three sections (**4.3.1–4.3.3**).

4.3.1 Diels-Alder Reactivity of CCCC, NCCC, NCCN, OCCC, and OCCO

The activation strain diagram for the Diels-Alder reactions between ethylene and **CCCC**, **NCCC**, **NCCN**, **OCCC**, and **OCCO** is shown in **Figure 4.3**. The terminal atoms of these dienes are systematically varied from carbon to nitrogen to oxygen. To be able to compare the different systems, energies will be compared at the consistent point along the reaction coordinate with an average bond forming distance of 2.10 Å, since this point is close, in both energy and position, to all TSs. **CCCC** is the most reactive diene of these five dienes. Reactivity decreases upon substitution of a terminal carbon atom with a nitrogen or oxygen atom and decreases further when both terminal carbon atoms are substituted. The differences in reactivity are mainly caused by a smaller *p*-orbital of the FMOs on the terminal atoms of the dienes with increasing electronegativity of the terminal atoms.^[40a, 46] For this reason the oxa-dienes are less reactive than their respective aza-dienes.

The total energies at the consistent geometry (**Figure 4.3**) as well as the heights of the activation barriers of the reactions (**Figure 4.2**) of dienes **NCCC**, **NCCN**, **OCCC**, and **OCCO** are larger than those of **CCCC**. In addition, the total energies at the consistent geometry are larger for the oxa-butadienes (**OCCC** and **OCCO**) than for the aza-butadienes (**NCCC** and **NCCN**). We find that ΔE_{int} follows the trend of ΔE : it is more stabilizing for systems with a lower ΔE and a

correlation is found between ΔE and ΔE_{int} at the consistent geometry (**Figure 4.3**). ΔE_{strain} increases with decreasing ΔE . Therefore, ΔE_{int} governs the differences in ΔE between the systems. This conclusion is consistent with our previous findings for cycloalkene Diels-Alder^[33b,36a] and aza-1,3-dipolar cycloadditions.^[40a] The differences between systems will be further discussed by the comparison of one set of dienes (**CCCC**, **NCCC**, and **OCCC**) based on the ASM, EDA, and Frontier Molecular Orbital (FMO) analyses. Analyses of two other sets of dienes (**CCCC**, **NCCC**, **NCCN** and **CCCC**, **OCCC**, **OCCO**) provided similar results and can be found in **Appendix 4.1–Appendix 4.4**.

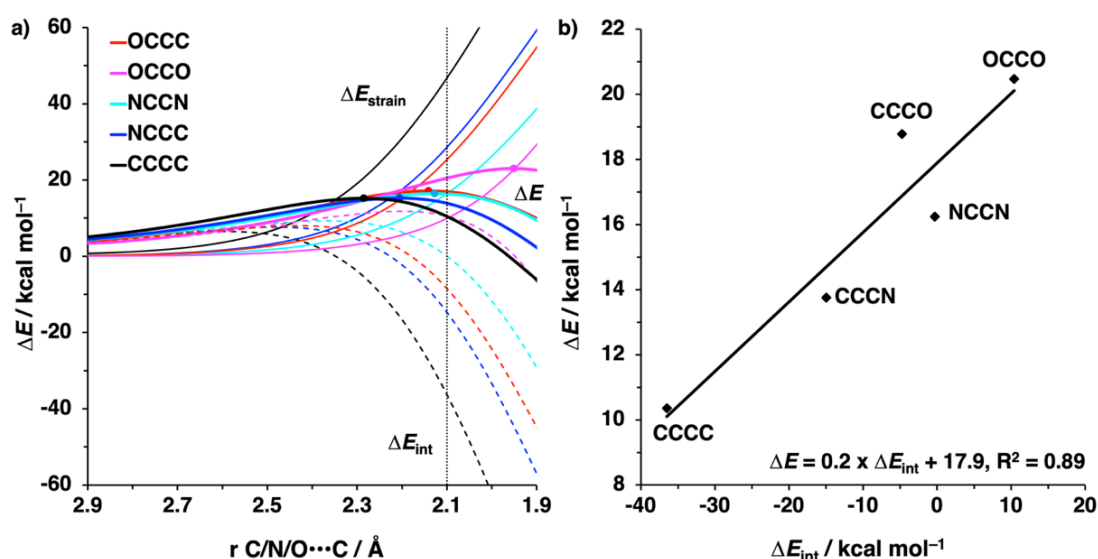


Figure 4.3 a) Activation strain analyses and b) plot of the total energies (ΔE) versus the interaction energies (ΔE_{int}) for Diels-Alder reactions between **CCCC**, **NCCC**, **NCCN**, **OCCC**, and **OCCO** with ethylene at the consistent geometry with an average $\text{C}\cdots\text{X}$ bond forming distance of 2.10 Å. All data were computed at the BP86/TZ2P level.

The ASM and EDA diagrams for the Diels-Alder reactions of **CCCC** (black), **NCCC** (blue), and **OCCC** (red) with ethylene are shown in **Figure 4.4a** and **Figure 4.4b**, respectively. At the consistent geometry, ΔE_{strain} decreases from **CCCC** to **NCCC** to **OCCC** due to the decreased number of terminal hydrogens in the hetero-butadienes, which need to be bent away during the reaction. However, this decrease in ΔE_{strain} does not yield a lower ΔE for the Diels-Alder reactions of these hetero-butadienes: ΔE_{int} plays a decisive role and governs the trends in ΔE . Decomposition of ΔE_{int} shows that ΔE_{int} is controlled by ΔE_{oi} and less so by ΔV_{elstat} , while ΔE_{Pauli} follows a trend opposite that of ΔE_{int} (**Figure 4.4b**).

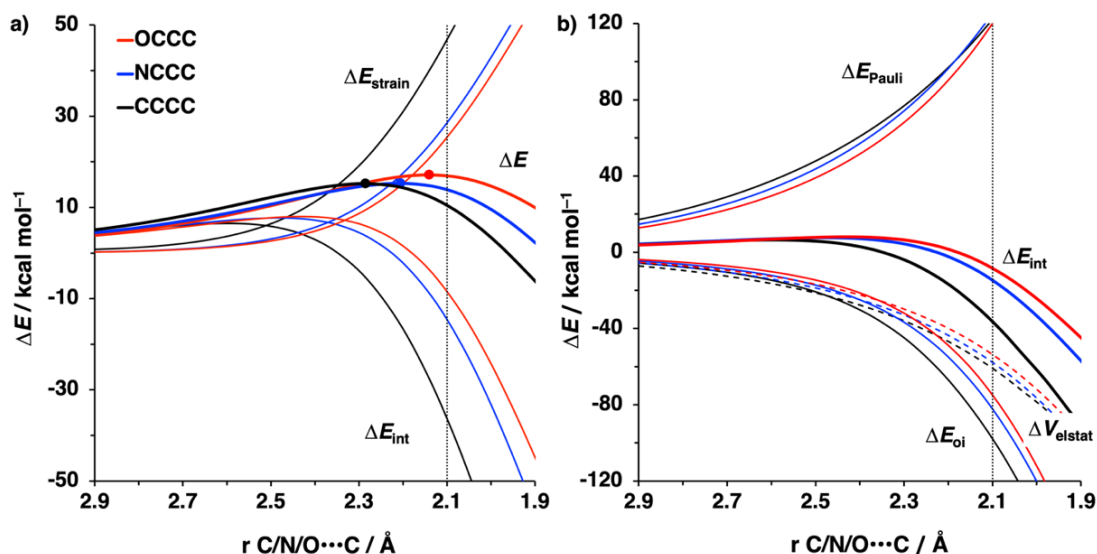


Figure 4.4 a) Activation strain and b) energy decomposition analyses of the Diels-Alder reactions between dienes CCCC, NCCC and OCCC with ethylene, computed at the BP86/TZ2P level.

The differences in ΔE_{oi} are caused by the decrease in the size of the lobe of the $\text{FMO}_{\text{diene}}$ and $\text{LUMO}_{\text{diene}}$ on the terminal atom, as it changes from C to N to O, due to the more compact nature of the $2p$ orbital of the nitrogen and oxygen atom, and by a decrease of the energy levels of both the occupied FMO and LUMO of the diene.^[40a, 46] The overlap and energy gaps between the $\text{FMO}_{\text{diene}}\text{-LUMO}_e$ and $\text{LUMO}_{\text{diene}}\text{-HOMO}_e$ (for the normal and inverse electron demand orbital interaction, respectively) are shown in **Figure 4.5**. ΔE_{oi} is most stabilizing for CCCC, and becomes weaker going to NCCC and OCCC. This destabilization is reflected in the $\text{FMO}_{\text{diene}}\text{-LUMO}_e$ and $\text{LUMO}_{\text{diene}}\text{-HOMO}_e$ gaps and the overlap between these orbitals. For the normal electron demand orbital interaction, the orbital energy gap and the overlap between the $\text{FMO}_{\text{diene}}$ and LUMO_e are smallest (3.1 eV) and largest (0.28) respectively for CCCC, while they are largest (5.3 eV) and smallest (0.19) for OCCC. The HOMO-1 of OCCC reacts with LUMO_e instead of the HOMO, due to the fact that the HOMO has become a lone pair MO. For the inverse electron demand orbital interaction, the orbital energy gap for CCCC is larger than for OCCC (3.4 and 2.8 eV, respectively), but the overlap is much larger for CCCC than for OCCC (0.25 and 0.18, respectively), thus also yielding a more stabilizing ΔE_{oi} in case of CCCC.

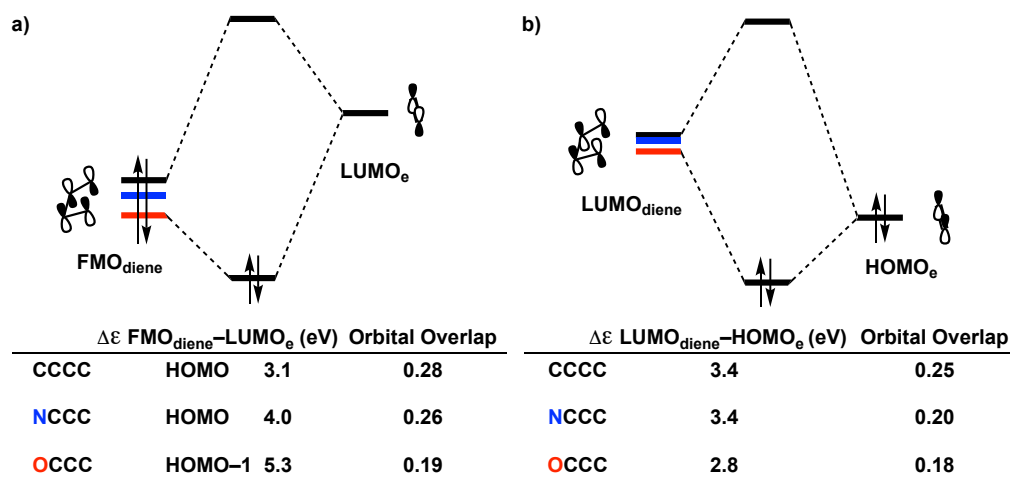


Figure 4.5 a) MO diagrams with calculated energy gaps and orbital overlaps for the normal electron demand FMO_{diene}-LUMO_e interaction and b) the inverse electron demand LUMO_{diene}-HOMO_e interaction of the Diels-Alder reactions between dienes CCCC, NCCC, and OSCC with ethylene (e). All data were computed at the BP86/TZ2P level at the consistent geometry with an average C••X bond forming distance of 2.10 Å.

4.3.2 Diels-Alder Reactivity of CCCC, CNCC, and CNNC

Next, we investigated Diels-Alder reactions between CCCC, CNCC, and CNNC with ethylene. Introducing nitrogen atoms in the backbone of butadiene raises the strain energy along the reaction coordinate, yielding the highest barrier for CNNC. The activation energy difference between CNCC and CCCC results from the difference in Pauli repulsion energy.

The reaction of CNNC with e has the highest barrier due to the large deformation of the diene in the transition state with respect to the ground state. In order to react with ethylene, the dienes must adopt an *s-cis* conformation where the dihedral angle of the backbone is $< 10^\circ$. For CNNC, the dihedral angle in the ground state is 95.6° . This has been attributed, very recently by Wiberg, Rablen, and Baraban, to the repulsion between the nitrogen lone pairs.^[47] Interestingly, the dihedral angle decreases to 55.5 and 30.7° for CNCC and CCCC, respectively. Compared to the C-C-C angle of CCCC (125.9°), the smaller C-N-C angle of CNCC (120.4°) leads to a larger dihedral angle of CNCC in order to reduce the repulsion between the terminal hydrogens on opposite ends (**Appendix 4.5**).^[47] Therefore ΔE_{strain} is the largest for CNNC (which has therefore the highest barrier) and decreases with a decreasing amount of nitrogen atoms (**Appendix 4.5** and **Figure 4.6**). Although ΔE_{strain} is larger for CNCC than for CCCC, the barrier height for CNCC is lower, due to a more stabilizing ΔE_{int} along the entire reaction coordinate. The lower ΔE_{int} is

caused by a lower ΔE_{Pauli} , while ΔE_{oi} and ΔV_{elstat} are very similar along the reaction coordinate (Figure 4.6b).

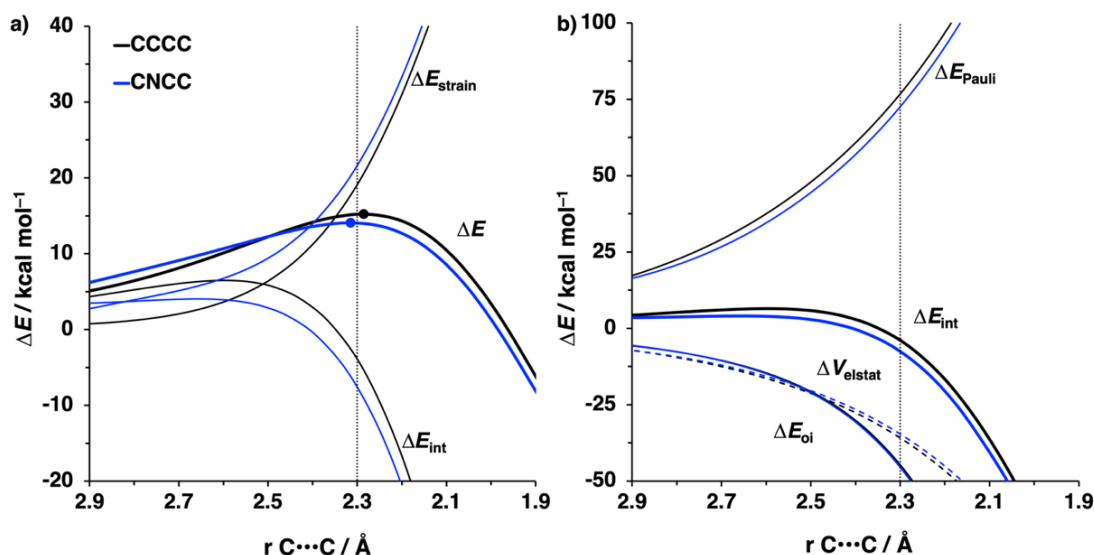


Figure 4.6 a) Activation strain and b) energy decomposition analyses of the Diels-Alder reactions between dienes CCCC and CNCC with ethylene, computed at the BP86/TZ2P level.

To rationalize the differences in the ΔE_{Pauli} between the Diels-Alder reactions of CNCC and CCCC, we quantified the most significant interactions between filled orbitals^[48] of the dienes and **e** (Figure 4.7a) at a consistent geometry with an average C•••C bond forming distance of 2.30 Å (which is close, in both energy and position, to both TSs). The highly symmetrical HOMO–1 of CCCC has a large overlap with the HOMO of **e** (0.18). However, the HOMO–3 of CNCC overlaps much less with the HOMO of **e** (overlap of 0.10), primarily due to the distortion of the HOMO–3 caused by the nitrogen atom in the backbone. The decreased four-electron two-center orbital overlap for CNCC results in a less destabilizing ΔE_{Pauli} and therefore a lower activation barrier due to the more stabilizing interaction.

To understand why the ΔE_{oi} is so similar for the reactions of CCCC and CNCC, an FMO analysis was performed (Figure 4.8). It turns out that the normal demand orbital interaction is more favorable for CCCC, while the inverse demand orbital interaction is more favorable for CNCC. These two interactions effectively offset each other, resulting in a very similar ΔE_{oi} for the two reactions. In the normal electron demand orbital interaction, the energy gap and orbital overlap between the HOMO_{diene} and LUMO_e are more favorable, i.e., smaller and larger, respectively for CCCC (3.9 eV and 0.23 compared to 4.2 eV and 0.19 for CNCC). In the inverse

electron demand orbital interaction, the energy gap and orbital overlap are more favorable, i.e., smaller and larger, respectively for **CNCC** (3.4 eV and 0.20 versus 4.0 eV and 0.19 for **CCCC**), thus yielding a very similar ΔE_{oi} . The difference in the overlap in the normal demand orbital interaction can be explained by inspecting the HOMOs of **CCCC** and **CNCC** (**Figure 4.7b**). Compared to the HOMO of **CCCC**, the HOMO of **CNCC** has a reduced amplitude on one of the terminal carbon atoms, thus yielding a smaller overlap between the $\text{HOMO}_{\text{diene}}$ and LUMO_{e} . The LUMOs of both dienes are more similar on the terminal carbon atoms (**Figure 4.7b**), resulting in a very similar overlap for the inverse demand orbital interaction.

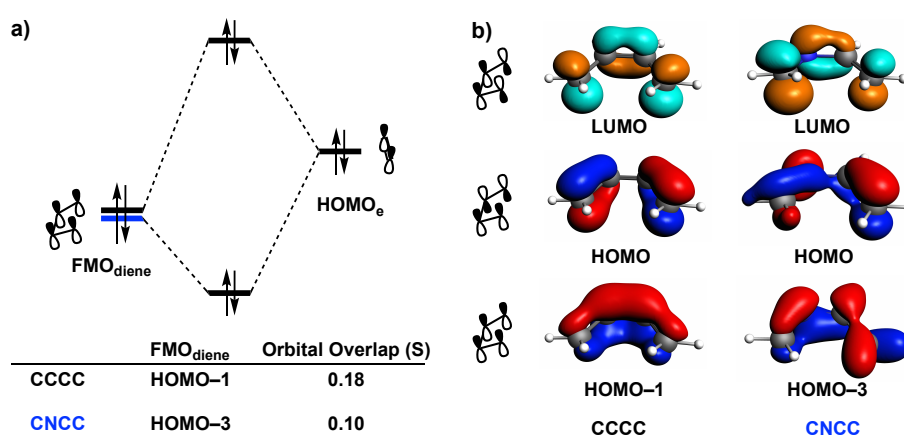


Figure 4.7 a) MO diagrams of the most significant occupied orbital overlaps for the Diels-Alder reactions between **CCCC** and **CNCC** with **e**, computed at the BP86/TZ2P level at the consistent geometry with an average $\text{C}\cdots\text{X}$ bond forming distance of 2.30 Å. b) FMO diagrams (isovalue = 0.07) for dienes **CCCC** and **CNCC** at the consistent geometry.

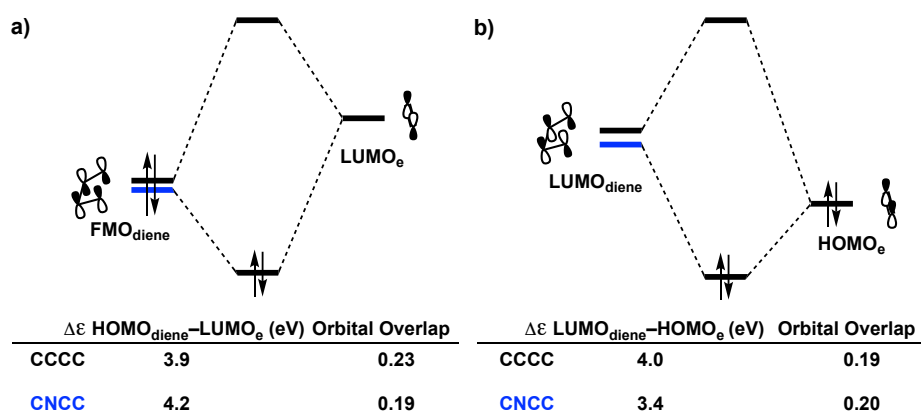


Figure 4.8 a) MO diagrams with calculated energy gaps and orbital overlaps for the normal electron demand $\text{FMO}_{\text{diene}}\text{-LUMO}_{\text{e}}$ interaction and b) the inverse electron demand $\text{LUMO}_{\text{diene}}\text{-HOMO}_{\text{e}}$ interaction of the Diels-Alder reactions between dienes **CCCC** and **CNCC** with ethylene (**e**). All data were computed at the BP86/TZ2P level at the consistent geometry with an average $\text{C}\cdots\text{X}$ bond forming distance of 2.30 Å.

4.3.3 Diels-Alder Reactivity of CNCC, NCNC, and NNCC

The Diels-Alder reactions of **CNCC**, **NCNC**, and **NNCC** were compared. These dienes all contain a single nitrogen atom in the backbone, but the number and position of the nitrogen atom in the terminal sites is varied. The Diels-Alder reaction of **CNCC** with **e** has a higher barrier compared to **NCNC** and **NNCC** caused by the more destabilizing ΔE_{strain} . This is the result of having to bend away more terminal hydrogen atoms in the case of the terminal $=\text{CH}_2$ compared to $=\text{NH}$, as previously discussed in section 4.3.1. ΔE_{int} is more stabilizing for **CNCC** than for both **NNCC** and **NCNC**, but is unable to compensate for the high ΔE_{strain} (**Figure 4.9a**). The Diels-Alder reaction of **NNCC** has the lowest reaction barrier of the three dienes, due to the more stabilizing ΔE_{oi} compared to **NCNC**.

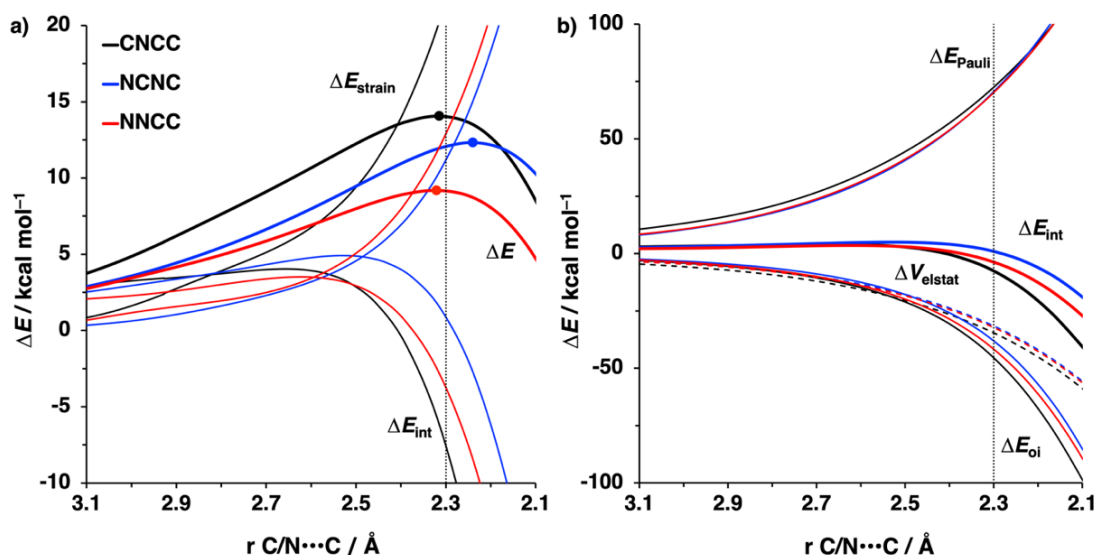


Figure 4.9 a) Activation strain and b) energy decomposition analyses of the Diels-Alder reactions between dienes **CNCC**, **NCNC**, and **NNCC** with ethylene, computed at the BP86/TZ2P level.

The lower barrier for **NNCC** compared to **NCNC** is determined by ΔE_{int} , since ΔE_{strain} for these reactions follows the opposite trend of the ΔE . The decomposition of ΔE_{int} (**Figure 4.9b**) shows that ΔE_{oi} is the sole factor determining the height of ΔE_{int} . To understand the difference in ΔE_{oi} , an FMO analysis was performed for both the normal and inverse electron demand orbital interactions at a consistent geometry with an average $\text{C}\cdots\text{X}$ bond forming distance of 2.30 \AA , which has been chosen since it is close, in both energy and position, to all TSs (**Figure 4.10**). The more stabilizing ΔE_{oi} for **NNCC** is due to smaller FMO gaps between the interacting orbitals in both the normal and inverse demand orbital interactions (5.3 and 2.9 eV respectively for **NNCC**

compared to 6.0 and 3.4 eV for **NCNC**) and to a larger $\text{FMO}_{\text{diene}}\text{-LUMO}_{\text{e}}$ overlap for **NNCC** (0.17 versus 0.11 for **NCNC**). The decreased orbital overlap for **NCNC** in the normal demand orbital interaction is due the presence of the nitrogen atom directly adjacent to the terminal carbon atom. This adjacent nitrogen atom effectively reduces the electron density on the terminal carbon atom, resulting in a smaller lobe of the $\text{FMO}_{\text{diene}}$ on the carbon atom and a less efficient overlap between the $\text{FMO}_{\text{diene}}$ and the LUMO_{e} . The LUMOs of **NNCC** and **NCNC** are very similar in shape and size, resulting in the same overlap (0.16) between the $\text{LUMO}_{\text{diene}}$ and the HOMO_{e} at a consistent forming bond length (**Appendix 4.6**).

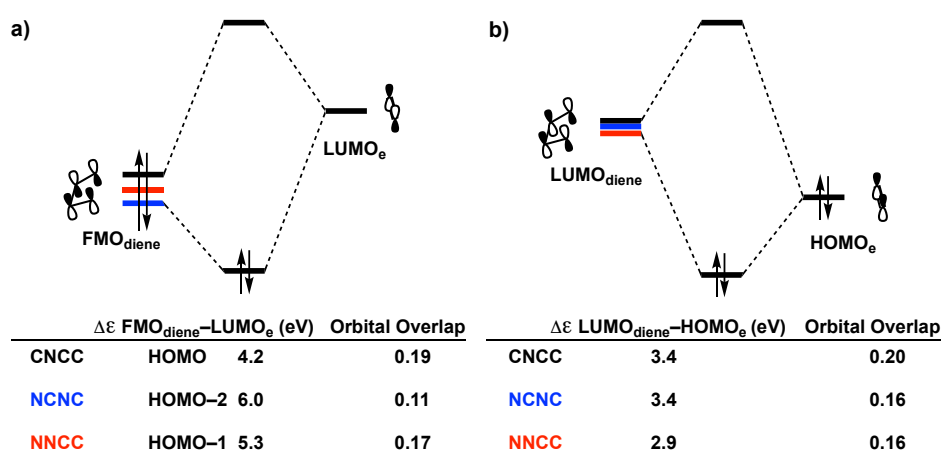


Figure 4.10 a) MO diagrams with calculated energy gaps and orbital overlaps for the normal electron demand $\text{FMO}_{\text{diene}}\text{-LUMO}_{\text{e}}$ interaction and b) the inverse electron demand $\text{LUMO}_{\text{diene}}\text{-HOMO}_{\text{e}}$ interaction of the Diels-Alder reactions between dienes **CNCC**, **NCNC**, and **NNCC** with ethylene (**e**). All data were computed at the BP86/TZ2P level at the consistent geometry with an average $\text{C}\cdots\text{X}$ bond forming distance of 2.30 Å.

4.4 Conclusions

The replacement of carbon atoms by the heteroatoms in 1,3-butadiene (**CCCC**) dramatically influences the Diels-Alder reactivity of these dienes with ethylene. Dienes with a terminal heteroatom (**NCCC** and **OSCC**) are less reactive than **CCCC** and replacement of the other terminal carbon atom by nitrogen or oxygen further decreases the reactivity. Replacing one of the carbon atoms in the backbone by nitrogen (**CNCC**) enhances the reactivity compared to **CCCC**. The replacement of two carbon atoms, one at the terminal position and one in the backbone (**NNCC** and **NCNC**), yields even more reactive systems.

For dienes in which one or two terminal carbon atoms are replaced by heteroatoms, the Diels-Alder reaction rate is decreased. The reason is the combination of a more contracted and lower energy *p*-orbital on the heteroatom in the highest occupied π -type orbital of the diene, which weakens the stabilizing donor–acceptor orbital overlap and interaction with the ethylene LUMO. This factor dominates a counteracting influence of the activation strain, which generally decreases as the number of terminal element-H bonds that have to bend away becomes smaller. Introduction of a nitrogen atom in the backbone (CNCC) furnishes a more reactive diene compared to CCCC, primarily due to a less destabilizing Pauli repulsion. This effect was traced back to the polarized nature of the HOMO of CNCC towards the nitrogen atom and away from the terminal carbon atom. Consequently, the four-electron two-center overlap between the HOMO of CNCC and HOMO of **e** is reduced. Finally, we arrive at NNCC, which is the most reactive diene and goes with a substantially reduced activation strain compared to CCCC, due to the decreased number of terminal hydrogens that must bend away during the reaction with **e**.

The reactivity of hetero-1,3-butadienes with ethylene turns out to be a delicate interplay between the overlap of bond forming orbitals, the energy levels of those orbitals, and the overlap of filled orbitals on both substrates. We envision dienes containing nitrogen atoms in the backbone (2-azadienes) to be more reactive than their all-carbon counterparts, while addition of heteroatoms on the bond forming positions (1-azadienes) to result in less reactive dienes, which is consistent with previous studies.^[31] However, the combination of nitrogen atoms in one of the bond-forming positions and in one of the backbone positions yields the most reactive diene. We believe these insights to be valuable in the design of Diels-Alder reactions in the future.

4.5 References

- [1] O. Diels, K. Alder, *Justus Liebigs Ann. Chem.* **1928**, 460, 98–122.
- [2] K. C. Nicolaou, S. A. Snyder, T. Montagnon, G. Vassilikogiannakis, *Angew. Chem. Int. Ed.* **2002**, 41, 1668–1698; *Angew. Chem.* **2002**, 114, 1742–1773.
- [3] M. A. Tasdelen, *Polym. Chem.* **2011**, 2, 2133–2145.
- [4] L. F. Tietze, G. Ketschau in *Stereoselective Heterocyclic Synthesis I*. (Eds.: P. Metz), Springer, **1997**, pp. 1–120.

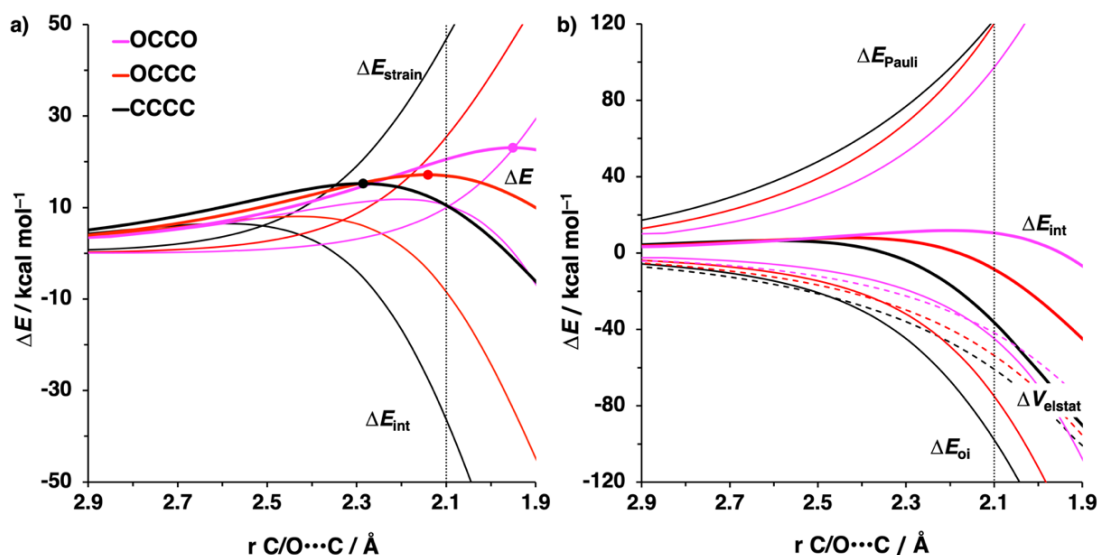
- [5] a) M.-H. Cao, N. J. Green, S.-Z. Xu, *Org. Biomol. Chem.* **2017**, *15*, 3105–3129; b) K. A. Jørgensen, *Angew. Chem. Int. Ed.* **2000**, *39*, 3558–3588; *Angew. Chem.* **2000**, *112*, 3702–3733.
- [6] D. L. Boger, K. C. Cassidy, S. Nakahara, *J. Am. Chem. Soc.* **1993**, *115*, 10733–10741.
- [7] S.J. Danishefsky, C. Vogel, *J. Org. Chem.* **1986**, *51*, 3915–3916.
- [8] N. S. Rajapaksa, M. A. McGowan, M. Rienzo, E. N. Jacobsen, *Org. Lett.* **2013**, *15*, 706–709.
- [9] G. Han, M. G. LaPorte, J. J. Folmer, K. M. Werner, S. M. Weinreb, *J. Org. Chem.* **2000**, *65*, 6293–6306.
- [10] J. Sauer, D. Lang, *Angew. Chem.* **1964**, *76*, 603–603.
- [11] M. L. Blackman, M. Royzen, J. M. Fox, *J. Am. Chem. Soc.* **2008**, *130*, 13518–13519.
- [12] N. K. Devaraj, R. Weissleder, S. A. Hilderbrand, *Bioconjugate Chem.* **2008**, *19*, 2297–2299.
- [13] a) T. Reiner, B. M. Zeglis, *J. Labelled Compd. Radiopharm.* **2014**, *57*, 285–290; b) C. Denk, D. Svatunek, S. Mairinger, J. Stanek, T. Filip, D. Matscheko, C. Kuntner, T. Wanek, H. Mikula, *Bioconjugate Chem.* **2016**, *27*, 1707–1712; c) T. Lämpchen, R. Rossin, T. R. van Mourik, G. Gruntz, F. J. M. Hoeben, R. M. Versteegen, H. M. Janssen, J. Lub, M. S. Robillard, *Nucl. Med. Biol.* **2017**, *55*, 19–26; d) R. Rossin, S. M. van den Bosch, W. ten Hoeve, M. Carvelli, R. M. Versteegen, J. Lub, M. S. Robillard, *Bioconjugate Chem.* **2013**, *24*, 1210–1217; e) M. Wang, D. Svatunek, K. Rohlfing, Y. Liu, H. Wang, B. Giglio, H. Yuan, Z. Wu, Z. Li, J. Fox, *Theranostics* **2016**, *6*, 887–895.
- [14] A. Darko, S. Wallace, O. Dmitrenko, M. M. Machovina, R. A. Mehl, J. W. Chin, J. M. Fox, *Chem. Sci.* **2014**, *5*, 3770–3776.
- [15] J. Yang, Y. Liang, J. Šečkutė, K. N. Houk, N. K. Devaraj, *Chem. Eur. J.* **2014**, *20*, 3365–3375.
- [16] C. M. Cole, J. Yang, J. Šečkutė, N. K. Devaraj, *ChemBioChem* **2013**, *14*, 205–208.
- [17] a) R. M. Versteegen, R. Rossin, W. ten Hoeve, H. M. Janssen, M. S. Robillard, *Angew. Chem. Int. Ed.* **2013**, *52*, 14112–14116; *Angew. Chem.* **2013**, *125*, 14362–14366; b) R. M. Versteegen, W. ten Hoeve, R. Rossin, M. A. R. de Geus, H. M. Janssen, M. S. Robillard,

- Angew. Chem. Int. Ed.* **2018**, *57*, 10494–10499; c) J. C. T. Carlson, H. Mikula, R. Weissleder, *J. Am. Chem. Soc.* **2018**, *140*, 3603–3612.
- [18] R. Rossin, S. M. J. van Duijnhoven, W. Ten Hoeve, H. M. Janssen, L. H. J. Kleijn, F. J. M. Hoeben, R. M. Versteegen, M. S. Robillard, *Bioconjugate Chem.* **2016**, *27*, 1697–1706.
- [19] S. Eising, F. Lelivelt, K. M. Bonger, *Angew. Chem. Int. Ed.* **2016**, *55*, 12243–12247; *Angew. Chem.* **2016**, *128*, 12431–12435.
- [20] S. Eising, N. G. A. van der Linden, F. Kleinpenning, K. M. Bonger, *Bioconjugate Chem.* **2018**, *29*, 982–986.
- [21] S. Eising, A. H. J. Engwerda, X. Riedijk, F. M. Bickelhaupt, K. M. Bonger, *Bioconjug. Chem.* **2018**, *29*, 3054–3059.
- [22] D. N. Kamber, Y. Liang, R. J. Blizzard, F. Liu, R. A. Mehl, K. N. Houk, J. A. Prescher, *J. Am. Chem. Soc.* **2015**, *137*, 8388–8391.
- [23] L.-A. Jouanno, A. Chevalier, N. Sekkat, N. Perzo, H. Castel, A. Romieu, N. Lange, C. Sabot, P.-Y. Renard, *J. Org. Chem.* **2014**, *79*, 10353–10366.
- [24] G. Desimoni, G. Tacconi, *Chem. Rev.* **1975**, *75*, 651–692.
- [25] a) A. Pałasz, *Top. Curr. Chem.* **2016**, *374*, 24; b) X. Hu, Y. Zhou, Y. Lu, S. Zou, L. Lin, X. Liu, X. Feng, *J. Org. Chem.* **2018**, *83*, 8679–8687; c) K. N. Houk, R. W. Strozier, *J. Am. Chem. Soc.* **1973**, *95*, 4094–4096.
- [26] S. Zhang, Y.-C. Luo, X.-Q. Hu, Z.-Y. Wang, Y.-M. Liang, P.-F. Xu, *J. Org. Chem.* **2015**, *80*, 7288–7294.
- [27] J.-L. Li, L. Fu, J. Wu, K.-C. Yang, Q.-Z. Li, X.-J. Gou, C. Peng, B. Han, X.-D. Shen, *Chem. Commun.* **2017**, *53*, 6875–6878.
- [28] a) A. Taheri kal Koshvandi, M. M. Heravi, *Tetrahedron: Asymmetry* **2017**, *28*, 1506–1556; b) M. Bednarski, S. Danishefsky, *J. Am. Chem. Soc.* **1983**, *105*, 3716–3717.
- [29] H. Vuong, B. P. Dash, S. O. Nilsson Lill, D. A. Klumpp, *Org. Lett.* **2018**, *20*, 1849–1852.
- [30] a) L. F. Tietze, T. Hübsch, M. Buback, W. Tost, *High Press. Res.* **1990**, *5*, 638–640; b) R. G. Iafe, K. N. Houk, *J. Org. Chem.* **2008**, *73*, 2679–2686; c) M. Buback, W. Tost, T. Hübsch, E. Voß, L. F. Tietze, *Chem. Ber.* **1989**, *122*, 1179–1186; d) D. Svatunek, C. Denk, H. Mikula, *Monatsh. Chem.* **2018**, *149*, 833–837.
- [31] J. S. Fell, B. N. Martin, K. N. Houk, *J. Org. Chem.* **2017**, *82*, 1912–1919.

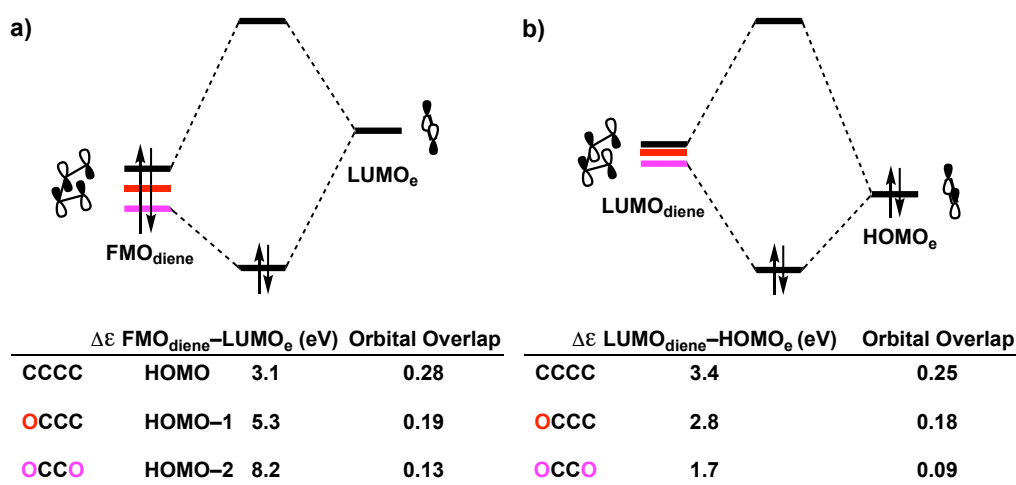
- [32] F. M. Bickelhaupt, K. N. Houk, *Angew. Chem. Int. Ed.* **2017**, *56*, 10070–10086; *Angew. Chem.* **2017**, *129*, 10204–10221.
- [33] a) W.-J. van Zeist, A. H. Koers, L. P. Wolters, F. M. Bickelhaupt, *J. Chem. Theory Comput.* **2008**, *4*, 920–928; b) B. J. Levandowski, T. A. Hamlin, R. C. Helgeson, F. M. Bickelhaupt, K. N. Houk, *J. Org. Chem.* **2018**, *83*, 3164–3170; c) A. Riesco-Domínguez, J. van de Wiel, T. A. Hamlin, B. van Beek, S. D. Lindell, D. Blanco-Ania, F. M. Bickelhaupt, P. J. Floris, *J. Org. Chem.* **2018**, *83*, 1779–1789.
- [34] P. A. Champagne, K. N. Houk, *J. Org. Chem.* **2017**, *82*, 10980–10988.
- [35] I. Fernández, F. P. Cossío, F. M. Bickelhaupt, *J. Org. Chem.* **2011**, *76*, 2310–2314.
- [36] a) B. J. Levandowski, T. A. Hamlin, F. M. Bickelhaupt, K. N. Houk, *J. Org. Chem.* **2017**, *82*, 8668–8675; b) H. Mikula, S. Kronister, D. Svatunek, C. Denk, *Synlett* **2018**, *29*, 1297–1302; c) Y. García-Rodeja, M. Solà, I. Fernández, *J. Org. Chem.* **2018**, *83*, 3285–3292; d) R. Jin, S. Liu, Y. Lan, *RSC Adv.* **2015**, *5*, 61426–61435; e) S. Liu, Y. Lei, X. Qi, Y. Lan, *J. Phys. Chem. A* **2014**, *118*, 2638–2645.
- [37] a) G. te Velde, F. M. Bickelhaupt, E. J. Baerends, C. Fonseca Guerra, S. J. A. van Gisbergen, J. G. Snijders, T. Ziegler, *J. Comput. Chem.* **2001**, *22*, 931–967; b) C. Fonseca Guerra, J. G. Snijders, G. te Velde, E. J. Baerends, *Theor. Chem. Acc.* **1998**, *99*, 391–403; c) ADF, SCM Theoretical Chemistry; Vrije Universiteit: Amsterdam, The Netherlands, **2016**; <http://www.scm.com>.
- [38] a) A. D. Becke, *Phys. Rev. A* **1988**, *38*, 3098–3100; b) J. P. Perdew, *Phys. Rev. B* **1986**, *33*, 8822–8824.
- [39] E. Van Lenthe, E. J. Baerends, *J. Comput. Chem.* **2003**, *24*, 1142–1156.
- [40] a) T. A. Hamlin, D. Svatunek, S. Yu, L. Ridder, I. Infante, L. Visscher, F. M. Bickelhaupt, *Eur. J. Org. Chem.* **2018**, 378–386; b) A. Talbot, D. Devarajan, S. J. Gustafson, I. Fernández, F. M. Bickelhaupt, D. H. Ess, *J. Org. Chem.* **2014**, *80*, 548–558.
- [41] L. Fan, L. Versluis, T. Ziegler, E. J. Baerends, W. Ravenek, *Int. J. Quantum Chem.* **1988**, *34*, 173–181.
- [42] C. Y. Legault, CYLview 1.0b, Université De Sherbrooke, Sherbrooke, QC, Canada, **2009**.
- [43] a) D. H. Ess, K. N. Houk, *J. Am. Chem. Soc.* **2007**, *129*, 10646–10647; b) L. P. Wolters, F. M. Bickelhaupt, *WIREs Comput. Mol. Sci.* **2015**, *5*, 324–343; c) I. Fernández, F. M.

- Bickelhaupt, *Chem. Soc. Rev.* **2014**, *43*, 4953–4967; d) W.-J. van Zeist, F. M. Bickelhaupt, *Org. Biomol. Chem.* **2010**, *8*, 3118–3127; e) F. M. Bickelhaupt, *J. Comput. Chem.* **1999**, *20*, 114–128.
- [44] a) T. Ziegler, A. Rauk, *Inorg. Chem.* **1979**, *18*, 1755–1759; b) F. M. Bickelhaupt, N. M. M. Nibbering, E. M. van Wezenbeek, E. J. Baerends, *J. Phys. Chem.* **1992**, *96*, 4864–4873; c) F. M. Bickelhaupt, A. Diefenbach, S. P. de Visser, L. J. de Koning, N. M. M. Nibbering, *J. Phys. Chem. A* **1998**, *102*, 9549–9553.
- [45] W.-J. van Zeist, C. Fonseca Guerra, F. M. Bickelhaupt, *J. Comput. Chem.* **2007**, *29*, 312–315.
- [46] a) K. N. Houk, *Acc. Chem. Res.* **1975**, *8*, 361–369; b) I. Fleming, J. P. Michael, L. E. Overman, G. F. Taylor, *Tetrahedron Lett.* **1978**, *19*, 1313–1314.
- [47] K. B. Wiberg, P. R. Rablen, J. H. Baraban, *J. Org. Chem.* **2018**, *83*, 8473–8482.
- [48] S. C. C. van der Lubbe, C. Fonseca Guerra, *Chem. Eur. J.* **2017**, *23*, 10249–10253.

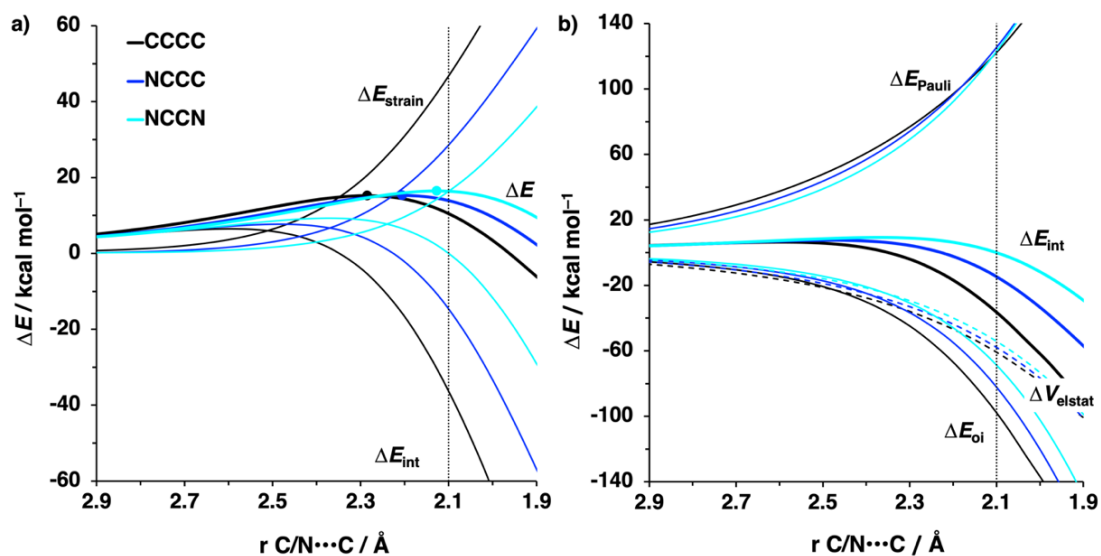
4.6 Appendices



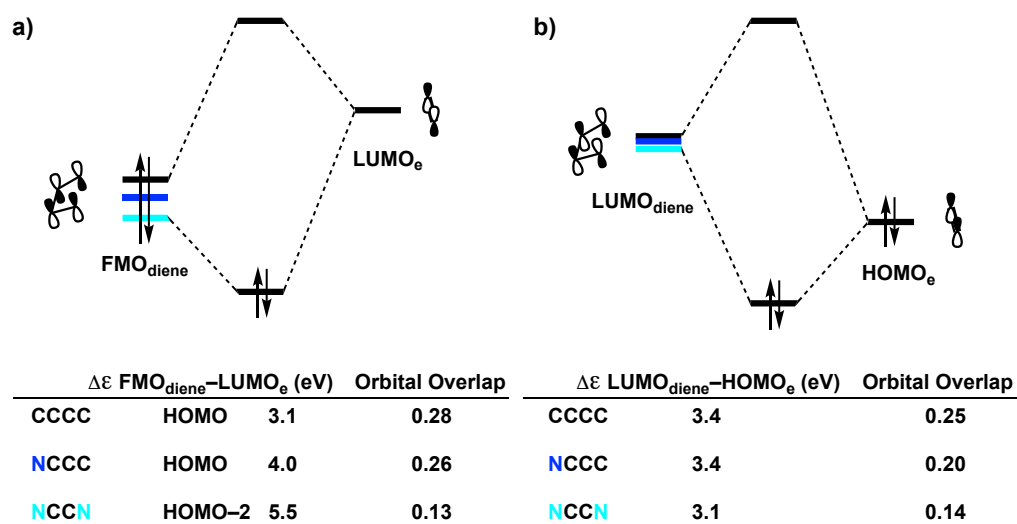
Appendix 4.1 a) Activation strain and b) energy decomposition analyses of the Diels-Alder reactions between dienes **CCCC**, **OCCC**, and **OCCO** with ethylene, computed at the BP86/TZ2P.



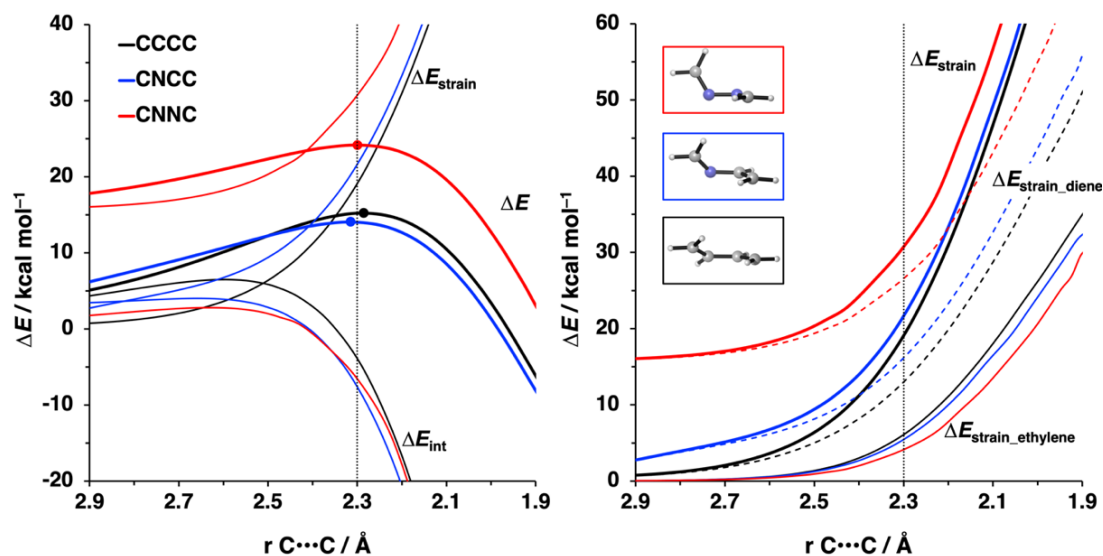
Appendix 4.2 a) MO diagrams with calculated energy gaps and orbital overlaps for the normal electron demand FMO_{diene}-LUMO_e interaction and b) inverse electron demand LUMO_{diene}-HOMO_e interaction for the Diels-Alder reactions between dienes **CCCC**, **OCCC**, and **OCCO** with ethylene (e). All data computed at the BP86/TZ2P level at a consistent geometry of 2.10 Å.



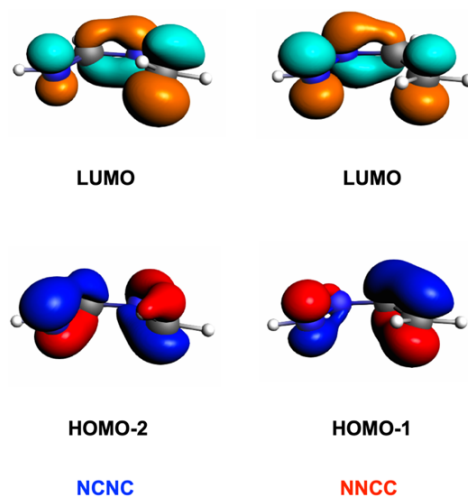
Appendix 4.3 a) Activation strain and b) energy decomposition analyses of the Diels-Alder reactions between dienes CCCC, NCCC, and NCCN with ethylene, computed at the BP86/TZ2P.



Appendix 4.4 a) MO diagrams with calculated energy gaps and orbital overlaps for the normal electron demand FMO_{diene}-LUMO_e interaction and b) inverse electron demand LUMO_{diene}-HOMO_e interaction for the Diels-Alder reactions between dienes CCCC, NCCC, and NCCN with ethylene (e). All data computed at the BP86/TZ2P level at a consistent geometry of 2.10 Å.



Appendix 4.5 a) Activation strain analyses and b) strain energy decomposition of the Diels-Alder reactions between dienes CCCC, CNCC, and CNNC with ethylene, computed at the BP86/TZ2P level.



Appendix 4.6 FMO diagrams (isovalue = 0.07) for dienes NCNC and NNCC at the consistent geometry (top row: interacting virtual orbitals, bottom row: interacting occupied orbitals).

Chapter 5 How Heteroatoms and Geometries Affect 1,3-Dipolar Cycloadditions of Allenes

This chapter previously appeared as

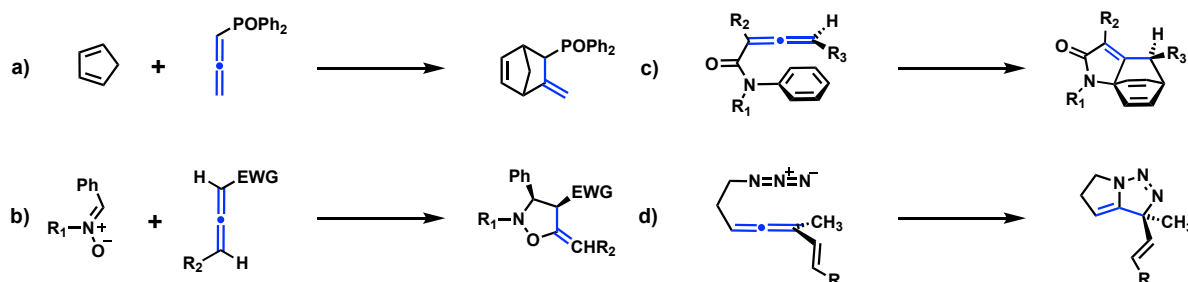
Chem. Eur. J. **2020**, *26*,11529–11539.

Song Yu, Pascal Vermeeren, Kevin van Dommelen, F. Matthias Bickelhaupt, Trevor A. Hamlin

In this chapter, we quantum chemically studied the reactivity, site-, and regioselectivity of the 1,3-dipolar cycloaddition reactions between methyl azide and various allenes, including the archetypal allene, propadiene, heteroallenes, and cyclic allenes, using density functional theory (DFT). The 1,3-dipolar cycloaddition reactivity of linear (hetero)allenes decreases as the number of heteroatoms in the allene increases and the formation of the 1,5-adduct is, in all cases, favored over the 1,4-adduct, both effects find their origin from the strength of the primary orbital interactions. The cycloaddition reactivity of cyclic allenes was also investigated, and the increased pre-distortion of allenes, which results upon cyclization, leads to systematically lower activation barriers not due to the expected variations in the strain energy, but instead from the differences in the interaction energy. The geometrical pre-distortion of cyclic allenes enhances the reactivity compared to linear allenes through a unique mechanism that involves a smaller HOMO–LUMO gap, which manifests into more stabilizing orbital interactions.

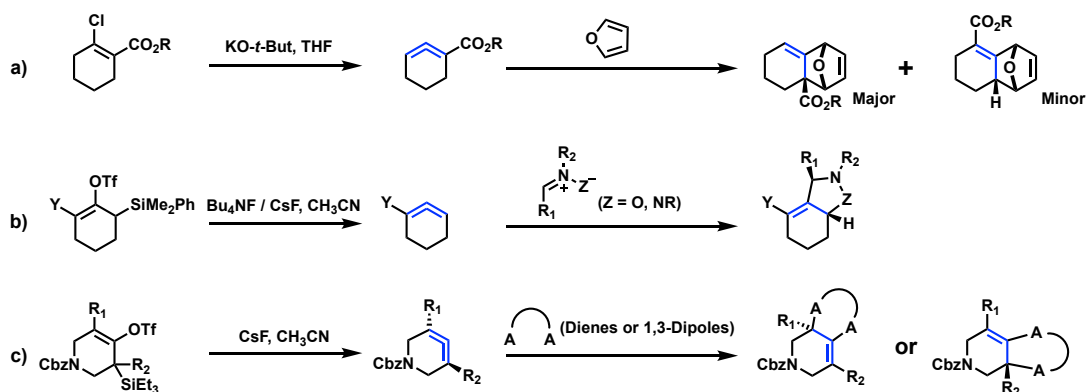
5.1 Introduction

Allenes are a class of unsaturated hydrocarbon that contain two cumulated double bonds and have received significant attention in the past decade due to their privileged role in the synthesis of natural products via cycloaddition reactions.^[1] The simplest allene, propadiene (CCC), for instance, reacts with both cyclopentadiene and 1,3-dipoles to form either a substituted norbornene^[2] or a heterocycle,^[3] respectively (**Scheme 5.1a** and **Scheme 5.1b**), both of which are common motifs in natural products. Intramolecular Diels-Alder reactions^[4] as well as 1,3-dipolar cycloadditions^[5] (**Scheme 5.1c** and **Scheme 5.1d**) of allenes provide strategies for the construction of complex polycyclic molecules.^[6] In addition, the cycloaddition reactivity of allenes can be broadened to heteroallenes, such as ketenimine (CCN),^[7] ketene (CCO),^[8] carbodiimide (NCN),^[9] isocyanate (NCO),^[10] and even to carbon dioxide (OCO).^[11]



Scheme 5.1 Diels-Alder reactions and 1,3-dipolar cycloadditions of propadiene.

In contrast, strained allenes, that is, cyclic allenes, have received less attention in the field likely due to their lower kinetic stabilities.^[12] Nevertheless, experimental studies have shown that strained allenes can be formed *in situ* and trapped instantaneously by either dienes or 1,3-dipoles.^[13] For example, Houk and co-workers studied the formation and subsequent trapping of 1,2-cyclohexadiene in a Diels-Alder reaction (**Scheme 5.2a**).^[13d] Lofstrand et al. synthesized and subsequently trapped 1,2-cyclohexadiene, through a 1,3-dipolar cycloaddition under mild conditions (**Scheme 5.2b**).^[13e] Houk and Garg recently carried out a systematic study on the synthesis of azacyclic allenes as well as their reactivity towards cycloadditions (**Scheme 5.2c**).^[13g] These examples clearly illustrate that cyclic allenes can serve as prominent building blocks in the construction of polycyclic compounds and may also engage in rapid reactions in analogy with strained alkenes and alkynes.^[14]



Scheme 5.2 Diels-Alder reactions and 1,3-dipolar cycloadditions of strained allenes.

A number of theoretical studies have shed light on the cycloaddition reactivity of allenes. A concerted asynchronous mechanism has been proposed to be a more energetically favorable reaction pathway for cycloadditions of allenes.^[13g, 15] Gandolfi and co-workers proposed that the differences in the extent of structural deformations determine the trends in reaction barrier heights of the cycloadditions of allenes.^[15a–15b] On the contrary, an activation strain analysis on transition structures, by Garg and co-workers, concluded just the opposite, namely, that the strength of the interaction plays a large role in determining the regioselectivity of the Diels-Alder reactions of azacyclic allenes.^[13g] To the best of our knowledge, a thorough investigation into the reactivity, site-, and regioselectivity of cycloadditions of allenes has not yet been reported.

We performed a systematic computational study of the concerted 1,3-dipolar cycloaddition reactions of allenes, including the linear (hetero)allenes propadiene (**CCC**; **L3**), ketenimine (**CCN**), ketene (**CCO**), carbodiimide (**NCN**), isocyanate (**NCO**), and carbon dioxide (**OCO**) and a series of cyclic allenes 1,2-cyclooctadiene (**C8**), 1,2-cycloheptadiene (**C7**), and 1,2-cyclohexadiene (**C6**). These cyclic allenes have all been synthesized^[16] and might be relevant reactive dienophiles/dipolarophiles in bioorthogonal chemistries in the future.^[17] As azides are common reactants in 1,3-dipolar cycloadditions,^[18] and strain-promoted azide–alkyne cycloadditions (SPAACs),^[14a–14c] methyl azide (**Az**) was chosen as the model 1,3-dipole in this study. The activation strain model (ASM)^[19] in combination with quantitative Kohn-Sham molecular orbital (KS-MO) theory and the matching energy decomposition analysis (EDA)^[20] were employed to provide insight into the factor controlling the reactivity in these cycloaddition reactions. This approach has proven valuable for understanding of the reactivity of related pericyclic reactions and continues our current research line into the reactivity of cyclic dienophiles and dipolarophiles.^[21]

5.2 Computational Details

All calculations were carried out in ADF2017,^[22] using the BP86^[23] functional with the TZ2P basis set.^[24] The exchange-correlation (XC) functional has been proven to be accurate in calculating the relative trends in activation and reaction energies for cycloadditions.^[25] Additionally, single-point energies were computed at BP86-D3(BJ)/TZ2P,^[26] M06-2X/TZ2P,^[27] and COSMO(toluene)BP86/TZ2P^[28] on the fully optimized BP86/TZ2P geometries in order to assess the effect of a meta-hybrid functional, dispersion-corrections, and solvation on the computed reactivity trends. Frequency calculations were performed in order to characterize the nature of the stationary points. Local minima presented only real frequencies, whereas transition state structures had one imaginary frequency. The potential energy surface (PES) was calculated using the intrinsic reaction coordinate (IRC) method, which follows the imaginary eigenvector of the transition structure towards the reactant and product. The resulting PES was analyzed with the aid of the PyFrag 2019 program.^[29] All chemical structures were illustrated using CYLview.^[30]

Quantitative analyses of the activation barriers associated with the studied reactions are obtained by means of the activation strain model (ASM) of reactivity.^[19] Herein, the PES, $\Delta E(\zeta)$, is decomposed into the strain energy, $\Delta E_{\text{strain}}(\zeta)$, and the interaction energy, $\Delta E_{\text{int}}(\zeta)$. All energy terms are projected onto the reaction coordinate ζ , the average distance of newly forming bonds, which undergoes a well-defined change during the course of the reactions and has been proven to provide reliable results for cycloaddition reactions.^[21a, 25b–25c, 31]

$$\Delta E(\zeta) = \Delta E_{\text{strain}}(\zeta) + \Delta E_{\text{int}}(\zeta)$$

The $\Delta E_{\text{strain}}(\zeta)$ is associated with the rigidity as well as the structural deformation of the reactants from their equilibrium geometry to the geometry acquired along the reaction coordinate. The total $\Delta E_{\text{strain}}(\zeta)$ can be further divided into the strain energy associated with deforming each respective reactant.

$$\Delta E_{\text{strain}}(\zeta) = \Delta E_{\text{strain,reactant,A}}(\zeta) + \Delta E_{\text{strain,reactant,B}}(\zeta)$$

The $\Delta E_{\text{int}}(\zeta)$ is related to the electronic structure of the reactants and their spatial orientation and takes the mutual interaction between the deformed reactants into account. In order to obtain a

deeper insight into the physical mechanism behind the interaction energy, we employ the canonical energy decomposition analysis (EDA).^[20] This analysis method decomposes the interaction energy between the two deformed reactants, within the framework of Kohn-Sham DFT, into three physically meaningful terms.

$$\Delta E_{\text{int}}(\zeta) = \Delta V_{\text{elstat}}(\zeta) + \Delta E_{\text{Pauli}}(\zeta) + \Delta E_{\text{oi}}(\zeta)$$

The electrostatic interaction, $\Delta V_{\text{elstat}}(\zeta)$, corresponds to the classical electrostatic interaction between the unperturbed charge distributions of the deformed reactants. The Pauli repulsion, $\Delta E_{\text{Pauli}}(\zeta)$, comprises the repulsion between closed-shell occupied orbitals and is, therefore, destabilizing. The orbital interaction, $\Delta E_{\text{oi}}(\zeta)$, accounts for the stabilizing orbital interactions such as electron-pair bonding, charge transfer (interaction between the occupied orbitals of fragment A with the unoccupied orbitals of fragment B, and vice versa), and polarization (e.g., occupied-unoccupied orbital mixing on fragment A due to the presence of fragment B and vice versa). A detailed step-by-step protocol on how to perform the activation strain and energy decomposition analysis can be found in ref. 19a.

The magnitude of the orbital interaction of a 1,3-dipolar cycloaddition mainly comes from two distinct orbital interaction mechanisms, namely, the normal electron demand (NED) interaction, occurring between occupied orbitals of the dipole and unoccupied orbitals of the dipolarophile (the allene in this study), and the inverse electron demand (IED) interaction, originating from the interaction between the unoccupied orbitals of the dipole with occupied orbitals of the dipolarophile. The stabilization of a specific orbital interaction mechanism is proportional to the orbital overlap squared divided by their respective orbital energy gap, that is, $S^2/\Delta\varepsilon$.^[32] Thus, with the help of this relation, we can quantify the importance of the individual orbital interaction mechanisms.

The atomic charge distribution was analyzed by using the Voronoi deformation density (VDD) method.^[33] The VDD method partitions the space into so-called Voronoi cells, which are non-overlapping regions of space that are closer to nucleus A than to any other nucleus. The charge distribution is determined by taking a fictitious promolecule as reference point, in which the electron density is simply the superposition of the atomic densities. The change in density in the Voronoi cell when going from this promolecule to the final molecular density of the interacting

system is associated with the VDD atomic charge Q . The VDD atomic charge Q_A of atom A is calculated according to the following:

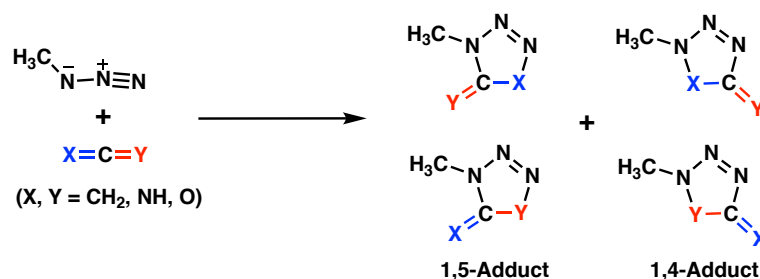
$$Q_A^{\text{VDD}} = - \int_{\text{Voronoi cell of A}} [\rho(r) - \rho_{\text{promolecule}}(r)] dr$$

So, instead of computing the amount of charge contained in an atomic volume, we compute the flow of charge from one atom to the other upon formation of the molecule. The physical interpretation is therefore straightforward. A positive atomic charge Q_A corresponds to the loss of electrons, whereas a negative atomic charge Q_A is associated with the gain of electrons in the Voronoi cell of atom A.

5.3 Results and Discussion

5.3.1 1,3-Dipolar Cycloadditions of Linear Allenes

As a starting point, we studied the 1,3-dipolar cycloaddition reaction between methyl azide (**Az**) and the following linear (hetero)allenes: propadiene (**CCC**), ketenimine (**CCN**), ketene (**CCO**), carbodiimide (**NCN**), isocyanic acid (**NCO**), and carbon dioxide (**OCO**). For each 1,3-dipolar cycloaddition, two regioselective cycloadducts can be formed, the 1,5-adduct with the methyl group adjacent to the second double bond and the 1,4-adduct with them on opposite sides (**Scheme 5.3**). Additionally, the asymmetric heteroallenes **CCN**, **CCO**, and **NCO** are able to form two site-specific adducts, i.e., coordinating with either of the two double bonds.



Scheme 5.3 1,3-dipolar cycloaddition between **Az** and a linear allene.

Table 5.1 lists the activation energies, ΔE^\ddagger , and reaction energies, ΔE_{rxn} , for the studied 1,3-dipolar cycloadditions between **Az** and linear (hetero)allenes. Three clear trends can be observed. In the first place, the cycloadditions towards the 1,5-adducts are kinetically and thermodynamically favored over the formation of the 1,4-adducts. Secondly, for the asymmetric heteroallenes, **Az** preferentially attacks at the more electropositive of the two terminal atoms. The only exception, however, is **CCO**, which has a *slightly* lower ΔE^\ddagger for the attack at the CO (19.2 kcal mol⁻¹) than the CC (20.0 kcal mol⁻¹). Thirdly, the cycloaddition reactivity decreases when heteroatoms are introduced in the linear allene, from **CCC** to **CCN** and **CCO**, as well as from **CCO** to **NCO** to **OCO** and from **CCN** to **NCN**. The above trends in reactivity agree well with those calculated at BP86-D3(BJ)/TZ2P//BP86/TZ2P and M06-2X/TZ2P//BP86/TZ2P. We note that, when using M06-2X/TZ2P//BP86/TZ2P, the two site-selective cycloadditions of **NCO**, forming the 1,5-adduct, have nearly identical reaction barriers. Furthermore, the observed trends in reactivity, site-, and regioselectivity also hold when solvent effects in toluene are included at COSMO (toluene)BP86/TZ2P//BP86/TZ2P (**Appendix 5.1**).

Table 5.1 Electronic reaction barriers ΔE^\ddagger and energies ΔE_{rxn} for the 1,3-dipolar cycloadditions between **Az** and linear allenes leading to 1,4- and 1,5-adducts computed at different theory.^[d]

Allene	Site	1,5-Adduct						1,4-Adduct					
		ΔE^\ddagger		ΔE_{rxn}			ΔE^\ddagger		ΔE_{rxn}				
		[a]	[b]	[c]	[a]	[b]	[c]	[a]	[b]	[c]	[a]	[b]	[c]
OCO		32.1	28.8	35.8	20.6	17.2	14.8	53.8	50.6	62.6	37.8	34.8	35.7
NCN		28.0	23.7	30.9	-15.3	-19.8	-25.2	35.8	31.6	43.5	1.6	-2.6	-6.6
NCO	CO	27.9	24.1	28.8	14.6	10.7	8.3	45.0	41.4	54.0	32.4	29.0	27.0
	NC	26.4	22.7	28.9	-14.9	-18.8	-24.0	42.8	39.0	50.8	6.6	2.9	-0.1
CCO	CO	19.2	15.0	21.7	3.5	-0.8	-2.6	27.1	23.4	40.2	16.5	12.9	11.5
	CC	20.0	15.7	26.2	-32.2	-36.4	-42.1	29.1	24.8	37.2	-24.5	-28.6	-32.2
CCN	CN	22.6	18.0	27.1	-20.3	-25.1	-29.1	26.4	22.2	34.3	-6.1	-10.4	-13.7
	CC	20.0	15.7	27.0	-30.8	-35.6	-41.3	23.5	19.0	30.8	-28.1	-32.6	-36.7
CCC		19.0	14.1	24.4	-34.0	-39.1	-43.7	19.5	14.8	25.2	-31.5	-36.2	-39.7

[a] Computed at BP86/TZ2P. [b] Computed at BP86-D3(BJ)/TZ2P//BP86/TZ2P. [c] Computed at M06-2X/TZ2P//BP86/TZ2P. [d] See **Appendix 5.1** for enthalpies and Gibbs free energies.

1,5- versus 1,4-Regioselectivity

Next, we turn to the activation strain model (ASM)^[19] of reactivity to gain a quantitative insight into the physical factors governing the 1,5- versus 1,4-regioselectivity in the 1,3-dipolar cycloadditions presented herein. In **Figure 5.1**, we focus on the ASM diagram for the 1,5- vs. 1,4-

regioselectivity of **OCO** for which the difference in ΔE^\ddagger is the largest (**Table 5.1**). The ASM diagrams of the other linear allenes possess the same characteristics, only less pronounced. The lower ΔE^\ddagger for the formation of the 1,5-adduct originates mainly from a more stabilizing ΔE_{int} term, whereas the ΔE_{strain} is nearly identical (**Figure 5.1a**). The canonical energy decomposition analysis (EDA)^[20] reveals that both the more stabilizing ΔV_{elstat} and ΔE_{oi} are the causes of the more favorable ΔE_{int} term for the 1,5-adduct formation compared to the 1,4-adduct (**Figure 5.1b**).

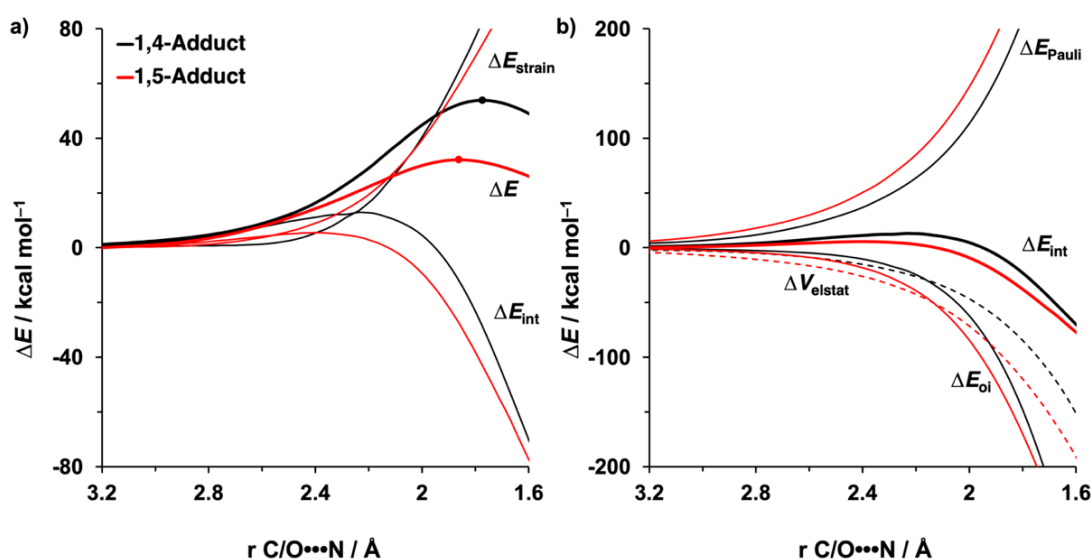
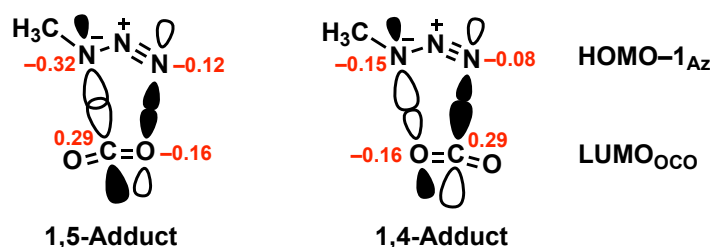


Figure 5.1 a) Activation strain model and b) energy decomposition analysis of the 1,3-dipolar cycloaddition between **Az** and **OCO**, projected onto the average newly forming C/O...N bond, computed at BP86/TZ2P.

The more stabilizing ΔE_{oi} for the 1,3-dipolar cycloaddition yielding the 1,5-adduct can be entirely described to the more effective orbital overlap of the normal electron demand (NED) interaction occurring between the HOMO-1_{Az} and LUMO_{OCO}. Only the lower-lying HOMO-1_{Az} participates in the NED interaction, because its lobes are oriented towards the LUMO of **OCO**, while the lobes of HOMO_{Az} are orthogonal to the LUMO_{OCO} (**Appendix 5.2a**). As shown in **Scheme 5.4**, the HOMO-1_{Az} has the largest lobe on the nitrogen next to the methyl group, due to a methyl-induced mix of the π -atomic orbitals of the N₃ fragment of **Az** (**Appendix 5.2e**). The LUMO_{OCO} has a larger lobe on the carbon atom than on the terminal oxygens, due to the more diffuse nature of the $2p$ atomic orbital of carbon compared to oxygen, which, in turn, leads to a better HOMO-1_{Az}-LUMO_{OCO} orbital overlap when forming the 1,5-adduct compared to the 1,4-adduct. The computed overlaps of the HOMO-1_{Az}-LUMO_{OCO} NED interaction for formation of both adducts on a consistent geometry with an average newly forming C/O...N bond length of

1.86 Å amounts $S_{1,5} = 0.30$ and $S_{1,4} = 0.16$. The larger orbital overlap for the formation of the 1,5-adduct is responsible for the more stabilizing ΔE_{oi} compared to the 1,4-adduct counterpart (**Figure 5.1b**). The NED orbital energy gaps, on the other hand, are identical for the formation of the 1,5- and 1,4-adduct, because the orbital interactions take place between the same molecular orbitals. In addition, the cycloaddition resulting in the 1,5-adduct also has a stronger electrostatic attraction between the more negatively charged nitrogen and the positively charged carbon atom (**Scheme 5.4**) and, therefore, a significantly more stabilizing ΔV_{elstat} term (**Figure 5.1b**).



Scheme 5.4 Schematic diagrams of the orbital interaction between the HOMO-1 of **Az** and the LUMO of **OCO** for the 1,4- and 1,5-adducts. VDD charges (red, in electrons) of key atoms in isolated fragment computed at BP86/TZ2P.

Site-Selectivity of Asymmetric Heteroallenes

After having established that the 1,3-dipolar cycloadditions between **Az** and (hetero)allenes preferentially form 1,5-adducts, we analyzed the site-selectivity of the asymmetric heteroallenes **CCN**, **NCO**, and **CCO**. First, we discuss the site-selectivity of **CCN** by applying the ASM analysis. From **Figure 5.2** we can clearly see that the attack of **Az** at the more electropositive CC bond is favored exclusively due to a more stabilizing ΔE_{int} term compared to the attack at the CN bond. The more stabilizing ΔE_{int} for attack at CC compared to CN compensates for the destabilizing ΔE_{strain} for this pathway. Our EDA indicates that the more stabilizing ΔE_{int} term for the attack at CC over CN originates mainly from a more favorable ΔE_{oi} supported by a moderately stronger ΔV_{elstat} (**Figure 5.2b**).

The more stabilizing ΔE_{oi} term for the **Az** attack at CC can exclusively be ascribed to its significantly more favorable inverse electron demand (IED) interaction term (**Figure 5.3a**), which overcomes its less stabilizing NED interaction (**Figure 5.3b**). The IED energy gap for the attack at CC is considerably smaller compared to the attack at CN, 1.7 and 5.0 eV, respectively, while the orbital overlap is also larger for the attack at CC. This manifest in an orbital stabilization term, that is, $10^3 \times S^2 / \Delta \epsilon$, of 17.0 and 4.0 for the attack at CC and CN, respectively. In contrast, the NED

interaction is slightly weaker for the attack at CC than for CN, due to a larger NED energy gap and a poorer orbital overlap. This, however, can easily be overcome by the much stronger IED interaction, which leads to a more stabilizing ΔE_{oi} and thus a lower reaction barrier for the attack at the CC bond (**Figure 5.2b**).

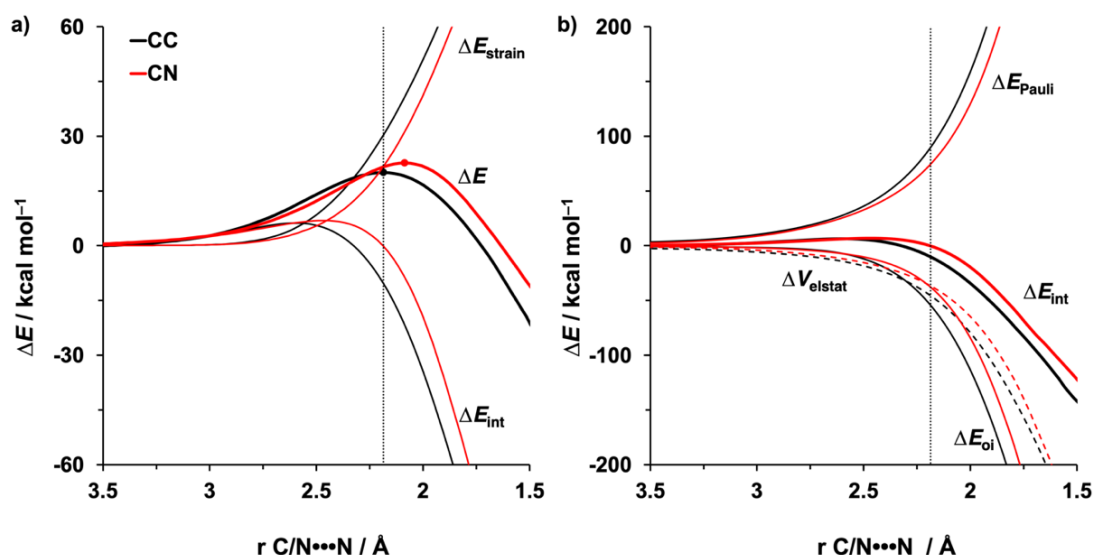


Figure 5.2 a) Activation strain and b) energy decomposition analysis of site-specific 1,3-dipolar cycloadditions between Az and CCN, projected onto the average newly forming C/N...N bond, computed at BP86/TZ2P. The vertical dotted line indicates the point along the reaction coordinate at which the average length of newly forming C/N...N bond is 2.19 Å.

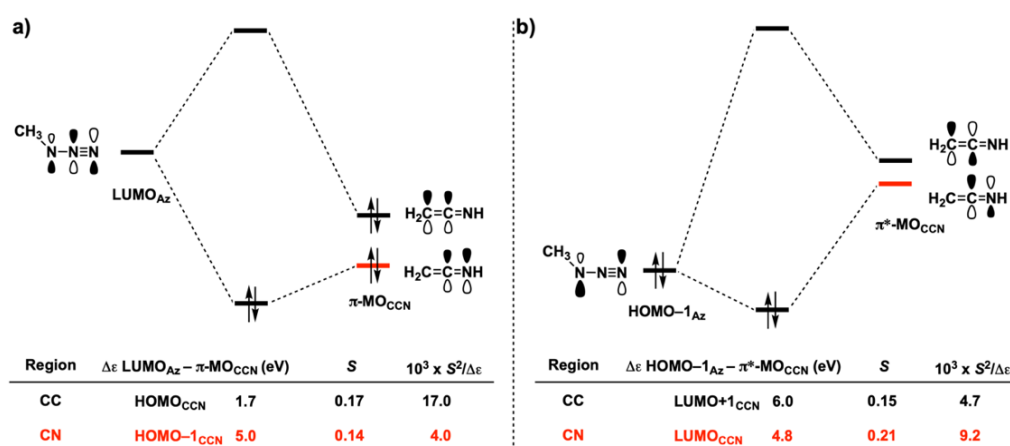


Figure 5.3 FMO diagrams with calculated orbital energy gaps and overlaps of a) the IED (LUMO_{Az}- π -MO_{CCN}) interaction and b) the NED (HOMO-1_{Az}- π^* -MO_{CCN}) interaction for site-specific 1,3-dipolar cycloadditions between Az and CCN at consistent geometries with the average newly forming C/N...N bond of 2.19 Å computed at BP86/TZ2P.

In the case of the asymmetric linear heteroallene **NCO**, the underlying mechanism behind the preference for the attack at NC over CO is identical to the above discussed **CCN** (see **Appendix 5.3a**). For heteroallene **CCO**, the ΔE_{strain} for the attack at CC is more destabilizing than for CO, because the terminal carbon atom needs to deform from a trigonal planar to a tetrahedral geometry, which overcomes the more favorable ΔE_{int} , leading to nearly identical reaction barriers (**Appendix 5.3b**). But, the cycloaddition at CO is reversible and goes with a positive reaction energy (see **Appendix 5.1** for Gibbs free reaction energies), therefore, the reaction at CC will be preferred thermodynamically. The finding that allenes prefer to undergo cycloadditions at the more electropositive terminal atom is in line with several experimental reports.^[7, 8, 10]

Influence of Heteroatoms on the Reactivity

In this section, we discuss the effect of heteroatoms on the reactivity of linear allenes towards the 1,3-dipolar cycloaddition with **Az** yielding the 1,5-adduct, by systematically modifying the nature and number of heteroatoms. Upon going from **CCC** to **CCN** and **CCO**, while attacking at the kinetically preferred CC site, the ΔE^\ddagger increases from 19.0 to 20.0 kcal mol⁻¹ solely due to a more destabilizing ΔE_{strain} (**Figure 5.4a**). Even though **CCC** requires a larger extent of bending over the course of the reaction compared to **CCN** and **CCO** (**CCC**: 24°; **CCN**: 18°; **CCO**: 22°), the difference in ΔE_{strain} can be ascribed to the more rigid heteroallene **CCX** (**X** = **N**, **O**) backbone, which can be reflected by the calculated bending vibrational frequencies of allenes (**CCC**: 361 cm⁻¹; **CCN**: 471 cm⁻¹; **CCO**: 503 cm⁻¹) as well as the analysis of the strain energy upon artificially bending of the heteroallene (**Appendix 5.4a**). The increased rigidity from **CCC** to **CCN** to **CCO** is due to the increased bond strength between carbon and the heteroatom along the same series.^[34] The ΔE_{int} term, on the other hand, shows a trend which is opposite to the strain energy, namely, **CCO** goes with the most stabilizing interaction energy followed by **CCN** and **CCC**. This trend in interaction energy is exclusively determined by the orbital interactions (see **Appendix 5.4b** for EDA diagrams), which, in turn, can be traced to a less stable LUMO_{allene} going from **CCO** to **CCN** and **CCC** (-2.4, -1.5, and -0.9 eV, respectively), and, therefore, a larger HOMO-1_{Az}-LUMO_{allene} energy gap. This trend in ΔE_{int} term, however, is overruled by the larger differences in ΔE_{strain} .

For the series **CCO**, **NCO**, and **OCO**, **Az** attacks at different sites, namely, CC, NC, and OC, respectively, but the neighboring heteroatom is always oxygen. Along this series, the ΔE^\ddagger systematically increases (**Table 5.1**), due to a less stabilizing ΔE_{oi} (**Appendix 5.5**). Similar to the analysis of the site-selectivity of the asymmetric heteroallenes (**Figure 5.3**), going from CC to the

hetero double bonds NC and OC causes a remarkably destabilized IED interaction ($\text{LUMO}_{\text{Az}}-\text{HOMO}_{\text{allene}}$), due to the increased IED orbital energy gap supported by less efficient orbital overlap (**Appendix 5.6**). This exact rationale also holds for the comparison of **CCN** and **NCN**.

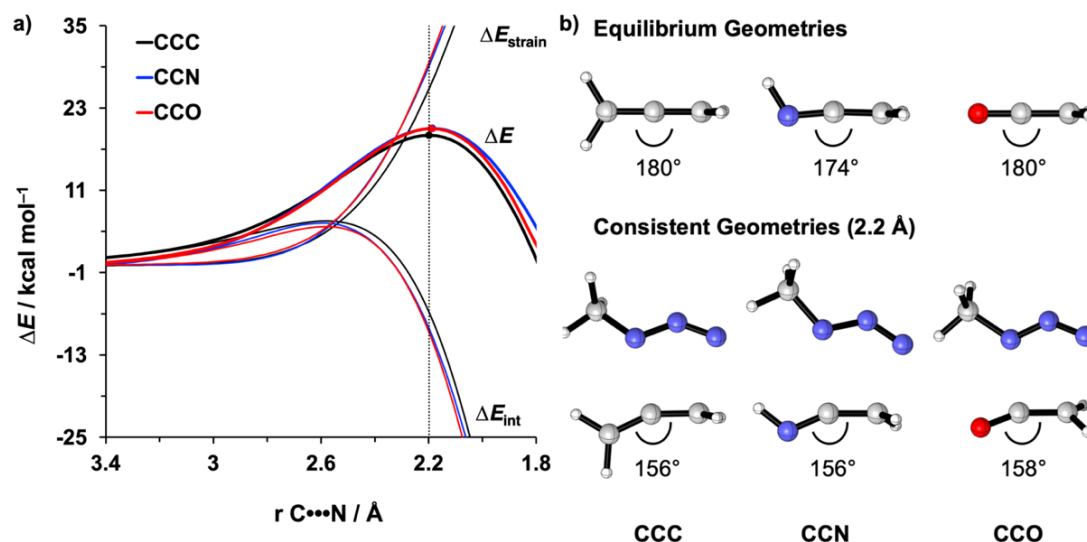


Figure 5.4 a) Activation strain analysis for the 1,3-dipolar cycloadditions between **Az** and **CCC**, **CCN**, and **CCO** attacking at the **CC** site and b) equilibrium geometries of the allene and respective consistent geometries with the average newly forming **C/N...N** bond of 2.20 Å with internal bending angles [°] computed at BP86/TZ2P.

Summarizing, we have analyzed and compared the 1,3-dipolar cycloaddition reactivity of linear (hetero)allenes with **Az**, which in all cases prefers to form the 1,5-adduct. The archetypal allene, **CCC**, is the most reactive. By introducing a heteroatom, the heteroallene becomes less reactive due to the increased rigidity of the **CCX** (**X = N, O**) backbone. Additionally, a second heteroatom diminishes the stabilizing ΔE_{oi} , making them even less reactive towards **Az**.

5.3.2 1,3-Dipolar Cycloadditions of Cyclic Allenes

At last, we also analyzed and compared the 1,3-dipolar cycloaddition reactions between methyl azide (**Az**) and a series of cyclic allenes, namely, 1,2-cyclooctadiene (**C8**), 1,2-cycloheptadiene (**C7**), and 1,2-cyclohexadiene (**C6**) as well as propadiene (**L3**), the most reactive linear allene (vide supra). These cyclic allenes have all been synthesized and featured in cycloaddition reactions.^[13]

Figure 5.5 shows the transition state structures of the 1,3-dipolar cycloadditions of **Az** with the linear allene (**Az-L3**) and the cyclic allenes (**Az-C8–Az-C6**). The transition structures are concerted asynchronous and become earlier, with regard to the average forming bond distances,

as the ring size of the cyclic allene decreases. The cycloaddition of the linear **L3** is predicted to proceed with the highest reaction barrier ($\Delta E^\ddagger = 19.0 \text{ kcal mol}^{-1}$) and has the least favorable reaction energy ($\Delta E_{\text{rxn}} = -34.0 \text{ kcal mol}^{-1}$). The reaction barrier height decreases along the series **L3** > **C8** > **C7** > **C6**, and the cycloaddition reaction becomes more exergonic when going from **L3** to **C6**, which is in line with the Hammond-Leffler postulate.^[35] The above trends computed at BP86/TZ2P agree well with those calculated at BP86-D3(BJ)/TZ2P//BP86/TZ2P and M06-2X/TZ2P//BP86/TZ2P, as well as when solvent effects are included at COSMO (toluene)BP86/TZ2P//BP86/TZ2P (**Appendix 5.7**).

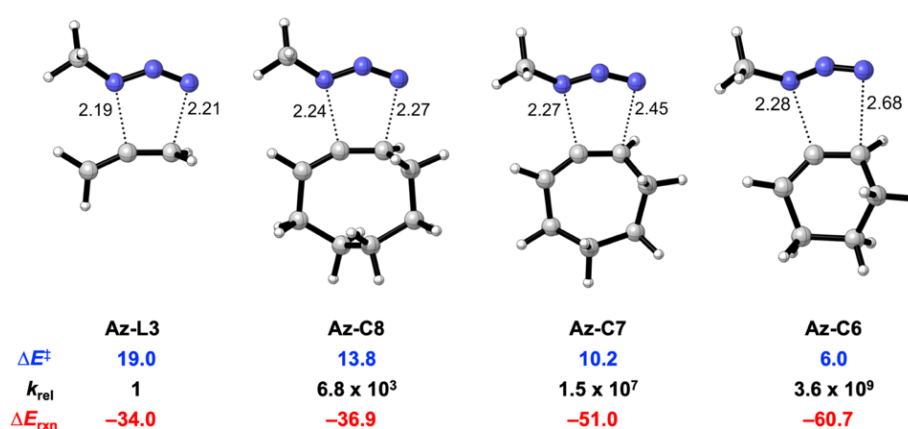


Figure 5.5 Transition structures with forming bond lengths (Å), computed reaction barriers (ΔE^\ddagger , kcal mol⁻¹, blue) with relative reaction rate constants (k_{rel} , black), and reaction energies (ΔE_{rxn} , kcal mol⁻¹, red) for 1,3-dipolar cycloadditions of **Az** with **L3** and **C8–C6** computed at BP86/TZ2P.

In order to understand the intrinsic differences in reactivity between linear and cyclic allenes in the 1,3-dipolar cycloadditions with **Az**, we performed an ASM analysis. **Figure 5.6a** graphically represents how the ΔE_{strain} and ΔE_{int} components evolve along the reaction coordinate for 1,3-dipolar cycloadditions of **Az** with **L3** and **C8–C6**. Surprisingly, the origin of the increased reactivity as the ring size of allene decreases can be entirely attributed to the differences in ΔE_{int} , which becomes more stabilizing from **L3** to **C6** (**Figure 5.6a**). The total ΔE_{strain} for all studied allenes are nearly identical (**Figure 5.6a**). As expected upon decreasing the size of the ring, the cyclic allene becomes more pre-distorted towards the cycloaddition reaction with **Az**, which leads to a smaller contribution of the cyclic allene to the total ΔE_{strain} , consistent with the earlier literature.^[13f] The contribution of the 1,3-dipole **Az** to the total ΔE_{strain} , however, is more destabilizing for **C6** than for **L3** (**Appendix 5.8**), due to the fact that the more reactive allenes (vide infra) deform **Az** to a larger degree (**Appendix 5.9**).

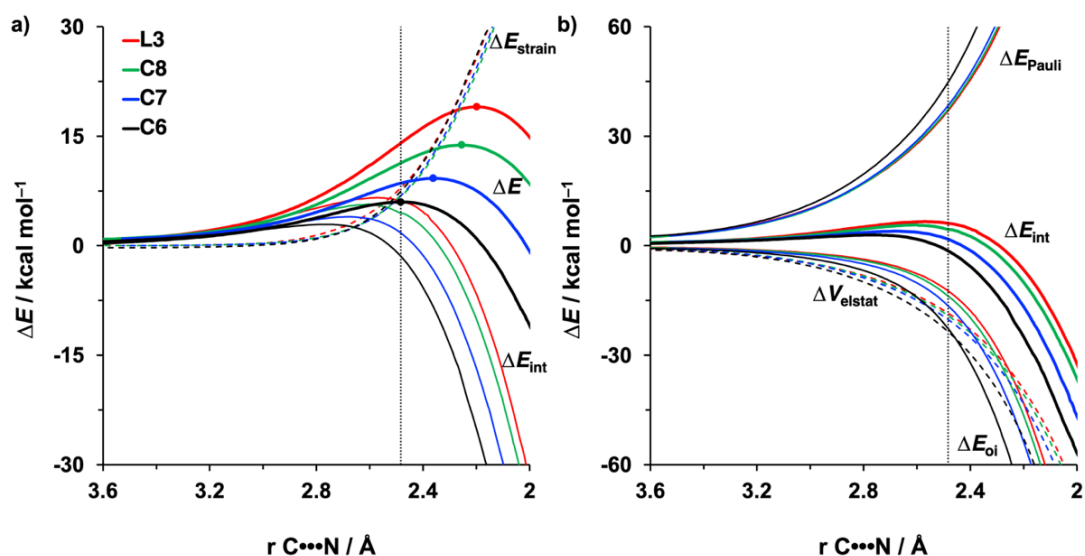


Figure 5.6 a) Activation strain and b) energy decomposition analysis of 1,3-dipolar cycloadditions of **Az** with **L3** and **C8–C6**, projected onto the average newly forming **C...N** bond, computed at BP86/TZ2P. The vertical dotted line indicates the point along the reaction coordinate where the average newly forming **C...N** bond is 2.48 Å.

The origin of the differences in ΔE_{int} was uncovered by means of the EDA method, and the results are shown in **Figure 5.6b**. It is apparent that the ΔE_{oi} is the major contributor to the trend in ΔE_{int} , guided by a smaller contribution of ΔV_{elstat} . The ΔE_{Pauli} shows a reverse trend, and, therefore, is not responsible for the trend in ΔE_{int} . To further probe the key orbital interactions, that cause this difference in ΔE_{oi} , involved in the 1,3-dipolar cycloadditions of **Az** with **L3** and **C8–C6**, we analyzed the FMOs participating in these interactions on consistent geometries with an average newly forming **C...N** bond of 2.48 Å (**Figure 5.7**).

The FMOs participating in the NED and IED reveal that the more stabilizing orbital interactions when going from **L3** to **C8** to **C6** are exclusively determined by a reduction in orbital energy gap (**Figure 5.7**). The NED interaction between **Az** and **L3** and **C8–C6** occurs between the $\text{HOMO}-1_{\text{Az}}$ and $\text{LUMO}_{\text{allene}}$ (**Figure 5.7a**). The least reactive allene **L3** has the largest and least favorable NED orbital energy gap ($\Delta\varepsilon = 6.4$ eV). As the ring size decreases from **L3** to **C8** to **C6**, the NED orbital energy gap continuously decreases from 6.4 to 4.8 eV. The orbital overlap in the NED interaction is identical for all reactions ($S = 0.15$). The IED interaction takes place between the LUMO_{Az} and $\text{HOMO}_{\text{allene}}$ (**Figure 5.7b**). Again, **L3** has the largest and, therefore, least favorable IED orbital energy gap ($\Delta\varepsilon = 3.7$ eV). The IED gap also systematically decreases from 3.7 eV for **L3** to 2.7 eV for **C6**. The increasingly stabilizing ΔE_{oi} term (**Figure 5.6b**), as the ring size of allene decreases, therefore, is a direct result of the diminishing energy gap for both the NED

and IED interaction, resulted from the continuously stabilizing LUMO and destabilizing HOMO of allene (**Figure 5.7** and **Appendix 5.10**).

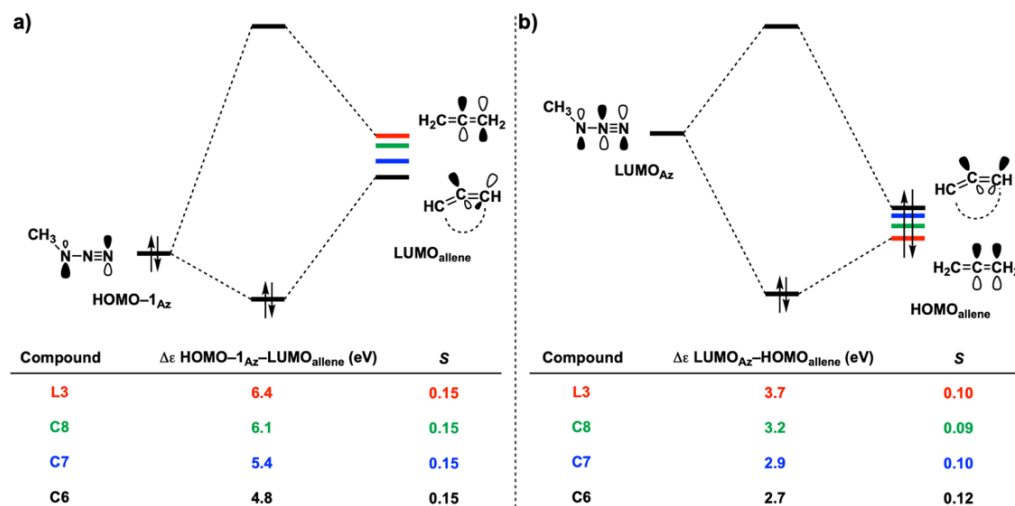


Figure 5.7 FMO diagrams with calculated key orbital energy gaps and overlaps of a) the NED (HOMO-1_{Az}-LUMO_{allene}) interaction and b) the IED (LUMO_{Az}-HOMO_{allene}) interaction for 1,3-dipolar cycloadditions between Az with L3 and C8-C6 at consistent geometries with the average newly forming C••N bond of 2.48 Å computed at BP86/TZ2P.

In order to quantify the effect of allene predistortion on the HOMO and LUMO, we chose to bent our model system L3. **Figure 5.8a** shows the optimized undistorted structure (top) and the distorted, bent, structures of L3 (middle and bottom). Bending of the allene backbone causes a loss in orthogonality of the two adjacent π -systems, because it is accompanied with a twist in the structure, reducing the dihedral angle from 90°, for the linear allene, to 64.1°, for the 130° bent allene. This observation not only holds for L3, but also for the cyclic allenes C6-C8 (**Appendix 5.11**) and is in line with earlier reported literature.^[13g] As the backbone of L3 becomes distorted, the LUMO is stabilized while the HOMO is destabilized (**Figure 5.8b**).

Detailed Kohn-Sham molecular orbital (KS-MO) analysis of the formation of the HOMO and LUMO of the undistorted (linear) and distorted (bent to 130°) H₂C=C=CH₂ (L3), in terms of an H₂C=C^{••} and a ^{••}CH₂ fragment, is shown in **Figure 5.9**. For the archetypal L3 (**Figure 5.9a**), one LUMO (the bold LUMOs in **Figure 5.9**) is solely formed by the π^* -orbital of H₂C=C^{••}, whereas the other degenerate LUMO, which is orthogonal to the former, is a result of the antibonding combination of the *p* orbitals of two individual fragments. Furthermore, the HOMO (the bold HOMOs in **Figure 5.9**) originates from the antibonding combination between the π -orbital of H₂C=C^{••} and the C-H σ -orbital of ^{••}CH₂, meanwhile the other degenerate HOMO is the

bonding combination of the p orbitals of both fragments. When **L3** is bent to 130° (**Figure 5.9b**), the π^* -orbital of $\text{H}_2\text{C}=\text{C}^{\bullet\bullet}$ has an in-phase overlap with the σ^* -orbital of $^{\bullet\bullet}\text{CH}_2$ which leads to a stabilization of the LUMO. In addition, due to the prior mentioned twisting effect, the fragment p orbitals mix into the LUMO which results in the additional stabilization. The HOMO, on the other hand, is stabilized due to the decreased anti-bonding π - σ overlap owing to the bending and twisting of the backbone, but, at the same time, obtains a slightly stronger destabilization from the mixing of the fragmental p orbitals. This destabilization effect overcomes the stabilizing counterpart, resulting in the overall destabilization of the HOMO.

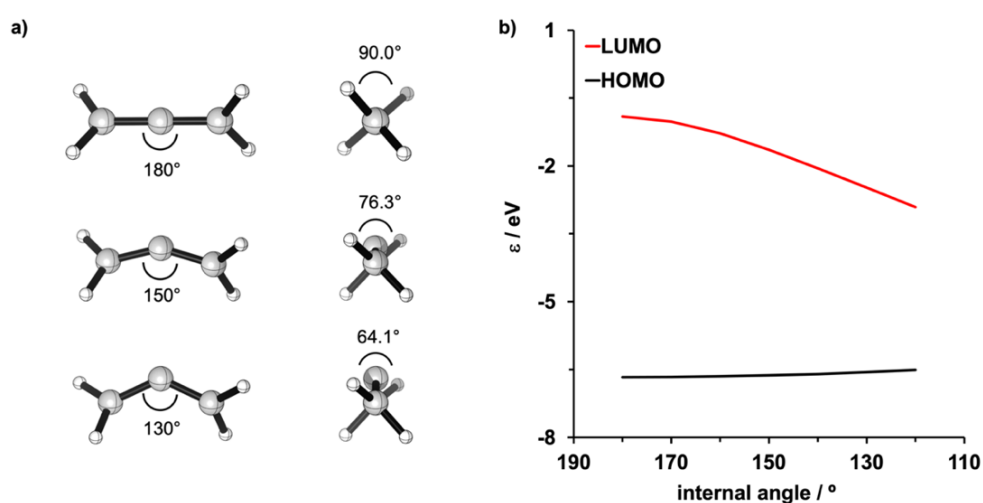


Figure 5.8 a) Front and right-side views of the pristine and constrained optimized structures of **L3**. b) FMO energies associated with the internal angle computed at BP86/TZ2P.

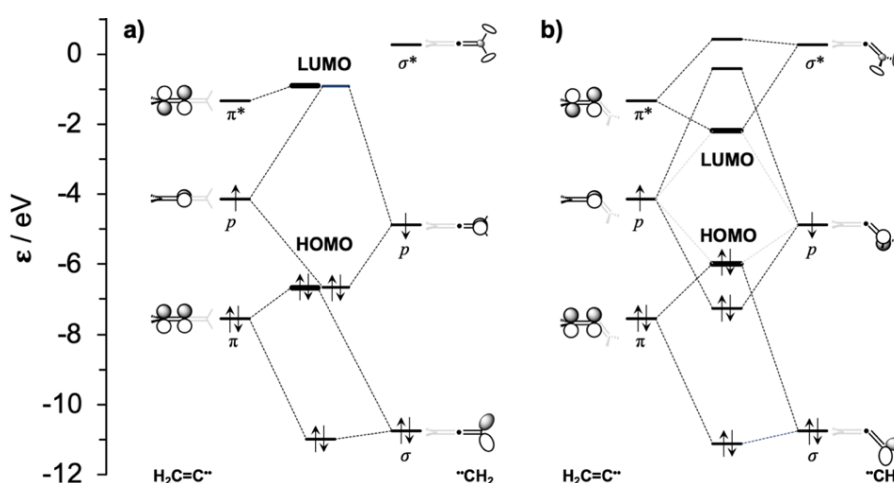


Figure 5.9 Diagrams for the Kohn-Sham MO analyses of a) the archetypal and b) 130° bent **L3**, where the fragments are $\text{H}_2\text{C}=\text{C}^{\bullet\bullet}$ and $^{\bullet\bullet}\text{CH}_2$ computed at BP86/TZ2P.

These analyses were further verified by investigating both the pure bending (no twisting) or twisting (no bending) of **L3**. Solely bending **L3** and maintaining orthogonality of the structure stabilizes the LUMO due to the enhanced $\pi^*-\sigma^*$ overlap and also stabilizes the HOMO because of the decreased $\pi-\sigma$ overlap (**Appendix 5.12**). On the other hand, solely twisting **L3** and maintaining a linear backbone induces a stabilization of the LUMO, because of an in-phase mixing between the π^* and p orbitals of the fragments, and a significantly destabilization of the HOMO, due to the mixing between the π and p orbitals (**Appendix 5.13**).

5.4 Conclusions

1,3-Dipolar cycloadditions of linear allenes and heteroallenes with methyl azide (**Az**) favor the formation of the 1,5-adduct over the 1,4-adduct. In addition, bond formation to the asymmetric heteroallene is preferred at the more electropositive terminal atom. This process becomes less reactive as the number of heteroatoms in the allene increases. Cyclic allenes experience a significant rate enhancement compared to their linear allene counterparts. These findings emerge from our quantum chemical study based on density functional theory calculations.

Our activation strain analyses furthermore identified that the site-selective preference for the 1,5-adduct compared to the 1,4-adduct is exclusively determined by a more favorable orbital overlap and thus more stabilizing orbital interactions between the reactants. Furthermore, in the case of the asymmetric heteroallenes, the preference for attacking at the more electropositive atoms is caused by a significantly stronger inverse electron demand (IED) orbital interaction. This is due to the fact that double bonds involving more electropositive atoms have lower-lying acceptor orbitals, leading to smaller IED energy gaps and, thus, more stabilizing orbital interactions with **Az**. The archetypal allene, propadiene (**CCC**) was found to be the most reactive linear allene. Introducing a heteroatom to **CCC** makes the allene less reactive, due to a more destabilizing ΔE_{strain} , originating from a more rigid backbone, as well as less stabilizing orbital interactions.

The enhanced reactivity of cyclic allenes with respect to linear ones originates from an enhancement of donor–acceptor orbital interactions, which become more stabilizing as the ring size of the cyclic allene decreases, and not from a previously reported reduced activation strain. Our activation strain analyses reveal that, in smaller rings, the allene moiety is more bent; this goes

with a smaller HOMO–LUMO gap in the π -electron system and, hence, with the aforementioned stabilization of the transition state by stronger donor–acceptor orbital interactions.

5.5 Reference

- [1] a) S. Yu, S. Ma, *Angew. Chem. Int. Ed.* **2012**, *51*, 3074–3112; *Angew. Chem.* **2012**, *124*, 3128–3167; b) A. Hoffmann-Röder, N. Krause, *Angew. Chem. Int. Ed.* **2004**, *43*, 1196–1216; *Angew. Chem.* **2004**, *116*, 1216–1236; c) N. Krause, A. S. K. Hashmi, *Modern Allene Chemistry*, Wiley-VCH, Weinheim, **2004**; d) T. M. V. D. Pinho e Melo, *Curr. Org. Chem.* **2009**, *13*, 1406–1431; e) T. M. V. D. Pinho e Melo, *Monatsh. Chem.* **2011**, *142*, 681–697; f) A. L. Cardoso, *Curr. Org. Chem.* **2019**, *23*, 3064–3134.
- [2] F. Scheufler, M. E. Maier, *Eur. J. Org. Chem.* **2000**, 3945–3948.
- [3] A. Padwa, D. N. Kline, K. F. Koehler, M. Matzinger, M. K. Venkatramanan, *J. Org. Chem.* **1987**, *52*, 3909–3917.
- [4] a) G. Himbert, L. Henn, *Angew. Chem. Int. Ed. Engl.* **1982**, *21*, 620–620; *Angew. Chem.* **1982**, *94*, 631–632; b) G. Himbert, D. Fink, K. Diehl, P. Rademacher, A. J. Bittner, *Chem. Ber.* **1989**, *122*, 1161–1173.
- [5] K. S. Feldman, M. R. Iyer, *J. Am. Chem. Soc.* **2005**, *127*, 4590–4591.
- [6] a) L. S. Trifonov, A. S. Orahovats, *Helv. Chim. Acta* **1989**, *72*, 59–64; b) Y. Schmidt, J. K. Lam, H. V. Pham, K. N. Houk, C. D. Vanderwal, *J. Am. Chem. Soc.* **2013**, *135*, 7339–7348; c) G. Cheng, X. He, L. Tian, J. Chen, C. Li, X. Jia, J. Li, *J. Org. Chem.* **2015**, *80*, 11100–11107; d) J. K. Lam, Y. Schmidt, C. D. Vanderwal, *Org. Lett.* **2012**, *14*, 5566–5569; e) K. S. Feldman, D. K. Hester, C. S. López, O. N. Faza, *Org. Lett.* **2008**, *10*, 1665–1668; f) K. S. Feldman, D. K. Hester, M. R. Iyer, P. J. Munson, C. Silva López, O. N. Faza, *J. Org. Chem.* **2009**, *74*, 4958–4974; g) K. S. Feldman, M. R. Iyer, C. Silva López, O. N. Faza, *J. Org. Chem.* **2008**, *73*, 5090–5099; h) K. S. Feldman, I. Y. Gonzalez, C. M. Glinkerman, *J. Am. Chem. Soc.* **2014**, *136*, 15138–15141; i) K. S. Feldman, I. Y. Gonzalez, C. M. Glinkerman, *J. Org. Chem.* **2015**, *80*, 11849–11862.

- [7] a) C. Larksarp, O. Sellier, H. Alper, *J. Org. Chem.* **2001**, *66*, 3502–3506; b) M. Alajarin, B. Bonillo, M.-M. Ortin, R.-A. Orenes, A. Vidal, *Org. Biomol. Chem.* **2011**, *9*, 6741–6749; c) W. J. Kauffman, *J. Org. Chem.* **1970**, *35*, 4244–4245.
- [8] a) X.-L. Huang, L. He, P.-L. Shao, S. Ye, *Angew. Chem. Int. Ed.* **2009**, *48*, 192–195; *Angew. Chem.* **2009**, *121*, 198–201; b) T.-Y. Jian, X.-Y. Chen, L.-H. Sun, S. Ye, *Org. Biomol. Chem.* **2013**, *11*, 158–163; c) M. Schmittel, H. von Seggern, *J. Am. Chem. Soc.* **1993**, *115*, 2165–2177; d) P.-L. Shao, X.-Y. Chen, S. Ye, *Angew. Chem. Int. Ed.* **2010**, *49*, 8412–8416; *Angew. Chem.* **2010**, *122*, 8590–8594; e) M. Presset, K. Mohana, M. Hamann, Y. Coquerel, J. Rodriguez, *Org. Lett.* **2011**, *13*, 4124–4127.
- [9] a) J. Světlík, J. Leško, A. Martvoň, *Monatsh. Chem.* **1980**, *111*, 635–642; b) W.-P. Yen, F.-C. Kung, F. F. Wong, *Eur. J. Org. Chem.* **2016**, 2328–2335.
- [10] a) K. M. Oberg, T. Rovis, *J. Am. Chem. Soc.* **2011**, *133*, 4785–4787; b) Z. Zheng, Y. Cao, D. Zhu, Z. Wang, K. Ding, *Chem. Eur. J.* **2019**, *25*, 9491–9497.
- [11] a) L.-L. Zhao, S.-Y. Wang, X.-P. Xu, S.-J. Ji, *Chem. Commun.* **2013**, *49*, 2569–2571; b) C.-X. Guo, W.-Z. Zhang, N. Zhang, X.-B. Lu, *J. Org. Chem.* **2017**, *82*, 7637–7642; c) F. Murillo, J. Barroso, M. G. de los Santos, G. Ávila, S. Pan, M. A. Fernández-Herrera, G. Merino, *J. Org. Chem.* **2018**, *83*, 13045–13050.
- [12] a) R. O. Angus, M. W. Schmidt, R. P. Johnson, *J. Am. Chem. Soc.* **1985**, *107*, 532–537; b) R. P. Johnson, *Chem. Rev.* **1989**, *89*, 1111–1124; c) K. J. Daoust, S. M. Hernandez, K. M. Konrad, I. D. Mackie, J. Winstanley, R. P. Johnson, *J. Org. Chem.* **2006**, *71*, 5708–5714.
- [13] a) P. Mohanakrishnan, S. R. Tayal, R. Vaidyanathaswamy, D. A. Devaprabhakara, *Tetrahedron Lett.* **1972**, *13*, 2871–2872; b) A. T. Bottini, L. L. Hilton, *Tetrahedron* **1975**, *31*, 2003–2004; c) M. Balci, W. M. Jones, *J. Am. Chem. Soc.* **1980**, *102*, 7607–7608; d) M. Nendel, L. M. Tolbert, L. E. Herring, M. N. Islam, K. N. Houk, *J. Org. Chem.* **1999**, *64*, 976–983; e) V. A. Lofstrand, F. G. West, *Chem. Eur. J.* **2016**, *22*, 10763–10767; f) J. S. Barber, E. D. Styduhar, H. V. Pham, T. C. McMahon, K. N. Houk, N. K. Garg, *J. Am. Chem. Soc.* **2016**, *138*, 2512–2515; g) J. S. Barber, M. M. Yamano, M. Ramirez, E. R. Darzi, R. R. Knapp, F. Liu, K. N. Houk, N. K. Garg, *Nat. Chem.* **2018**, *10*, 953–960.
- [14] a) R. Manova, T. A. van Beek, H. Zuilhof, *Angew. Chem. Int. Ed.* **2011**, *50*, 5428–5430; *Angew. Chem.* **2011**, *123*, 5540–5542; b) S. S. van Berkel, S. Brauch, L. Gabriel, M. Henze,

- S. Stark, D. Vasilev, L. A. Wessjohann, M. Abbas, B. Westermann, *Angew. Chem. Int. Ed.* **2012**, *51*, 5343–5346; *Angew. Chem.* **2012**, *124*, 5437–5441; c) C. Wendeln, I. Singh, S. Rinnen, C. Schulz, H. F. Arlinghaus, G. A. Burley, B. J. Ravoo, *Chem. Sci.* **2012**, *3*, 2479–2484; d) S. H. Lee, O. K. Park, J. Kim, K. Shin, C. G. Pack, K. Kim, G. Ko, N. Lee, S.-H. Kwon, T. Hyeon, *J. Am. Chem. Soc.* **2019**, *141*, 13829–13840; e) J. Escorihuela, A. Das, W. J. E. Looijen, F. L. van Delft, A. J. A. Aquino, H. Lischka, H. Zuilhof, *J. Org. Chem.* **2018**, *83*, 244–252.
- [15] a) A. Rastelli, M. Bagatti, R. Gandolfi, *Tetrahedron* **1994**, *50*, 5561–5568; b) A. Rastelli, M. Bagatti, R. Gandolfi, *J. Am. Chem. Soc.* **1995**, *117*, 4965–4975; c) M. Manoharan, P. Venuvanalingam, *J. Chem. Soc. Perkin Trans. 2* **1996**, 1423–1427; d) A. B. G. Pérez, A. B. González Pérez, J. A. Souto, C. S. López, Á. R. de Lera, *Eur. J. Org. Chem.* **2011**, 2933–2939; e) C. S. López, O. N. Faza, K. S. Feldman, M. R. Iyer, D. K. Hester, *J. Am. Chem. Soc.* **2007**, *129*, 7638–7646.
- [16] a) C. Wentrup, G. Gross, A. Maquestiau, R. Flammang, *Angew. Chem. Int. Ed. Engl.* **1983**, *22*, 542–543; *Angew. Chem.* **1983**, *95*, 551–551; b) W. R. Moore, W. R. Moser, *J. Am. Chem. Soc.* **1970**, *92*, 5469–5474; c) I. Quintana, D. Peña, D. Pérez, E. Guitián, *Eur. J. Org. Chem.* **2009**, 5519–5524; d) G. Wittig, P. Fritze, *Angew. Chem. Int. Ed. Engl.* **1966**, *5*, 846; *Angew. Chem.* **1966**, *78*, 905; e) J. D. Price, R. P. Johnson, *Tetrahedron Lett.* **1986**, *27*, 4679–4682; f) E. T. Marquis, P. D. Gardner, *Tetrahedron Lett.* **1966**, *7*, 2793–2798.
- [17] a) N. J. Agard, J. A. Prescher, C. R. Bertozzi, *J. Am. Chem. Soc.* **2004**, *126*, 15046–15047; b) S. T. Laughlin, J. M. Baskin, S. L. Amacher, C. R. Bertozzi, *Science* **2008**, *320*, 664–667; c) M. F. Debets, C. W. J. van der Doelen, F. P. J. T. Rutjes, F. L. van Delft, *ChemBioChem* **2010**, *11*, 1168–1184.
- [18] a) R. Huisgen, *Angew. Chem. Int. Ed. Engl.* **1963**, *2*, 565–598; *Angew. Chem.* **1963**, *75*, 604–637; b) F. Himo, T. Lovell, R. Hilgraf, V. V. Rostovtsev, L. Noodleman, K. B. Sharpless, V. V. Fokin, *J. Am. Chem. Soc.* **2005**, *127*, 210–216; c) V. V. Rostovtsev, L. G. Green, V. V. Fokin, K. B. Sharpless, *Angew. Chem. Int. Ed.* **2002**, *41*, 2596–2599; *Angew. Chem.* **2002**, *114*, 2708–2711; d) C. W. Tornøe, C. Christensen, M. Meldal, *J. Org. Chem.* **2002**, *67*, 3057–3064.

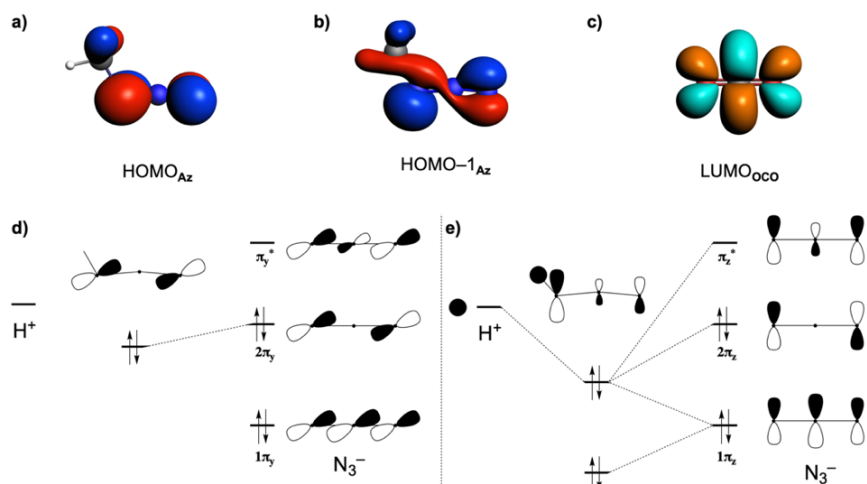
- [19] a) P. Vermeeren, S. C. C. van der Lubbe, C. Fonseca Guerra, F. M. Bickelhaupt, T. A. Hamlin, *Nat. Protoc.* **2020**, *15*, 649–667; b) F. M. Bickelhaupt, K. N. Houk, *Angew. Chem. Int. Ed.* **2017**, *56*, 10070–10086; *Angew. Chem.* **2017**, *129*, 10204–10221; c) F. M. Bickelhaupt, K. N. Houk, *Angew. Chem.* **2017**, *129*, 10204–10221; d) D. H. Ess, K. N. Houk, *J. Am. Chem. Soc.* **2008**, *130*, 10187–10198; e) L. P. Wolters, F. M. Bickelhaupt, *Wiley Interdiscip. Rev.: Comput. Mol. Sci.* **2015**, *5*, 324–343; f) I. Fernández, F. M. Bickelhaupt, *Chem. Soc. Rev.* **2014**, *43*, 4953–4967; g) W.-J. van Zeist, F. M. Bickelhaupt, *Org. Biomol. Chem.* **2010**, *8*, 3118–3127.
- [20] a) F. M. Bickelhaupt, E. J. Baerends in *Reviews in Computational Chemistry* (Eds: K. B. Lipkowitz, D. B. Boyd), Wiley, Hoboken, **2000**, pp. 1–86; b) R. van Meer, O. V. Gritsenko, E. J. Baerends, *J. Chem. Theory Comput.* **2014**, *10*, 4432–4441; c) L. Zhao, M. von Hopffgarten, D. M. Andrada, G. Frenking, *WIREs Comput. Mol. Sci.* **2018**, *8*, e1345.
- [21] a) B. J. Levandowski, T. A. Hamlin, F. M. Bickelhaupt, K. N. Houk, *J. Org. Chem.* **2017**, *82*, 8668–8675; b) T. A. Hamlin, B. J. Levandowski, A. K. Narsaria, K. N. Houk, F. M. Bickelhaupt, *Chem. Eur. J.* **2019**, *25*, 6342–6348.
- [22] a) G. te Velde, F. M. Bickelhaupt, E. J. Baerends, C. Fonseca Guerra, S. J. A. van Gisbergen, J. G. Snijders, T. Ziegler, *J. Comput. Chem.* **2001**, *22*, 931–967; b) C. Fonseca Guerra, J. G. Snijders, G. te Velde, E. J. Baerends, *Theor. Chem. Acc.* **1998**, *99*, 391–403; c) ADF, SCM Theoretical Chemistry; Vrije Universiteit, Amsterdam (The Netherlands), **2017**; <http://www.scm.com>.
- [23] a) A. D. Becke, *Phys. Rev. A* **1988**, *38*, 3098–3100; b) J. P. Perdew, *Phys. Rev. B* **1986**, *33*, 8822–8824.
- [24] E. van Lenthe, E. J. Baerends, *J. Comput. Chem.* **2003**, *24*, 1142–1156.
- [25] a) A. Talbot, D. Devarajan, S. J. Gustafson, I. Fernández, F. M. Bickelhaupt, D. H. Ess, *J. Org. Chem.* **2015**, *80*, 548–558; b) T. A. Hamlin, D. Svatunek, S. Yu, L. Ridder, I. Infante, L. Visscher, F. M. Bickelhaupt, *Eur. J. Org. Chem.* **2019**, 378–386; c) S. Yu, H. M. de Bruijn, D. Svatunek, T. A. Hamlin, F. M. Bickelhaupt, *ChemistryOpen* **2018**, *7*, 995–1004.
- [26] a) S. Grimme, S. Ehrlich, L. Goerigk, *J. Comput. Chem.* **2011**, *32*, 1456–1465; b) J. G. Brandenburg, J. E. Bates, J. Sun, J. P. Perdew, *Phys. Rev. B* **2016**, *94*, 115144.

- [27] a) Y. Zhao, D. G. Truhlar, *J. Chem. Phys.* **2006**, *125*, 194101; b) Y. Zhao, D. G. Truhlar, *Theor. Chem. Acc.* **2008**, *120*, 215–241.
- [28] a) A. Klamt, G. Schüürmann, *J. Chem. Soc. Perkin Trans. 2* **1993**, 799–805; b) A. Klamt, *J. Phys. Chem.* **1995**, *99*, 2224–2235; c) A. Klamt, V. Jonas, *J. Chem. Phys.* **1996**, *105*, 9972; d) C. C. Pye, T. Ziegler, *Theor. Chem. Acc.* **1999**, *101*, 396–408.
- [29] a) W.-J. van Zeist, C. Fonseca Guerra, F. M. Bickelhaupt, *J. Comput. Chem.* **2008**, *29*, 312–315; b) X. Sun, T. M. Soini, J. Poater, T. A. Hamlin, F. M. Bickelhaupt, *J. Comput. Chem.* **2019**, *40*, 2227–2233.
- [30] C. Y. Legault, *CYLview*, 1.0b; Université de Sherbrooke, Sherbrooke (QC, Canada), **2009**; <http://www.cylview.org>.
- [31] D. Svatunek, N. Houszka, T. A. Hamlin, F. M. Bickelhaupt, H. Mikula, *Chem. Eur. J.* **2019**, *25*, 754–758.
- [32] T. A. Albright, J. K. Burdett, M.-H. Whangbo, *Orbital Interactions in Chemistry*, 2nd ed., Wiley, Hoboken, **2013**.
- [33] C. Fonseca Guerra, J.-W. Handgraaf, E. J. Baerends, F. M. Bickelhaupt, *J. Comput. Chem.* **2004**, *25*, 189–210.
- [34] Y.-R. Luo, *Comprehensive Handbook of Chemical Bond Energies*, CRC Press, Boca Raton, **2007**.
- [35] G. S. Hammond, *J. Am. Chem. Soc.* **1955**, *77*, 334–338.

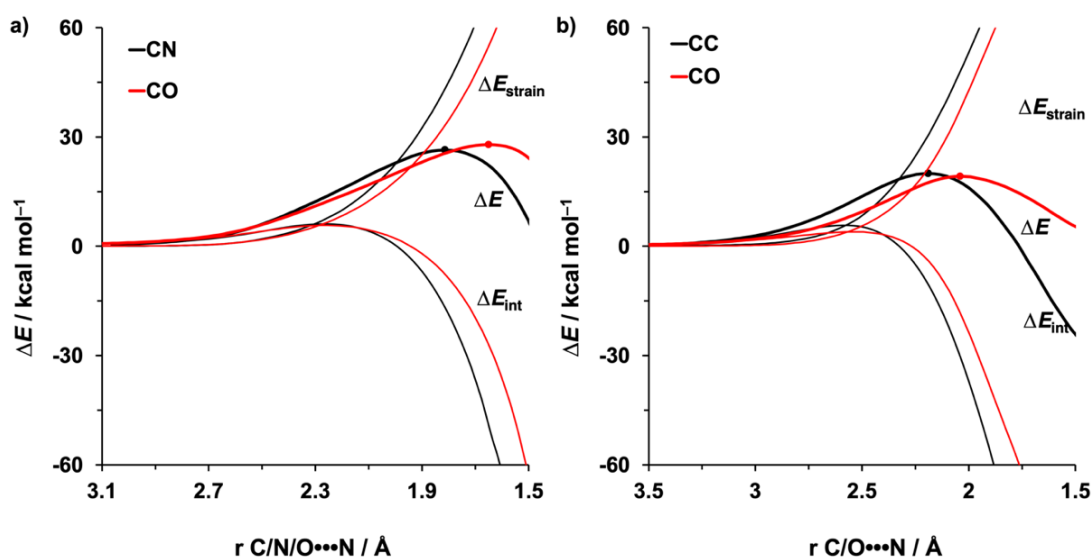
5.6 Appendices

Appendix 5.1 Reaction barriers and energies (kcal mol⁻¹) for 1,3-dipolar cycloadditions between **Az** and linear allenes to 1,5-adducts, computed at BP86/TZ2P, BP86-D3(BJ)/TZ2P//BP86/TZ2P, M06-2X/TZ2P//BP86/TZ2P, and COSMO(toluene)BP86/TZ2P//BP86/TZ2P.

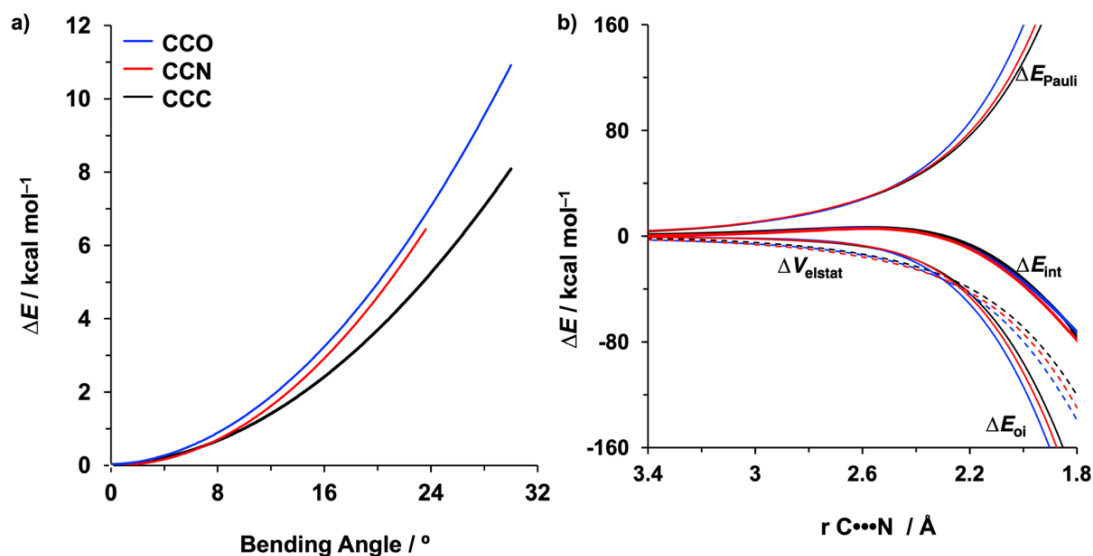
Allene and Site		BP86/TZ2P					
		ΔE^\ddagger	ΔH^\ddagger	ΔG^\ddagger	ΔE_{rxn}	ΔH_{rxn}	ΔG_{rxn}
OCO		32.1	31.9	43.2	20.6	21.8	33.7
NCN		28.0	28.3	40.2	-15.3	-12.6	1.7
NCO	CO	27.9	28.6	41.1	14.6	16.9	29.6
	NC	26.4	26.9	38.1	-14.9	-11.7	1.8
CCO	CO	19.2	20.1	32.3	3.5	6.0	19.3
	CC	20.0	20.3	31.3	-32.2	-29.1	-15.6
CCN	CN	22.6	23.2	34.9	-20.3	-17.2	-4.0
	CC	20.0	20.4	31.4	-30.7	-27.5	-13.7
CCC		19.0	19.5	30.5	-34.0	-30.9	-17.6
Allene and Site		BP86-D3(BJ)/TZ2P//BP86/TZ2P					
		ΔE^\ddagger	ΔH^\ddagger	ΔG^\ddagger	ΔE_{rxn}	ΔH_{rxn}	ΔG_{rxn}
OCO		28.8	28.5	39.8	17.2	18.4	30.3
NCN		23.7	24.0	35.9	-19.8	-17.0	-2.8
NCO	CO	24.1	24.8	37.3	10.7	13.0	25.7
	NC	22.7	23.1	34.4	-18.8	-15.6	-2.1
CCO	CO	15.0	15.9	28.2	-0.8	1.8	15.1
	CC	15.7	16.0	27.0	-36.4	-33.3	-19.9
CCN	CN	18.0	18.6	30.4	-25.1	-22.0	-8.7
	CC	15.7	16.0	27.1	-35.6	-32.3	-18.5
CCC		14.1	14.5	25.6	-39.1	-35.9	-22.7
Allene and Site		M06-2X/TZ2P//BP86/TZ2P					
		ΔE^\ddagger	ΔH^\ddagger	ΔG^\ddagger	ΔE_{rxn}	ΔH_{rxn}	ΔG_{rxn}
OCO		35.8	35.5	46.8	14.8	16.1	28.0
NCN		30.9	31.2	43.1	-25.2	-22.4	-8.2
NCO	CO	28.8	29.5	41.9	8.3	10.6	23.2
	NC	28.9	29.3	40.6	-24.0	-20.8	-7.3
CCO	CO	21.7	22.6	34.8	-2.6	-0.1	13.2
	CC	26.2	26.6	37.6	-42.1	-39.0	-25.5
CCN	CN	27.1	27.7	39.4	-29.1	-26.0	-12.8
	CC	27.0	27.4	38.4	-41.3	-38.0	-24.2
CCC		24.4	24.8	35.9	-43.7	-40.5	-27.3
Allene and Site		COSMO(toluene)BP86/TZ2P//BP86/TZ2P					
		ΔE^\ddagger	ΔH^\ddagger	ΔG^\ddagger	ΔE_{rxn}	ΔH_{rxn}	ΔG_{rxn}
OCO		31.0	30.8	42.1	19.7	21.0	32.9
NCN		29.2	29.6	41.5	-16.3	-13.6	0.7
NCO	CO	27.5	28.2	40.6	14.8	17.1	29.8
	NC	27.0	27.4	38.7	-16.4	-13.3	0.3
CCO	CO	17.9	18.8	31.1	3.8	6.3	19.6
	CC	21.1	21.4	32.4	-34.0	-30.9	-17.5
CCN	CN	23.0	23.6	35.3	-20.6	-17.5	-4.3
	CC	20.8	21.1	32.2	-32.3	-29.1	-15.2
CCC		19.6	20.1	31.1	-34.9	-31.7	-18.5



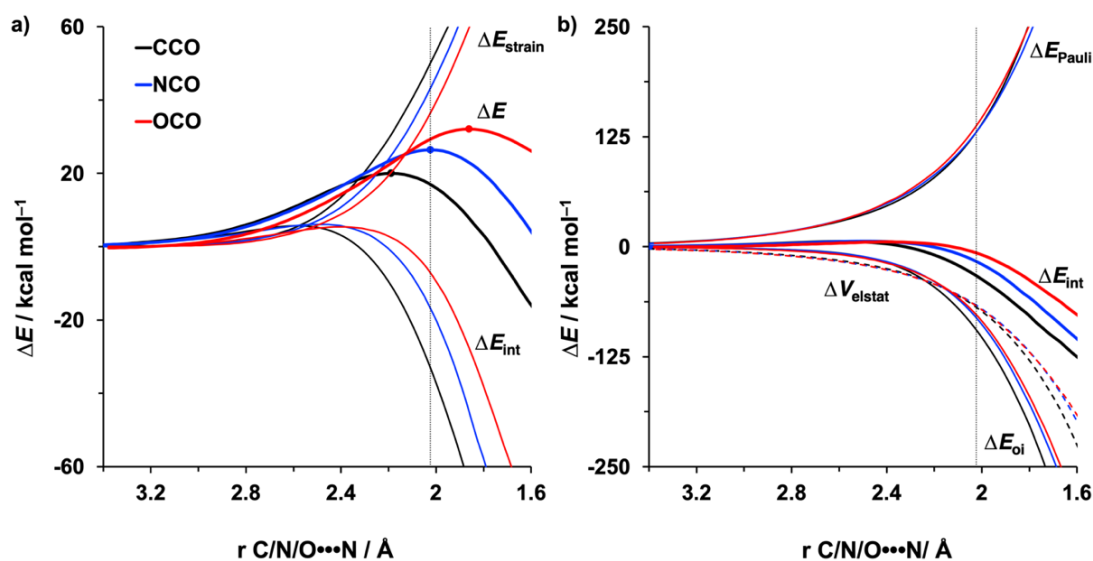
Appendix 5.2 The computed a) HOMO and b) HOMO-1 of methyl azide, and c) LUMO of OCO. Schematic diagrams of the formation of the d) HOMO and e) HOMO-1 of the model azide (HN₃) based on the H⁺ and N₃⁻ fragment.



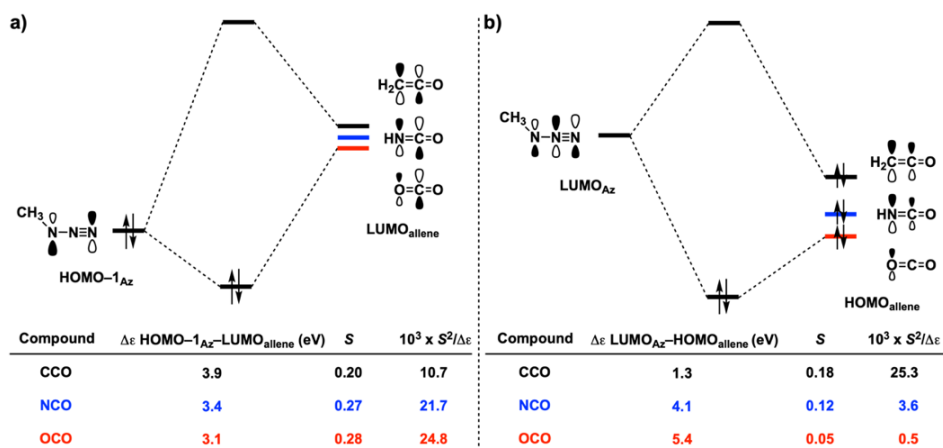
Appendix 5.3 Activation strain analyses of the regioselective cycloadditions of the allene a) NCO and b) CCO with Az, projected onto the average lengths of the newly forming bonds. Computed at BP86/TZ2P.



Appendix 5.4 a) Plot of the strain energy vs. the bending angle of the allene CCC, CCN and CCO relative to the equilibrium bond angle and b) energy decomposition analysis of the 1,3-dipolar cycloaddition between Az and CCC, CCN and CCO, projected onto the average newly forming C...N bond, computed at BP86/TZ2P.



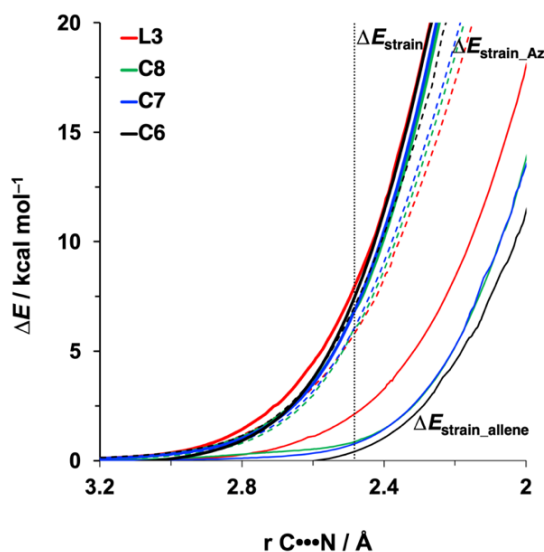
Appendix 5.5 a) Activation strain and b) energy decomposition analysis for the 1,3-dipolar cycloadditions between Az and CCO, NCO and OCO at CC, NC, and OC, respectively, affording 1,5-adducts, projected onto the average lengths of newly forming bonds. The vertical dotted line indicates the point along the reaction coordinate where the average length of newly forming C/N/O...N bond is 2.02 Å. Computed at BP86/TZ2P.



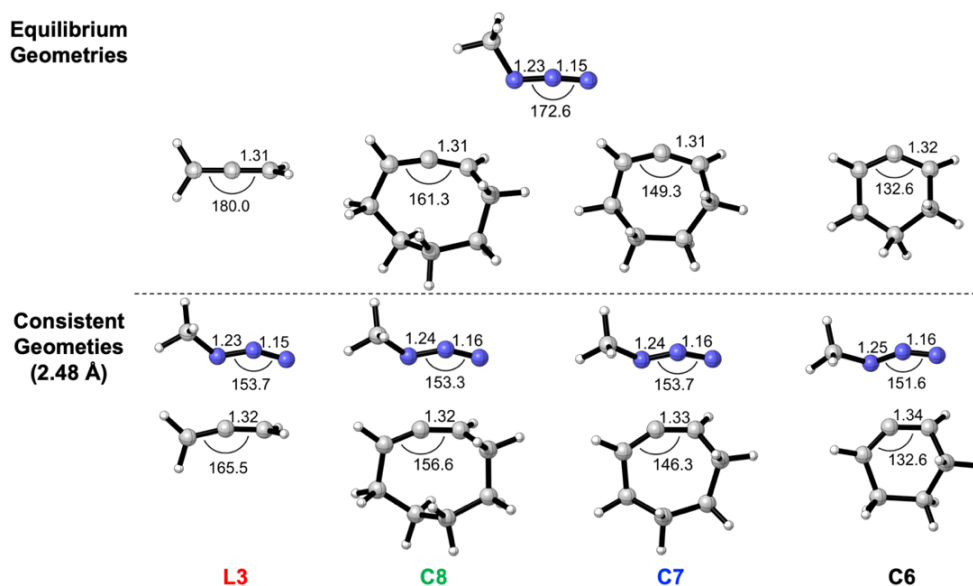
Appendix 5.6 FMO diagrams with calculated key orbital energy gaps and overlaps of a) the NED (HOMO-1_{Az}–LUMO_{allene}) interaction and b) the IED (LUMO_{Az}–HOMO_{allene}) interaction for the cycloadditions between Az and CCO, NCO and OCO, at consistent geometries with the average newly forming C/N/O•••N bond of 2.02 Å. Computed at BP86/TZ2P.

Appendix 5.7 Reaction barriers and energies (in kcal mol⁻¹) for the 1,3-dipolar cycloadditions between Az and C6–C8 or L3, computed at BP86/TZ2P, BP86-D3(BJ)/TZ2P//BP86/TZ2P, M06-2X/TZ2P//BP86/TZ2P, and COSMO(toluene)BP86/TZ2P//BP86/TZ2P.

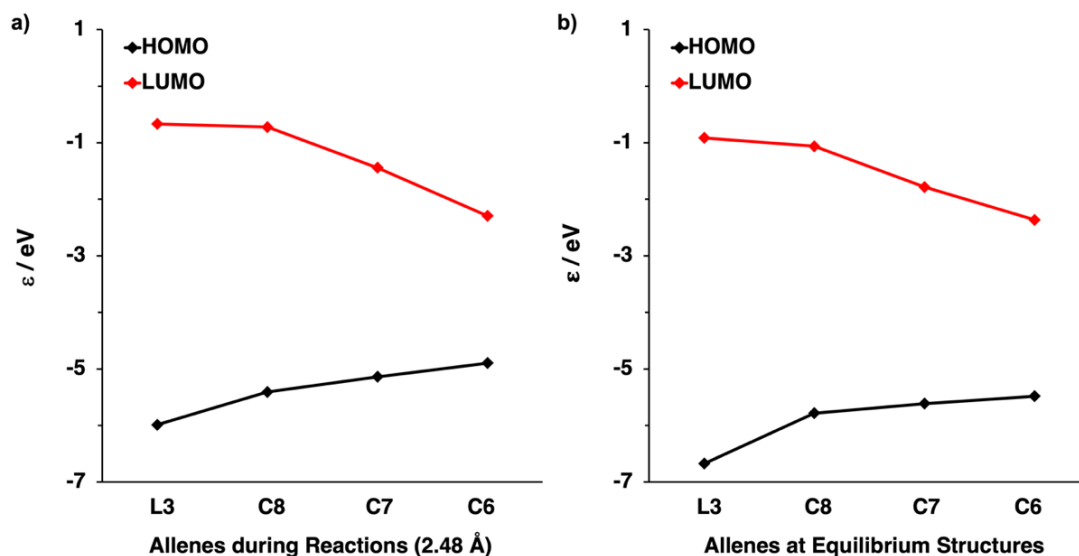
Allene	BP86/TZ2P					
	ΔE^\ddagger	ΔH^\ddagger	ΔG^\ddagger	ΔE_{rxn}	ΔH_{rxn}	ΔG_{rxn}
C6	6.0	6.8	17.1	-60.7	-57.1	-43.4
C7	10.2	9.6	21.5	-51.0	-48.0	-33.4
C8	13.8	14.1	26.3	-36.9	-34.0	-19.5
L3	19.0	19.5	30.5	-34.0	-30.9	-17.6
Allene	BP86-D3(BJ)/TZ2P//BP86/TZ2P					
	ΔE^\ddagger	ΔH^\ddagger	ΔG^\ddagger	ΔE_{rxn}	ΔH_{rxn}	ΔG_{rxn}
C6	0.8	1.7	11.9	-66.7	-63.1	-49.4
C7	3.7	3.0	14.9	-57.1	-54.1	-39.5
C8	7.8	8.1	20.3	-43.1	-40.3	-25.8
L3	14.1	14.5	25.6	-39.1	-36.0	-22.7
Allene	M06-2X/TZ2P//BP86/TZ2P					
	ΔE^\ddagger	ΔH^\ddagger	ΔG^\ddagger	ΔE_{rxn}	ΔH_{rxn}	ΔG_{rxn}
C6	8.1	9.0	-5.7	-74.4	-70.7	-57.0
C7	12.6	12.0	-1.2	-62.2	-59.2	-44.6
C8	18.1	18.4	4.2	-47.4	-44.6	-30.1
L3	24.4	24.9	35.9	-43.7	-40.6	-27.3
Allene	COSMO(toluene)BP86/TZ2P//BP86/TZ2P					
	ΔE^\ddagger	ΔH^\ddagger	ΔG^\ddagger	ΔE_{rxn}	ΔH_{rxn}	ΔG_{rxn}
C6	6.6	7.5	17.7	-61.1	-57.4	-43.7
C7	9.9	9.3	21.2	-51.5	-48.6	-34.0
C8	14.5	14.8	27.0	-37.6	-34.7	-20.2
L3	19.6	20.1	31.1	-34.9	-31.8	-18.5



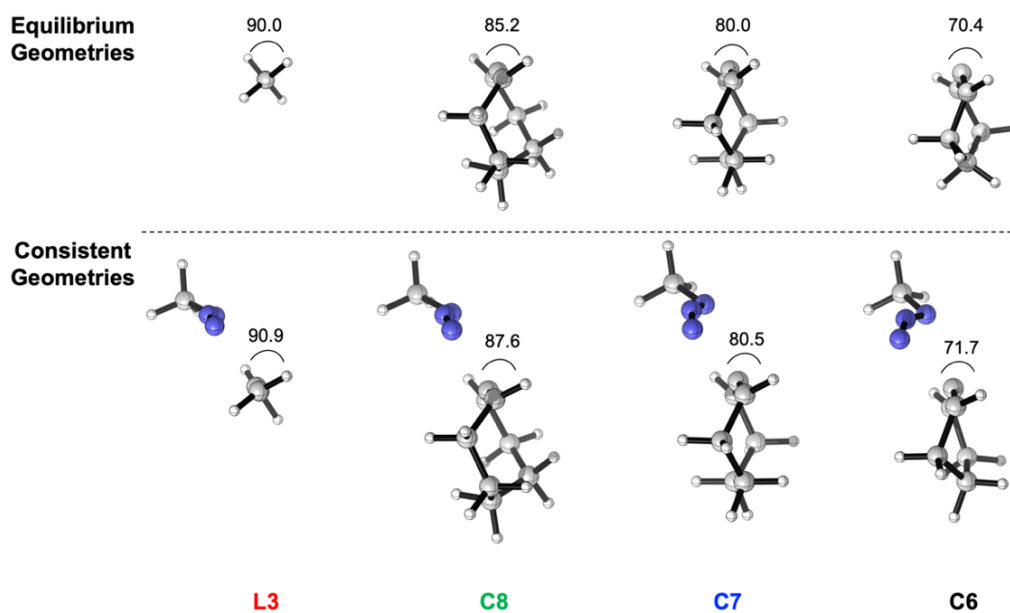
Appendix 5.8 Strain decomposition analysis of the 1,3-dipolar cycloaddition between Az and L3 and C6–C8, computed at BP86/TZ2P.



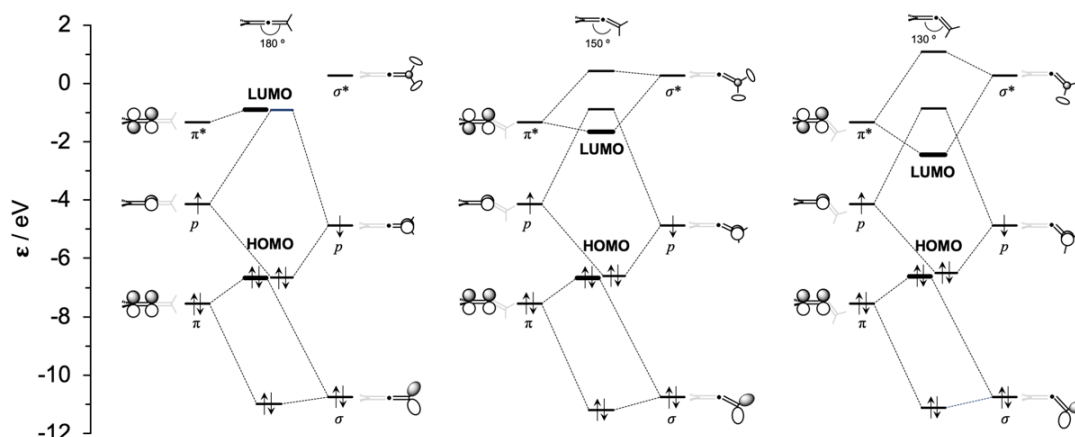
Appendix 5.9 The equilibrium geometries of isolated Az, L3 and C8–C6 (top) and the consistent geometries with the average newly forming C...N bond of 2.48 Å (bottom), including geometry details about the angles (in °) and lengths (in Å), computed at BP86/TZ2P.



Appendix 5.10 Computed FMOs energies of L3 and C8–C6 a) during reactions with the consistent geometries with the average newly forming C•••N bond of 2.48 Å and b) at equilibrium geometries, computed at BP86/TZ2P.

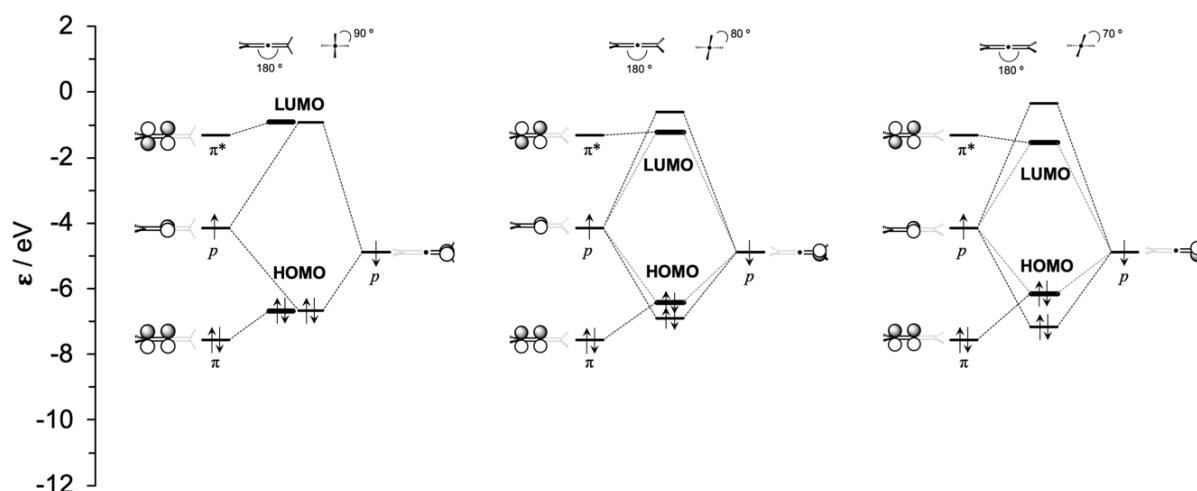


Appendix 5.11 The side view of the equilibrium geometries of isolated reactants (top) and consistent geometries with the average newly forming C•••N bond of 2.48 Å, for L3 and C8–C6, including the geometrical detail about the dihedral angle (in °) between the two C=CH planes. All were computed at BP86/TZ2P.



Appendix 5.12 Diagrams for the Kohn-Sham molecular orbital analyses of the archetypal **L3** and the exclusively bent **L3**, based on $\text{H}_2\text{C}=\text{C}''$ and $''\text{CH}_2$. Computed at BP86/TZ2P.

As the internal angle bents from 180° to 150° to 130° , while keeping the two $\text{C}=\text{CH}_2$ planes orthogonal, the LUMO becomes stabilized, with the $\pi^*-\sigma^*$ overlap increasing from 0 to 0.08 and 0.12, and the HOMO (HOMO-1 for bent allenes) is becoming slightly stabilized due to the decreasing of the $\pi-\sigma$ overlap from 0.15 to 0.14 and 0.13.



Appendix 5.13 Diagrams for the Kohn-Sham molecular orbital analyses of the archetypal **L3** and the exclusively twisted **L3**, based on $\text{H}_2\text{C}=\text{C}''$ and $''\text{CH}_2$. Computed at BP86/TZ2P.

As the dihedral angle between the two $\text{C}=\text{CH}_2$ planes decreases from 90° to 80° to 70° , while keeping the structure linear, the LUMO becomes stabilized, with the contribution of p orbitals increasing from 0 to 54% and 57%, and the HOMO becomes destabilized with the contribution of p orbitals increasing from 0 to 52% and 54%.

Chapter 6 How Oriented External Electric Fields Modulate Diels-Alder Reactions

This chapter previously appeared as

Chem. Eur. J. **2021**, *27*, 5683–5693.

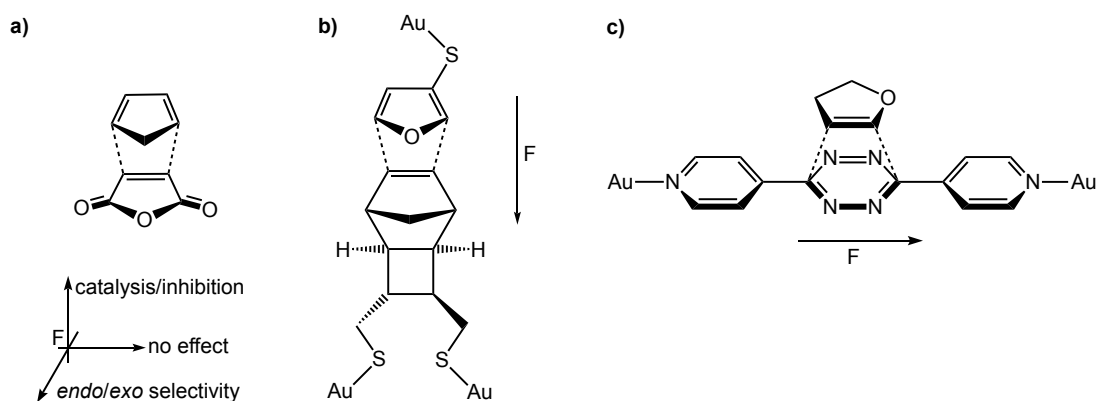
Song Yu, Pascal Vermeeren, Trevor A. Hamlin, F. Matthias Bickelhaupt

A judiciously oriented external electric field (OEEF) can catalyze a wide range of reactions and even induce *endo/exo* stereoselectivity of cycloaddition reactions. In this chapter, we studied the Diels-Alder reaction between cyclopentadiene and maleic anhydride using quantitative activation strain and Kohn-Sham molecular orbital theory to pinpoint the origin of these catalytic and stereoselective effects. Our quantitative analyses revealed that an OEEF along the reaction axis induces an enhanced electrostatic and orbital interaction between the reactants, which in turn lowers the reaction barrier. The stronger electrostatic interaction originates from an increased electron density difference between the reactants at the reactive center, while the enhanced orbital interaction arises from the promoted normal electron demand donor–acceptor interaction driven by the OEEF. An OEEF perpendicular to the plane of the reaction axis solely stabilizes the *exo* pathway of this reaction while the *endo* pathway remains unaltered and efficiently steers the *endo/exo* stereoselectivity. Furthermore, we investigated the influence of OEEFs on the inverse electron demand Diels-Alder reaction, which, unexpectedly, inhibits the reaction, as the electric field now suppresses the critical inverse electron demand donor–acceptor interaction.

6.1 Introduction

Recently, the study of electrostatically catalyzed non-redox reactions has become a thriving field in chemistry.^[1] The reactivity, as well as selectivity, of non-redox reactions can be manipulated by orienting the electric field in a specific direction with respect to the interacting reactants. In nature, for example, electric fields have been proposed to play a role in enzyme-catalyzed reactions.^[2] In the last decade, artificially designed electric fields have also been utilized to mediate non-redox reactions through, for example, the electrode/electrolyte interface,^[3] a voltage-biased STM tip,^[4] and the active site under the electric field possibly created by charged functional groups^[5] or catalysts.^[6] From a theoretical point of view, a large number of studies have been dedicated to the understanding and prediction of the effect of an oriented external electric field (OEEF) on various chemical transformations^[7] such as C-H bond activation reactions,^[6a–6c, 7a–7c] Diels-Alder reactions,^[5e, 6d, 7d–7e] methyl transfer reactions,^[7f] electrophilic aromatic substitution reactions,^[7g] nucleophilic substitutions of halogen-bond complexes,^[7h] and oxidative addition reactions.^[7i]

The pioneering theoretical predictions made by Shaik et al. in 2010 on the effect of the OEEF on Diels-Alder (DA) reactions^[7d] were proven in cutting-edge experimental studies by Coote and co-workers six years later.^[4a] Shaik et al. discovered that, for the DA reaction between cyclopentadiene and maleic anhydride (**Scheme 6.1a**), an electric field directed along the reaction axis, that is, the electric field along the forming bonds, can catalyze (positive field) or inhibit (negative field) the reaction, whereas an electric field perpendicular to the reaction axis and the bond-forming plane will lead to an enhanced *endo* (negative field) or *exo* (positive field) selectivity. Furthermore, an electric field along the C=C double bond of maleic anhydride shows negligible effect on the reactivity or selectivity of the reaction.^[7d] Coote and co-workers probed a single-molecule DA reaction between furan and a norbornylogous bridge, which were separately tethered to a gold STM tip and gold surface, respectively (**Scheme 6.1b**).^[4a] In this way, the orientation of the electric field was aligned along the reaction axis, leading to a fivefold increase in the frequency of the formation of the single-molecule junction, observed through a so-called “blinking” technique.^[4a] In addition, Hong and co-workers confirmed, by using an electric-field-mediated single-molecule reaction, that the reactivity of the studied DA reaction remains unaltered under an electric field aligned to the C=C double bond of the dienophile (**Scheme 6.1c**).^[8]



Scheme 6.1 a) Theoretical predictions on the effect of the oriented external electric field (OEEF) on the Diels-Alder reaction, and experimental verifications of the OEEF b) along the reaction axis and c) aligned with the double bond of the dienophile.

The molecular dipole moment has long been considered critical to understanding the effect of an OEEF on the reactivity and selectivity of a DA reaction.^[7d, 7e] As the reactants and transition state of a DA reaction have distinct dipole moments along a particular direction, an OEEF is able to (de)stabilize the reactants and transition state, depending on the direction of the electric field, and hence, has an immediate effect on the activation barrier of the reaction. On the other hand, qualitative valence bond (VB) theory^[9] has also been utilized to understand the catalytic effect of an OEEF aligned to the reaction axis on the DA reaction. This model revealed that the charge transfer state along the reaction pathway is significantly stabilized by a positive electric field, which, as a consequence, mixes into the wavefunction at and around the transition state. This phenomenon stabilizes the transition state, and therefore lowers the activation barrier.^[7d] On the other hand, the OEEF-induced *endo/exo* selectivity has been understood solely by the interaction between the OEEF and the molecular dipole moment in a specific stereoisomer, but has not been explained within the framework of VB theory.

In this study, for the first time, we aim to investigate the OEEF-mediated DA reaction within the context of Kohn-Sham molecular orbital (KS-MO) theory. The ultimate physical factors dictating the catalytic, as well as *endo/exo* selective, effects of an OEEF on the Diels-Alder reaction are elucidated using quantitative KS-MO analyses. The results obtained herein, together with the VB study of Shaik et al., effectively provide a complete framework for understanding the effects of the OEEF, and hence, will act as a toolbox for the design of novel electric-field-catalyzed organic reactions. To this end, we have performed a systematic computational study on OEEF-mediated Diels-Alder reactions between cyclopentadiene (**Cp**), acting as a diene, and maleic

anhydride (**MA**), acting as the dienophile, at the BP86/TZ2P level. The activation strain model (ASM)^[10] of reactivity in combination with quantitative KS-MO theory and a matching canonical energy decomposition analysis (EDA)^[11] have been employed to perform analyses on the Diels-Alder reactions under the OEEF along different axes. This methodology has been utilized to investigate various types of cycloaddition reactions, and has proven to be valuable for understanding the trends in reactivity.^[12]

6.2 Computational Details

All calculations were performed in ADF2017^[13] using the BP86^[14] functional with the TZ2P basis set.^[15] The exchange-correlation (XC) functional has been proven to be accurate in calculating the relative trends in activation and reaction energies for this reaction.^[7d, 12a, 16] Geometries and energies were recomputed at COSMO(DCM)-BP86/TZ2P^[17] to assess the effect of the solvation on the reactivity trends. Additionally, single-point energies were computed at B3LYP/TZ2P^[18] and M06-2X/TZ2P^[19] on the optimized BP86/TZ2P geometries to evaluate the effect of the hybrid and *meta*-hybrid functional on the reactivity trends. Frequency calculations were performed to characterize the nature of the stationary points. Local minima present only real frequencies, whereas transition structures have one imaginary frequency. The potential energy surface (PES) was calculated using the intrinsic reaction coordinate (IRC) method,^[20] which follows the imaginary eigenvector of the transition structure toward the reactant and product. The resulting PES was analyzed with the aid of the PyFrag 2019 program.^[21] All chemical structures were illustrated using CYLview.^[22]

Quantitative analyses of the activation barriers associated with the studied reactions were obtained by means of the activation strain model (ASM) of reactivity.^[10] Herein, the PES, $\Delta E(\zeta)$, was decomposed into the strain energy, $\Delta E_{\text{strain}}(\zeta)$, and the interaction energy, $\Delta E_{\text{int}}(\zeta)$. In this study, the reaction coordinate was projected on the length of the newly forming C••C bond, which undergoes a well-defined change throughout the reaction and has been used in the past in analyses of similar reactions.^[12]

$$\Delta E(\zeta) = \Delta E_{\text{strain}}(\zeta) + \Delta E_{\text{int}}(\zeta)$$

The $\Delta E_{\text{strain}}(\zeta)$ value is associated with the rigidity as well as the structural deformation of the reactants from their equilibrium geometry to the geometry acquired along the reaction coordinate. The $\Delta E_{\text{int}}(\zeta)$ value is related to the electronic structure of the reactants and their spatial orientation, and takes the mutual interaction between the deformed reactants into account. To obtain a deeper insight into the physical mechanism behind the interaction energy, we employed canonical energy decomposition analysis (EDA).^[11] This analysis method decomposes the interaction energy between the two deformed reactants, within the framework of Kohn-Sham DFT, into three physically meaningful terms.

$$\Delta E_{\text{int}}(\zeta) = \Delta V_{\text{elstat}}(\zeta) + \Delta E_{\text{Pauli}}(\zeta) + \Delta E_{\text{oi}}(\zeta)$$

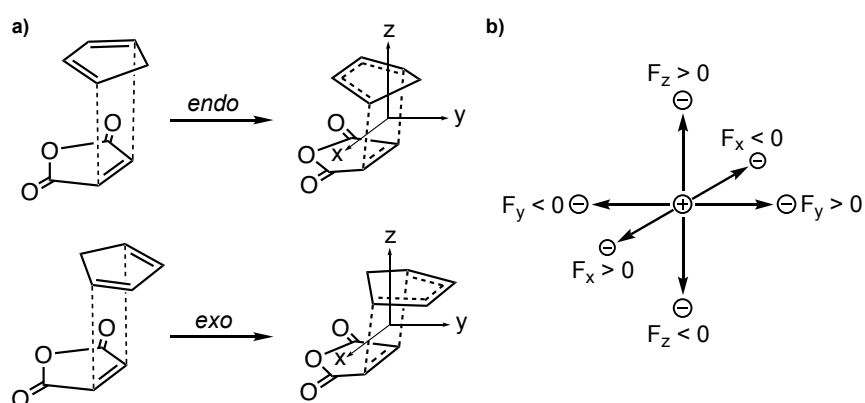
The electrostatic interaction, $\Delta V_{\text{elstat}}(\zeta)$, corresponds to the classical electrostatic interaction between the unperturbed charge distributions of the deformed reactants. The Pauli repulsion, $\Delta E_{\text{Pauli}}(\zeta)$, comprises the repulsion between closed-shell occupied orbitals, and is, therefore, destabilizing. The orbital interaction, $\Delta E_{\text{oi}}(\zeta)$, accounts for the stabilizing orbital interactions such as electron-pair bonding, charge transfer (interaction between the occupied orbitals of fragment A with the unoccupied orbitals of fragment B, and vice versa), and polarization (e.g., occupied–unoccupied orbital mixing on fragment A owing to the presence of fragment B, and vice versa). A detailed step-by-step protocol on how to perform the activation strain and energy decomposition analysis can be found in ref. 10e.

6.3 Results and Discussion

6.3.1 Definition of the Directions of Oriented External Electric Fields

The effect of an oriented external electric field (OEEF) on the reactivity and *endo/exo* selectivity of the Diels-Alder (DA) reactions between cyclopentadiene (**Cp**) and maleic anhydride (**MA**) is highly dependent on the direction of the field.^[7d] For this reason, we applied an electric field (**F**) individually from three distinct directions (**Scheme 6.2b**), namely, F_x , F_y , and F_z . These axes are defined as follows: F_x is along the C=C double bond of **MA**, F_y is perpendicular to the reaction axis, that is, perpendicular to the plane of the newly forming C–C bonds, and F_z is aligned along the reaction axis, that is, along the axis of a newly forming C–C bond. For the isolated reactants,

the F_z is perpendicular to the molecular plane of **Cp** and **MA**. Shaik et al. revealed that a switch in the reaction mechanism, from a concerted to a stepwise reaction mode, will occur in solution if F_z is above 0.008 au.^[7d] Therefore, we limit the strength of the electric field applied in this study to ± 0.008 au (1 au = 514 V nm⁻¹), to ensure that the reaction mechanism remains concerted for all studied electric field strengths. Note that applying an electric field will, as discussed later, make the reaction slightly asynchronous; however, this has a negligible effect on the activation barrier. In addition, this range of electric field strengths is also accessible in the laboratory.^[23]



Scheme 6.2 a) Schematic representation of the Diels-Alder reaction between cyclopentadiene (**Cp**) and maleic anhydride (**MA**) including the axis of the coordinate systems; b) directions of the electric fields (the electric field is defined from the positive to negative charge, as the conventional definition in physics and ADF software).

Table 6.1 displays the computed activation energies, ΔE^\ddagger , and reaction energies, ΔE_{rxn} , of the *endo/exo* Diels-Alder reactions between **Cp** and **MA** under the strongest electric fields ($F = \pm 0.008$ au) along the different axes. To solely evaluate the critical electronic effect of the OEEF on the DA reactivity, we follow the routine of Shaik and analyze energies from OEEF calculations on non-OEEF geometries.^[6d, 7c–7e, 7f] Analysis of geometries and energies in the OEEF provides the same conclusions (**Appendix 6.1–Appendix 6.5**).^[7d] The reactivity and selectivity trends in Gibbs free activation energies (ΔG^\ddagger) are in line with the trends observed in activation energies (ΔE^\ddagger) (**Appendix 6.1**); and the computed reactivity and selectivity trends at BP86/TZ2P agree well with those computed at B3LYP/TZ2P//BP86/TZ2P and M06-2X/TZ2P//BP86/TZ2P (**Appendix 6.2**). An electric field along the x axis was found to have negligible impact on ΔE^\ddagger and ΔE_{rxn} of both the *endo* and *exo* reaction pathways. An electric field along the y axis, however, alters the *endo/exo* selectivity, namely, a negative field favors the *endo* pathway whereas a positive field goes via the *exo* pathway. Furthermore, an electric field along the z axis can either inhibit (negative

field) or catalyze (positive field) both *endo* and *exo* reaction pathways. In the following sections, we will discuss the effects of the electric field along the various axes individually.

Table 6.1 Activation barriers (ΔE^\ddagger , kcal mol⁻¹) and reaction energies (ΔE_{rxn} , kcal mol⁻¹) of the *endo/exo* Diels-Alder reaction between **Cp** and **MA** without the electric fields ($F = 0$) and under the electric fields ($F = \pm 0.008$ au) along different axes, computed at BP86/TZ2P.

F / au	<i>endo</i>		<i>exo</i>	
	ΔE^\ddagger	ΔE_{rxn}	ΔE^\ddagger	ΔE_{rxn}
0	9.6	-17.8	10.5	-18.7
<i>x</i> -0.008	9.5	-17.8	10.4	-18.7
0.008	9.5	-17.8	10.4	-18.7
<i>y</i> -0.008	10.0	-18.7	12.9	-17.6
0.008	9.9	-16.1	8.3	-19.0
<i>z</i> -0.008	16.3	-12.5	16.7	-13.7
0.008	0.7	-24.4	2.2	-25.0

6.3.2 Oriented External Electric Field in the *z* Direction

First, we focus on the effect of the electric field in the *z* direction (F_z ; along the reaction axis) on the DA reactions studied herein. An electric field in the *z* direction has, as shown previously,^[7d] a significant catalytic (positive field) or inhibitive (negative field) effect on the DA reaction (**Figure 6.1**). A negative F_z (i.e., positive end at **Cp**, negative end at **MA**) leads to an increase in activation barrier ($\Delta\Delta E^\ddagger = 6$ kcal mol⁻¹ for $F_z = -0.008$ au), whereas a positive F_z (i.e., positive end at **MA**, negative end at **Cp**) results in a decrease in activation barrier ($\Delta\Delta E^\ddagger = -9$ kcal mol⁻¹ for $F_z = 0.008$ au), for both the *endo* and *exo* pathways. The reaction is *endo* selective for all screened F_z . In line with the work of Shaik et al.,^[7d] the inclusion of implicit solvation in our variable OEEF calculations has no effect on reactivity trends and *endo/exo* selectivity (**Appendix 6.1**).

To gain quantitative insight into the driving force leading to the catalytic or inhibitive effect of F_z on the DA reaction between **Cp** and **MA**, we turned to the activation strain model (ASM) of reactivity.^[10] In **Figure 6.2a**, we focus on the activation strain diagram (ASD) of the energetically preferred *endo* pathway, as the ASD of the *exo* pathway possess the same characteristics (see **Appendix 6.6**). The DA reaction is catalyzed by a positive F_z owing to both a less destabilizing ΔE_{strain} as well as a more stabilizing ΔE_{int} (**Figure 6.2a**). The increase in F_z from -0.008 to 0.008 au leads to a ΔE_{strain} at the transition state that becomes 5.0 kcal mol⁻¹ less destabilizing. The individual reactants undergo a deformation and reorientation over the course of the reaction,

(Appendix 6.7), which results in a more favorable alignment of the dipole moment of distorted reactants with a positive F_z and hence a stabilization of these distorted reactants. As a result, the total strain energy along this reaction pathway will become less destabilizing. The stabilization of the ΔE_{int} at the transition state, upon increasing the F_z from -0.008 to 0.008 au, is, on the other hand, more significant, that is, $\Delta\Delta E_{\text{int}} = -10.6$ kcal mol $^{-1}$, indicating that the ΔE_{int} term is the predominant driving force leading to the catalytic or inhibitive effect of the F_z on the DA reaction.

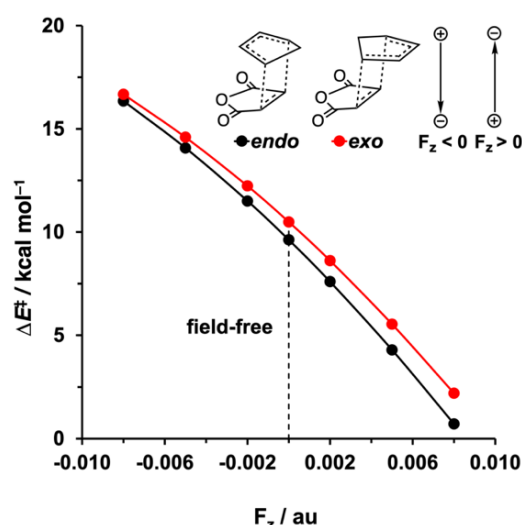


Figure 6.1 Plots of the activation energy ΔE^\ddagger (in kcal mol $^{-1}$) of the endo and exo Diels-Alder reactions between **Cp** and **MA** versus the strength of the F_z (in au), computed at BP86/TZ2P.

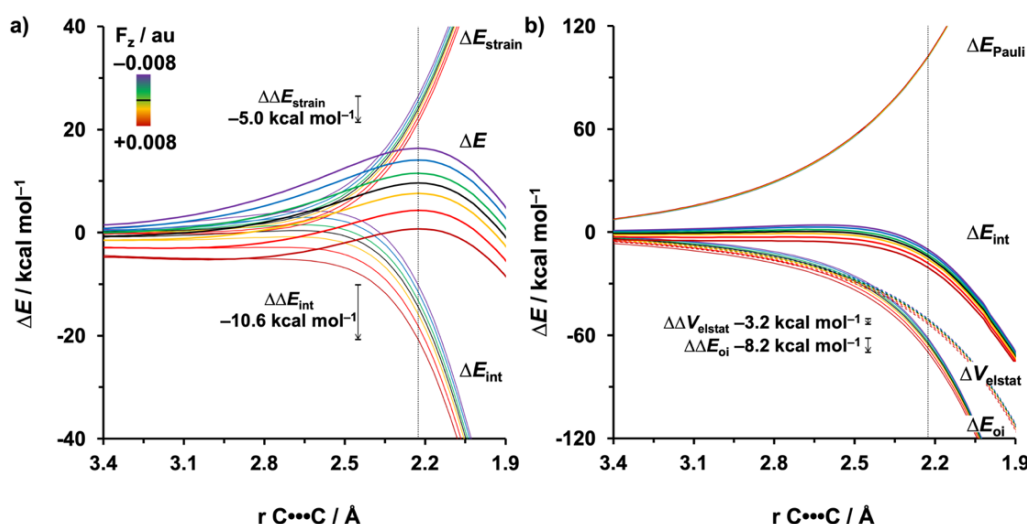


Figure 6.2 a) Activation strain and b) energy decomposition analyses of the endo Diels-Alder reactions between **Cp** and **MA** under F_z ranging from -0.008 to 0.008 au along the reaction coordinate projected onto the average length of the newly forming $\text{C}\cdots\text{C}$ bonds, computed at BP86/TZ2P. The vertical dotted line at 2.23 Å indicates the transition state.

The decisive role of ΔE_{int} on the reactivity prompted the analysis of the different contributors to the interaction energy ΔE_{int} by using a canonical energy decomposition analysis (EDA).^[11] The corresponding EDA results for the *endo* DA reaction between **Cp** and **MA** under the F_z ranging from -0.008 to 0.008 au are presented in **Figure 6.2b**. We have found that the consistently more stabilizing ΔE_{int} , as F_z is varied from -0.008 to 0.008 au, originates from both a more stabilizing ΔV_{elstat} and ΔE_{oi} . The ΔE_{Pauli} value, on the other hand, is hardly affected by the F_z , and thus, has little effect on the observed trend in reactivity.

To understand the origin of the systematically more stabilizing ΔV_{elstat} upon going from the negative to positive F_z , we analyzed the molecular electrostatic potential map (MEP) of the distorted fragments in their transition state geometry (**Figure 6.3**). From these MEPs together with the computed dipole moment in the z direction (μ_z), it becomes clear that the enhanced stabilization of the ΔV_{elstat} originates from a larger (more favorable) difference in charge density between the reactive side of the reactants going from $F_z = -0.008$ au (left) to $F_z = 0$ au (middle) to $F_z = 0.008$ au (right) (**Figure 6.3**). For the field-free reaction, **Cp** and **MA** have a charge separation that leads to a net negative and positive potential, respectively, on the carbon atoms involved in the formation of the new C–C bonds. These features are also reflected by their positive values of the dipole moment μ_z (**Cp**: $\mu_z = 0.5$ D, **MA**: $\mu_z = 0.7$ D). By applying a positive F_z , the intramolecular charge separation increases and amplifies the μ_z (**Cp**: $\mu_z = 1.3$ D, **MA**: $\mu_z = 1.4$ D), leading to a stronger electrostatic attraction between reactants and hence a more stabilizing ΔV_{elstat} . A negative F_z , on the contrary, suppresses the μ_z (**Cp**: $\mu_z = -0.2$ D, **MA**: $\mu_z = 0.1$ D), which results in a smaller difference in the charge density between reactants in the reactive regions, and thus, a less stabilizing ΔV_{elstat} term.

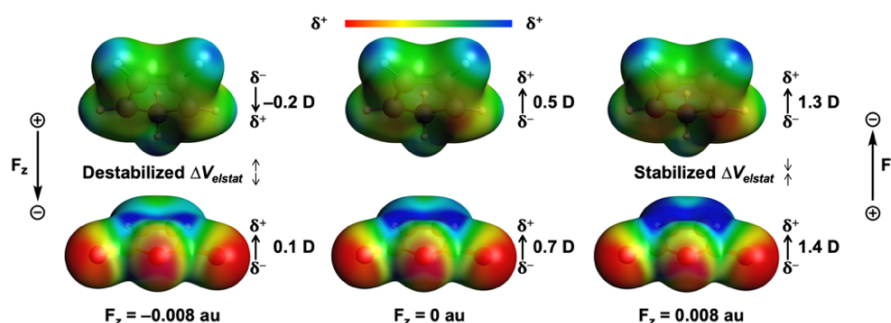


Figure 6.3 Molecular electrostatic potential maps (at 0.01 Bohr^{-3}) from -0.03 (red) to 0.1 (blue) Hartree e^{-1} and dipole moments (μ_z ; in Debye) of isolated reactants for *endo* Diels-Alder reactions between **Cp** and **MA** in the F_z at -0.008 au (left), 0 au (middle), and 0.008 au (right), computed at the transition state structures at BP86/TZ2P.

Next, Kohn-Sham molecular orbital (KS-MO) analyses were performed to understand why ΔE_{oi} becomes increasingly more stabilizing from $F_z = -0.008$ to $F_z = 0.008$ au.^[11b,24] The normal electron demand (NED) between the HOMO_{Cp} and LUMO_{MA} is the dominant orbital interaction contributing to the ΔE_{oi} . Analysis of the MOs reveals that the HOMO_{Cp} is predominantly located on the two C=C double bonds of **Cp**, whereas the LUMO_{MA} is centered on the C=C double bond of the five-membered ring of **MA** (**Figure 6.4a**). During the NED interaction, the HOMO_{Cp} mixes with the LUMO_{MA} to give a more stabilized bonding MO. The energy gain of forming this two-center-two-electron interaction (i.e., orbital stabilization) relates to the energy difference between the HOMO_{Cp} and bonding MO ($\Delta \epsilon_{\text{NED}}$).^[24] The electron density deformation associated with the NED interaction involves the flow of electrons from the HOMO_{Cp} to LUMO_{MA} and is stabilized under a positive F_z owing to the fact that the electrons move toward the positive side of the electric field (**Figure 6.4b**), a process that goes with negative (stabilizing) work. As a result, the NED interaction is strengthened by the external electrical force, which leads to a more stabilized bonding MO, or increased $\Delta \epsilon_{\text{NED}}$, and hence, a more stabilizing ΔE_{oi} (**Figure 6.4a**). On the contrary, a negative F_z counteracts the electron flow from the HOMO_{Cp} to LUMO_{MA} because the electron is forced to move toward the negative side of the electric field, a process that results in positive (destabilizing) work. For this reason, the corresponding $\Delta \epsilon_{\text{NED}}$ becomes smaller, quenching the NED interaction. These effects can be quantified by looking at the charge transfer from the HOMO_{Cp} to LUMO_{MA} , which increases from 0.39 e to 0.50 e⁻ by changing the F_z from -0.008 to 0.008 au.

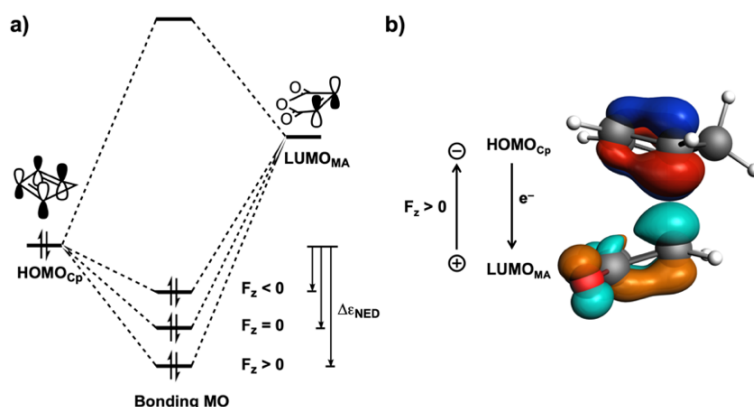


Figure 6.4 a) Schematic diagrams of the normal electron demand (NED) interaction between the HOMO_{Cp} and LUMO_{MA} for the Diels-Alder reactions between **Cp** and **MA** under different F_z ; b) computed HOMO_{Cp} and LUMO_{MA} (isovalue = 0.03 Bohr^{-3/2}) participating in the NED interaction of the field-free reaction, including the direction of the electron flow in this interaction.

6.3.3 Oriented External Electric Field in the y Direction

After providing a causal model to understand how the rate of the DA reaction between **Cp** and **MA** can be tuned by an electric field along the reaction axis (F_z), we next examined the effect of an electric field perpendicular to the reaction axis (F_y). In analogy with the work of Shaik et al.,^[7d] we found that F_y has a significant impact on the *endo/exo* selectivity of the DA reaction studied herein (**Figure 6.5**). The activation barrier of the *endo* pathway remains nearly unaffected in both a negative or positive F_y , whereas the barrier for the *exo* pathway becomes systematically stabilized on going from $F_y = -0.008$ au to $F_y = 0.008$ au. This results in a switch in the *endo/exo* selectivity, because an F_y of 0.003 au or higher stabilizes the *exo* pathway to such an extent that the activation barrier becomes lower than the *endo* analog.

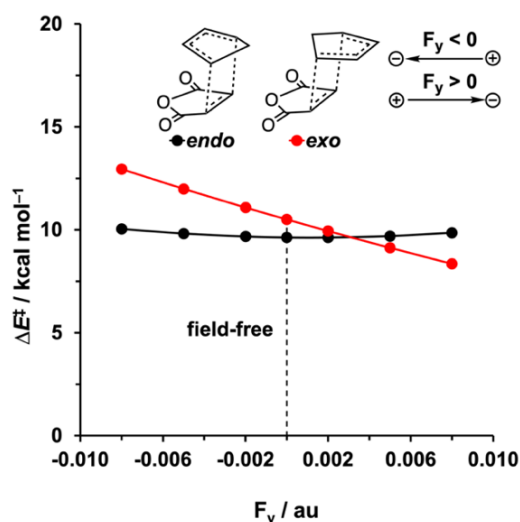


Figure 6.5 Plots of the activation energy ΔE^\ddagger (in kcal mol⁻¹) of the *endo* and *exo* Diels-Alder reactions between **Cp** and **MA** versus the strength of the F_y (in au), computed at BP86/TZ2P.

To reveal why F_y influences the *exo* activation barrier, and thus, induces a switch in the *endo/exo* selectivity, we again turn to the ASM. The activation barrier of the *endo* pathway remains unaltered upon applying F_y because the ΔE_{strain} and ΔE_{int} are nearly unaffected by this field (**Figure 6.6a**). Along the *exo* pathway, the ΔE_{int} is increasingly more stabilizing and lowers the activation barrier as F_y increases from -0.008 to 0.008 au (**Figure 6.6c**). Our quantitative EDA results reveal the stabilization of ΔE_{int} for the *exo* pathway, along this series, can be attributed to both a more stabilizing ΔE_{oi} and ΔV_{elstat} (**Figure 6.6d**). In the next section, we will discuss why the different EDA terms along the *endo* and *exo* pathway are affected in a different manner, which ultimately explains the switch in *endo/exo* selectivity.

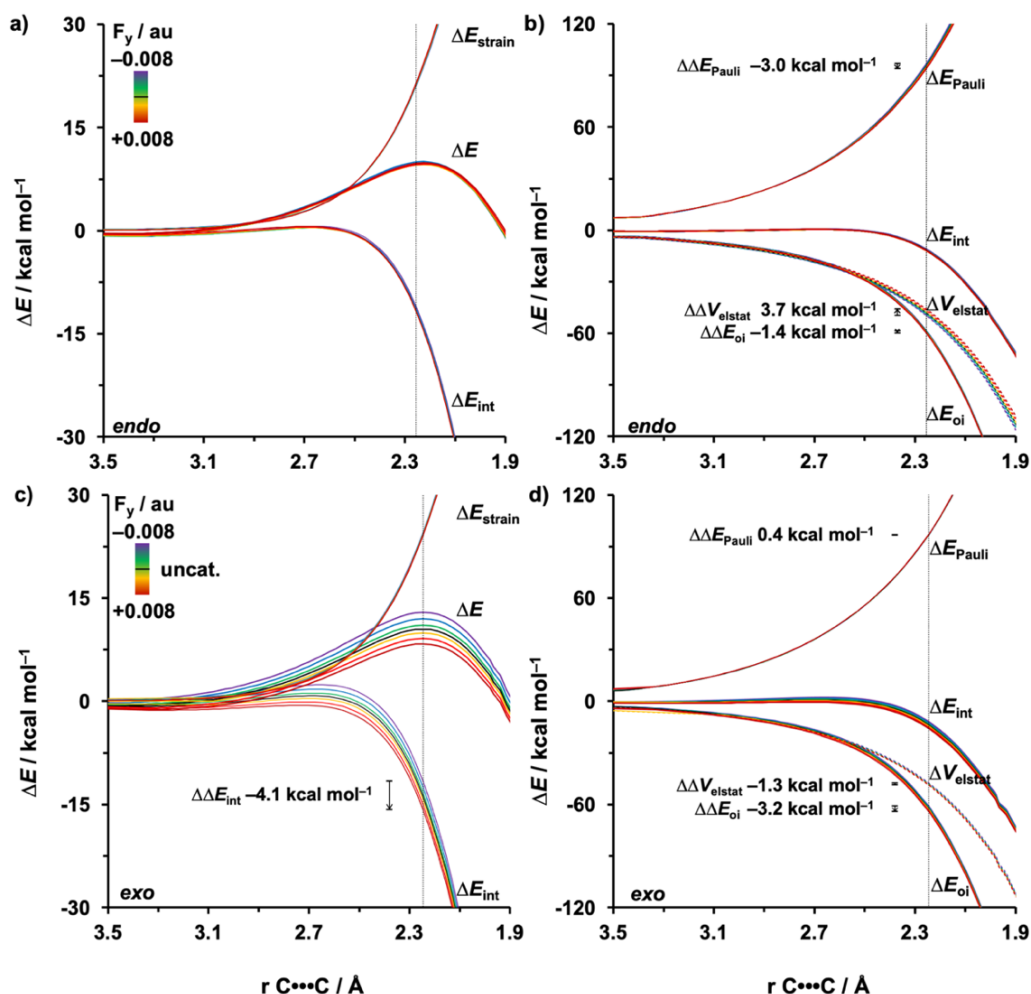


Figure 6.6 a, c) Activation strain and b, d) energy decomposition analyses of the *endo* and *exo* Diels-Alder reactions between **C_p** and **MA** in F_y ranging from -0.008 to 0.008 au, projected onto the length of newly forming $C\cdots C$ bonds, computed at BP86/TZ2P.

First, we discuss ΔE_{oi} , which is the major contributor to the stabilization of ΔE_{int} for the *exo* pathway going from $F_y = -0.008$ to $F_y = 0.008$ au. To this end, we performed a KS-MO analysis and identified that the NED interactions between the previously discussed $HOMO_{C_p}$ and $LUMO_{MA}$ are much more stabilizing than the inverse electron demand (IED) interaction $HOMO_{MA}$ and $LUMO_{C_p}$. The direction of the NED charge transfer with respect to the F_y determines if the electric field affects this interaction, and hence, catalyzes or inhibits the Diels-Alder reaction (**Figure 6.7a**). For the *endo* pathway, both a positive and negative F_y have little effect on the electron donation capability of $HOMO_{C_p}$ into $LUMO_{MA}$ as F_y is nearly perpendicular (80°) to the direction of NED charge transfer between reactants (**Figure 6.7a**). As a result, the ΔE_{oi} , along the *endo* pathway, remains nearly unaffected upon applying an electric field in the y direction (**Figure 6.7b**). In contrast, the charge transfer, and thus ΔE_{oi} , along the *exo* pathway does become diminished

(negative F_y) or enhanced (positive F_y) upon application of an electric field (**Figure 6.7b**). The charge transfer accompanying the *exo* pathway is aligned more parallel to F_y (65°) (**Figure 6.7a**), and therefore, the electron donation from the HOMO_{Cp} to the LUMO_{MA} is increased from 0.41 to $0.44 e^-$ upon varying F_y from -0.008 to 0.008 au (**Figure 6.7b**). This amplified charge transfer more effectively stabilizes the bonding MO and leads to a larger $\Delta\varepsilon_{\text{NED}}$ (i.e., energy gap between the HOMO_{Cp} and bonding MO; see **Appendix 6.8**), and ultimately, a more favorable ΔE_{oi} along the *exo* pathway.

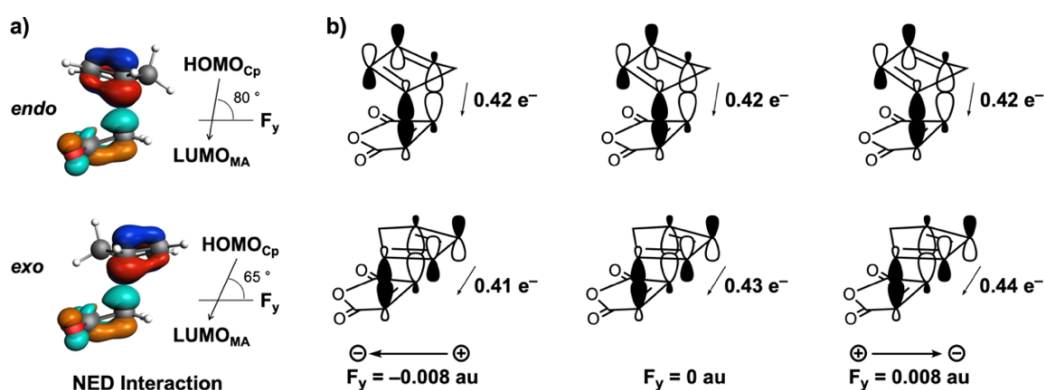


Figure 6.7 a) Computed HOMO_{Cp} and LUMO_{MA} (isovalue = $0.03 \text{ Bohr}^{-3/2}$) participating in the NED interaction for the *endo* and *exo* field-free Diels-Alder reaction between **Cp** and **MA**; and b) schematic representation of the charge transfer in the NED interaction of the reaction under F_y at -0.008 au (left), 0 au (middle), and 0.008 au (right), computed at the transition-state structures at BP86/TZ2P.

Next, we analyzed ΔV_{elstat} , which becomes increasingly less stabilizing for the *endo*, but more stabilizing for the *exo*, pathway on going from a negative to positive F_y . The MEPs of the individual reactants in the geometries they obtain in the *endo* (**Figure 6.8a**) and *exo* (**Figure 6.8b**) transition states were generated for $F_y = -0.008$ au (left), $F_y = 0$ au (middle), and $F_y = 0.008$ au (right). From these MEPs, together with the computed dipole moment in the y direction (μ_y), it becomes clear that a positive F_y tends to shift the charge density toward the left ($-y$ direction), whereas a negative F_y polarizes the charge density toward the right ($+y$ direction). Thus, for the *endo* pathway (**Figure 6.8a**), as F_y varies from 0 to 0.008 au, the dipole moments of the reactants become more positive (**Cp**: $\mu_y = 1.8$ D; **MA**: $\mu_z = 5.1$ D). The larger intramolecular charge separation leads to an enhanced electrostatic repulsion between the reactants, as both reactants have a more electron-deficient area in the reactive center. A negative F_y , on the other hand, induces an electrostatic attraction between the reactants, because the dipole moments of the reactants become smaller (**Cp**: $\mu_y = -0.9$ D; **MA**: $\mu_z = 3.1$ D), resulting in an electron-deficient (on **MA**) and

-accumulated (on **Cp**) area in the reactive region. For the *exo* pathway (**Figure 6.8b**), however, the opposite behavior is observed. In this case, a positive F_y stabilizes the electrostatic attraction between the reactants, whereas a negative F_y , in turn, suppresses this interaction.

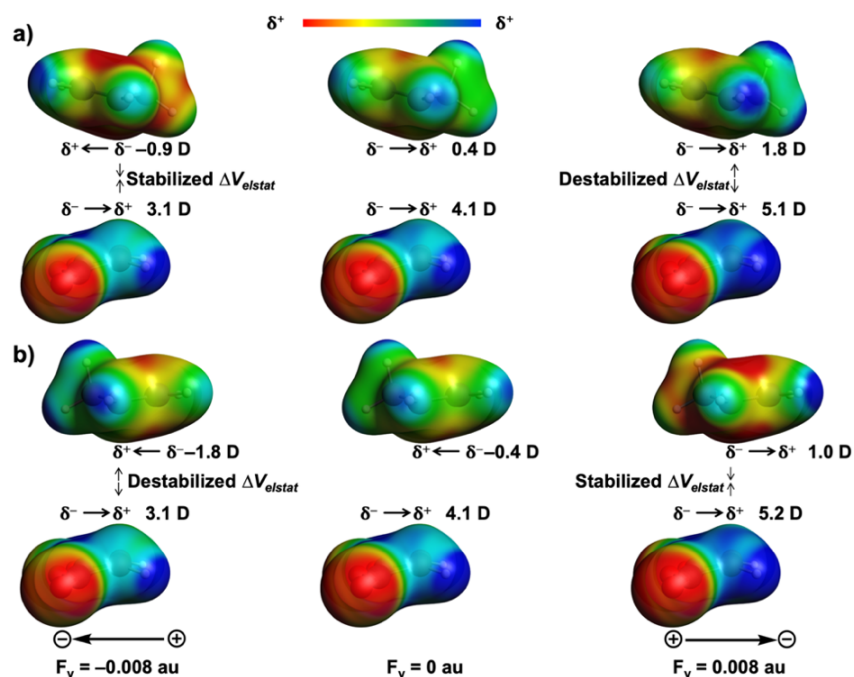


Figure 6.8 Molecular electrostatic potential maps (at 0.01 Bohr^{-3}) from -0.03 (red) to 0.1 (blue) Hartree e^{-1} with dipole moments (μ_y , D) of the isolated reactants of a) *endo* and b) *exo* Diels-Alder reactions between **Cp** and **MA** in the F_y at -0.008 au, 0 au, and 0.008 au, computed at the transition-state structures at BP86/TZ2P.

The less stabilizing ΔV_{elstat} of the *endo* Diels-Alder reaction under a positive F_y , on the other hand, is compensated by a less destabilizing ΔE_{Pauli} , as the F_y changes the shape of the MOs that participate in the two-center-four-electron orbital interaction, reducing the corresponding orbital overlap (see **Appendix 6.9**).^[25] The total interaction energy, ΔE_{int} , along the *endo* pathway, therefore, remains nearly invariant under application of a field F_y . For the *exo* pathway, on the contrary, the progressively more stabilizing ΔV_{elstat} and ΔE_{oi} lead to a more favorable ΔE_{int} of this reaction under a positive F_y , which, in turn, lowers the activation barrier height of the *exo* pathway.

6.3.4 Oriented External Electric Field in the x Direction

An oriented external electric field in the x direction (F_x) changes the Diels-Alder reaction from a concerted synchronous to a concerted slightly asynchronous reaction mode (*endo*: $\Delta r^{\text{TS}}_{\text{C}\cdots\text{C}} = 0.07 \text{ \AA}$ and *exo*: $\Delta r^{\text{TS}}_{\text{C}\cdots\text{C}} = 0.09 \text{ \AA}$, in which $\Delta r^{\text{TS}}_{\text{C}\cdots\text{C}}$ is the difference between the newly forming $\text{C}\cdots\text{C}$

bonds in the TS; **Appendix 6.3**). This electric field, however, does not affect the reactivity or *endo/exo* selectivity of the DA reaction studied herein (**Appendix 6.1**),^[7d, 8b] because it is unable to either promote the charge transfer or induce a change in electrostatic interaction between the reactants, because the reactants do not have a dipole moment along the *x* axis. Shaik and co-workers did find that an F_x induces an enantioselectivity in DA reactions between **Cp** and various asymmetric substituted ethenes such as haloethene or cyanoethene, by suppressing the formation of one of the enantiomers, which becomes highly destabilized along the pathway.^[7e]

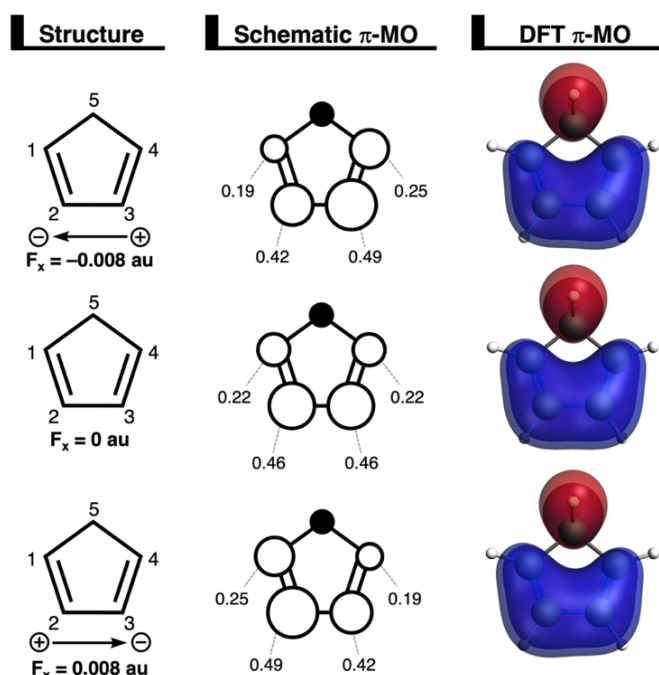


Figure 6.9 Key occupied π -MO (isovalue=0.03 Bohr^{-3/2}) computed at the equilibrium geometries of **Cp** in the F_x at -0.008 au , 0 au , and 0.008 au , in which the MO coefficients of the carbon $2p_\pi$ atomic orbitals, contributing to the occupied orbitals, are shown in the schematic π -MO.

Despite the fact that F_x does not affect the reactivity or selectivity of the DA reaction, it is of interest to understand how this electric field alters the reaction mode (i.e., synchronicity) of this reaction. In our recent study, we established that the driving force behind the asynchronicity of Diels-Alder reactions is the asymmetry in the occupied orbitals of the reactants and the accompanied relief of destabilizing Pauli repulsion.^[26] This asymmetry introduces a bias toward the formation of one C•••C bond later than the other, hence making the reaction asynchronous. Unsurprisingly, we also found this exact behavior in the DA reactions studied herein (**Figure 6.9**). In the absence of an electric field, the carbon $2p_\pi$ atomic orbitals (AOs) constructing the HOMO-1 of **Cp**, in which $2p_\pi$ AOs on the reacting C=C double bonds and the $\sigma_{\text{C-H}}$ (pseudo- π) on the

methylene bridge are out-of-phase, are distributed symmetrically ($C1_{2p\pi}$ and $C4_{2p\pi} = 0.22$; $C2_{2p\pi}$ and $C3_{2p\pi} = 0.46$). Applying an F_x introduces an asymmetry in the HOMO-1_{Cp}, by polarizing HOMO-1_{Cp} toward the positive side of the electric field. This effect of an external electric field on the spatial distribution of a molecular orbital has also been shown experimentally by using various laser-spectroscopy techniques.^[25] As a result, **Cp** experiences, during the course of the Diels-Alder reaction, more Pauli repulsion with the incoming **MA** at either C1 and C2 (positive F_x) or C3 and C4 (negative F_x). To relieve this larger Pauli repulsion, the newly forming bond between **Cp** and **MA** at C1 (positive F_x) or C4 (negative F_x) remains longer than the other new bond, making the DA reaction in an electric field in the x direction asynchronous.

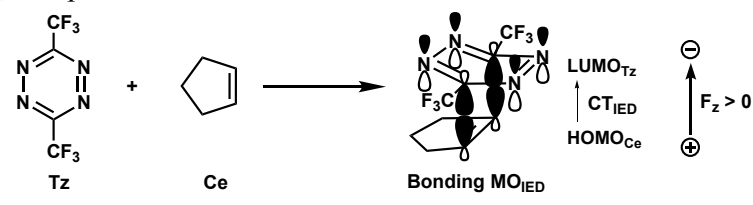
6.3.5 Inverse Electron Demand Diels-Alder Reactions

In the final section, we investigate the effect of an OEEF in the z direction on an inverse electron demand Diels-Alder (IED-DA) reaction.^[27] The reactivity of this class of DA reactions is controlled by the IED interaction, that is, the interaction between the LUMO of diene and HOMO of dienophile.^[27] On the basis of the insight that emerged from the study of the normal electron demand DA reaction above, we expect that the F_z will have a completely opposite effect on the reactivity for the IED-DA reaction. In other words, a positive F_z will destabilize the activation barrier by suppressing the IED interaction, and a negative F_z will now enhance the IED interaction, and therefore, lower the activation barrier.

To this end, we chose the typical IED-DA reaction between an electron-deficient diene, 3,6-bistrifluoromethyltetrazine (**Tz**), and cyclopentene (**Ce**) as our model (**Table 6.2**).^[16, 27a, 28] For the first time, we show that the IED-DA reaction between **Tz** and **Ce** is catalyzed by a negative F_z and inhibited by a positive F_z . As the F_z goes from -0.008 to 0.008 au, the ΔE^\ddagger increases from -1.8 to 15.4 kcal mol⁻¹ (**Table 6.2**). Our ASM results reveal that the increase in activation barrier is caused predominantly by the increasingly less stabilizing ΔE_{int} ($\Delta\Delta E_{\text{int}} = 10.6$ kcal mol⁻¹), followed by a more destabilizing ΔE_{strain} ($\Delta\Delta E_{\text{strain}} = 6.6$ kcal mol⁻¹). Next, we performed an energy decomposition analysis to pinpoint the origin of the changing ΔE_{int} . We found that the positive F_z destabilizes the ΔV_{elstat} and ΔE_{oi} , and hence, leads to a less favorable ΔE_{int} . The less stabilizing ΔV_{elstat} under a more positive F_z arises from a smaller charge density difference between reactants in the reactive center (see **Appendix 6.10** for MEPs). The less favorable ΔE_{oi} term under the positive F_z , as expected, results from a weakening of the IED interaction: the positive F_z suppresses

the charge transfer within the IED interaction (CT_{IED}), namely, the electron donation from $HOMO_{Ce}$ to $LUMO_{Tz}$ (**Table 6.2**), and therefore, destabilizes the ΔE_{oi} term. This case, again, confirms the critical role of both the electrostatic and orbital interactions in determining the effect of electric fields on the reactivity of DA reactions.

Table 6.2 The Diels-Alder reaction of 3,6-bis(trifluoromethyl)tetrazine (**Tz**) and cyclopentene (**Ce**) with the bonding MO of the IED interaction; and the ASM and EDA results for this reaction under the F_z at -0.008 au, 0 au, and 0.008 au, computed at the transition state structures at BP86/TZ2P.



F_z au	ΔE^\ddagger	ΔE_{strain}	ΔE_{int}	ΔE_{Pauli}	ΔV_{elstat}	ΔE_{oi}	CT_{IED} e^-
-0.008	-1.8	13.6	-15.4	97.5	-55.3	-57.6	0.46
0	8.1	17.5	-9.4	93.8	-50.6	-52.6	0.39
0.008	15.4	20.2	-4.8	91.0	-46.9	-48.9	0.34
$\Delta\Delta E$	17.2	6.6	10.6	-6.5	8.4	8.7	

6.4 Conclusions

A judiciously oriented external electric field can modulate the reactivity as well as *endo/exo* selectivity of the Diels-Alder reaction between cyclopentadiene (**Cp**) and maleic anhydride (**MA**). A positive electric field along the forming bonds ($F_z > 0$: positive end at **MA**, negative end at **Cp**) accelerates this reaction, whereas one oriented perpendicular to the plane of the forming bonds ($F_y > 0$: positive end at the double bond of **MA**, negative end at the anhydride group of **MA**) makes the field-free *endo*-selective Diels-Alder reaction *exo*-selective. These findings emerge from our quantum chemical activation strain and Kohn-Sham molecular orbital analyses based on density functional theory calculations.

The rate enhancement provoked by F_z is caused by both enhanced electrostatic and orbital interactions between the reactants. The former originates from an increased charge density difference between the reactants in the reactive region directly induced by the electric field. The positive F_z also enhances the orbital interactions by promoting the electron transfer within the normal electron demand donor-acceptor interaction between the $HOMO_{Cp}$ and $LUMO_{MA}$. In addition, for the *exo* pathway, a positive F_y can strengthen the orbital interactions by promoting

charge transfer from HOMO_{Cp} to LUMO_{MA}. The *endo* pathway, on the other hand, remains nearly unaffected, owing to a mismatch between the orientation of the reactants and the electric field. As a result, the *endo*-selective field-free Diels-Alder reaction becomes an *exo*-selective Diels-Alder reaction under an adequately positive F_y .

Interestingly, we have established that an F_z has an opposite effect on inverse electron demand Diels-Alder reactions, in which the most dominant orbital interaction occurs between the LUMO of the diene and HOMO of the dienophile. This orbital interaction, in contrast with the normal electron demand Diels-Alder reaction between **Cp** and **MA**, becomes strengthened by a negative F_z . The results obtained herein display, for the first time, the physical factors dictating the reactivity and selectivity of Diels-Alder reactions under an external oriented electric field within the framework of Kohn-Sham molecular orbital (KS-MO) theory, which can be applied for the understanding and design of electrostatically catalyzed reactions.

6.5 References

- [1] a) S. Shaik, D. Mandal, R. Ramanan, *Nat. Chem.* **2016**, *8*, 1091–1098; b) S. Shaik, R. Ramanan, D. Danovich, D. Mandal, *Chem. Soc. Rev.* **2018**, *47*, 5125–5145; c) S. Ciampi, N. Darwish, H. M. Aitken, I. Díez-Pérez, M. L. Coote, *Chem. Soc. Rev.* **2018**, *47*, 5146–5164; d) S. Shaik, D. Danovich, J. Joy, Z. Wang, T. Stuyver, *J. Am. Chem. Soc.* **2020**, *142*, 12551–12562.
- [2] a) A. Warshel, P. K. Sharma, M. Kato, Y. Xiang, H. Liu, M. H. M. Olsson, *Chem. Rev.* **2006**, *106*, 3210–3235; b) A. R. Finkelmann, M. T. Stiebritz, M. Reiher, *Chem. Commun.* **2013**, *49*, 8099–8101; c) S. D. Fried, S. Bagchi, S. G. Boxer, *Science* **2014**, *346*, 1510–1514; d) S. D. Fried, S. G. Boxer, *Annu. Rev. Biochem.* **2017**, *86*, 387–415; e) J.-G. Zhou, S. Yang, Z.-Y. Deng, *J. Phys. Chem. B* **2017**, *121*, 11053–11061.
- [3] a) C. F. Gorin, E. S. Beh, Q. M. Bui, G. R. Dick, M. W. Kanan, *J. Am. Chem. Soc.* **2013**, *135*, 11257–11265; b) C. F. Gorin, E. S. Beh, M. W. Kanan, *J. Am. Chem. Soc.* **2012**, *134*, 186–189.
- [4] a) A. C. Aragonès, N. L. Haworth, N. Darwish, S. Ciampi, N. J. Bloomfield, G. G. Wallace, I. Diez-Perez, M. L. Coote, *Nature* **2016**, *531*, 88–91; b) L. Zhang, E. Laborda, N. Darwish,

- B. B. Noble, J. Tyrell, S. Pluczyk, A. P. L. Brun, G. G. Wallace, J. Gonzalez, M. L. Coote, S. Ciampi, *J. Am. Chem. Soc.* **2018**, *140*, 766–774; c) G. Reece, C. Lotze, D. Sysoiev, T. Huhn, K. J. Franke, *J. Phys. Condens. Matter* **2017**, *29*, 294001; d) R. L. Starr, T. Fu, E. A. Doud, I. Stone, X. Roy, L. Venkataraman, *J. Am. Chem. Soc.* **2020**, *142*, 7128–7133.
- [5] a) G. Gryn'ova, D. L. Marshall, S. J. Blanksby, M. L. Coote, *Nat. Chem.* **2013**, *5*, 474–481; b) G. Gryn'ova, M. L. Coote, *J. Am. Chem. Soc.* **2013**, *135*, 15392–15403; c) M. Klinska, L. M. Smith, G. Gryn'ova, M. G. Banwell, M. L. Coote, *Chem. Sci.* **2015**, *6*, 5623–5627; d) G. Gryn'ova, L. M. Smith, M. L. Coote, *Phys. Chem. Chem. Phys.* **2017**, *19*, 22678–22683; e) H. M. Aitken, M. L. Coote, *Phys. Chem. Chem. Phys.* **2018**, *20*, 10671–10676.
- [6] a) C. Geng, J. Li, T. Weiske, M. Schlangen, S. Shaik, H. Schwarz, *J. Am. Chem. Soc.* **2017**, *139*, 1684–1689; b) L. Yue, J. Li, S. Zhou, X. Sun, M. Schlangen, S. Shaik, H. Schwarz, *Angew. Chem. Int. Ed.* **2017**, *56*, 10219–10223; *Angew. Chem.* **2017**, *129*, 10353–10357; c) C. Geng, J. Li, M. Schlangen, S. Shaik, X. Sun, N. Wang, T. Weiske, L. Yue, S. Zhou, H. Schwarz, *Dalton Trans.* **2018**, *47*, 15271–15277; d) C. Q. He, C. C. Lam, P. Yu, Z. Song, M. Chen, Y.-H. Lam, S. Chen, K. N. Houk, *J. Org. Chem.* **2020**, *85*, 2618–2625.
- [7] a) S. Shaik, S. P. de Visser, D. Kumar, *J. Am. Chem. Soc.* **2004**, *126*, 11746–11749; b) H. Hirao, H. Chen, M. A. Carvajal, Y. Wang, S. Shaik, *J. Am. Chem. Soc.* **2008**, *130*, 3319–3327; c) T. Stuyver, R. Ramnan, D. Mallick, S. Shaik, *Angew. Chem. Int. Ed.* **2020**, *59*, 7915–7920; *Angew. Chem.* **2020**, *132*, 7989–7994; d) R. Meir, H. Chen, W. Lai, S. Shaik, *ChemPhysChem* **2010**, *11*, 301–310 (Corrigendum: R. Meir, H. Chen, W. Lai, S. Shaik, *ChemPhysChem* **2020**, *21*, 1737–1737); e) Z. Wang, d. Danovich, R. Ramanan, S. Shaik, *J. Am. Chem. Soc.* **2018**, *140*, 13350–13359; f) R. Ramanan, D. Danovich, D. Mandal, S. Shaik, *J. Am. Chem. Soc.* **2018**, *140*, 4354–4362; g) T. Stuyver, D. Danovich, F. de Proft, S. Shaik, *J. Am. Chem. Soc.* **2019**, *141*, 9719–9730; h) C. Wang, D. Danovich, H. Chen, S. Shaik, *J. Am. Chem. Soc.* **2019**, *141*, 7122–7136; i) J. Joy, T. Stuyver, S. Shaik, *J. Am. Chem. Soc.* **2020**, *142*, 3836–3850.
- [8] X. Huang, C. Tang, J. Li, L.-C. Chen, J. Zheng, P. Zhang, J. Le, R. Li, X. Li, J. Liu, Y. Yang, J. Shi, Z. Chen, M. Bai, H.-L. Zhang, H. Xia, J. Cheng, Z.-Q. Tian, W. Hong, *Sci. Adv.* **2019**, *5*, eaaw3072.

- [9] D. Usharani, W. Lai, C. Li, H. Chen, D. Danovich, S. Shaik, *Chem. Soc. Rev.* **2014**, *43*, 4968–4988.
- [10] a) W.-J. van Zeist, F. M. Bickelhaupt, *Org. Biomol. Chem.* **2010**, *8*, 3118–3127; b) I. Fernández, F. M. Bickelhaupt, *Chem. Soc. Rev.* **2014**, *43*, 4953–4967; c) L. P. Wolters, F. M. Bickelhaupt, *WIREs Comput. Mol. Sci.* **2015**, *5*, 324–343; d) F. M. Bickelhaupt, K. N. Houk, *Angew. Chem. Int. Ed.* **2017**, *56*, 10070–10086; *Angew. Chem.* **2017**, *129*, 10204–10221; e) P. Vermeeren, S. C. C. van der Lubbe, C. Fonseca Guerra, F. M. Bickelhaupt, T. A. Hamlin, *Nat. Protoc.* **2020**, *15*, 649–667.
- [11] a) F. M. Bickelhaupt, E. J. Baerends, *Reviews in Computational Chemistry*, Eds.: K. B. Lipkowitz, D. B. Boyd, Wiley, Hoboken **2000**, pp. 1–86; b) R. van Meer, O. V. Gritsenko, E. J. Baerends, *J. Chem. Theory Comput.* **2014**, *10*, 4432; c) L. Zhao, M. von Hopffgarten, D. M. Andrada, G. Frenking, *WIREs Comput. Mol. Sci.* **2018**, *8*, e1345.
- [12] a) T. A. Hamlin, D. Svatunek, S. Yu, I. Infante, L. Visscher, F. M. Bickelhaupt, *Eur. J. Org. Chem.* **2019**, 378–386; b) S. Yu, H. M. de Bruijn, D. Svatunek, T. A. Hamlin, F. M. Bickelhaupt, *ChemistryOpen* **2018**, *7*, 995–1004; c) P. Vermeeren, F. Brinkhuis, T. A. Hamlin, F. M. Bickelhaupt, *Chem. Asian J.* **2020**, *15*, 1167–1174; d) P. Vermeeren, T. A. Hamlin, I. Fernández, F. M. Bickelhaupt, *Angew. Chem. Int. Ed.* **2020**, *59*, 6201–6206; *Angew. Chem.* **2020**, *132*, 6260–6265; e) S. Yu, P. Vermeeren, K. van Dommelen, F. M. Bickelhaupt, T. A. Hamlin, *Chem. Eur. J.* **2020**, *26*, 11529–11539.
- [13] a) G. te Velde, F. M. Bickelhaupt, E. J. Baerends, C. Fonseca Guerra, S. J. A. van Gisbergen, J. G. Snijders, T. Ziegler, *J. Comput. Chem.* **2001**, *22*, 931–967; b) C. Fonseca Guerra, J. G. Snijders, G. te Velde, E. J. Baerends, *Theor. Chem. Acc.* **1998**, *99*, 391–403; c) ADF, SCM Theoretical Chemistry; Vrije Universiteit, Amsterdam, The Netherlands, **2017**, <http://www.scm.com>.
- [14] a) A. D. Becke, *Phys. Rev. A* **1988**, *38*, 3098–3100; b) J. P. Perdew, *Phys. Rev. B* **1986**, *33*, 8822–8824.
- [15] E. van Lenthe, E. J. Baerends, *J. Comput. Chem.* **2003**, *24*, 1142–1156.
- [16] A. Talbot, D. Devarajan, S. J. Gustafson, I. Fernández, F. M. Bickelhaupt, D. H. Ess, *J. Org. Chem.* **2015**, *80*, 548–558.

- [17] a) A. Klamt, G. Schüürmann, *J. Chem. Soc. Perkin Trans. 2* **1993**, 799; b) A. Klamt, *J. Phys. Chem.* **1995**, *99*, 2224; c) A. Klamt, V. Jonas, *J. Chem. Phys.* **1996**, *105*, 9972; d) C. C. Pye, T. Ziegler, *Theor. Chem. Acc.* **1999**, *101*, 396.
- [18] a) A. D. Becke, *J. Chem. Phys.* **1993**, *98*, 5648–5652; b) C. Lee, W. Yang, R. G. Parr, *Phys. Rev. B* **1988**, *37*, 785–789.
- [19] a) Y. Zhao, D. G. Truhlar, *J. Chem. Phys.* **2006**, *125*, 194101; b) Y. Zhao, D. G. Truhlar, *Theor. Chem. Acc.* **2008**, *120*, 215–241.
- [20] a) L. Deng, T. Ziegler, L. Fan, *J. Chem. Phys.* **1993**, *99*, 3823–3835; b) L. Deng, T. Ziegler, *Int. J. Quantum Chem.* **1994**, *52*, 731–765.
- [21] a) W.-J. van Zeist, C. Fonseca Guerra, F. M. Bickelhaupt, *J. Comput. Chem.* **2008**, *29*, 312–315; b) X. Sun, T. M. Soini, J. Poater, T. A. Hamlin, F. M. Bickelhaupt, *J. Comput. Chem.* **2019**, *40*, 2227–2233.
- [22] C. Y. Legault, CYLview, 1.0b; Université de Sherbrooke, Sherbrooke, QC, Canada, **2009**, <http://www.cylview.org>.
- [23] a) R. J. Clarke, *Adv. Colloid Interface Sci.* **2001**, *89–90*, 263–281; b) D. H. Murgida, P. Hildebrandt, *Acc. Chem. Res.* **2004**, *37*, 854–861; c) K.-B. Cho, H. Hirao, H. Chen, M. A. Carvajal, S. Cohen, E. Derat, W. Thiel, S. Shaik, *J. Phys. Chem. A* **2008**, *112*, 13128–13138; d) S. D. Fried, L.-P. Wang, S. G. Boxer, P. Ren, V. S. Pande, *J. Phys. Chem. B* **2013**, *117*, 16236–16248.
- [24] T. A. Albright, J. K. Burdett, M.-H. Whangbo, *Orbital Interactions in Chemistry*, 2nd ed., Wiley, Hoboken **2013**.
- [25] a) H. Akagi, T. Otobe, R. Itakura, *Sci. Adv.* **2019**, *5*, eaaw1885; b) P. M. Kraus, O. I. Tolstikhin, D. Baykusheva, A. Rupenyan, J. Schneider, C. Z. Bisgaard, T. Morishita, F. Jensen, L. B. Madsen, H. J. Wörner, *Nat. Commun.* **2015**, *6*, 7039.
- [26] P. Vermeeren, T. A. Hamlin, I. Fernández, F. M. Bickelhaupt, *Chem. Sci.* **2020**, *11*, 8105–8112.
- [27] a) F. Thalhammer, U. Wallfahrer, J. Sauer, *Tetrahedron Lett.* **1990**, *31*, 6851–6685; b) M. L. Blackman, M. Royzen, J. M. Fox, *J. Am. Chem. Soc.* **2008**, *130*, 13518–13519; c) B. L. Oliveira, Z. Guo, G. J. L. Bernardes, *Chem. Soc. Rev.* **2017**, *46*, 4895–4950; d) J. Zhang,

- V. Shukla, D. L. Boger, *J. Org. Chem.* **2019**, *84*, 9397–9445; e) J. M. J. M. Ravasco, J. A. S. Coelho, *J. Am. Chem. Soc.* **2020**, *142*, 4235–4241.
- [28] a) F. Liu, R. S. Paton, S. Kim, Y. Liang, K. N. Houk, *J. Am. Chem. Soc.* **2013**, *135*, 15642–15649; b) B. J. Levandowski, T. A. Hamlin, F. M. Bickelhaupt, K. N. Houk, *J. Org. Chem.* **2017**, *82*, 8668–8675.

6.6 Appendices

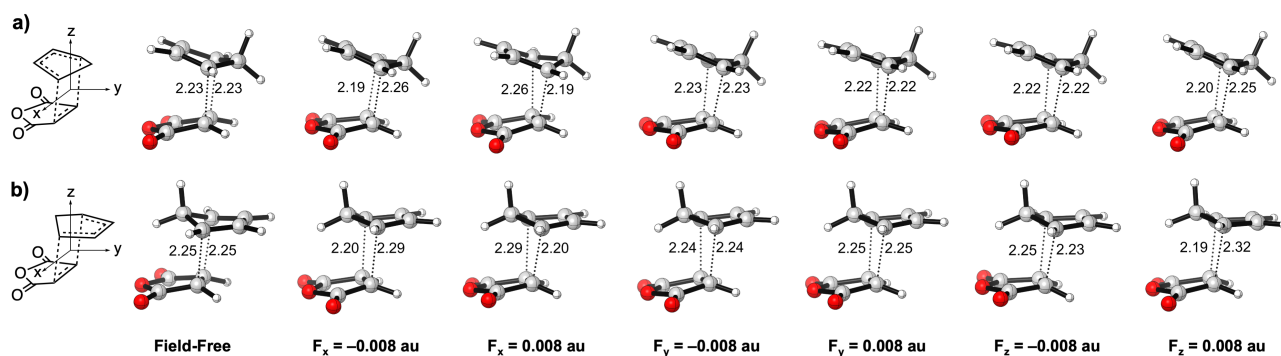
Appendix 6.1 Computed activation energies (kcal mol⁻¹)^[a] of the *endo/exo* Diels-Alder reactions between **Cp** and **MA** without electric fields ($F = 0$) and under the electric field ($F = \pm 0.008$ au).

Adduct	F / au	Spt ^[b]				Opt _{gas} ^[c]		Opt _{sol} ^[d]		
		ΔE^\ddagger	ΔH^\ddagger	$\Delta(-TS)^\ddagger$	ΔG^\ddagger	ΔE^\ddagger	ΔG^\ddagger	ΔE^\ddagger	ΔG^\ddagger	
<i>endo</i>	0	9.6	10.7	13.3	24.0	9.6	24.0	8.8	23.1	
	<i>x</i>	-0.008	9.5	8.2	16.6	24.8	9.9	24.8	8.7	23.2
		0.008	9.5	8.2	16.6	24.8	9.9	24.8	8.7	23.2
	<i>y</i>	-0.008	10.0	8.8	15.2	24.0	10.0	23.9	9.9	23.8
		0.008	9.9	9.0	14.8	23.8	9.9	23.9	8.3	22.3
	<i>z</i>	-0.008	16.3	9.5	16.7	26.3	16.2	31.1	17.5	32.6
0.008		0.7	-3.6	16.1	12.6	0.3	11.0	-5.3	8.2	
<i>exo</i>	0	10.5	11.6	13.2	24.8	10.5	24.8	10.5	24.5	
	<i>x</i>	-0.008	10.4	9.7	15.5	25.2	10.7	25.5	10.1	24.1
		0.008	10.4	9.7	15.5	25.2	10.7	25.5	10.1	24.0
	<i>y</i>	-0.008	12.9	11.1	16.8	27.9	12.9	26.8	14.4	28.2
		0.008	8.3	7.9	12.9	20.8	8.3	18.5	5.0	19.8
	<i>z</i>	-0.008	16.7	9.9	16.3	26.2	16.5	31.4	18.6	33.6
		0.008	2.2	-2.7	17.4	14.7	1.8	16.1	-3.1	10.1

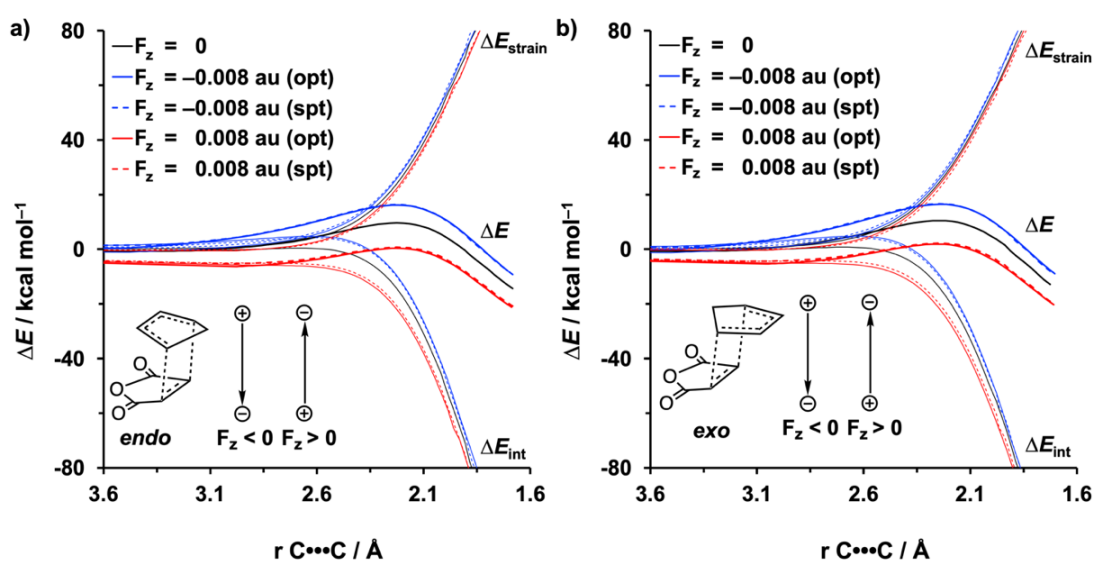
[a] Computed at BP86/TZ2P. The F_x is defined along the C=C double bond of **MA**, F_y is perpendicular to the reaction axis, i.e., perpendicular to the plane of the newly forming C-C bonds, and F_z is aligned along the reaction axis, i.e., along the axis of a newly forming C-C bond. [b] Single-point calculations using non-OEEF geometries at BP86/TZ2P. [c] Optimized in the presence of the electric field in the gas phase at BP86/TZ2P. [d] Optimized in the presence of the electric field at COSMO(DCM)-BP86/TZ2P.

Appendix 6.2 Computed activation energies (kcal mol⁻¹) of the *endo/exo* Diels-Alder reactions between **Cp** and **MA** without electric fields ($F = 0$) and under the electric field ($F = \pm 0.008$ au) at BP86/TZ2P, B3LYP/TZ2P//BP86/TZ2P, and M06-2X/TZ2P//BP86/TZ2P.

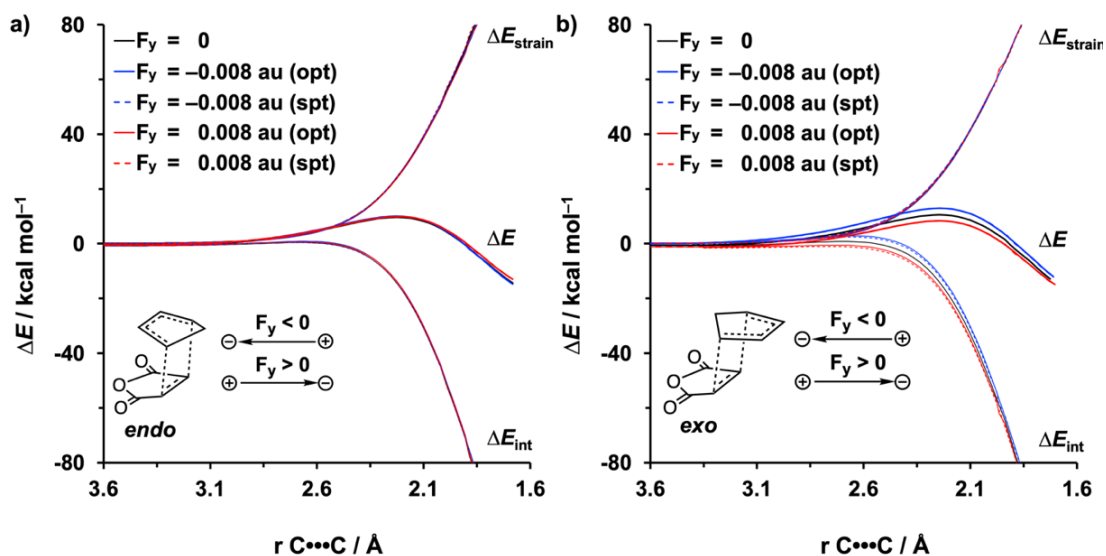
Adduct	F / au	ΔE^\ddagger / kcal mol ⁻¹			
		BP86	B3LYP	M06-2X	
<i>endo</i>	0	9.6	17.0	7.6	
	<i>x</i>	-0.008	9.5	17.3	8.0
		0.008	9.5	17.3	8.0
	<i>y</i>	-0.008	10.0	17.3	8.0
		0.008	9.9	17.1	7.9
	<i>z</i>	-0.008	16.3	23.8	14.5
0.008		0.7	7.8	-1.4	
<i>exo</i>	0	10.5	18.5	10.0	
	<i>x</i>	-0.008	10.4	18.8	10.3
		0.008	10.4	18.8	10.3
	<i>y</i>	-0.008	12.9	20.8	12.2
		0.008	8.3	16.3	8.0
	<i>z</i>	-0.008	16.7	24.8	16.3
		0.008	2.2	9.9	1.7



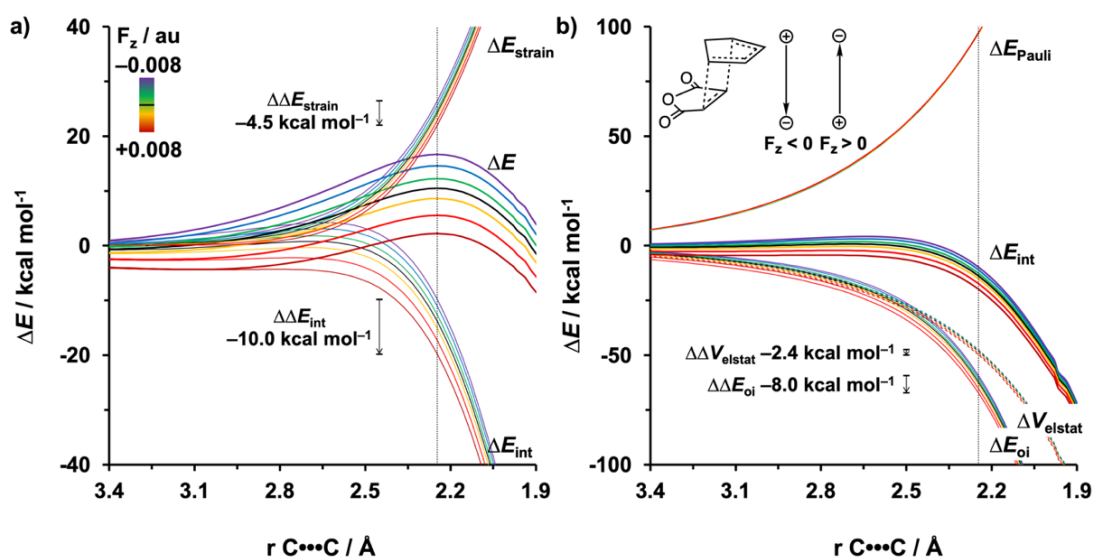
Appendix 6.3 Optimized transition state structures of the a) *endo* and b) *exo* Diels-Alder reactions between Cp and MA in the gas phase under electric fields, computed at BP86/TZ2P.



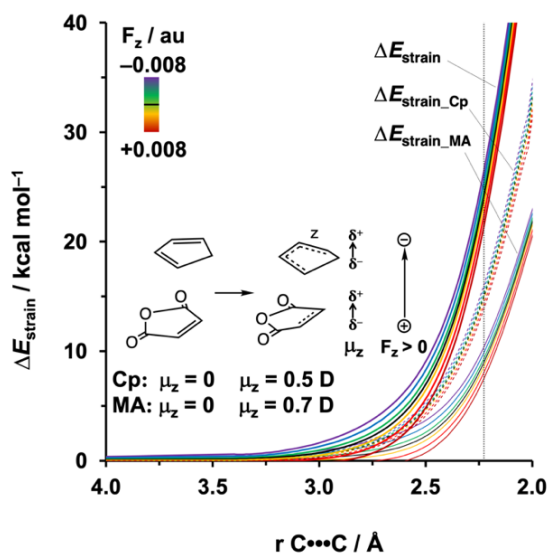
Appendix 6.4 Activation strain diagrams for the a) *endo* and b) *exo* Diels-Alder reactions between Cp and MA without electric fields and under the F_z at ± 0.008 au, where energy terms are projected on the average length of newly forming bonds. Solid lines were computed by reoptimizing the PES in the F_z ; dashed lines were obtained by single-point calculations on the PES of field free reactions.



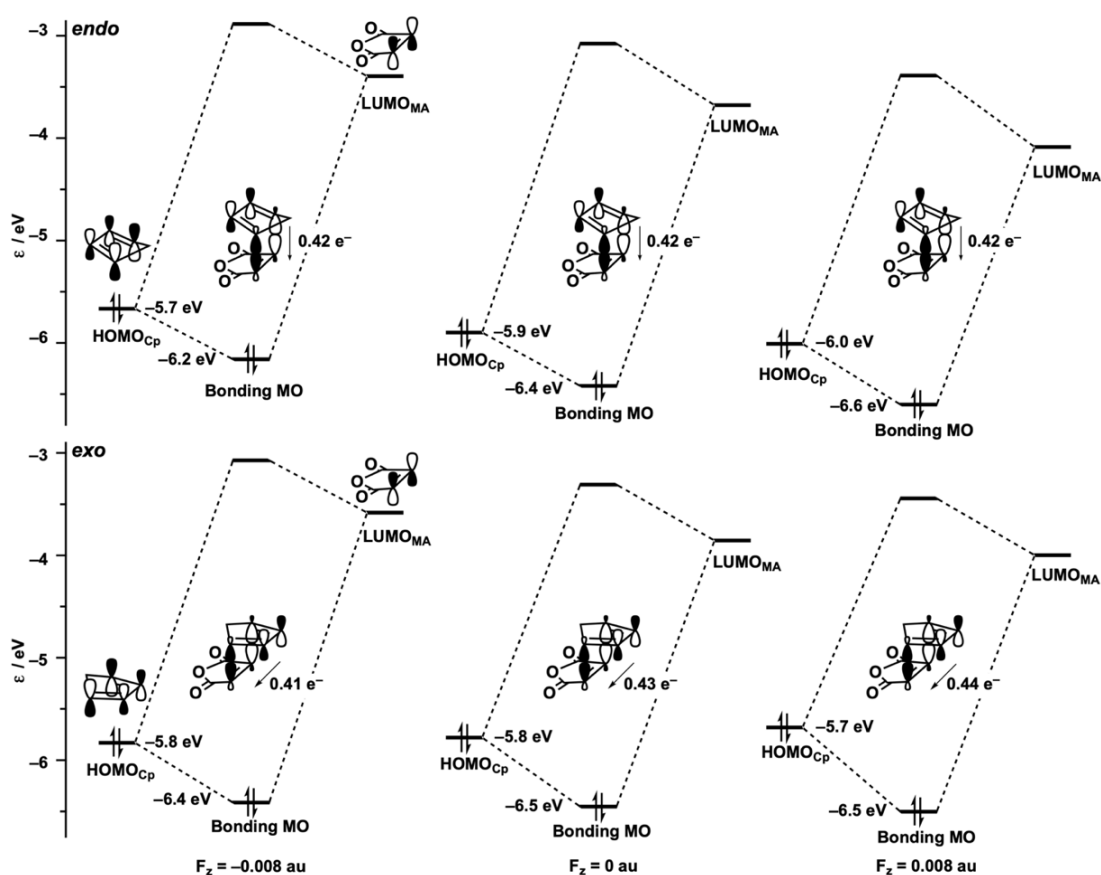
Appendix 6.5 Activation strain diagrams for the a) *endo* and b) *exo* Diels-Alder reactions between **Cp** and **MA** without electric fields and under the F_y at ± 0.008 au, where energy terms are projected on the average length of newly forming bonds. Solid lines were computed by reoptimizing the PES in the F_z ; dashed lines were obtained by single-point calculations on the PES of field free reactions.



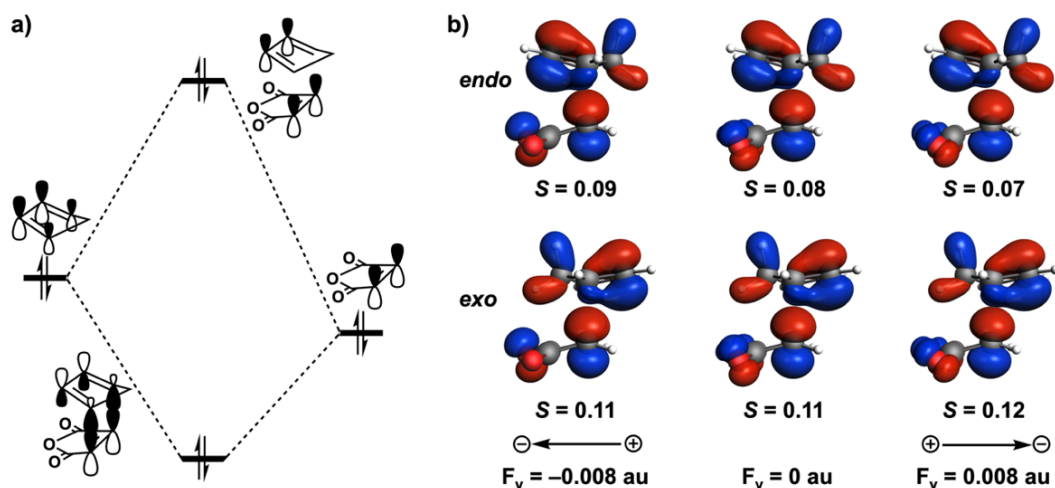
Appendix 6.6 a) Activation strain and b) energy decomposition analyses of the *exo* Diels-Alder reactions between **Cp** and **MA** under the F_z ranging from -0.008 to 0.008 au along the reaction coordinate projected onto the average length of the newly forming $C\cdots C$ bonds, computed at BP86/TZ2P. The vertical dotted line at 2.25 Å indicates the transition state.



Appendix 6.7 Decomposition of the ΔE_{strain} of the *endo* Diels-Alder reactions between **Cp** with **MA** under the F_z ranging from -0.008 to 0.008 au, projected onto the newly forming bond length. All results were computed at BP86/TZ2P.

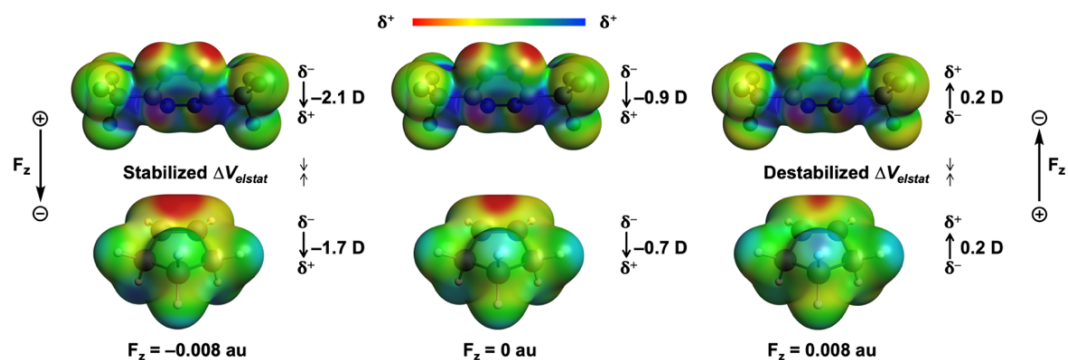


Appendix 6.8 Diagrams of the NED interactions for the *endo* (top) and *exo* (bottom) Diels-Alder reactions between **Cp** and **MA** under a F_y at -0.008 au (left), 0 au (middle), and 0.008 au (right), computed at the transition states structures at BP86/TZ2P.



Appendix 6.9 a) Schematic diagram for the HOMO-1_{Cp}|HOMO-2_{MA} interaction of the Diels-Alder reaction between **Cp** and **MA** (*endo* pathway is chosen as the example); b) the HOMO-1_{Cp}|HOMO-2_{MA} overlaps and computed MOs of isolated reactants (isovalue = 0.06 Bohr^{-3/2}) for the *endo* and *exo* reactions under the F_y at -0.008 au, 0 au, and 0.008 au, where F_y is perpendicular to the reaction axis, *i.e.*, perpendicular to the plane of the newly forming C-C bonds, computed at the transition state structures at BP86/TZ2P.

The key two-center four-electron interaction have been quantified for the *endo* and *exo* Diels-Alder reactions between **Cp** and **MA** under a F_y of -0.008 au, 0 au, and 0.008 au. In all cases, the most profound interaction occurs between the HOMO-1_{Cp} and HOMO-2_{MA}, which is predominantly located on the C=C double bonds of **Cp** and the C=C double bond of the five-membered ring of **MA**, respectively (**Appendix 6.9a**). Since the shape of a MO can be modified by an external electric field, the HOMO-1_{Cp}, an orbital delocalized along the y -direction, is polarized by a positive F_y towards the C^{sp2}-C^{sp2} single bond for the *endo* pathway (**Appendix 6.9b**). Consequently, the orbital overlap of the HOMO-1_{Cp}|HOMO-2_{MA} in the reactive region, along the *endo* pathway, decreases from $S = 0.09$ to $S = 0.07$. On the other hand, along the *exo* pathway, a positive field polarized the HOMO-1_{Cp} towards the methylene bridge, increasing the overlap from $S = 0.11$ to $S = 0.12$, when F_y goes from -0.008 to 0.008 au. Note that the spatial distribution of the HOMO-2_{MA} remains nearly unchanged upon applying an electric field and for that reason has no effect on the observed change in orbital overlap. As a result, the ΔE_{Pauli} term for the *endo* pathway is getting less destabilizing while that for the *exo* pathway is becoming slightly more destabilizing going from a negative to positive F_y .



Appendix 6.10 Molecular electrostatic potential maps (at 0.01 Bohr^{-3}) from -0.03 (red) to 0.1 (blue) Hartree e^{-1} and the dipole moments (μ_z , D) of isolated reactants for the Diels-Alder reactions between **Tz** and **Ce** under the F_z at -0.008 , 0 , and 0.008 au, where F_z is aligned along the reaction axis, i.e., along the axis of a newly forming C–C bond, computed at transition states at BP86/TZ2P.

Chapter 7 How Brønsted Acids Catalyze Aza-Diels-Alder Reactions

This chapter previously appeared as

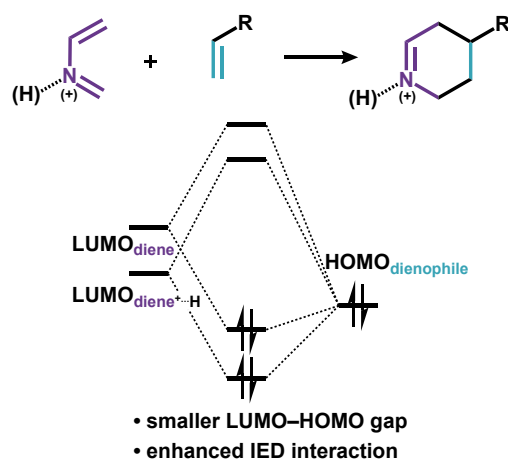
ChemistryOpen **2021**, *10*, 784–789.

Song Yu, F. Matthias Bickelhaupt, Trevor A. Hamlin

In this chapter, Brønsted acid-catalyzed inverse-electron demand (IED) aza-Diels-Alder reactions of 2-aza-dienes and ethylene were studied using quantum chemical calculations. The computed activation energy systematically decreases as the basic sites of the diene progressively become protonated. Our activation strain and Kohn-Sham molecular orbital analyses traced the origin of this enhanced reactivity to i) “Pauli-lowering catalysis” for *mono*-protonated 2-aza-dienes due to the induction of an asynchronous, but still concerted, reaction pathway that reduces the Pauli repulsion between the reactants; and ii) “LUMO-lowering catalysis” for *multi*-protonated 2-aza-dienes due to their highly stabilized LUMO(s) and more concerted synchronous reaction path that facilitates more efficient orbital overlaps in IED interactions. In all, we illustrated how the novel concept of “Pauli-lowering catalysis” can be overruled by the traditional concept of “LUMO-lowering catalysis” when the degree of LUMO stabilization is extreme as in the case of multi-protonated 2-aza-dienes.

7.1 Introduction

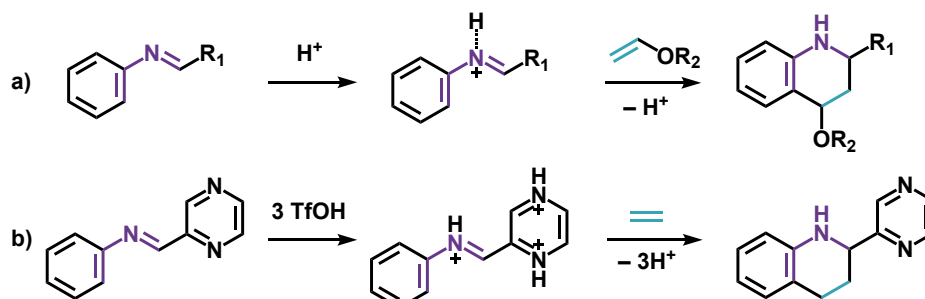
Aza-Diels-Alder reactions are among the most efficient routes to access heterocycles.^[1] The aza-Diels-Alder reactions of 2-aza-dienes, for instance, furnishes piperidine derivatives that are the common motifs in natural compounds and pharmaceuticals.^[2] It is generally understood that the reactivity of 2-aza-dienes in Diels-Alder reactions is governed by the donor–acceptor interactions between the $LUMO_{\text{diene}}$ and the $HOMO_{\text{dienophile}}$, i.e., the inverse electron demand (IED) interactions (**Scheme 7.1**).^[3] These reactions, therefore, are commonly catalyzed by Lewis or Brønsted acids,^[4] which upon complexation of the acid to the 2-aza-diene induces a stabilization of the $LUMO_{\text{diene}}$. This “LUMO-lowering catalysis” concept^[5] is thought to lead to a much smaller and more favorable $LUMO_{\text{diene}}-HOMO_{\text{dienophile}}$ gap that leads to strongly stabilizing IED orbital interactions (**Scheme 7.1**).^[6]



Scheme 7.1 Acid-catalyzed aza-Diels-Alder reactions of 2-aza-dienes, with schematic diagram of the critical donor–acceptor orbital interactions.

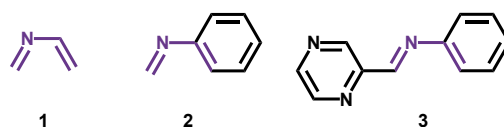
Besides the parent 2-aza-dienes shown in **Scheme 7.1**,^[7] N-aryl imines also commonly feature in the acid-catalyzed aza-Diels-Alder reactions.^[8] The Povarov reaction, a Diels-Alder cycloaddition of N-aryl imines catalyzed by the acids (**Scheme 7.2a**)^[9] provides convenient access to densely functionalized quinoline derivatives,^[10] which are key blocks in various bioactive compounds.^[11] Typically, this transformation is limited to electron-rich alkenes, such as ethyl vinyl ether and ethyl vinyl sulfide.^[8c] Recently, Klumpp and coworkers disclosed the Brønsted superacid, CF_3SO_3H , catalyzed aza-Diels-Alder between the N-aryl imines containing multiple basic sites and ethylene.^[12] The *multi*-protonated N-aryl imines “superelectrophiles”^[13] were expected to

exhibit highly stabilized LUMOs that could be the origin of the enhanced Diels-Alder reactivity (**Scheme 7.2b**).^[12–13]



Scheme 7.2 a) Acid-catalyzed aza-Diels-Alder reactions of N-aryl imines (Povarov reactions); b) the superacid-catalyzed Povarov reaction.

As described above, the acid-catalyzed aza-Diels-Alder reaction of various 2-aza-dienes are employed in organic synthesis, but the “LUMO-lowering catalysis” mechanism^[5] has solely been attributed to the enhanced donor–acceptor interactions caused by the stabilized LUMOs of cationic 2-aza-dienes upon protonation.^[6, 12] Our previous studies of Lewis acid-catalyzed Diels-Alder reactions revealed that Lewis acids activate dienophiles by reducing the Pauli repulsion between the reactants and not due to the previously expected enhanced donor–acceptor interactions.^[14, 15] In the present study, we aimed to uncover the actual mechanism of Brønsted acid-catalyzed inverse electron demand aza-Diels-Alder reactions of 2-aza-dienes using density functional theory (DFT) calculations at BP86/TZ2P.^[14, 16] Three representative 2-aza-dienes were investigated (**Scheme 7.3**): the parent 2-aza-diene **1**,^[7] the archetypal N-aryl imine used in Povarov reactions **2**,^[8–9] and the N-aryl imine containing multiple protonation sites **3**.^[10] Ethylene was chosen as the dienophile and proton (H)^[7d–7e, 9, 12] was selected as the Brønsted acid. The activation strain model (ASM) of reactivity^[17] in combination with the matching canonical energy decomposition analysis (EDA)^[18] were employed to elucidate the ultimate physical factors controlling the Diels-Alder reactivity of 2-aza-dienes.



Scheme 7.3 2-Aza-dienes studied in this study.

7.2 Results and Discussion

7.2.1 Brønsted Acid-Catalyzed Reactions

First, the catalytic effect of Brønsted acids in aza-Diels-Alder reactions were studied by comparing the reactivity of the archetypal 2-aza-dienes **1–3** and the corresponding protonated 2-aza-diene **1*–3***, which are proposed intermediates of Brønsted acid-catalyzed aza-Diels-Alder reactions.^[7d–7e, 9, 12] **Figure 7.1** shows the transition state structures and computed activation and reaction energies of the aza-Diels-Alder reactions between 2-aza-dienes (**1–3** and **1*–3***) and ethylene. It is evident that the catalyzed reactions, that is, the reactions of the protonated 2-aza-dienes (**1*–3***) go with significantly lowered activation barriers and more favorable reaction energies compared to their uncatalyzed counterparts. These computed trends in reactivity at BP86/TZ2P^[19] agree well with those calculated with an explicit dispersion correction (BP86-D3(BJ)/TZ2P//BP86/TZ2P)^[20] and M06-2X/TZ2P//BP86/TZ2P,^[21] as well as when solvent effects are included at COSMO(DCM) BP86/TZ2P//BP86/TZ2P^[22] (see **Appendix 7.1**). Moreover, inspection of the transition state geometries reveals that the aza-Diels-Alder reactions of protonated 2-aza-dienes are much more asynchronous than the original reactions: the length differences between two newly forming bonds (Δr) become more pronounced (**Figure 7.1**). The differing degree of asynchronicity and its role in Lewis acid-catalyzed Diels-Alder reactions has previously been highlighted by us.^[14]

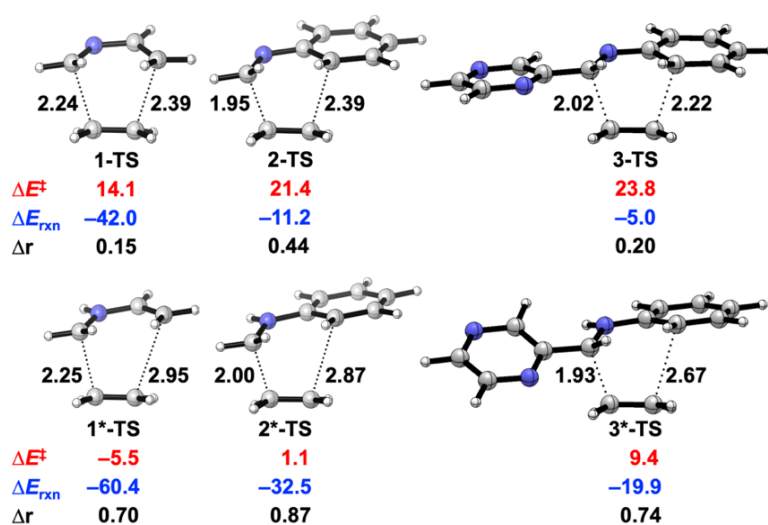


Figure 7.1 Transition state structures with newly forming bond lengths (Å), activation energies (ΔE^\ddagger , kcal mol⁻¹), reaction energies (ΔE_{rxn} , kcal mol⁻¹), and length differences between newly forming bonds (Δr , Å), for aza-Diels-Alder reactions between 2-aza-dienes (**1–3** and **1*–3***) and ethylene. Note that **3*** is the most stable tautomer among others (see **Appendix 7.2**). All data were computed at BP86/TZ2P.

To probe the origin of the enhanced reactivity and the increased asynchronicity of the aza-Diels-Alder reactions of protonated 2-aza-dienes, we turned to the activation strain model (ASM). The electronic energy (ΔE) is decomposed into two terms: the strain energy (ΔE_{strain}) that results from the distortion of the individual reactants and the interaction energy (ΔE_{int}) between the deformed reactants along the reaction coordinate.^[17] In this study, all energy terms were projected onto the length of the shorter one of the two forming C•••C bonds, which undergoes a well-defined change during the reaction and has proven to provide reliable results for Diels-Alder reactions.^[14–16, 23] In the following, we compare the reactivity of **1** and **1*** (**Figure 7.2**) and also find that the same general conclusions hold for the other systems, that is, **2/2*** and **3/3*** (**Appendix 7.7–Appendix 7.8**). Analysis of **Figure 7.2a** reveals that the aza-Diels-Alder reaction of **1*** (red) goes with a lower activation barrier than the reaction of **1** (black), due to the combined effect of a less destabilizing ΔE_{strain} and a much more stabilizing ΔE_{int} .

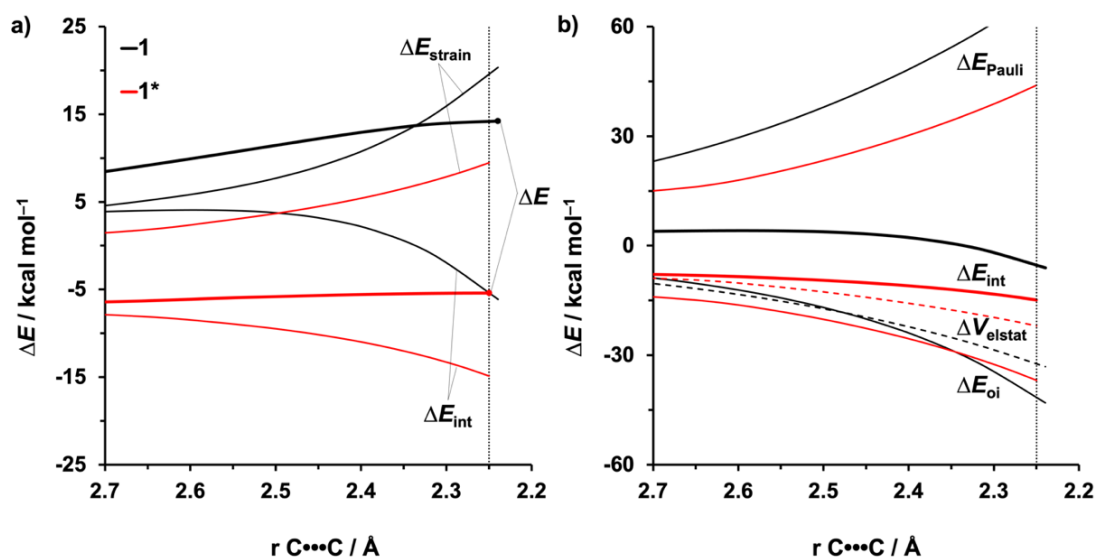


Figure 7.2 a) Activation strain and b) energy decomposition analyses of aza-Diels-Alder reactions between **1/1*** and ethylene along the intrinsic reaction coordinate projected onto the length of the shorter of the two newly forming C•••C bond, computed at BP86/TZ2P. The vertical dotted line indicates the consistent point where the distance of the shorter forming bond is 2.25 Å.

The less destabilizing ΔE_{strain} associated with the aza-Diels-Alder reaction of **1*** originates from a combined effect of the more asynchronous reaction mode and the pre-distorted structure of the diene (**Appendix 7.3**). From our previous work, we know that the more asynchronous Diels-Alder reaction goes with the formation of the first C–C bond ahead of the other C–C bond, causing the involved terminal carbons to pyramidalize sequentially instead of simultaneously, which goes

with less deformation along the reaction around the TS (even though in the eventual product of the addition, the strain is identical for the synchronous and asynchronous reactions).^[14, 24] In this case, we again see that the more asynchronous reaction **1*** goes with less pyramidalization of the terminal carbons, as compared with the reaction **1** (**Figure 7.3a**): at the consistent geometries (2.25 Å), the SoAs (sum of angles around the atom) of the terminal carbons at the longer forming bond (i.e., SoA₂ and SoA₄) are less than 360° (slightly pyramidal) for **1** but nearly exactly 360° (planar) for **1***.

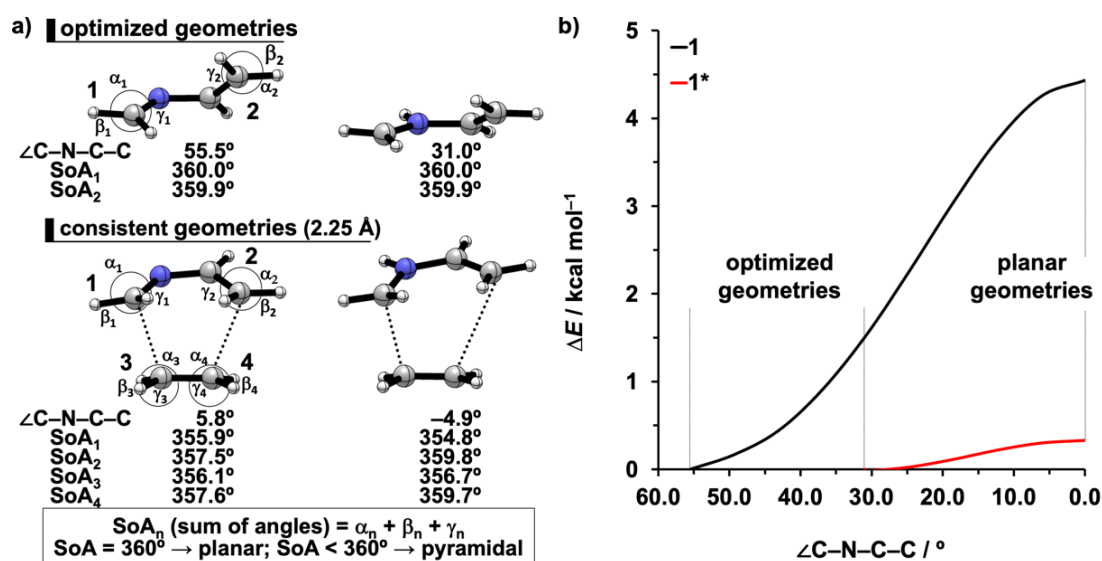


Figure 7.3 a) Optimized geometries and consistent geometries (2.25 Å) of **1** and **1***, including the geometric information in structures; b) computed relative energies of **1/1*** optimized at various constrained dihedral angles of the backbone. All data were computed at BP86/TZ2P.

Another contributor to a reduced strain of **1*** comes from the less distortion of the backbone. The optimized geometry of **1** has a large dihedral angle of the C–N–C–C backbone (55.5°, **Figure 7.3a**).^[3a, 25] In order to react with ethylene, the 2-aza-diene **1** must adopt an *s-cis* conformation in the transition state where the dihedral angle of the backbone is < 10° (**Figure 7.3a**) and this change in conformation goes with a large destabilizing energy (**Figure 7.3b**). The protonated **1***, however, is pre-distorted by the interaction with the proton, yielding a larger C–N–C angle (**1**: 120.5°; **1***: 128.2°) that maximizes the interaction with the proton (please see **Appendix 7.4** and associated text for a more detailed analysis). The increased C–N–C angle reduces the repulsion between the hydrogens on the terminal carbons of the **1***.^[3a, 25] This, in turn, allows for a smaller dihedral angle of the backbone (31.0°, **Figure 7.3a**) which is electronically preferred by the conjugated π system. Therefore, only relatively low strain energy is needed for **1*** to adopt a planar geometry, as

compared with **1** (**Figure 7.3b**). These same general conclusions also rationalize the less destabilizing strain energy for reactions of **2*** and **3*** compared to reactions of **2** and **3**, respectively (**Appendix 7.9**).

The even more profound difference in ΔE_{int} between the aza-Diels-Alder reaction of **1** and **1*** was then analyzed by means of the energy decomposition analysis (**Figure 7.2b**). Our canonical EDA decomposes the ΔE_{int} into three physically meaningful energy terms: classical electrostatic interaction (ΔV_{elstat}), steric (Pauli) repulsion (ΔE_{Pauli}) which, in general, arises from the repulsion between the closed-shell orbitals of both reactants, and stabilizing orbital interaction (ΔE_{oi}) that accounts, among others, for the HOMO–LUMO interactions.^[18] We found that the aza-Diels-Alder reaction of **1*** benefits predominantly from a less destabilizing ΔE_{Pauli} along the entire course of the reaction coordinate, which ultimately leads to the more stabilizing interaction energy when compared with **1**. Interestingly, **1*** goes with a less stabilizing ΔV_{elstat} and ΔE_{oi} at and around the transition state structure seemingly at odds with the “LUMO-lowering concept”. The difference in ΔE_{Pauli} between the reaction of **1** and **1*** can be understood by inspecting the critical closed-shell, two-orbital four-electron, orbital interactions between the reactants at the consistent geometries (2.25 Å, **Figure 7.4a**).^[26] The most significant contributor takes place between the π -HOMO–1_{diene}, i.e., the highest occupied π -orbital of the diene with no nodal plane (see **Appendix 7.5a** for the nomenclature of frontier molecular orbitals), and the π -HOMO_{ene}. The aza-Diels-Alder reaction of **1*** has a smaller overlap of this interaction (0.09) than that of **1** (0.12), which manifests as the less destabilizing ΔE_{Pauli} for the reaction of **1***. The reduced overlap between the π -HOMO–1_{diene} of **1***, which is the in-phase π -orbital of the imine, and π -HOMO_{ene}, the in-phase π -orbital, is the result of the increased degree of asynchronicity compared to **1** (see **Figure 7.4b**). The role of the asynchronicity was further verified by performing a numerical experiment whereby the reaction of **1*** was forced to be synchronous: the overlap of this closed-shell orbital interaction increases from 0.09 to 0.10. The other contributor to the reduced π -HOMO–1_{diene}– π -HOMO_{ene} overlap of **1*** is the smaller π -HOMO–1_{diene} lobe at the C=C bond (**Figure 7.4b**). Since the π -HOMO–1_{diene} is the bonding combination of the π orbitals of the C=N and C=C bonds and the protonated C=N (i.e., C=NH⁺) has a lowered π orbital, the C=N bond acquires a larger weight in the π -HOMO–1_{diene} of **1*** at the expense of a reduced contribution from the C=C bond (see **Appendix 7.6**). Therefore, the π -HOMO–1_{diene} of **1*** has a smaller orbital lobe at the C=C bond (**Figure 7.4b** and **Appendix 7.6**), which overlaps less efficiently with the π -HOMO_{ene}.

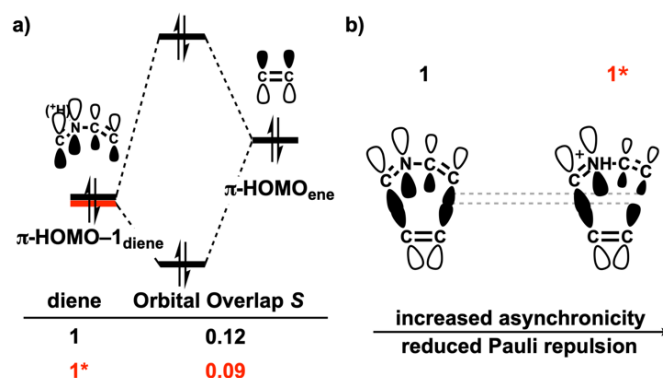


Figure 7.4 a) Schematic diagrams of the key closed-shell orbital interactions with overlaps for the aza-Diels-Alder reactions between **1/1*** and ethylene, computed at 2.25 Å at BP86/TZ2P; b) the illustration of the closed-shell orbital interactions.

The widely-adopted “LUMO-lowering catalysis”^[5] is not the operative mechanism for the general Brønsted acid-catalyzed Diels-Alder reactions of *mono*-protonated 2-aza-dienes (**Figure 7.2b**). Despite the fact that the protonated **1*** exhibits a stabilized $\pi^*\text{-LUMO}_{\text{diene}}$ and, thus, a smaller and more favorable IED $\pi^*\text{-LUMO}_{\text{diene}}\text{-}\pi\text{-HOMO}_{\text{ene}}$ gap, it goes with a poor orbital overlap ($S_1 = 0.20$, $S_{1^*} = 0.18$. See **Appendix 7.5**), due to the combined effect of the smaller amplitude of the $\pi^*\text{-LUMO}_{\text{diene}}$ at the C=C bond involved in the longer newly forming bond and the increased asynchronicity. Similar to the $\pi\text{-HOMO}-1_{\text{diene}}$, the $\pi^*\text{-LUMO}_{\text{diene}}$ is the bonding combination of the π^* orbitals of the C=N and C=C bonds, the protonated C=N (i.e., C=NH⁺) has a lowered π^* orbital that contributes more to the $\pi^*\text{-LUMO}_{\text{diene}}$, making the C=C bond contribute less to the $\pi^*\text{-LUMO}_{\text{diene}}$ (see **Appendix 7.6**). Thus, the less efficient IED orbital overlap acts to offset the stabilization-effect of the IED energy gap and ultimately leads to very similar orbital interactions for **1** and **1*** in the TS region of the potential energy surface (**Figure 7.2b**).

7.2.2 Brønsted Superacid-Catalyzed Reactions

The Nazarov^[27] and Povarov reactions^[12] are two examples of pericyclic reactions that can also be catalyzed by Brønsted superacids. The highly reactive *multi*-protonated reactants, which are known as the “superelectrophiles”,^[13] are confirmed intermediates that feature in the Brønsted superacid-catalyzed reactions.^[13c] In order to reveal the mechanism of the Brønsted superacid-catalyzed aza-Diels-Alder reactions, the aza-Diels-Alder reactivity of the *multi*-protonated N-aryl imine **3**^[12] was studied by systematic protonation of the basic N-sites on the diene. **Figure 7.5** shows the transition state structures for the aza-Diels-Alder reactions of the *mono*-protonated (**3***), *di*-protonated (**3****), and *tri*-protonated (**3*****) aza-dienes. Interestingly, we see that the activation

and reaction energy become progressively more stabilized and the transition state becomes *less* asynchronous on going from 3^* to 3^{***} .

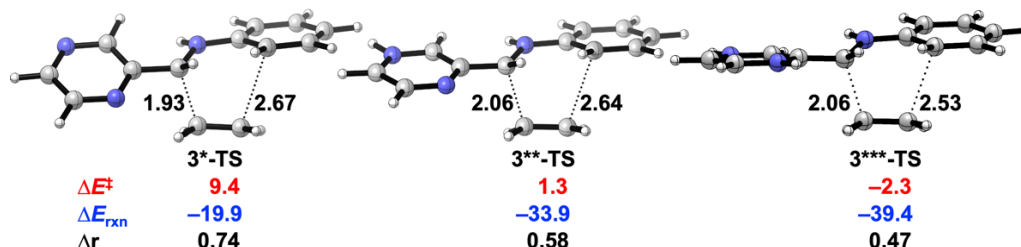


Figure 7.5 Transition state structures with forming bond lengths (Å), activation energies (ΔE^\ddagger , kcal mol⁻¹), reaction energies (ΔE_{rxn} , kcal mol⁻¹), and length differences between newly forming bonds (Δr , Å) for aza-Diels-Alder reactions between protonated N-aryl imines 3^* , 3^{**} , and 3^{***} with ethylene. Note that 3^{**} is the most stable tautomer among others (**Appendix 7.2**). All were computed at BP86/TZ2P.

To pinpoint the origin of the additionally enhanced reactivity of the *multi*-protonated 3^{**} and 3^{***} in aza-Diels-Alder reactions, we again turned to the ASM. The results shown in **Figure 7.6a** reveal that the reaction barrier becomes lower from 3^* to 3^{***} , exclusively due to an increasingly more stabilizing ΔE_{int} . The ΔE_{strain} term, in this case, is not responsible for the enhanced reactivity of 3^{**} and 3^{***} . Furthermore, the EDA of **Figure 7.6b** shows that the more stabilizing ΔE_{int} of 3^{**} and 3^{***} originates from a more stabilizing ΔE_{oi} supported by a slightly more stabilizing ΔV_{elstat} .

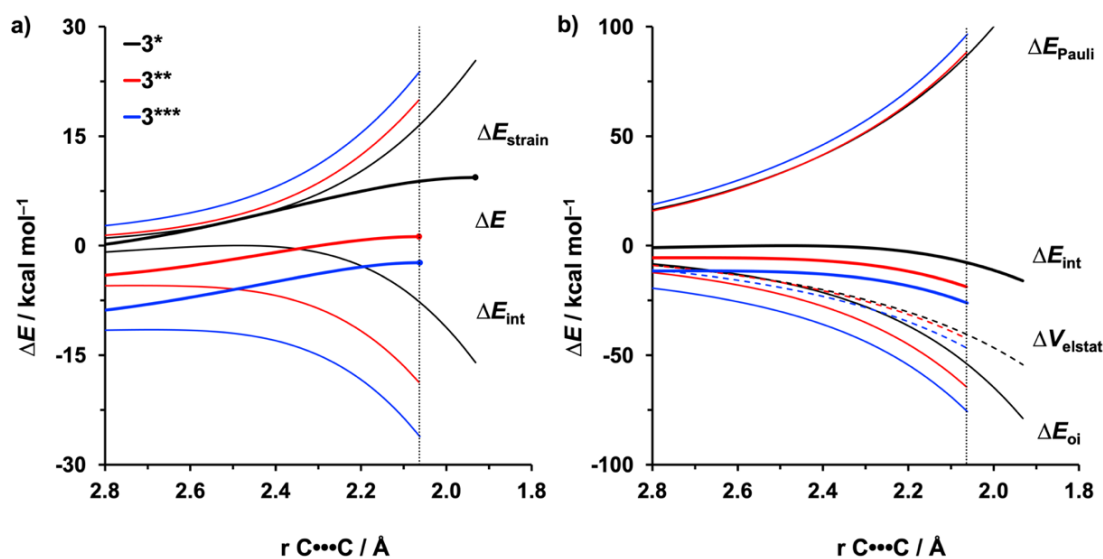


Figure 7.6 a) Activation strain and b) energy decomposition analyses of aza-Diels-Alder reactions between $3^*/3^{**}/3^{***}$ and ethylene along the intrinsic reaction coordinate projected onto the length of the shorter of the two newly forming C...C bond, computed at BP86/TZ2P. The vertical dotted line indicates the consistent point where the distance of the shorter forming bond is 2.06 Å.

The origin of the more stabilizing ΔE_{oi} for the aza-Diels-Alder reactions of **3**** and **3***** was uncovered by inspecting the critical frontier molecular orbital interactions at the consistent geometries where the distance of the shorter forming C•••C bond is 2.06 Å. The NED interaction occurs between the π -HOMO_{diene} and π^* -LUMO_{ene} and becomes moderately stabilized when going from **3*** to **3***** (for numerical results see **Appendix 7.10a**).^[28] This slight enhancement in NED interaction on going from **3*** to **3***** was also confirmed by NOCV (natural orbitals for chemical valence) analyses (**Appendix 7.10c**).^[29] We noticed that the π -HOMO_{diene} becomes increasingly more stabilized as the diene becomes progressively protonated, as does the corresponding π^* -LUMO_{ene} (**Appendix 7.11a**),^[30] which, in turn, leads to the smaller π -HOMO_{diene}– π^* -LUMO_{ene} gaps (**Figure 7.7a**) and slightly enhanced NED interactions for the reactions of **3*** and **3*****. The stabilization of the π^* -LUMO_{ene} upon the protonation of the diene originates from the π^* -LUMO_{ene} being oriented towards, and in close proximity to, the external positive potential of the protonated diene (**Appendix 7.12**).

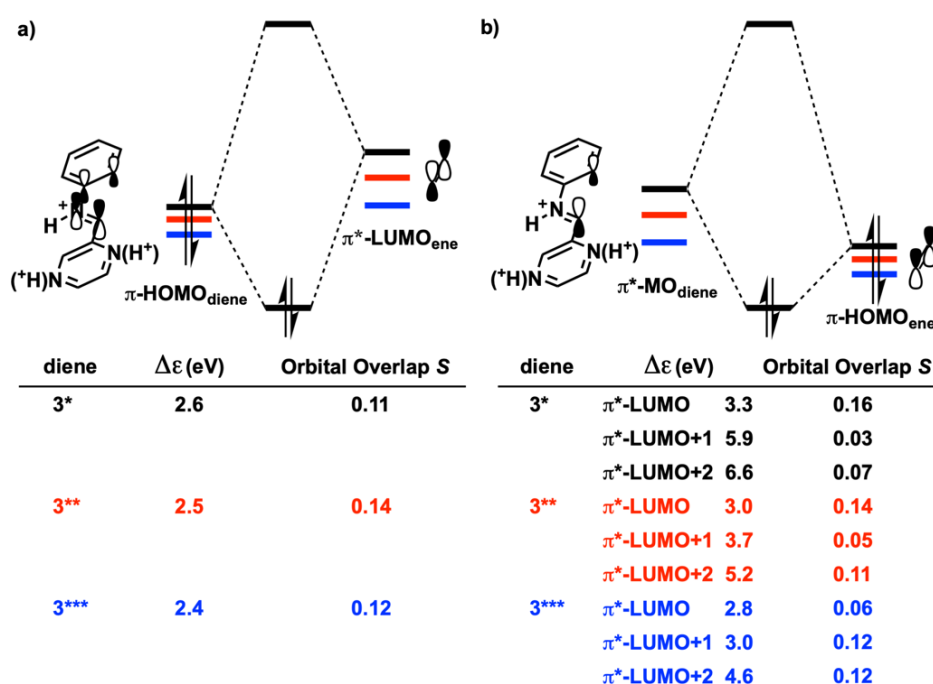


Figure 7.7 Schematic diagrams of the a) normal electron demand (NED) interactions of the π -HOMO_{diene}– π^* -LUMO_{ene} and b) inverse electron demand (IED) interactions of the π^* -MO_{diene}– π -HOMO_{ene}, with the computed gaps $\Delta\epsilon$ (in eV) and orbital overlaps S , for the aza-Diels-Alder reactions of **3***, **3****, and **3***** at the consistent geometries (distance of the shorter forming C•••C bond is 2.06 Å). All were computed at BP86/TZ2P.

In addition, we see that the IED interaction is substantially strengthened on going from **3*** to **3***** (for numerical results see **Appendix 7.10b** and NOCV results in **Appendix 7.10d**), and this is the main source of the stabilized ΔE_{oi} and enhanced reactivity of the aza-Diels-Alder reactions on going from **3*** to **3*****. Three π^* -molecular orbitals of the diene (π^* -MO_{diene}) were identified to contribute to the IED interactions with the π -HOMO_{ene}: the π^* -LUMO_{diene} and two higher lying virtual orbitals denoted π^* -LUMO+1_{diene} and π^* -LUMO+2_{diene} (see DFT-computed plots of π^* -MO_{diene} in **Appendix 7.13**). These π^* -LUMO(s) are all stabilized upon protonation on going from **3*** to **3***** (**Appendix 7.11b**) which causes the IED gaps of π^* -LUMO_{diene}- π -HOMO_{ene}, π^* -LUMO+1_{diene}- π -HOMO_{ene} and π^* -LUMO+2_{diene}- π -HOMO_{ene} all to become much smaller (**Figure 7.7b**), leading to the significantly enhanced IED interactions for the reactions of **3**** and **3*****. Therefore, it becomes evident that the multi-protonated 2-aza-dienes adopt the “LUMO-lowering catalysis”.

Our analysis also reveals how the degree of asynchronicity in the transition state of a Diels-Alder reaction is the result of two counteracting factors: the minimization of the destabilizing Pauli repulsions (asynchronous mode) and the maximization of the stabilizing orbital and electrostatic interactions (synchronous mode). In the previous section, we have already established that the “Pauli-lowering catalysis”-controlled reactions have the more asynchronous TS (**Figure 7.1**) that minimizes the overlaps of the closed-shell orbital interactions (**Figure 7.4**).^[14, 15] In this case, the superelectrophiles **3**** and **3***** display such stabilized LUMO(s) that the “LUMO-lowering catalysis” becomes operative (**Figure 7.6** and **Figure 7.7**). Accordingly, these “LUMO-lowering catalysis”-controlled reactions of **3**** and **3***** become more synchronous (**Figure 7.5**), to maximize the stabilizing orbital and electrostatic interactions. This was verified by a comparison between the optimized **3***-TS** with the constrained asynchronous **3***-TS'** (**Figure 7.8**): the **3***-TS** ($\Delta r = 0.47 \text{ \AA}$) is more synchronous and benefits from additional stabilizing interactions compared to the artificially asynchronous **3***-TS'** ($\Delta r = 0.74 \text{ \AA}$). The stabilizing orbital and electrostatic interactions of **3***-TS** overrule the increase in the Pauli repulsion and ultimately lead to a more stabilizing total interaction energy and thus a more favorable transition state structure compared to **3***-TS*** (**Figure 7.8**).

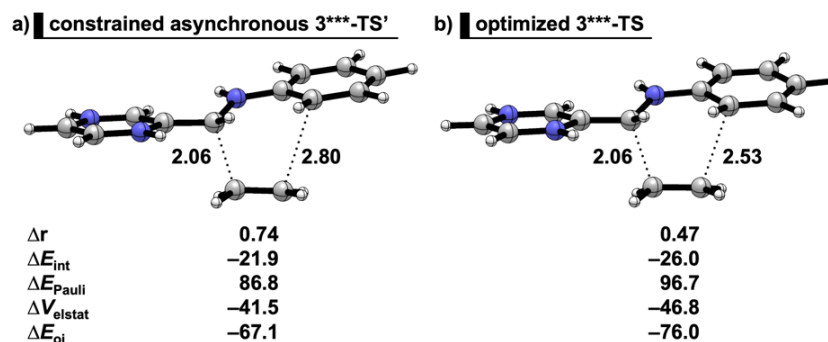


Figure 7.8 Energy decomposition analyses on the a) constrained asynchronous $3^{***}\text{-TS}'$ where the Δr is forced to be 0.74 Å, and b) optimized 3^{***}-TS where $\Delta r = 0.47$. All energy terms are in kcal mol⁻¹ and computed at BP86/TZ2P.

7.3 Conclusions

Our quantum chemical exploration pinpointed the factors that determine the trends in reactivity of Brønsted acid-catalyzed aza-Diels-Alder reactions between various 2-aza-dienes and ethylene. Protonation vastly enhances the reactivity of 2-aza-dienes in Diels-Alder reactions with ethylene. *Mono*-protonated 2-aza-dienes operate under the regime of “Pauli-lowering catalysis” whereas *multi*-protonated 2-aza-dienes operate under the widely-established regime of “LUMO-lowering catalysis.”

Our findings based on the activation strain model and Kohn-Sham molecular orbital theory revealed that the *mono*-protonation of 2-aza-dienes catalyzes the reactions by reducing the strain energy of the diene and Pauli repulsion between the reactants. This is due to that the *mono*-protonated reaction adopts a more asynchronous reaction mode that demands less deformation of the terminal carbons of the diene and experiences a smaller overlap of the closed-shell orbital interaction. The expected “LUMO-lowering catalysis” is not the driving force, because the *mono*-protonated reaction goes with a poor orbital overlap of the IED interaction that offsets the LUMO-stabilization effect and ultimately leads to an unvaried IED interaction. On the other hand, the *multi*-protonation of 2-aza-dienes additionally enhances their reactivity by the “LUMO-lowering catalysis”. In this case, the *multi*-protonated dienes have such stabilized LUMOs that the LUMO-lowering effect becomes operative. Moreover, we found that the reactions of *multi*-protonated 2-aza-dienes proceed via a more synchronous pathway which facilitates the orbital overlap of the orbital interactions.

This study shows how “Pauli-lowering catalysis” can switch to “LUMO-lowering catalysis”

when the degree of LUMO stabilization is extreme as in the case of *multi*-protonated 2-aza-dienes. Furthermore, we establish that Pauli-lowering catalysis and asynchronous TS structures occur if the reduction in Pauli repulsion is bigger than the loss in stabilizing NED and/or IED HOMO–LUMO interactions whereas LUMO-lowering catalysis and synchronous TS structures occur if the gain in stabilizing NED and/or IED HOMO–LUMO interactions is bigger than the increase in Pauli repulsion.

7.4 References

- [1] a) L. F. Tietze, G. Kettschau, *Stereoselective Heterocyclic Synthesis I*, Springer, New York, **1997**; b) D. L. Boger, S. N. Weinreb, *Hetero Diels-Alder Methodology in Organic Synthesis*, Academic Press, San Diego, **2012**.
- [2] a) P. M. Weintraub, J. S. Sabol, J. M. Kane, D. R. Borcharding, *Tetrahedron* **2003**, *59*, 2953–2989; b) M. G. P. Buffat, *Tetrahedron* **2004**, *60*, 1701–1729; c) V. Eschenbrenner-Lux, K. Kumar, H. Waldmann, *Angew. Chem. Int. Ed.* **2014**, *53*, 11146–11157.
- [3] a) S. Yu, H. de Bruijn, D. Svatunek, T. A. Hamlin, F. M. Bickelhaupt, *ChemistryOpen* **2018**, *7*, 995–1004; b) J. Zhang, V. Shukla, D. L. Boger, *J. Org. Chem.* **2019**, *84*, 9397–9445.
- [4] a) G. Masson, C. Lalli, M. Benohoud, G. Dagousset, *Chem. Soc. Rev.* **2013**, *42*, 902–923; b) J.-M. M. Monbaliu, K. G. R. Masschelein, C. V. Stevens, *Chem. Soc. Rev.* **2011**, *40*, 4708–4739.
- [5] J. Clayden, N. Greeves, S. Warren, *Organic Chemistry, 2nd edition*, Oxford University Press, Oxford, **2012**.
- [6] a) J. Gonzalez, K. N. Houk, *J. Org. Chem.* **1992**, *57*, 3031–3037; b) A. Venturini, J. Joglar, S. Fustero, J. González, *J. Org. Chem.* **1997**, *62*, 3919–3926; c) Y.-Q. Ding, D.-C. Fang, *J. Org. Chem.* **2003**, *68*, 4382–4387.
- [7] a) Y.-S. Cheng, E. Ho, P. S. Mariano, H. L. Ammon, *J. Org. Chem.* **1985**, *50*, 5678–5686; b) E. Ho, Y.-S. Cheng, P. S. Mariano, *Tetrahedron Lett.* **1988**, *29*, 4799–4802; c) J. Barluenga, J. Joglar, S. Fustero, V. Gotor, C. Kruger, M. J. Romão, *Chem. Ber.* **1985**, *118*, 3652–3663; d) E. C. Meurer, M. N. Eberlin, *Int. J. Mass Spectrom.* **2001**, *210*, 469–482; e) E. C. Meurer, R. Sparrapan, M. N. Eberlin, *J. Mass Spectrom.* **2003**, *38*, 1075–1080.

- [8] a) L. S. Povarov, B. M. Mikhailov, *Izv. Akad. Nauk SSR, Ser. Khim.* **1963**, 953–956; b) L. S. Povarov, *Russ. Chem. Rev.* **1967**, 36, 656–670; c) V. V. Kouznetsov, *Tetrahedron* **2009**, 65, 2721–2750.
- [9] a) G. A. Swan, *J. Chem. Soc. D* **1969**, 20a–20a; b) R. B. Roy, G. A. Swan, *Chem. Commun. (London)* **1968**, 1446–1447; c) K.-D. Hesse, *Justus Liebigs Ann. Chem.* **1970**, 741, 117–123; d) V. V. Kouznetsov, *Tetrahedron* **2009**, 65, 2721–2750; e) D. Leca, F. Gaggini, J. Cassayre, O. Loiseleur, S. N. Pieniazek, J. A. R. Luft, K. N. Houk, *J. Org. Chem.* **2007**, 72, 4284–4287.
- [10] a) H. Liu, G. Dagousset, G. Masson, P. Retailleau, J. Zhu, *J. Am. Chem. Soc.* **2009**, 131, 4598–4599; b) J. Barluenga, A. Mendoza, F. Rodríguez, F. J. Fañanás, *Angew. Chem. Int. Ed.* **2008**, 47, 7044–7047; c) G. Bergonzini, L. Gramigna, A. Mazzanti, M. Fochi, L. Bernardi, A. Ricci, *Chem. Commun.* **2010**, 46, 327–329; d) H. Xu, S. J. Zuend, M. G. Woll, Y. Tao, E. N. Jacobsen, *Science* **2010**, 327, 986–990; e) O. Ghashghaei, C. Masdeu, C. Alonso, F. Palacios, R. Lavilla, *Drug Discov. Today Technol.* **2018**, 29, 71–79.
- [11] a) J. P. Michael, *Nat. Prod. Rep.* **2007**, 24, 223–246; b) V. R. Solomon, H. Lee, *Curr. Med. Chem.* **2011**, 18, 1488–1508; c) A. R. Katritzky, S. Rachwal, B. Rachwal, *Tetrahedron* **1996**, 52, 15031–15070; d) V. Sridharan, P. A. Suryavanshi, J. C. Menéndez, *Chem. Rev.* **2011**, 111, 7157–7259.
- [12] a) H. Vuong, B. P. Dash, S. O. Nilsson Lill, D. A. Klumpp, *Org. Lett.* **2018**, 20, 1849–1852; b) H. Vuong, D. A. Klumpp, *Synth. Commun.* **2019**, 49, 316–323.
- [13] a) G. A. Olah, A. Germain, H. C. Lin, D. A. Forsyth, *J. Am. Chem. Soc.* **1975**, 97, 2928–2929; b) G. A. Olah, D. A. Klumpp, *Superelectrophiles and Their Chemistry*, Wiley & Sons, New York, **2008**; c) R. R. Naredla, C. Zheng, S. O. Nilsson Lill, D. A. Klumpp, *J. Am. Chem. Soc.* **2011**, 133, 13169–13175.
- [14] a) P. Vermeeren, T. A. Hamlin, I. Fernández, F. M. Bickelhaupt, *Angew. Chem.* **2020**, 132, 6260–6265; *Angew. Chem. Int. Ed.* **2020**, 59, 6201–6206; b) P. Vermeeren, T. A. Hamlin, I. Fernández, F. M. Bickelhaupt, *Chem. Sci.* **2020**, 11, 8105–8112.
- [15] T. A. Hamlin, F. M. Bickelhaupt, I. Fernández, *Acc. Chem. Res.* **2021**, 54, 1972–1981.
- [16] a) T. A. Hamlin, D. Svatunek, S. Yu, L. Ridder, I. Infante, L. Visscher, F. M. Bickelhaupt, *Eur. J. Org. Chem.* **2019**, 378–386; b) S. Yu, P. Vermeeren, K. van Dommelen, F. M.

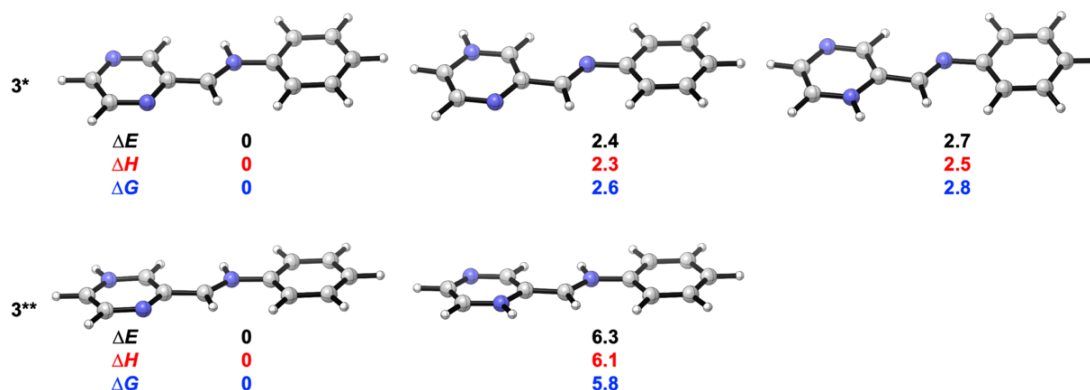
- Bickelhaupt, T. A. Hamlin, *Chem. Eur. J.* **2020**, *26*, 11529–11539; c) S. Yu, P. Vermeeren, T. A. Hamlin, F. M. Bickelhaupt, *Chem. Eur. J.* **2021**, *27*, 5683–5693.
- [17] a) D. H. Ess, K. N. Houk, *J. Am. Chem. Soc.* **2008**, *130*, 10187–10198; b) W.-J. van Zeist, F. M. Bickelhaupt, *Org. Biomol. Chem.* **2010**, *8*, 3118–3127; c) I. Fernández, F. M. Bickelhaupt, *Chem. Soc. Rev.* **2014**, *43*, 4953–4967; d) L. P. Wolters, F. M. Bickelhaupt, *Wiley Interdiscip. Rev. Comput. Mol. Sci.* **2015**, *5*, 324–343; e) F. M. Bickelhaupt, K. N. Houk, *Angew. Chem. Int. Ed.* **2017**, *56*, 10070–10086; f) I. F. M. Bickelhaupt, K. N. Houk, *Angew. Chem.* **2017**, *129*, 10204–10221; g) P. Vermeeren, S. C. C. van der Lubbe, C. Fonseca Guerra, F. M. Bickelhaupt, T. A. Hamlin, *Nat. Protoc.* **2020**, *15*, 649–667; h) P. Vermeeren, T. A. Hamlin, F. M. Bickelhaupt, *Chem. Commun.* **2021**, *57*, 5880–5896.
- [18] a) F. M. Bickelhaupt, E. J. Baerends in *Reviews in Computational Chemistry* (Eds: K. B. Lipkowitz, D. B. Boyd), Wiley, Hoboken, **2000**, pp 1–86; b) R. van Meer, O. V. Gritsenko, E. J. Baerends, *J. Chem. Theory Comput.* **2014**, *10*, 4432; c) L. Zhao, M. von Hopffgarten, D. M. Andrada, G. Frenking, *WIREs Comput. Mol. Sci.* **2018**, *8*, e1345; d) T. A. Hamlin, P. Vermeeren, C. Fonseca Guerra, F. M. Bickelhaupt, “Energy decomposition analysis in the context of quantitative molecular orbital theory” in *Complementary Bonding Analysis* (Ed: S. Grabowsky), De Gruyter, Berlin, Boston, **2021**, pp 199–212.
- [19] a) A. D. Becke, *Phys. Rev. A* **1988**, *38*, 3098–3100; b) J. P. Perdew, *Phys. Rev. B* **1986**, *33*, 8822–8824; c) E. van Lenthe, E. J. Baerends, *J. Comput. Chem.* **2003**, *24*, 1142–1156.
- [20] a) S. Grimme, S. Ehrlich, L. Goerigk, *J. Comput. Chem.* **2011**, *32*, 1456–1465; b) J. G. Brandenburg, J. E. Bates, J. Sun, J. P. Perdew, *Phys. Rev. B*, **2016**, *94*, 115144.
- [21] a) Y. Zhao, D. G. Truhlar, *J. Chem. Phys.* **2006**, *125*, 194101; b) Y. Zhao, D. G. Truhlar, *Theor. Chem. Acc.* **2008**, *120*, 215–241.
- [22] a) A. Klamt, G. Schüürmann, *J. Chem. Soc. Perkin Trans. 2* **1993**, 799; b) A. Klamt, *J. Phys. Chem.* **1995**, *99*, 2224; c) A. Klamt, V. Jonas, *J. Chem. Phys.* **1996**, *105*, 9972; d) C. C. Pye, T. Ziegler, *Theor. Chem. Acc.* **1999**, *101*, 396.
- [23] W.-J. van Zeist, A. H. Koers, L. P. Wolters, F. Matthias Bickelhaupt, *J. Chem. Theory Comput.* **2008**, *4*, 920–928.
- [24] K. Yamazaki, P. Gabriel, G. D. Carmine, J. Pedroni, M. Farizyan, T. A. Hamlin, D. J. Dixon, *ACS Catal.* **2021**, *11*, 7489–7497.

- [25] a) K. B. Wiberg, P. R. Rablen, J. H. Baraban, *J. Org. Chem.* **2018**, *83*, 8473–8482; b) C. W. Bock, P. George, M. Trachtman, *J. Comput. Chem.* **1984**, *5*, 395–410.
- [26] Analysis at the consistent geometry, instead of at the transition state, is advised when the transition states occur at different points on the reaction coordinate. A single-point analysis on the transition state geometries results in skewed conclusions since the position of the transition state (i.e., early- or late-transition state) has a significant impact on the magnitude of the energy terms.
- [27] a) D. A. Klumpp, Y. Zhang, M. J. O'Connor, P. M. Esteves, L. S. de Almeida, *Org. Lett.* **2007**, *9*, 3085–3088; b) T. Suzuki, T. Ohwada, K. Shudo, *J. Am. Chem. Soc.* **1997**, *119*, 6774–6780; c) I. Karthikeyan, D. Arunprasath, G. Sekar, *Chem. Commun.* **2015**, *51*, 1701–1704; d) R. Narayan, C.-G. Daniliuc, E.-U. Würthwein, *Eur. J. Org. Chem.* **2012**, 6021–6032.
- [28] The specific NED/IED orbital interactions were confirmed by manually deleting all virtual orbitals except the interacting LUMO(s). For instance, the NED interaction energies were obtained by deleting all virtual orbitals but the π^* -LUMO_{ene}, and the IED interaction energies were obtained by deleting all virtual orbitals but the interacting π^* -MO_{diene}. See **Appendix 7.10a** and **Appendix 7.10b** for numerical details.
- [29] M. P. Mitoraj, A. Michalak, T. A. Ziegler, *J. Chem. Theory Comput.* **2009**, *5*, 962–975.
- [30] The orbital energies of the fragments (or reactants) were obtained from the Fock matrix of the complex in the basis of the symmetrized fragment orbitals (SFOs) by using the FmatSFO keyword in ADF. This allows us to compute the orbital energies of one fragment in the presence of the other fragment.

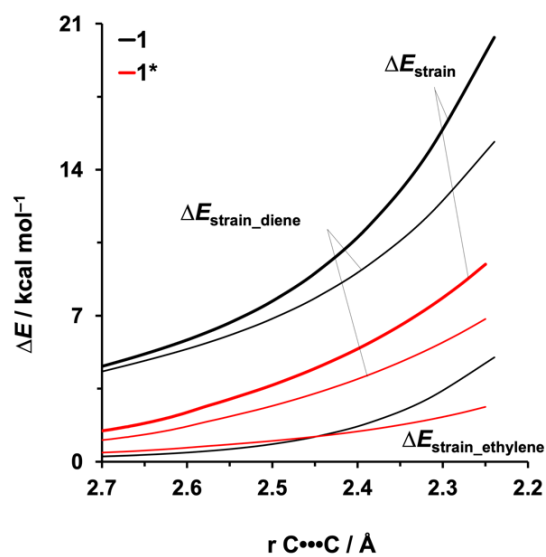
7.5 Appendices

Appendix 7.1 Activation and reaction energies, enthalpies, and Gibbs free energies (in kcal mol⁻¹) for aza-Diels-Alder reactions between 2-aza-dienes and ethylene, computed at BP86/TZ2P, BP86-D3(BJ)/TZ2P, M06-2X/TZ2P and COSMO(DCM)BP86/TZ2P, using BP86/TZ2P geometries.

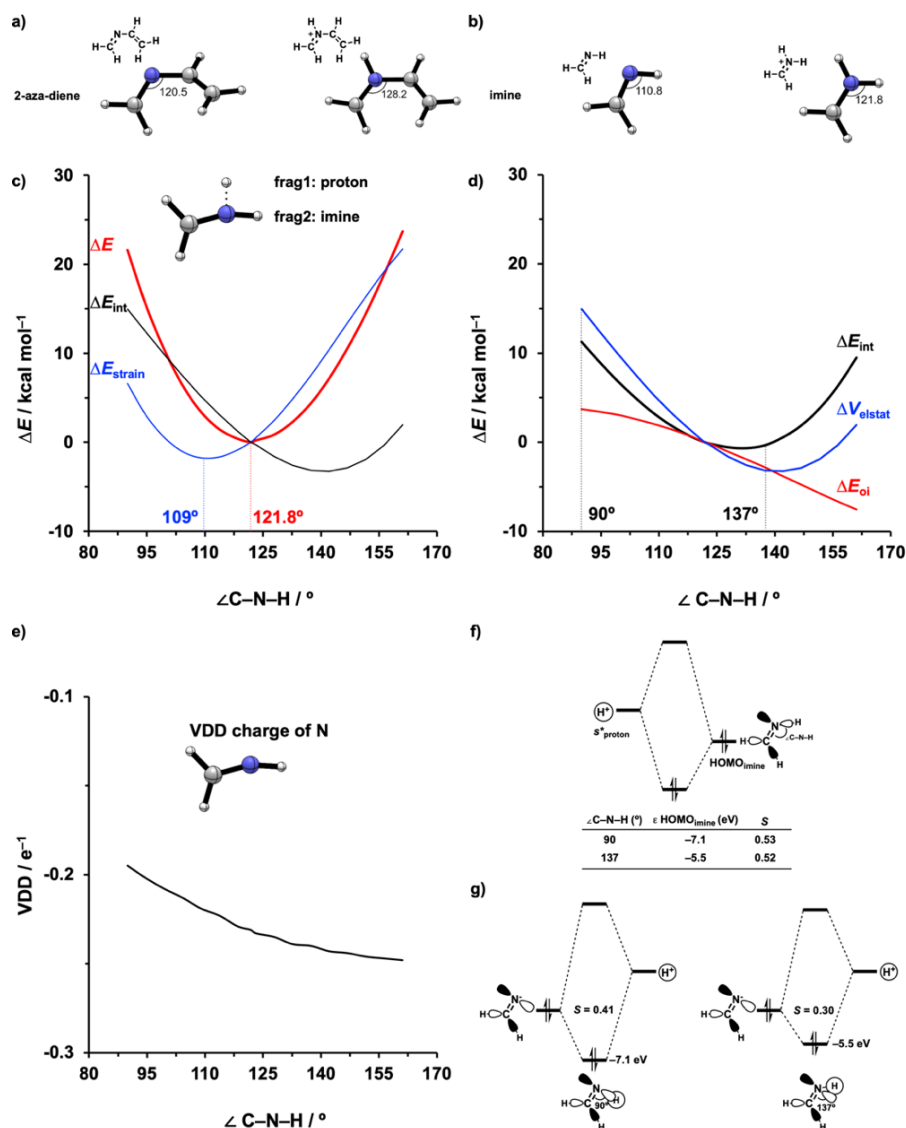
	BP86/TZ2P					
	ΔE^\ddagger	ΔH^\ddagger	ΔG^\ddagger	ΔE_{rxn} kcal mol ⁻¹	ΔH_{rxn}	ΔG_{rxn}
1	14.1	15.0	27.2	-42.0	-37.8	-24.3
1*	-5.5	-4.5	7.0	-60.4	-56.2	-42.5
2	21.4	22.4	35.1	-11.2	-7.7	5.6
2*	1.1	2.1	14.2	-32.5	-29.0	-15.7
3	23.8	24.7	37.8	-5.0	-1.9	11.6
3*	9.4	10.2	23.3	-19.9	-17.3	-1.6
3**	1.2	2.2	14.6	-33.9	-31.2	-16.1
3***	-2.3	-1.6	10.6	-39.4	-36.4	-22.6
	BP86-D3(BJ)/TZ2P//BP86/TZ2P					
	ΔE^\ddagger	ΔH^\ddagger	ΔG^\ddagger	ΔE_{rxn} kcal mol ⁻¹	ΔH_{rxn}	ΔG_{rxn}
1	8.2	9.1	21.4	-46.8	-42.5	-29.1
1*	-10.8	-9.8	1.7	-65.2	-60.9	-47.3
2	14.7	15.7	28.4	-17.2	-13.7	-0.5
2*	-5.0	-4.0	8.1	-38.7	-35.2	-21.8
3	15.3	16.1	29.2	-12.6	-9.5	4.1
3*	1.4	2.3	15.4	-27.5	-24.9	-9.3
3**	-7.1	-6.1	6.3	-41.5	-38.7	-23.7
3***	-10.7	-10.0	2.3	-46.8	-43.9	-30.1
	M06-2X/TZ2P//BP86/TZ2P					
	ΔE^\ddagger	ΔH^\ddagger	ΔG^\ddagger	ΔE_{rxn} kcal mol ⁻¹	ΔH_{rxn}	ΔG_{rxn}
1	16.6	17.6	29.8	-48.8	-44.5	-31.1
1*	-4.1	-3.1	8.4	-67.0	-62.8	-49.2
2	26.0	27.0	39.7	-16.2	-12.8	0.5
2*	2.1	3.1	15.1	-39.1	-35.6	-22.3
3	25.5	26.3	39.4	-13.2	-10.1	3.4
3*	8.9	9.7	22.8	-29.6	-26.9	-11.3
3**	-1.0	0.0	12.4	-47.1	-44.4	-29.4
3***	-3.7	-3.0	9.2	-53.6	-50.6	-36.8
	COSMO(DCM)BP86/TZ2P//BP86/TZ2P					
	ΔE^\ddagger	ΔH^\ddagger	ΔG^\ddagger	ΔE_{rxn} kcal mol ⁻¹	ΔH_{rxn}	ΔG_{rxn}
1	13.5	14.4	26.7	-42.4	-38.2	-24.7
1*	2.5	3.5	15.0	-53.5	-49.3	-35.6
2	20.6	21.6	34.2	-11.8	-8.3	4.9
2*	7.5	8.5	20.6	-25.1	-21.6	-8.2
3	23.9	24.7	37.9	-5.3	-2.2	11.3
3*	14.5	15.4	28.5	-16.7	-14.0	1.6
3**	11.0	11.9	24.3	-22.1	-19.3	-4.3
3***	11.2	11.9	24.1	-23.9	-20.9	-7.1



Appendix 7.2 Relative electronic energies (kcal mol⁻¹), entropies (kcal mol⁻¹), and Gibbs free energies (kcal mol⁻¹) for different tautomers of 3^* and 3^{**} , computed at BP86/TZ2P.

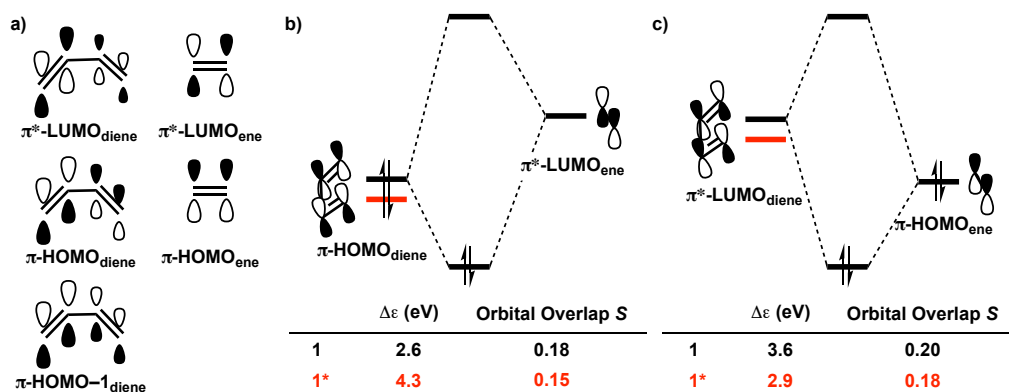


Appendix 7.3 Decomposition of the strain energies in aza-Diels-Alder reactions between $1/1^*$ and ethylene along the IRC projected on the newly forming C...C bond, computed at BP86/TZ2P.

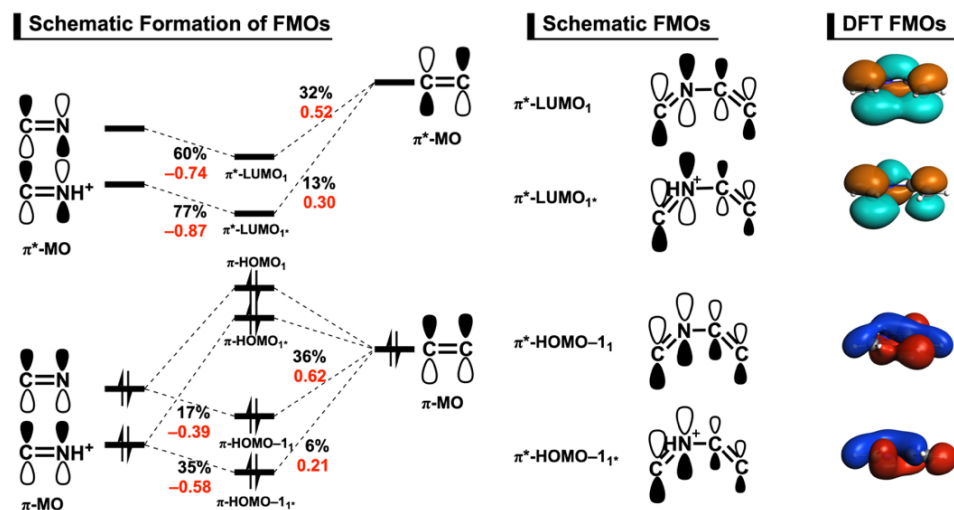


Appendix 7.4 Analyses of the protonated 2-aza-diene and imine computed at BP86/TZ2P.

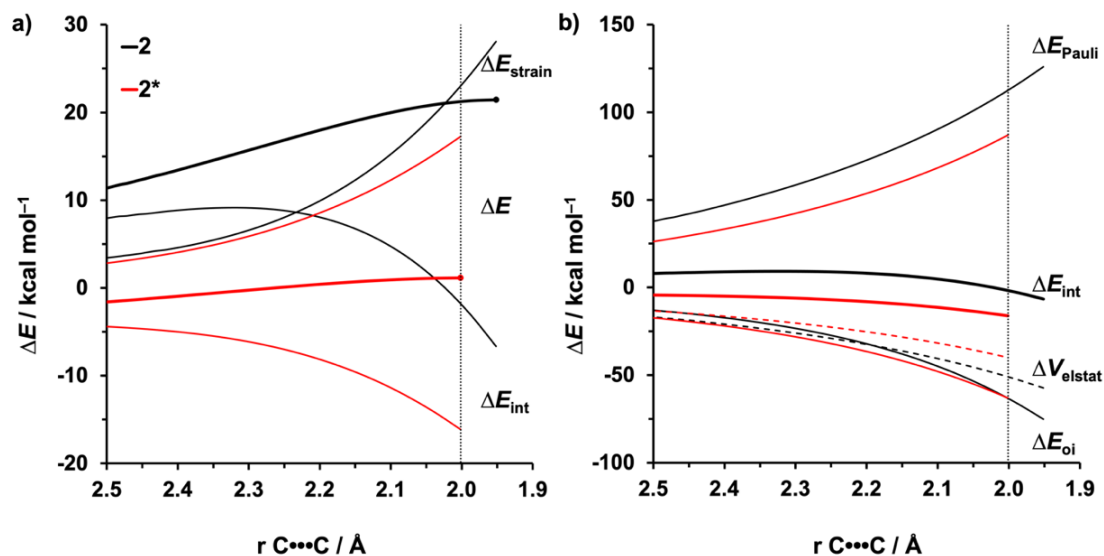
The C-N-C angle of the 2-aza-diene increases from 120.5° to 128.2° upon protonation (Figure **Appendix 7.4a**). To rationalize this protonation induced geometric change, we studied an iminium archetypal model system. This model also displays a larger C-N-H angle (121.8°) than the pristine imine (110.8°) (**Appendix 7.4b**). A relaxed C-N-H scan was performed on the protonated imine followed by an activation strain analysis based on a heterolytic fragmentation involving a proton, H⁺, and imine, H₂C=NH (**Appendix 7.4c**). The C-N-H scan reveals a minimum in ΔE , at 121.8°, while the ΔE_{strain} , i.e., the energy of the imine fragment, has a minimum at 109° (**Appendix 7.4c**). When the C-N-H angle is larger there is a more stabilizing interaction ΔE_{int} between proton and imine. The energy decomposition analysis reveals that the electrostatic and orbital interactions between proton and imine become more stabilizing when the C-N-H angle of imine increases up to 137° (**Appendix 7.4d**). The stronger electrostatic interaction originates from a more negatively-charged nitrogen of imine with a larger C-N-H angle (**Appendix 7.4e**). The enhanced orbital interaction is traced back to the higher HOMO of the imine with a larger C-N-H angle that can interact more efficiently with the s^* orbital of proton (**Appendix 7.4f**). Since the HOMO_{imine} is the bonding mixing of the in-plane orbital of H₂C=N⁻ and the s^* orbital of H⁺ (**Appendix 7.4g**), the imine with the larger C-N-H angle has a less efficient overlap of this interaction that leads to a less stabilizing bonding orbital, i.e., a higher HOMO of imine (**Appendix 7.4g**). In summary, the protonated imine has a larger C-N-H angle to maximize the stabilizing interaction between proton and the imine.



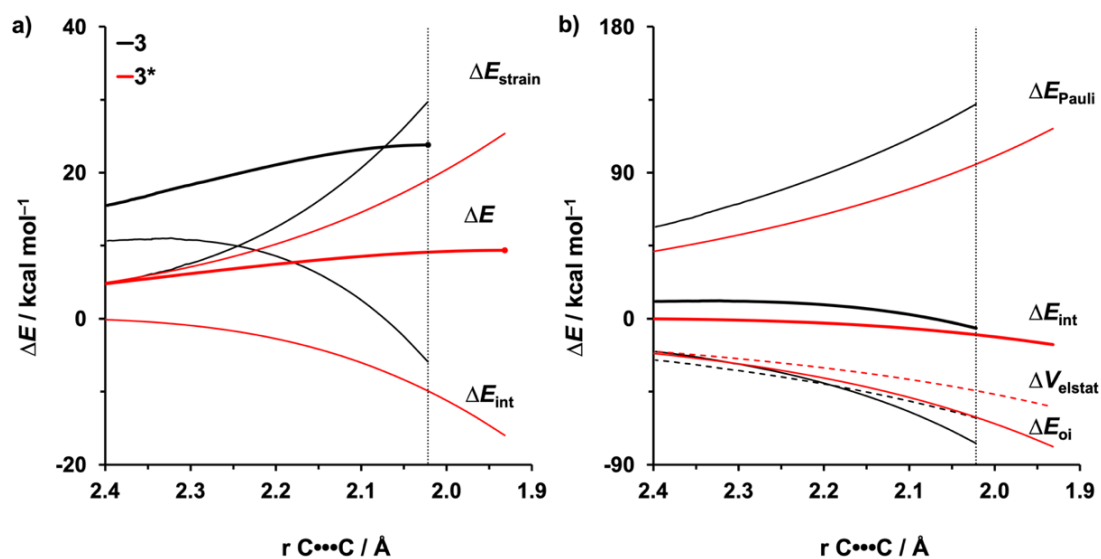
Appendix 7.5 a) Scheme of frontier molecular orbitals (FMO) involved in the Diels-Alder reactions. Diagrams with energy gaps and overlaps of b) the NED π -HOMO_{diene}- π^* -LUMO_{ene} and c) the IED π^* -LUMO_{diene}- π -HOMO_{ene} interactions for aza-Diels-Alder reactions of **1** and **1*** with ethylene at the consistent geometry (new C•••C bond of 2.25 Å), computed at BP86/TZ2P.



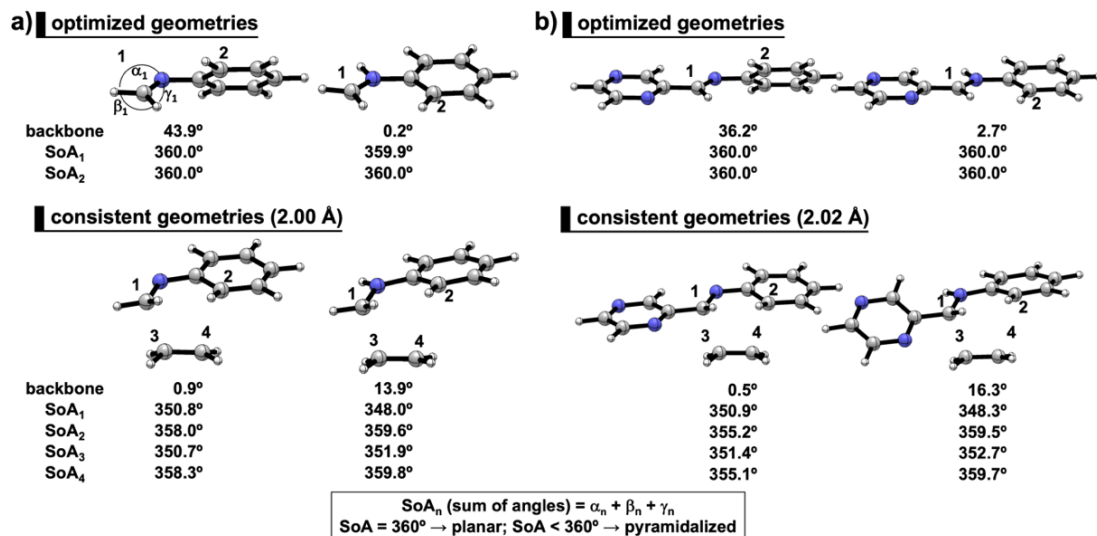
Appendix 7.6 Schematic formation of the frontier molecular orbitals (FMOs) of **1** and **1***, including the contributions (blue) and coefficients (red) of the constituting fragment MOs, with schematic and DFT-computed plots of the FMOs.



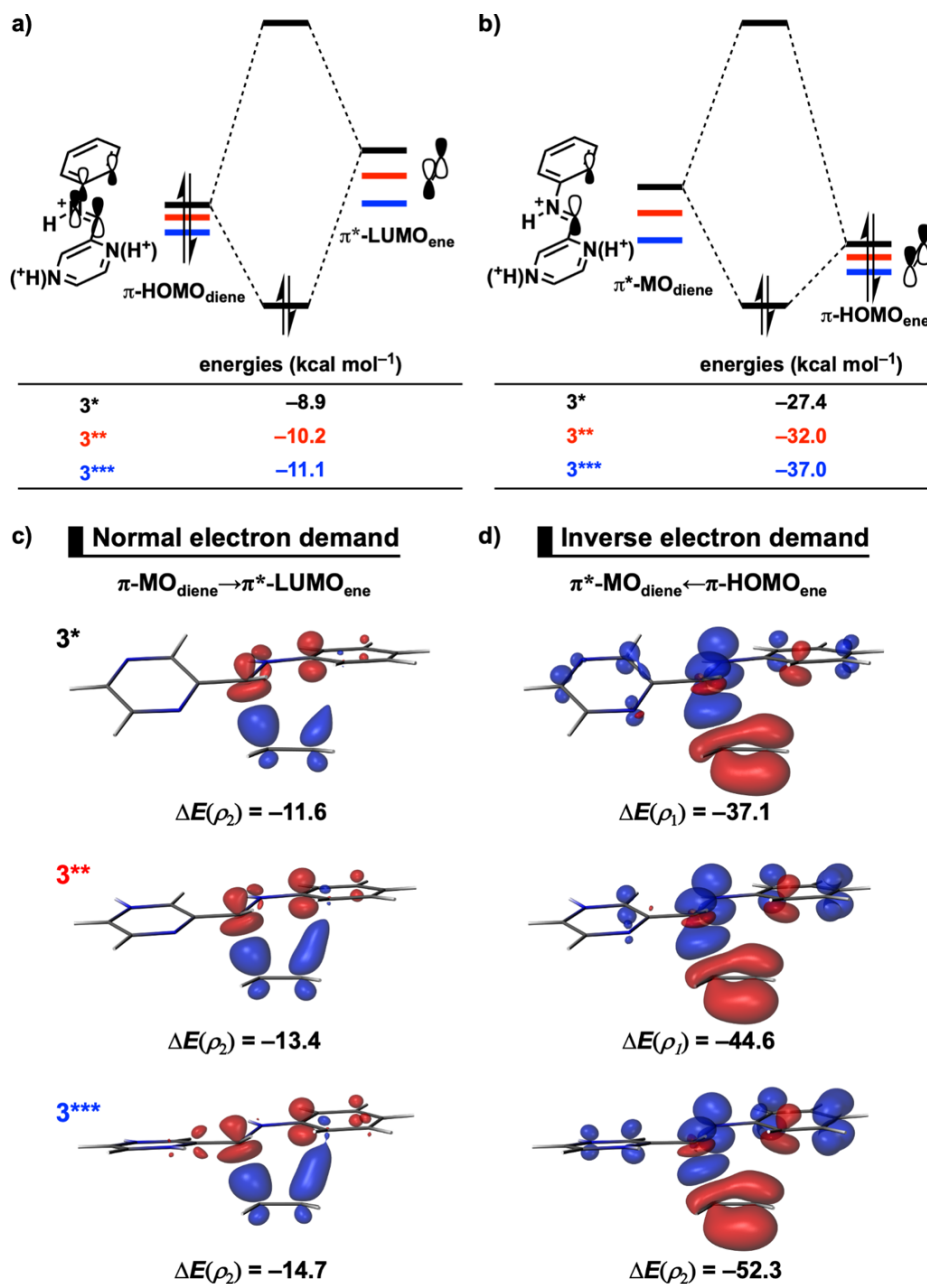
Appendix 7.7 a) Activation strain and b) energy decomposition analyses of aza-Diels-Alder reactions of **2** and **2*** with ethylene along the IRC projected onto the length of the shorter newly forming C...C bond, computed at BP86/TZ2P. The vertical dotted line indicates the consistent point where the distance of the shorter forming bond is 2.00 Å.



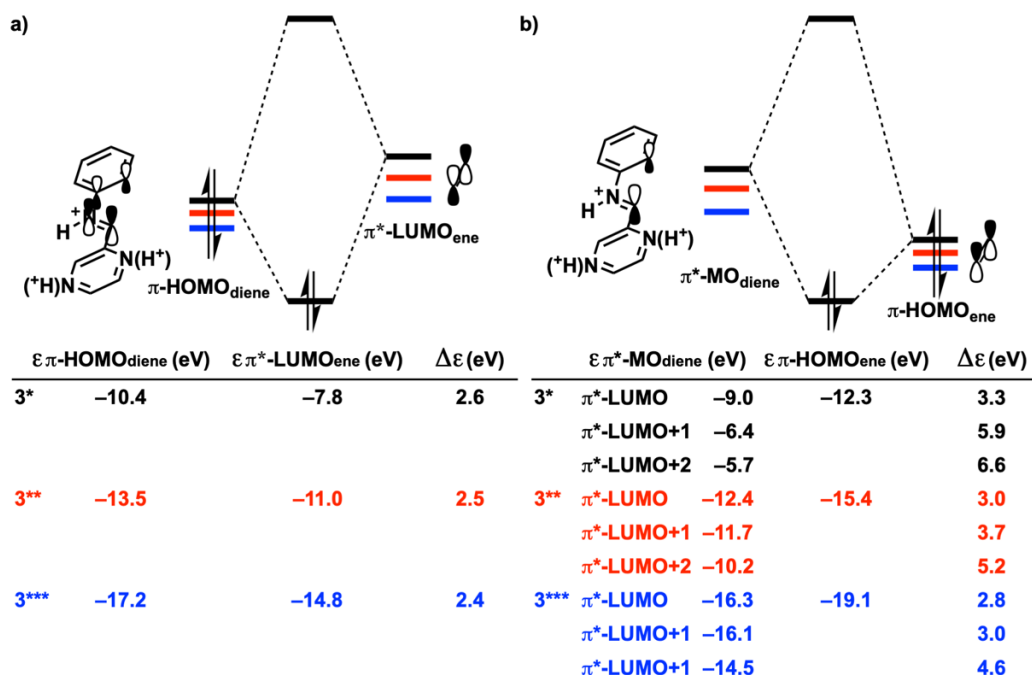
Appendix 7.8 a) Activation strain and b) energy decomposition analyses of aza-Diels-Alder reactions of **3** and **3*** with ethylene along the IRC projected onto the length of the shorter newly forming C...C bond, computed at BP86/TZ2P. The vertical dotted line indicates the consistent point where the distance of the shorter forming bond is 2.02 Å.



Appendix 7.9 a) Optimized and consistent (2.00 Å) geometries of **2** and **2***, and b) optimized and consistent (2.02 Å) geometries of **3** and **3***, including the geometric information within structures. All were computed at BP86/TZ2P.

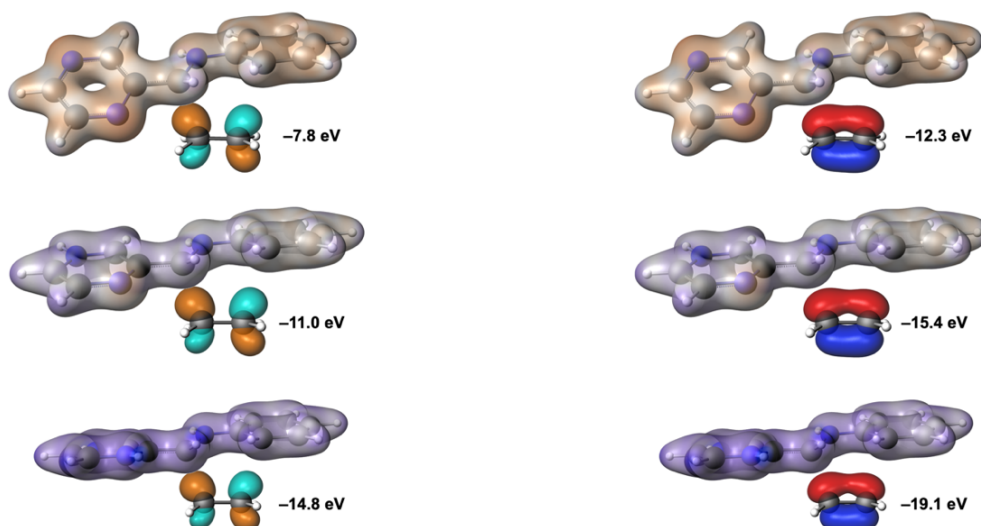


Appendix 7.10 Computed energies for the a) normal electron demand (NED) interactions between the filled orbitals of diene with the $\pi^*\text{-LUMO}_{\text{ene}}$ and b) inverse electron demand (IED) interactions between the $\pi^*\text{-MO}_{\text{diene}}$ with the filled orbitals of ethylene, for the aza-Diels-Alder reactions of **3***, **3****, and **3*****. The NED energies were obtained by deleting all virtual orbitals but the $\pi^*\text{-LUMO}_{\text{ene}}$, and the IED energies were obtained by deleting all virtual orbitals but the interacting $\pi^*\text{-MO}_{\text{diene}}$. NOCV deformation densities $\Delta\rho$ (isovalue = 0.002 au; electron flow: red \rightarrow blue) and associated energies $\Delta E(\rho)$ (in kcal mol⁻¹) for the c) NED and d) IED interactions of the aza-Diels-Alder reactions of **3***, **3****, and **3*****. All were computed at the consistent geometries (2.06 Å) at BP86/TZ2P.

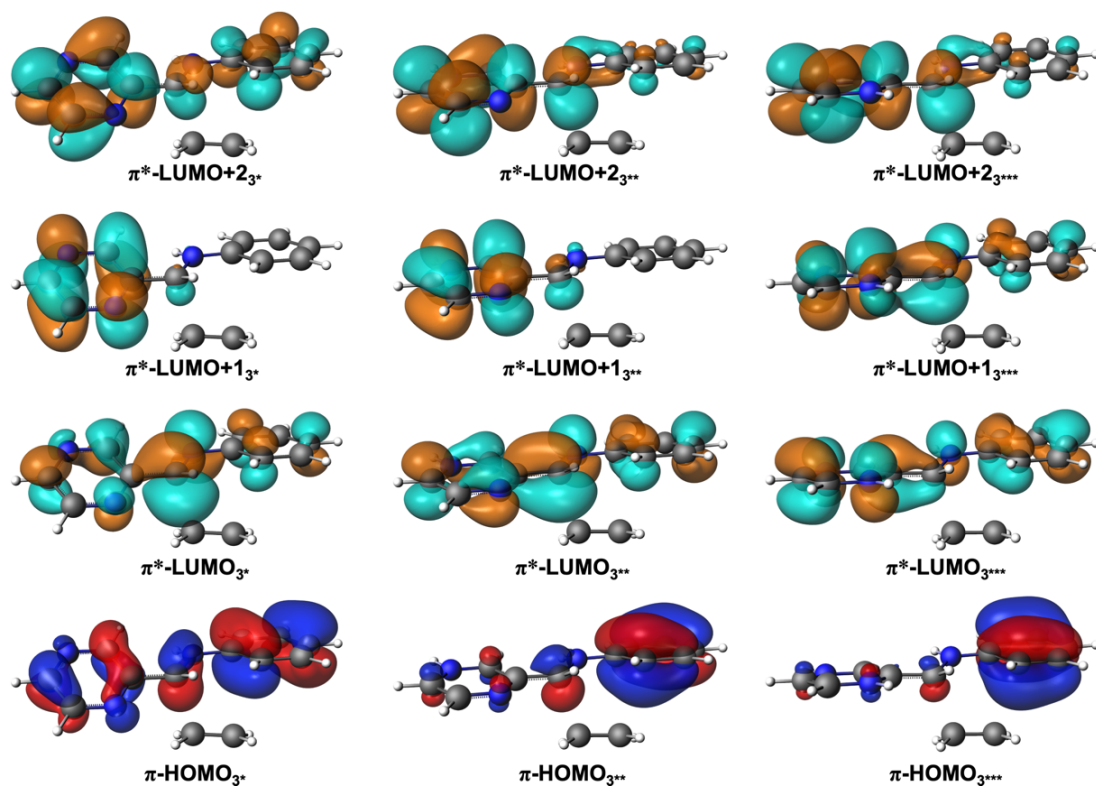


Appendix 7.11 Schematic diagrams of the a) normal electron demand (NED) interactions between the $\pi\text{-HOMO}_{\text{diene}}$ and $\pi^*\text{-LUMO}_{\text{ene}}$ and b) inverse electron demand (IED) interactions between the $\pi^*\text{-MO}_{\text{diene}}$ and $\pi\text{-HOMO}_{\text{ene}}$, with the computed orbital energies ϵ (in eV) and energy gaps $\Delta\epsilon$ (in eV), for the aza-Diels-Alder reactions of **3***, **3****, and **3*****. All data were computed at the consistent geometries (2.06 Å) at BP86/TZ2P.

■ Computed energies of $\pi^*\text{-LUMO}_{\text{ene}}$ in the presence of the charged dienes ■ Computed energies of $\pi\text{-HOMO}_{\text{ene}}$ in the presence of the charged dienes



Appendix 7.12 Electrostatic potential maps (at 0.06 Bohr^{-3}) from 0 (red) to +1 (blue) Hartree⁻¹ of the fragmental **3***, **3****, and **3*****, and the DFT-computed plots of the MOs (isovalue = $0.09 \text{ Bohr}^{-3/2}$) and energies of ethylene in proximity to the fragmental **3***, **3****, and **3*****. All data were computed in the consistent geometries (2.06 Å) at BP86/TZ2P.



Appendix 7.13 DFT-computed plots of the MOs (isovalue = 0.03 Bohr^{-3/2}) of the diene in the aza-Diels-Alder reactions of **3***, **3****, and **3***** at the consistent geometries (2.06 Å), computed at BP86/TZ2P.

Summary

Cycloaddition reactions provide facile access to cyclic compounds with a high atom economy. As such, these reactions have found applications in almost all fields of chemistry, including organic synthesis, material science, medicinal chemistry, and biological chemistry. In particular, the most studied and useful concerted cycloadditions (pericyclic reactions) are the Diels-Alder reaction and 1,3-dipolar cycloaddition. A systematic understanding of the reactivity, regio- and stereo-selectivity of pericyclic reactions is a prerequisite for the rational design of these reactions. This thesis is dedicated to a study of four critical factors that are used to tune the reactivity of pericyclic reactions: the heteroatom, geometry of the reactant, catalyst, and external electric field. These factors are studied by performing computational studies on four representative Diels-Alder reactions or 1,3-dipolar cycloadditions using DFT calculations and quantum chemical analyses, including the activation strain model (ASM), energy decomposition analysis (EDA) and quantitative Kohn-Sham molecular orbital (KS-MO) theory. Our findings based on these analyses furnish fundamental insights into how these internal and external factors alter the reactivity of cycloaddition reactions.

Firstly, we began with an introduction to the research subject and an overview of the theoretical background in Chapter 2 and 3, respectively. Then, in Chapter 3 we described a benchmark study of the DFT method for cycloaddition reactions, by using the composite ab initio method G3B3 as a reference. The performance of BP86, BP86-D3, PBE, PBE-D3, BLYP, BLYP-D3, and OLYP functionals with the TZ2P basis set was evaluated by reproducing the G3B3-computed activation and reaction enthalpies for 24 1,3-dipolar cycloadditions. After factoring in the performance and cost of the computational approach, the BP86/TZ2P method outperformed all other methods for computing the reactivity trends of cycloaddition reactions, and the BLYP-D3/TZ2P method would be the more suitable choice when non-covalent interactions are suspected to play a role. The BP86/TZ2P method was then selected to study all reactions in the following chapters.

In Chapter 4, we explored the effect of the heteroatom on the Diels-Alder reactivity of 1,3-butadiene (CCCC). It was determined that the replacement of carbon atoms by heteroatoms in 1,3-butadiene dramatically influences the Diels-Alder reactivity. 1,3-Butadienes with a single

terminal heteroatom (**NCCC** and **OCCC**) are much less reactive than **CCCC** and the replacement of a second terminal carbon by nitrogen or oxygen (**NCCN**, **NCCO**, **OCCO**) further decreases the Diels-Alder reactivity. Our Kohn-Sham molecular orbital (KS-MO) theory analyses revealed that this is due to the combined effect of a more contracted and lower-lying *p*-orbital on the heteroatom in the π -type highest occupied molecular orbital (π -HOMO) of the diene, which weakens the donor–acceptor orbital overlap and interaction with the LUMO of ethylene. On the other hand, the introduction of a nitrogen atom into the backbone (**CNCC**) furnishes a more reactive diene compared to **CCCC**, primarily due to a less destabilizing Pauli repulsion. This effect was traced back to the nature of the π -HOMO–1 of **CNCC** that is polarized towards the nitrogen and away from the terminal carbon. Consequently, the destabilizing four-electron two-center orbital interaction between the π -HOMO–1 of **CNCC** and the HOMO of ethylene is reduced. Lastly, an extra introduction of a nitrogen atom into the terminal site of **CNCC**, that is, **NNCC** and **NCNC**, yields even more reactive systems, due to the decreased number of terminal hydrogens that substantially reduces the activation strain for the reaction. This study shows that the Diels-Alder reactivity of hetero-1,3-butadienes is a delicate interplay between the overlaps of bond-forming orbitals, the energy levels of those orbitals, and the overlaps of filled orbitals on both substrates. These insights can be very valuable in the design of hetero-Diels-Alder reactions.

In Chapter 5, we sought to reveal the reactivity of allenes, a class of unsaturated compounds containing two consecutive double bonds, in 1,3-dipolar cycloadditions. This is a novel class of cycloaddition reactions developed recently that show enormous potential in organic synthesis and biological chemistry. We evaluated the effect of the heteroatoms on the 1,3-dipolar cycloaddition reactivity of allene. The archetypal allene propadiene (**CCC**) was found to be the most reactive one. Introducing the heteroatom to **CCC** makes it less reactive, due to the more destabilizing activation strain that emerges from the more rigid backbone, as well as the less stabilizing orbital interaction. More importantly, we also presented a study of the influence of geometry on the cycloaddition reactivity of allene. We found that the increased pre-distortion of allene that results upon cyclization can lead to systematically lowered activation barriers, not due to the expected reduced activation strain, but instead from the differences in the interaction energy. The geometrical pre-distortion of cycloallene enhances the cycloaddition reactivity compared to the linear allene through a unique mechanism that involves a smaller HOMO-LUMO gap, which manifests into more stabilizing orbital interactions.

After having established the rules and the underlying mechanisms of how heteroatoms and geometries influence the cycloaddition reactivity, we moved to study the external factors that can modulate the reactivity of cycloaddition reactions. In Chapter 6, we exploited how external electric fields tune the Diels-Alder reactions. Previous theoretical predictions, as well as experiments, have proven that the orientation of the external electric field can alter the reactivity and the *endo/exo* selectivity of the Diels-Alder reaction between cyclopentadiene (**Cp**) and maleic anhydride (**MA**): a positive electric field along the forming bonds ($F_z > 0$: positive end at **MA**, negative end at **Cp**) accelerates this reaction, whereas one oriented perpendicular to the plane of the forming bonds ($F_y > 0$: positive end at the double bond of **MA**, negative end at the anhydride group of **MA**) makes the *endo*-selective field-free Diels-Alder reaction *exo*-selective. Our ASM-EDA study unraveled that the reaction rate enhancement induced by a positive F_z is caused by both enhanced electrostatic and orbital interactions between the reactants. The former originates from an increased charge density difference between the reactants in the reactive region directly induced by the electric field. The positive F_z enhances the orbital interactions by promoting the electron transfer within the normal electron demand (NED) donor–acceptor interaction between the HOMO_{Cp} and LUMO_{MA} . In addition, for the *exo* pathway, a positive F_y can strengthen the orbital interactions by promoting the charge transfer from the HOMO_{Cp} to LUMO_{MA} . The *endo* pathway, on the other hand, remains nearly unaffected, owing to a mismatch between the orientation of the reactants and the electric field. As a result, the *endo*-selective field-free Diels-Alder reaction becomes an *exo*-selective Diels-Alder reaction under an adequately positive F_y . Interestingly, we also found that an F_z shows the opposite effect on the inverse electron demand (IED)-Diels-Alder reaction, where the most dominant orbital interaction occurs between the $\text{LUMO}_{\text{diene}}$ and the $\text{HOMO}_{\text{dienophile}}$. This orbital interaction, in contrast with the Diels-Alder reaction between **Cp** and **MA**, becomes strengthened under a negative F_z . Our results elucidated, for the first time, the physical factors that dictate the reactivity and stereoselectivity of Diels-Alder reactions under an external oriented electric field in the framework of the KS-MO theory. The knowledge obtained from this study can be applied to the understanding and design of more electrostatically catalyzed reactions.

In the last chapter, we turned our attention to study how the catalyst, another external factor, affects the cycloaddition reactivity. The representative Brønsted acid-catalyzed aza-Diels-Alder reactions of 2-aza-dienes were selected as our model. Previous experiments have shown that the protonation vastly enhances the reactivity of 2-aza-dienes in Diels-Alder reactions with ethylene.

Our studies based on the ASM and KS-MO theory revealed that the *mono*-protonation of 2-azadienes catalyzes the reactions by reducing the strain energy of the diene and the Pauli repulsion between the reactants. This is due to that the *mono*-protonated reaction adopts a more asynchronous reaction mode that demands less deformation of the terminal carbons of the diene and experiences a smaller overlap of the closed-shell orbital interaction. The previously expected “LUMO-lowering catalysis” is not the driving force, because the *mono*-protonated reaction goes with a poor orbital overlap of the IED interaction that offsets the LUMO-stabilization effect and ultimately leads to an unvaried IED interaction. On the other hand, the *multi*-protonation of 2-azadienes additionally enhances their reactivity by the “LUMO-lowering catalysis”. In this case, the *multi*-protonated dienes have such stabilized LUMO(s) that the LUMO-lowering effect becomes operative and the reactions of the *multi*-protonated 2-azadienes proceed via a more synchronous pathway which can facilitate the orbital overlaps of the orbital interactions. This study shows how “Pauli-lowering catalysis” can switch to “LUMO-lowering catalysis” when the degree of LUMO stabilization is extreme as in the case of the *multi*-protonated 2-azadienes. Moreover, we also established that Pauli-lowering catalysis and asynchronous TS structures occur if the reduction in Pauli repulsion is bigger than the loss in stabilizing NED and/or IED interactions whereas LUMO-lowering catalysis and synchronous TS structures occur if the gain in stabilizing NED and/or IED interactions is bigger than the increase in Pauli repulsion.

In summary, a great deal of effort has been devoted to understanding how the internal and external factors, including the heteroatom, geometry of the reactant, catalyst, and electric field, affect the cycloaddition reactivity. We selected to study four representative uncatalyzed/catalyzed cycloadditions via DFT calculations together with ASM and KS-MO analyses. Our fundamental insights obtained herein can serve as a toolbox for the rational design of cycloaddition reactions.

Samenvatting

Cycloadditiereacties verschaffen gemakkelijk toegang tot cyclische verbindingen met een hoge atomeconomie. Hierdoor hebben deze reacties toepassingen in bijna alle gebieden binnen de chemie, waaronder organische synthese, materiaalwetenschap, medicinale chemie en biochemie. De meest bestudeerde en bruikbare geconcentreerde cycloaddities (pericyclische reacties) zijn de Diels-Alderreactie en 1,3-dipolaire cycloadditie. Een systematisch begrip van de reactiviteit, regio- en stereoselectiviteit van pericyclische reacties is een voorwaarde voor het rationele ontwerp van deze reacties. Dit proefschrift is gewijd aan een studie van vier kritische factoren die worden gebruikt om de reactiviteit van pericyclische reacties te veranderen: het heteroatoom, de geometrie van de reactant, de katalysator en het externe elektrische veld. Deze factoren worden bestudeerd door computationele studies uit te voeren op vier representatieve Diels-Alderreacties of 1,3-dipolaire cycloaddities met behulp van DFT-berekeningen en kwantumchemische analyses, waaronder het activatie spannings model (ASM), energie decompositie-analyse (EDA) en kwantitatieve Kohn-Sham moleculaire orbitaal (KS-MO) theorie. Onze bevindingen, gebaseerd op deze analyses, verschaffen fundamentele inzichten in hoe deze interne en externe factoren de reactiviteit van cycloadditiereacties veranderen.

Acknowledgements

Throughout my four-year research work as a PhD student, I was fortunate to receive a great deal of guidance and support from my supervisor team, colleagues, friends, and family. I could not have accomplished such a challenging task without their help. As such, it is justified to conclude this thesis by expressing my deepest gratitude to them individually.

First, I would like to thank my supervisor team. Thanks to my esteemed supervisor, Prof. F. Matthias Bickelhaupt, for having me here study and carry out research in such a beautiful city with a group of excellent researchers. I am grateful for his guidance at every stage of my PhD project and insightful comments and suggestions in all of my studies. I admire his broad knowledge and deep understanding of chemistry. The way he conducts himself in science and life will also inspire me in my life and research career. I would like to say many thanks to my co-supervisor, Dr. Trevor A. Hamlin, for his daily supervision. I appreciate his careful guidance on conducting research, writing papers, and making presentations throughout the entire course of my PhD study. I have learned a lot from his meticulous attitude toward science and his extraordinary enthusiasm for chemistry.

I am indebted to Prof. Célia Fonseca Guerra for her encouragement and inspirational talks in the past four years; Xiaobo for his hands-on teaching in ADF and PyFrag, the most important tools used throughout this thesis; and Pascal for his close involvement and excellent collaboration in multiple works.

I am grateful to my old and new R-158 office colleagues: Ayush, Francesco, Zakaria, Hans, Nicolai, Eva, Celine, and Stephanie. Additionally, I want to thank more TheoChem members: Bryan, Dani, Lucas, Marco, Stephanie ten Brinck, Thomas, Eveline for their valuable sharing and discussion about science as well as life during every online meeting. Thanks to all the TC members: Arno, Bas, Chandan, Enrico, Jelena, Johann, Souloke, Stan.

I would like to thank my family for their unwavering support and belief in me. A special thanks to my girlfriend, Dr. Jia-Li Chen, for her daily love and encouragement.

List of Publications

1. “Switch from Pauli-Lowering to LUMO-Lowering Catalysis in Brønsted Acid-Catalyzed Aza-Diels-Alder Reactions”

S. Yu, F. M. Bickelhaupt, and T. A. Hamlin

ChemistryOpen **2021**, *10*, 784–789.

2. “How Oriented External Electric Fields Modulate Reactivity”

S. Yu, P. Vermeeren, T. A. Hamlin, F. M. Bickelhaupt,

Chem. Eur. J. **2021**, *27*, 5683–5693.

3. “Understanding the 1,3-Dipolar Cycloadditions of Allenes”

S. Yu, P. Vermeeren, K. van Dommelen, F. M. Bickelhaupt, T. A. Hamlin

Chem. Eur. J. **2020**, *26*, 11529–11539.

4. “Elucidating the Trends in Reactivity of Aza-1,3-Dipolar Cycloadditions”

T. A. Hamlin, D. Svatunek, S. Yu, L. Ridder, I. Infante, L. Visscher, F. M. Bickelhaupt

Eur. J. Org. Chem. **2019**, 378–386.

5. “Factors Controlling the Diels-Alder Reactivity of Hetero-1,3-Butadienes”

S. Yu, H. M. de Bruijn, D. Svatunek, T. A. Hamlin, F. M. Bickelhaupt

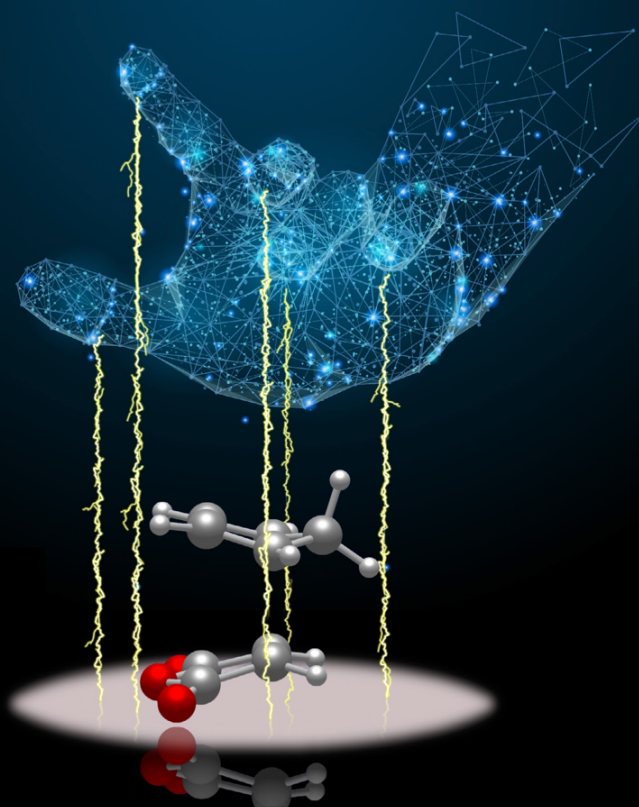
ChemistryOpen **2018**, *7*, 995–1004.

Chemistry A European Journal

 **Chemistry
Europe**
European Chemical
Societies Publishing

Cover Feature:

T. A. Hamlin, F. M. Bickelhaupt et al.
How Oriented External Electric Fields Modulate Reactivity



18/2021

WILEY-VCH